

© 2019 by Robert Shannon Heitz. All rights reserved.

TRANSVERSE MOMENTUM DEPENDENT NUCLEON STRUCTURE FROM PIONS  
IMPINGED ON A TRANSVERSELY POLARIZED PROTON TARGET

BY

ROBERT SHANNON HEITZ

DISSERTATION

Submitted in partial fulfillment of the requirements  
for the degree of Doctor of Philosophy in Physics  
in the Graduate College of the  
University of Illinois at Urbana-Champaign, 2019

Urbana, Illinois

Doctoral Committee:

Associate Professor Liang Yang, Chair  
Professor Matthias Grosse Perdekamp, Co-Director of Research  
Research Assistant Professor Caroline Riedl, Co-Director of Research  
Professor John Stack  
Professor Alexey Bezryadin

# Abstract

The transverse momentum structure of the nucleon generalizes the 1-dimensional parton distribution functions (PDFs) to a 3-dimensional description. The extended distributions are called transverse momentum dependent (TMD) parton distribution functions. TMD functions include transverse quark and gluon momentum to parameterize the non-perturbative description of a nucleon. Eight TMDs parameterize a nucleon at leading order. The Sivers TMD is special in that it is spin-dependent and theorized to change signs between the Drell-Yan process and Semi-Inclusive Deep Inelastic Scattering (SIDIS).

The COMPASS spectrometer is unique in that it has the ability to measure the products from a polarized target and also because the beam can be modified to measure the SIDIS and Drell-Yan processes. The COMPASS collaboration collected transverse spin-dependent data to measure the Sivers function from SIDIS and in 2016 COMPASS published the results of a Sivers asymmetry amplitude from the SIDIS process. In 2015 COMPASS collected data to study the Drell-Yan process from a transversely polarized proton target and a  $190 \text{ GeV}/c^2$  negatively charged pion beam. Therefore COMPASS has the unique ability conclude on the non-universality of the Sivers TMD between the SIDIS and Drell-Yan processes.

This thesis presents analysis of the 2015 COMPASS Drell-Yan data taking. The analysis focuses on the Sivers TMD but also provides results on the transversity and pretzelosity TMD functions which are expected to be universal. The Sivers results presented in this thesis are consistent with a sign flip between Drell-Yan and SIDIS.

*To my parents for always supporting me.*

# Acknowledgments

I would like to thank my co-advisors Caroline Riedl and Matthias Grosse Perdekamp for giving me the opportunity to learn about new and interesting physical phenomena and as well for giving me the opportunity to learn about different cultures. I would like to thank Vincent Andrieux for many interesting discussions both about physics and life in France.

I would like to thank the funding agencies for make this research possible. This research is part of the Blue Waters sustained-petascale computing project, which is supported by the National Science Foundation (awards OCI-0725070 and ACI-1238993) and the state of Illinois. Blue Waters is a joint effort of the University of Illinois at Urbana-Champaign and its National Center for Supercomputing Applications. This work is also part of the "Mapping Proton Quark Structure using Petabytes of COMPASS Data" PRAC allocation supported by the National Science Foundation (award number OCI 1713684 ).

Lastly I would like to acknowledge my cat Fox Trot for being both a source of stress and an anxiety reliever.



Fox Trot

# Table of Contents

<b>List of Tables . . . . .</b>	<b>viii</b>
<b>List of Figures . . . . .</b>	<b>ix</b>
<b>Chapter 1 Introduction . . . . .</b>	<b>1</b>
<b>Chapter 2 Theoretical and Experimental Overview . . . . .</b>	<b>3</b>
2.1 Deep Inelastic Scattering . . . . .	3
2.2 The Parton Model . . . . .	5
2.3 Transverse Momentum Dependence . . . . .	7
2.3.1 Sivers and Boer-Mulders Distributions . . . . .	10
2.3.2 Transversity and Pretzelosity . . . . .	11
2.4 Semi-Inclusive Deep Inelastic Scattering . . . . .	11
2.4.1 SIDIS TMD Results . . . . .	15
2.5 Drell-Yan . . . . .	17
2.5.1 Drell-Yan Sivers Result . . . . .	21
2.5.2 Left-Right Asymmetry . . . . .	21
2.5.3 Weighted Asymmetries from Drell-Yan . . . . .	24
2.5.4 J/ $\Psi$ Production . . . . .	27
<b>Chapter 3 The COMPASS Experiment at CERN . . . . .</b>	<b>29</b>
3.1 The Beam . . . . .	31
3.1.1 Muon Beam . . . . .	31
3.1.2 Hadron Beam . . . . .	33
3.1.3 Additional Beam Line Components . . . . .	33
3.2 The Polarized Target . . . . .	35
3.3 Tracking Detectors . . . . .	38
3.3.1 Very Small Angle Trackers . . . . .	38
3.3.2 Small Angle Trackers . . . . .	39
3.3.3 Large Area Trackers . . . . .	41
3.4 Particle Identification . . . . .	44
3.5 Trigger . . . . .	47
3.6 Data Acquisition . . . . .	50
3.7 Data Reconstruction . . . . .	50
3.7.1 Monte-Carlo Production . . . . .	51
3.8 2015 Drell-Yan Data Taking . . . . .	52
3.8.1 Hadron Absorber . . . . .	52

<b>Chapter 4 Drift Chamber 05 . . . . .</b>	<b>54</b>
4.1 Motivation for Drift Chamber 05 . . . . .	54
4.2 Operating Principle . . . . .	54
4.3 Preparation for DC05 . . . . .	57
4.4 Design . . . . .	59
4.5 Construction . . . . .	61
4.6 2015 Performance . . . . .	63
<b>Chapter 5 Spectrometer Alignment . . . . .</b>	<b>66</b>
5.1 Data Sample to Align the Spectrometer . . . . .	67
5.2 Procedure . . . . .	68
5.3 Results . . . . .	73
<b>Chapter 6 Analysis of High Mass Drell-Yan Transverse Spin Phenomena . . . . .</b>	<b>77</b>
6.1 Data Sample . . . . .	77
6.1.1 Data Collection . . . . .	77
6.1.2 Stability Tests . . . . .	78
6.1.3 Event Selection . . . . .	80
6.1.4 Binning . . . . .	82
6.1.5 Analysis Notation . . . . .	83
6.2 Transverse Spin-Dependent Asymmetries . . . . .	83
6.3 Double Ratio Analysis . . . . .	86
6.3.1 Asymmetry Extraction . . . . .	86
6.3.2 Results . . . . .	89
6.4 $q_T$ -Weighted Asymmetries . . . . .	90
6.4.1 Event Selection . . . . .	91
6.4.2 Binning . . . . .	91
6.4.3 Asymmetry Method . . . . .	91
6.4.4 Results . . . . .	94
6.5 Left-Right Asymmetries . . . . .	94
6.5.1 Asymmetry Extractions . . . . .	95
6.5.2 Systematic Studies . . . . .	99
6.5.3 Results . . . . .	109
<b>Chapter 7 J/<math>\Psi</math> Transverse Spin Dependent Phenomena . . . . .</b>	<b>113</b>
7.1 Data Collection and Event Selection . . . . .	113
7.1.1 J/ $\Psi$ Invariant Mass Range . . . . .	114
7.2 Binning . . . . .	117
7.3 Asymmetry Extraction . . . . .	119
7.4 Systematic Studies . . . . .	120
7.4.1 Period Compatibility (Time Dependence) . . . . .	120
7.4.2 Left/Right Event Migration . . . . .	123
7.4.3 J/ $\Psi$ Purity . . . . .	123
7.4.4 False Asymmetries . . . . .	124
7.4.5 Total Systematics . . . . .	127
<b>Chapter 8 Conclusion . . . . .</b>	<b>132</b>
<b>References . . . . .</b>	<b>133</b>
<b>Appendix A Systematic Error Derivations . . . . .</b>	<b>140</b>
A.1 Systematic Error From Acceptance . . . . .	140
A.2 Systematic Error From Left-Right Event Migration . . . . .	141
A.3 Systematic Error From Event Contamination . . . . .	141

<b>Appendix B Cross-Check . . . . .</b>	<b>143</b>
B.1 Left-Right Asymmetry Cross-Check . . . . .	143

# List of Tables

5.1	COMPASS 2015 alignment data runs . . . . .	68
6.1	COMPASS 2015 data taking periods . . . . .	78
6.2	Stability analysis rejection percentages . . . . .	80
6.3	Numbers of selected di-muon events in this analysis of 2015 COMPASS data . . . . .	82
6.4	Analysis binning limits . . . . .	83
6.5	Notations used for defining the asymmetry analysis . . . . .	83
6.6	Measured counts as a function of each $\Phi$ angle . . . . .	88
6.7	Monte-Carlo settings produced on Blue Waters . . . . .	101
6.8	Summary of systematic error impacts from false asymmetries. The maximum systematic error is chosen as the systematic error. . . . .	107
6.9	Summary of systematic uncertainty impacts to the integrated asymmetry . . . . .	109
7.1	J/ $\Psi$ purity as a function of the invariant mass range . . . . .	117
7.2	Selected dimuon events for the first five data periods from the intermediate mass range analysis of 2015 COMPASS data . . . . .	117
7.3	Selected dimuon events for the last four data periods and the total number of events from the intermediate mass range analysis of 2015 COMPASS data . . . . .	118
7.4	COMPASS spectrometer resolutions in the intermediate mass range 2.5-4.3GeV/ $c^2$ . . . . .	119
7.5	The J/ $\Psi$ analysis bin limits for the four analysis bins . . . . .	119
7.6	Summary of systematic error impacts from false asymmetries changes in time. The maximum systematic error is chosen as the systematic error. . . . .	127
7.7	Summary of systematic error impacts to the integrated asymmetry . . . . .	128

# List of Figures

2.1	The leading order Feynman diagram for deep inelastic scattering . . . . .	3
2.2	The $F_2$ structure function of the proton measured by several experiments. Note that the data is shifted up by a factor $2^{i_x}$ to see the $x$ dependence. Image taken from [11]. . . . .	6
2.3	The spin-independent parton distribution functions times the momentum fraction. The different colors correspond to different quarks or gluons. Image taken from [11]. . . . .	8
2.4	The longitudinally polarized parton distribution functions times the momentum fraction for the u-quark (top) and the d-quark (bottom) in a proton. Image taken from [11] . . . . .	8
2.5	The eight TMDs needed to describe a spin 1/2 nucleon at leading order. The columns represent the different nucleon polarizations and the rows represent the different quark polarizations. The individual figures give a visual representation of the TMD's interpretation. This image taken from [24]. . . . .	9
2.6	The semi-inclusive deep inelastic scattering leading order Feynman diagram . . . . .	11
2.7	The $\gamma$ -nucleon lab frame, where the target nucleon is at rest and the virtual photon momentum is pointing along the z-axis. The lepton scattering plane defines the xz-plane where the outgoing lepton defines the positive x-direction. This image was taken from [14]. . . . .	13
2.8	The asymmetry amplitude related to the Sivers function measured by COMPASS [28] and HERMES [29] . . . . .	15
2.9	The valence quark distributions for the first moment of the Sivers function. The left plots are using TMD evolution and the right plots are using $Q^2$ evolution to globally include all measured data. This image was taken from [30] . . . . .	16
2.10	COMPASS SIDIS data from muons scattered off of a deuteron target for positively scattered hadrons (red) and negatively scattered hadrons (black). The asymmetry amplitude is related to the Boer-Mulders functions. This image was taken from [31] . . . . .	17
2.11	The transversity distribution for u-quarks (top) and d-quarks (bottom) determined from SIDIS data and $e^+e^-$ data. Image taken from [42]. . . . .	17
2.12	The Drell-Yan leading order diagram . . . . .	18
2.13	Drell-Yan analysis frames. . . . .	18
2.14	All plots show a left-right asymmetry from STAR data which is related to the Sivers function. The top right plot is for $Z^0$ production while the other three plots are for $W^\pm$ production. $Q^2$ evolution and resulting error bars from EIKV [46] and KQ [47]. Image taken from [45]. . . . .	22
2.15	Large $A_N$ values where found at ANL [6], BNL [48], FNAL [49, 50] and RHIC [51]. . . . .	24
3.1	The CERN experiments and accelerators. This figure is taken from [63]. . . . .	30
3.2	A schematic of the 2015 COMPASS setup. This figure was taken from [65]. . . . .	30
3.3	The M2 beam line at CERN. This image is taken from [66]. . . . .	32
3.4	Bending the beam to a horizontal position. The BMS detectors (green boxes) are upstream and downstream of the bend 6 magnet (red triangle labeled B6). This image was taken from [64].	33
3.5	The momentum distribution of the $\pi^-$ beam, determined during dedicated low intensity beam conditions. This figure was taken from [67]. . . . .	34
3.6	Light lines emitted inside CEDARs at COMPASS. The red(green) lines correspond to Cherenkov light emitted from a particle lower(higher) momentum. This image is taken from [66]. . . . .	34

3.7	The polarized target at COMPASS. This image taken from [68]. . . . .	35
3.8	The empty polarized target cells side by side along with their NMR coil positions. This image taken from [72]. . . . .	37
3.9	Principle of operation for the micromesh gaseous structures (micromegas). This image was taken from [64]. . . . .	40
3.10	The operation principle of the gas electron multiplier (GEM) detectors. This image was taken from [64]. . . . .	41
3.11	Side view of a drift cell in a drift chamber with the ionized drift electron lines coming from the incident charged particle. The larger circles (green) represent field wires and the smaller circles (blue) represent sense wires. This image was taken from [64]. . . . .	42
3.12	Front on view of a the active area of a straw detector at COMPASS. This image was taken from [64]. . . . .	43
3.13	The richwall mini drift tubes. This image is taken from [66]. . . . .	43
3.14	Side view demonstrating the principle of operation of the RICH detector. This image was taken from [64]. . . . .	45
3.15	Frontal view of the electromagnetic calorimeter 1. This image is taken from [66]. . . . .	45
3.16	Frontal view of the electromagnetic calorimeter 2. This image is taken from [66]. . . . .	46
3.17	A side view sketch of the muon wall 1 detector. This image was taken from [64]. . . . .	47
3.18	Top view of the spectrometer highlighting how different particles can signal a trigger. This image was taken from [74]. . . . .	48
3.19	The two types of triggers (left is target pointing and right is energy loss) at COMPASS and an illustration of the coincidence matrix used to select events of interest. This image was taken from [75]. . . . .	48
3.20	The kinematic coverage for the 2015 triggers determined from Monte-Carlo studies. This image was taken from [76]. . . . .	49
3.21	The hadron absorber downstream of the polarized target in 2015. This image was taken from [76]. . . . .	53
3.22	Side view of the hadron absorber used in 2015. This image was taken from [76]. . . . .	53
4.1	Reconstruction with and without DC05 included. . . . .	55
4.2	View down the axis of a drift cell and the equal voltages for this drift cell configuration. This image is taken from [83] . . . . .	56
4.3	A simulation of the position resolution as a function of the number of primary electrons needed to record a signal. This image is taken from [83]. . . . .	57
4.4	Garfield simulation of the induced signal current versus the arrival time. The green line corresponds to the arrival time of the fifth election. This image is taken from [83]. . . . .	58
4.5	Inside view of prototype A. This image was taken from [85]. . . . .	58
4.6	The completed DC05 being craned into the COMPASS large area spectrometer. . . . .	59
4.7	A side view sketch of the layers in DC05. This image taken from [86]. . . . .	60
4.8	The drift cell dimensions of one plane in DC05. This image taken from [86]. . . . .	60
4.9	Stretching mylar on a cathode plane at CERN . . . . .	62
4.10	Hand soldering DC05 wires in the clean room at the NPL . . . . .	62
4.11	The process of stacking the G-10 frames at CERN . . . . .	62
4.12	Two dimensional efficiency on the DC05Y1 plane. The center region with zero efficiency is a result of the beam killer. This image taken from [87]. . . . .	64
4.13	Time versus position relation, or RT relation, after calibrating. The red fit shows the calibration determined. This image taken from [87] . . . . .	64
4.14	The double residual distribution for the U plane together with a Gaussian fit in red to determine the variance of the distribution. This image taken from [87]. . . . .	65
5.1	An exaggerated alignment example where the reconstructed track (blue) is in a different location than the true track position (red). The alignment minimizes the residual distance (purple) for all the detectors in the spectrometer and tracks in the data sample. . . . .	67
5.2	The residual distribution for a straw detector plane . . . . .	74

5.3	The residual as a function of the detector v-coordinate for a straw detector . . . . .	75
5.4	The residual as a function of the detector u-coordinate for a straw detector . . . . .	75
5.5	The reduced $\chi^2$ from alignment data tracks . . . . .	76
6.1	Basic pictorial setup of the target region in 2015 COMPASS Drell-Yan data collection. . . . .	78
6.2	The 2015 COMPASS invariant dimuon mass distribution and a fit to this data. The data fit is from Monte-Carlo and combinatorial background analysis and is provided to show the background processes. This image is taken from [90]. . . . .	84
6.3	High mass Drell-Yan kinematic variables: $q_T$ and $x_N$ vs. $x_\pi$ . . . . .	85
6.4	The integrated TSAs with statistical error bars and systematic uncertainty bands. $A_T^{\sin(\phi_S)}$ , $A_T^{\sin(2\phi_{CS}+\phi_S)}$ , and $A_T^{\sin(2\phi_{CS}-\phi_S)}$ are leading order TSAs and $A_T^{\sin(\phi_{CS}+\phi_S)}$ and $A_T^{\sin(\phi_{CS}-\phi_S)}$ are sub-leading order TSAs. . . . .	85
6.5	The Sivers TSA along with theory curves for the expected sign change (solid curves) and without the sign change (opaque curves). Theory curves and uncertainties are calculated using $Q^2$ evolution from DGLAP [91], TMD-1 [92], TMD-2 [93]. This image is taken from [90].	86
6.6	An example double ratio and corresponding fit (red) to determine the amplitude $A_T^{\sin(2\phi-\phi_S)}$ . . . . .	89
6.7	The results and statistical error bars for the transverse spin-dependent asymmetry amplitudes $A_T^{\sin \phi_S}$ (top), $A_T^{\sin(2\phi+\phi_S)}$ (middle) and $A_T^{\sin(2\phi-\phi_S)}$ (bottom) determined from the double ratio method. . . . .	90
6.8	$q_T$ distributions without and with momentum conservation cuts. . . . .	92
6.9	Event selection statistics for $q_T$ -weighed asymmetry analysis from all periods combined . . . . .	92
6.10	The double ratio as a function of $\phi_S$ used to determine the Sivers asymmetry amplitude. This is for period W07 and the lowest bin in $x_N$ . The red line shows the fit. The results of the fit are shown in the statistics box. . . . .	94
6.11	The comparison of weighted asymmetry amplitude results from the released values from Jan Matousek (black) and the cross checker Robert Heitz (red). From the top row down the asymmetry amplitudes are $A_T^{\sin(\phi_S)q_T/M_N}$ , $A_T^{\sin(2\phi+\phi_S)q_T^3/(2M_\pi M_N^2)}$ and $A_T^{\sin(2\phi-\phi_S)q_T/M_\pi}$ respectively.	95
6.12	The definition of the left plane (red) and right plane (green) defined from a target spin up configuration in the target frame . . . . .	96
6.13	$A_{lr}$ determined for each period . . . . .	99
6.14	Pull distribution from the two-target geometric mean . . . . .	100
6.15	Uncorrelated pull distributions and Results of the Gaussian fit for the pull distributions . . . . .	101
6.16	The rate of identified correctly and incorrectly left-right events as a function of $\phi_S$ . This is determined by comparing the generated outgoing direction with the reconstructed outgoing direction. The left-right boundary is clearly visible at $\phi_S = 0$ rad and $\phi_S = -\pi$ rad and $\phi_S = \pi$ rad . . . . .	102
6.17	Percent left-right migration as a function of the amount of $\phi_S$ cut. . . . .	103
6.18	False asymmetry, $A_{lr, False}$ , to estimate fluctuations in acceptance in time . . . . .	104
6.19	Acceptance ratio $\alpha_{\text{pha2Targ}}$ , Eq. 6.34, used to determine the systematic effects from acceptance changes in time . . . . .	104
6.20	Systematic uncertainty due to acceptance effects normalized to the statistical error. . . . .	105
6.21	Two-target geometric mean false asymmetry. This is non-zero due to acceptance effects . . . . .	106
6.22	Uncorrelated pulls of the two-target geometric mean false asymmetry and Gaussian fit results . . . . .	107
6.23	One target false asymmetries for the upstream target (red) and the downstream target (blue), as a function of $x_N$ . Each graph is from a different period in time. . . . .	108
6.24	Pull values from one-target geometric mean false asymmetries. Both upstream and downstream values are used to make this pull . . . . .	108
6.25	Pull distribution for a nearly acceptance free two-target false geometric mean asymmetry . . . . .	109
6.26	$A_{lr}$ determined from the geometric mean method for the upstream target cell (red) and the downstream target cell (blue) for all kinematic binnings . . . . .	110
6.27	$A_{lr}$ determined by the two-target geometric mean method for all kinematic binnings . . . . .	110
6.28	The left-right asymmetry adjusted (analyzing power, blue) to be compared with Sivers amplitude determined from the double ratio method (red). . . . .	111

6.29	Including the left-right asymmetry to show it's compatibility with the sign flip.	112
7.1	The 2015 COMPASS invariant dimuon mass distribution and a fit to this data. The data fit is from Monte-Carlo and combinatorial background analysis and is provided to show the background processes. The shaded blue region shows the analysis mass range for the analysis in this chapter. This image is taken from [90].	115
7.2	The normalized invariant mass distributions from the four simulated Monte-Carlo processes. These distributions are used to fit the real data.	116
7.3	An example of the Monte-Carlo fit to real data in one $q_T$ bin of the real data. This fit is used to determine the distribution of J/ $\Psi$ purity.	117
7.4	The distribution of generated $x_N$ minus reconstructed $x_N$ . The leading Gaussian width (red) is used to determine the resolution.	118
7.5	The binning variable distributions. The longitudinal momentum fractions $x_N$ (top left) and $x_\pi$ (top right) and the $x_F$ (bottom left) and the virtual photon transverse momentum $q_T$ (bottom right). These distributions are plotted from in the mass range 2.87-3.38 GeV/ $c^2$ .	119
7.6	The left-right asymmetry in the J/ $\Psi$ mass region as a function of time. The red line is a constant fit and therefore shows the weighted averaged of the periods.	121
7.7	The left-right asymmetry time fluctuations in each bin of $x_N$ .	121
7.8	The uncorrelated pull distributions for each of the kinematical variables and a pull distribution from the integrated asymmetry from each time period.	122
7.9	The left-right migration as a function of the generated $\phi_S$ angle in the mass range 2.87-3.38.	123
7.10	Acceptance fluctuations in each bin of the kinematic variables.	124
7.11	Systematic error divided by statistical error due to acceptance	125
7.12	Pull distribution for a nearly acceptance free two-target false geometric mean asymmetry	126
7.13	Pull distributions from the false asymmetry in the upstream target cell	126
7.14	Pull distributions from the false asymmetry in the downstream target cell	127
7.15	The integrated left-right asymmetry from the mass range 2.87-3.38 GeV/ $c^2$ . The systematic error bands are shown in red at the bottom of the plot.	128
7.16	The kinematic dependencies of the left-right asymmetry from the mass range 2.87-3.38 GeV/ $c^2$ .	129
7.17	Predictions for the analyzing power, $A_N$ , from J/ $\Psi$ production at COMPASS as a function of $x_N$ and $q_T$ . This image was taken from [62].	130
7.18	The analyzing power at COMPASS determined by modifying the left-right asymmetry as a function of $x_N$ and $q_T$ to be compared with the predictions in Fig. 7.17.	130
7.19	J/ $\Psi$ production cross-section from gluon-gluon fusion (blue) and quark-quark annihilation (red) and the sum (black) as a function of $x_F$ . This plot is made assuming the color evaporation model [58].	131
7.20	The Sivers amplitude determined from the left-right asymmetry with theory curves for no gluon contamination (gray), 51% gluon fusion (magenta) and 63% gluon fusion (purple).	131
B.1	The left-right asymmetry without corrections for polarization or dilution factor from the W07 period. The values from this thesis are the black circles and the cross-check values are the red triangles.	143

# Chapter 1

## Introduction

More than 100 years ago, Rutherford's famous scattering experiment discovered the atom was composed of a small but massive nucleus [1]. Rutherford scattered high energy particles off a fixed target and by measuring the angular products was able to propose the existence of a nucleus. His technique provided the blue prints to study the nucleus over the next century and with higher energies and new probes the nucleus was as well found to have a substructure. The nucleus is now known to be composed of protons and neutrons which are collectively called nucleons.

With still higher energy scattering experiments the nucleons were found to be composite particles as well. In 1964 Gell-Mann and Zweig proposed the quark model to describe the substructure of nucleons [2, 3]. In the quark model the proton is composed of two u-quarks and a d-quark. Quarks were defined as elementary particles with fractional electric charge and a spin of  $1/2$ . Later Feynman proposed the parton model to explain the results of deep inelastic scattering (DIS) experiments [4]. In the parton model, DIS takes place between a distribution of partons inside a nucleon. The parton was defined as a point like particle which can be either a quark or a gluon. Later these two theories were unified by the theory of quantum chromodynamics (QCD) which describes the nucleon as being held together by force carrier gluons. In the QCD model, a nucleon is composed of a distribution of valence quarks surrounded by sea quarks and gluons. The valence quarks are responsible for the charge of the nucleon as the sea quarks occur in quark-antiquark pairs of net zero electric charge. QCD is now the accepted theory for describing the dynamics inside a nucleon.

While there is a theory to describe the quark and gluon interactions, there is currently no theory to describe the bound dynamics of quarks and gluons inside a nucleon. Instead the bound nuclear properties are input as parameters. High energy hadron scattering can be factorized as a hard scattering process multiplied by a soft non-perturbative scattering process. The hard scattering can be calculated ab initio using perturbative QCD, while the soft scattering, on the other hand, is parameterized as the hadron structure or a fragmentation process. Both the hadron structure and fragmentation processes are determined experimentally as either parton distribution functions (PDF) or fragmentation functions (FF) respectively. The former describes how quarks and gluons are bound in a hadron while the latter describes the probability

for a quark to fragment into a detectable hadron.

The quark and gluon parton distribution functions (PDFs) have been determined with increasing precision from QCD analysis of DIS, Drell-Yan and semi-inclusive deep inelastic scattering (SIDIS) high energy experiments. When the scattered nucleon has large momentum, the PDFs describe the parton distributions in longitudinal momentum space along the direction of the nucleon's momentum. The most recent theories of the nucleon attempt to give a three dimensional tomographic image of the quark and gluon structure which extend beyond the longitudinal picture to include transverse effects. The extended distributions include either transverse position or transverse momentum to the parton's longitudinal momentum. The former are described by generalized parton distributions (GPD) and the latter are described by transverse momentum dependent (TMD) PDFs. This thesis focuses on TMDs.

A unique way to probe TMDs is by studying transverse spin effects. Polarizing the nucleon transverse to its momentum gives access to the internal nucleon structure which cannot be accessed from spin-independent experiments. As an example the Sivers TMD PDF is a correlation between transverse spin of the nucleon and transverse momentum of a constituent parton [5]. It therefore makes sense that the only way to measure the Sivers function is through experiments with a transversely polarized target or beam.

The first TMDs were proposed to explain the results from large single-spin asymmetries (SSA). A SSA is defined as a normalized difference between spin related counts from a given reaction. One SSA, for example, is the normalized difference between left and right counts from collisions of a transversely polarized beam. This left-right asymmetry was first measured in 1976 and found to be non-zero in proton-proton collisions [6]. The Sivers function was proposed to describe large SSAs which lead to a the theoretical frame work of TMDs and is the subject of this thesis.

This thesis is organized into nine chapters. Chapter 2 provides the theoretical and experimental background needed to describe the analysis results in this thesis. Chapter 3 describes the data taking setup, particularly by describing the experimental apparatus and the beam. Chapter 4 gives details on the DC05 large area drift chamber which was needed for data taking and which the author of this thesis helped construct and maintain. Chapter 5 provides details on the spectrometer alignment which is a crucial preprocessing step for reconstructing data and which the author of this thesis was responsible for in 2015. Chapters 6- 7 go over the author's analysis techniques, results and conclusions and chapter 8 provides a final summary and conclusion.

## Chapter 2

# Theoretical and Experimental Overview

### 2.1 Deep Inelastic Scattering

To understand the structure of the nucleon it is useful to first introduce the original process that describes the nucleon as having a sub-structure. This process is the Deep Inelastic Scattering (DIS) process where a point-like lepton impinges on a nucleon denoted as

$$l(\ell) + N(P) \rightarrow l(\ell') + X(P_X), \quad (2.1)$$

where  $l$  denotes a lepton,  $N$  denotes a nucleon,  $X$  represents all products not detected and  $\ell, \ell', P$  and  $P_X$  are the four momenta for their respective lepton or nucleon. This process is an electromagnetic reaction where a lepton is scattered via virtual photon exchange with the nucleon. The leading order Feynman diagram for this reaction is shown in Fig. 2.1.

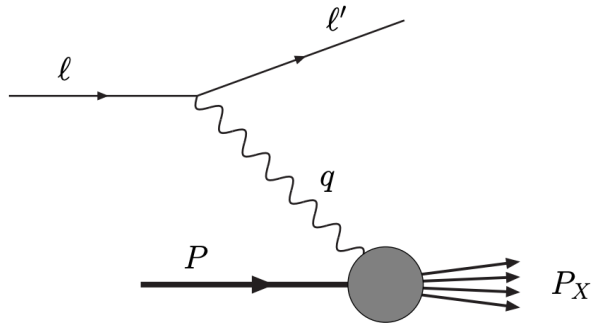


Figure 2.1: The leading order Feynman diagram for deep inelastic scattering

DIS was initially studied with a high energy lepton beam and a fixed nuclear target. The initial state kinematics are described by

$$s = (\ell + P)^2 \quad \text{or} \quad E, \quad (2.2)$$

where  $s$  is the center of mass energy and  $E$  is the energy of the lepton beam. The detected reaction kinematics in the lab frame are described by

$$Q^2 = -q^2 = -(\ell - \ell')^2 \approx EE'(1 - \cos \theta), \quad (2.3)$$

$$x = \frac{Q^2}{2P \cdot q} = \frac{Q^2}{2M\nu}, \quad (2.4)$$

$$\nu = E - E', \quad (2.5)$$

$$y = \frac{P \cdot q}{P \cdot \ell} = \frac{E - E'}{E} = \frac{\nu}{E}, \quad (2.6)$$

$$W^2 = (P + q)^2, \quad (2.7)$$

where  $q$  is the virtual photon four momentum,  $E'$  is the scattered lepton's energy,  $x$  is Bjorken x,  $\nu$  is the change in energy of the scattered lepton,  $y$  is the inelasticity and  $W^2$  is the invariant mass of the hadron final state. In the last relation from Eq. 2.3,  $\theta$  is the scattering angle of the lepton with respect to the beam and the approximation is only true when the lepton mass is assumed to be zero. This assumption and the assumption that a quark's mass is zero will be made throughout this thesis. In Eq. 2.4,  $M$  is the nucleon mass.

In the parton model, section 2.2,  $x$  has the interpretation as being the longitudinal momentum fraction of the struck parton with respect to its parent hadron and therefore  $x$  ranges between 0 and 1. The inelasticity,  $y$ , measures the proportional energy reduction of the lepton and therefore it also ranges between 0 and 1.

The process is called deep if  $Q^2 \gg M^2$  and inelastic if  $y < 1$ . For practical purposes, in experiments, the deep inelastic criteria corresponds to a  $Q^2 > 1 \text{ GeV}$  and  $W^2 > M^2$ . As can be seen in Eq. [2.3-2.7], not all the variables are independent. DIS is described by two independent variables usually given by  $(x, Q^2)$  or  $(x, y)$ . For reference, in the limit as  $y \rightarrow 1$  the process becomes elastic scattering and can then be described by only one independent variable.

The differential cross-section for DIS is defined as [7]

$$d\sigma = \frac{1}{4P \cdot \ell} \frac{e^4}{Q^4} L_{\mu\nu} W^{\mu\nu} 2\pi \frac{d^3 \ell'}{(2\pi)^3 2E'} \quad (2.8)$$

where  $L_{\mu\nu}$  is the leptonic tensor and  $W^{\mu\nu}$  is the hadronic tensor. The leptonic tensor describes free leptons and can therefore be calculated in perturbation theory. It can be decomposed into a symmetric spin-independent tensor and an anti-symmetric spin-dependent tensor. Summing over all the possible spins of the lepton beam, the leptonic tensor is

$$L_{\mu\nu} = 2 \left( \ell_\mu \ell'_\nu + \ell_\nu \ell'_\mu - g_{\mu\nu} \ell \cdot \ell' \right) + 2m\epsilon_{\mu\nu\rho\sigma} s^\rho q^\sigma \quad (2.9)$$

where  $m$  is the lepton mass and  $s^\rho$  is the spin four vector of the lepton.

Generically the hadronic tensor is defined as

$$W^{\mu\nu} = \frac{1}{2\pi} \int d^4\xi e^{iq\cdot\xi} \langle PS | J^\mu(\xi) J^\nu(0) | PS \rangle \quad (2.10)$$

where  $J$  is an electromagnetic current and  $|PS\rangle$  represents the nucleon with momentum  $P$  and spin  $S$ . The hadronic tensor describes a hadron bound together by quantum chromo-dynamics (QCD). As of yet there is no known technique for calculating the hadronic tensor in a perturbation theory or otherwise. Instead the hadronic tensor can be written in the most general Lorentz invariant form using structure functions to parameterize the non-perturbative nature of the tensor. With the use of these structure functions, the differential DIS cross-section for a spin 1/2 target can be written

$$\frac{d\sigma}{dxdy} = \frac{8\pi\alpha^2 ME}{Q^4} \left\{ xy^2 F_1(x, Q^2) + \left(1-y\right) \frac{F_2(x, Q^2)}{x} + c_1(y, \frac{Q^2}{\nu}) g_1(x, Q^2) + c_2(y, \frac{Q^2}{\nu}) g_2(x, Q^2) \right\} \quad (2.11)$$

where  $\alpha$  is the electromagnetic coupling constant;  $F_1$ ,  $F_2$ ,  $g_1$ ,  $g_2$  are structure functions of the proton; and  $c_1$  and  $c_2$  are functions which depend on the polarization of the target. The SLAC collaboration measured the structure functions,  $F_1$  and  $F_2$ , and found mild variations as a function of  $Q^2$  [8, 9]. This phenomenon now known as Bjorken scaling lead to the theory of the parton model where the DIS reaction no longer depends on  $Q^2$  [10]. Fig. 2.2 shows the  $F_2$  structure function which is approximately constant as a function of  $Q^2$ .

## 2.2 The Parton Model

The parton model is described in an infinite momentum frame which for practical measurements is defined as the frame where the nucleon is moving with momentum larger than its invariant mass. In the parton model the nucleon, in high energy scattering processes, is considered to be composed of point like constituent massless particles called partons. At high energy scattering the QCD strong force, binding the partons together, becomes asymptotically small and therefore the partons appear to be free. The cross-section in DIS can then be described as a lepton scattering incoherently off a free parton in the nucleon. In the parton model the hadron tensor for scattering off a quark can be written as [7]

$$W^{\mu\nu} = \frac{1}{2\pi} \sum_q e_q^2 \sum_X \int \frac{d^3 P_X}{(2\pi)^3 2E_X} \int \frac{d^4 k}{(2\pi)^4} \int \frac{d^4 k'}{(2\pi)^4} \delta(k'^2) \times [\bar{u}(k') \gamma^\mu \langle X | u(k) | PS \rangle] \times [\bar{u}(k') \gamma^\nu \langle X | u(k) | PS \rangle] \times (2\pi)^4 \delta^{(4)}(P - k - P_X) (2\pi)^4 \delta^{(4)}(k + q - k'), \quad (2.12)$$

where  $e_q$  is the electric charge of quark flavor  $q$ ,  $u(\bar{u})$  is a free Dirac spinor and  $k(k')$  are the four momenta

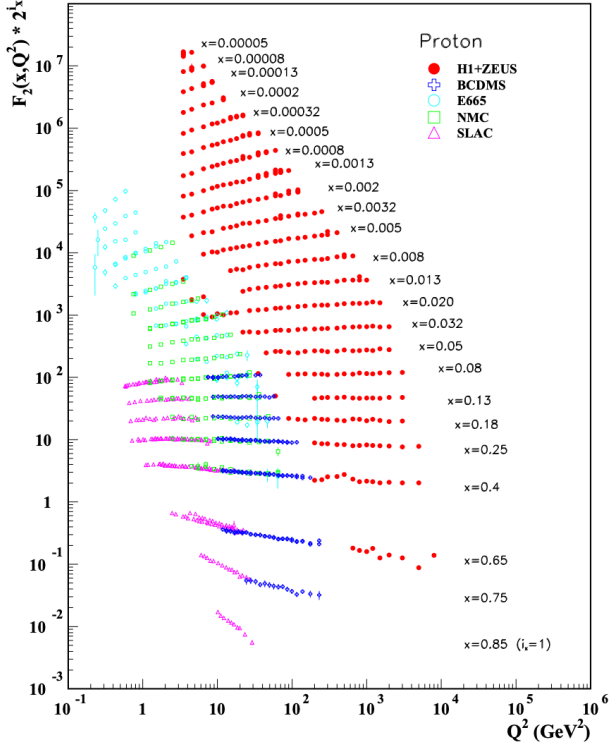


Figure 2.2: The  $F_2$  structure function of the proton measured by several experiments. Note that the data is shifted up by a factor  $2^{i_x}$  to see the  $x$  dependence. Image taken from [11].

of the scattering quarks. This hadronic tensor can be simplified by introducing the quark-quark correlation matrix as

$$\Theta_{ij}(k, P, S) = \sum_X \int \frac{d^3 P_X}{(2\pi)^3 2E_X} (2\pi)^4 \delta^{(4)}(P - k - P_X) \times \langle PS | \phi_j(0) | X \rangle \langle X | \phi_i(0) | PS \rangle, \quad (2.13)$$

where  $\phi(\xi) = e^{-ip \cdot \xi} u(p)$  is a quark field. Using the quark-quark correlation matrix, the hadronic tensor can be written as

$$W^{\mu\nu} = \sum_q e_q^2 \int \frac{d^4 k}{(2\pi)^4} \int \frac{d^4 k'}{(2\pi)^4} \delta(k'^2) (2\pi)^4 \delta^{(4)}(k + q - k') \times \text{Tr}[\Theta \gamma^\mu k'' \gamma^\nu]. \quad (2.14)$$

In the cases of spin-independent or longitudinal polarization dependent DIS the leading order contributing terms from the quark-quark correlator are [12–14]

$$\Theta = \frac{1}{2} \left( f_1(x) \not{p} + g_{1L}(x) \lambda \gamma_5 \not{p} \right), \quad (2.15)$$

where  $\lambda$  is the longitudinal polarization of the hadron. In this case, the hadronic tensor simplifies to a

symmetric contribution and an anti-symmetric contribution as [7]

$$W_{\mu\nu}^{\text{symmetric}} = \frac{1}{P \cdot q} \sum_q e_q^2 \left( (k_\mu + q_\mu) P_\nu + (k_\nu + q_\nu) P_\mu - g_{\mu\nu} \right) f_1^q(x), \quad (2.16)$$

$$W_{\mu\nu}^{\text{anti-symmetric}} = \lambda \epsilon_{\mu\nu\rho\sigma} (k^\sigma + q^\sigma) P^\rho \sum_q e_q^2 g_{1L}^q(x), \quad (2.17)$$

where in Eq. 2.15-2.17,  $f_1$  and  $g_1$  are parton distribution functions (PDFs).

$f_1$  is interpreted as the quark number density and  $g_{1L}$  is interpreted as the total quark helicity distribution in a hadron.  $f_1$  refers to the density of unpolarized quarks in a hadron and  $g_{1L}$  refers to the net density of quarks longitudinally polarized in the same longitudinal direction as the hadron. To make this explicit,  $f_1$  and  $g_{1L}$  can be written

$$f_1 = f_1^+ + f_1^-, \quad (2.18) \quad g_{1L} = f_1^+ - f_1^-, \quad (2.19)$$

where  $+(-)$  denotes the helicity of the parton is in the same(opposite) direction as its parent hadron. To be clear while there is a relationship between the two functions, Eq. 2.21, the parton distribution  $g_{1L}$  is not the same as the structure function  $g_1$ .

The unpolarized quark number density,  $f_1$ , has been extracted from global analysis of several DIS experiments [15]. Fig. 2.3 shows the current  $xf_1$  values and confidence intervals for different quarks and gluons in the proton.

The longitudinal spin structure,  $g_{1L}$ , has also been measured at SMC, HERMES, and COMPASS [16–18]. The global analysis fit is shown in Fig. 2.4 using the parameterizations from NNPDF2014, AAC2008, DSSV2008 and LSS2010 [19–22].

In the parton model the structure functions  $F_1$  and  $F_2$  are related to each other and to the unpolarized quark number as

$$F_2(x) = 2xF_1(x) = \sum_q e_q^2 x \left( f_1^q + f_1^{\bar{q}} \right), \quad (2.20)$$

which is known as the Callan-Gross relation [23]. As well the structure function  $g_1$  is related to the helicity distribution,  $g_{1L}$ , as

$$g_1(x) = \frac{1}{2} \sum_q e_q^2 g_{1L}(x). \quad (2.21)$$

## 2.3 Transverse Momentum Dependence

In inclusive deep inelastic scattering the detected final state lepton is not sensitive to the parton's transverse momentum. That is when measuring the inclusive DIS cross-section, all transverse parton momentums

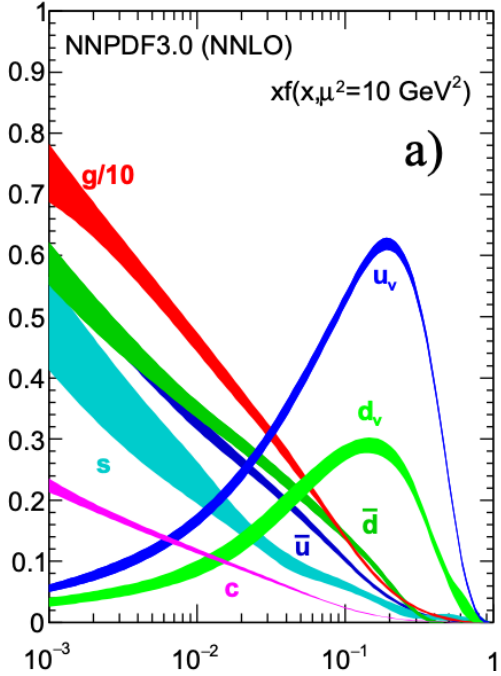


Figure 2.3: The spin-independent parton distribution functions times the momentum fraction. The different colors correspond to different quarks or gluons. Image taken from [11].

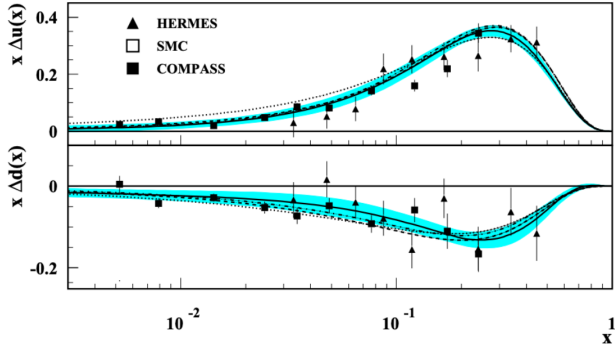


Figure 2.4: The longitudinally polarized parton distribution functions times the momentum fraction for the u-quark (top) and the d-quark (bottom) in a proton. Image taken from [11]

are possible which therefore means the scattered parton's transverse momentum is integrated over. As a result, inclusive DIS cannot be used to study parton's transverse momentum dependence. In general inclusive measurements have less information because fewer variables are measured. On the other hand semi-inclusive measurements collect additional information from a reaction and therefore are sensitive to more variables. The Drell-Yan process, Sec 2.5, and the SIDIS process, Sec 2.4, are sensitive to the internal transverse momentum of the partons. In the limit of small transverse momentum compared to the virtual photon momentum, the most generic leading order quark-quark correlator including the transverse parton

momentum can be written [12–14]

$$\begin{aligned} \Theta = & \frac{1}{2} \left[ f_1(x, k_\perp) \not{P} + \frac{1}{M} h_1^\perp(x, k_\perp) \sigma^{\mu\nu} k_\mu P_\nu + g_{1L}(x, k_\perp) \lambda \gamma_5 \not{P} \right. \\ & + \frac{1}{M} g_{1T}(x, k_\perp) \gamma_5 \not{P} (k_\perp \cdot S_\perp) + \frac{1}{M} h_{1L}(x, k_\perp) \lambda i \sigma_{\mu\nu} \gamma_5 P^\mu k_\perp^\nu + h_1(x, k_\perp) i \sigma_{\mu\nu} \gamma_5 P^\mu S_\perp^\nu \\ & \left. + \frac{1}{M^2} h_{1T}^\perp(x, k_\perp) i \sigma_{\mu\nu} \gamma_5 P^\mu \left( k_\perp \cdot S_\perp k_\perp^\nu - \frac{1}{2} k_\perp^2 S_\perp^\nu \right) + \frac{1}{M} f_{1T}^\perp(x, k_\perp) \epsilon^{\mu\nu\rho\sigma} \gamma_\mu P_\nu k_\rho S_\sigma \right], \end{aligned} \quad (2.22)$$

where  $k_\perp$  denotes the transverse parton momentum and  $S_\perp$  denotes the transverse hadron spin. Eq. 2.22 includes eight transverse momentum dependent (TMD) PDFs which are functions of  $x$  and  $k_\perp$ .

The notation used to depict the TMD functions is the so-called Amsterdam notation. The letters represent the different quark polarizations, where  $f$ ,  $g$ ,  $h$  stand for unpolarized, longitudinally polarized and transversely polarized respectively. The subscript 1 denotes leading order and the subscripts  $T$  and  $L$  denote a transversely polarized hadron and a longitudinally polarized hadron respectively. Finally the superscript  $\perp$  denotes that the distribution is the coefficient of a term in which the parton's transverse momentum Lorentz indices are not contracted. Fig. 2.5 organizes the TMDs by nucleon and quark polarizations and gives a visual of each TMD's interpretation.

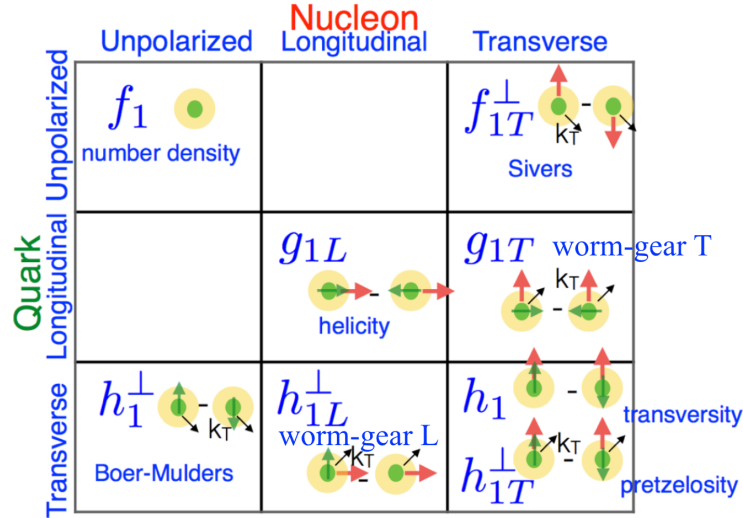


Figure 2.5: The eight TMDs needed to describe a spin 1/2 nucleon at leading order. The columns represent the different nucleon polarizations and the rows represent the different quark polarizations. The individual figures give a visual representation of the TMD's interpretation. This image taken from [24].

The TMD functions needed to describe Drell-Yan scattering from a transversely polarized target, as in the data taking conditions in this thesis are: the Sivers function, the Boer-Mulders function, the transversity function and the pretzelosity function.

### 2.3.1 Sivers and Boer-Mulders Distributions

The Sivers TMD,  $f_{1,T}^{q\perp}(x, \mathbf{k}_T)$ , was first proposed to explain large nucleon spin-dependent asymmetries [5]. The interpretation of the Sivers TMD,  $f_{1,T}^{q\perp}(x, \mathbf{k}_T)$ , is that it gives a correlation between transverse spin of the parent hadron and transverse momentum of the scattered parton. When viewing the hadron in the direction opposite to its momentum and using the sign conventions in this thesis, if  $f_{1,T}^{q\perp}(x, \mathbf{k}_T)$  is positive then it is expected that there are more partons with momentum pointing left than pointing to the right. A non-zero  $f_{1,T}^{q\perp}(x, \mathbf{k}_T)$  then implies that the bound partons in a transversely polarized hadron are traveling transverse to the hadron's momentum which can intuitively make sense if the partons have orbital angular momentum. As of yet however, there is no theoretical link between orbital angular momentum and the Sivers function.

The Boer-Mulders TMD PDF,  $h_1^\perp$ , was proposed in 1998 as a correlation between the transverse momentum and the transverse spin of a parton inside an unpolarized hadron [13]. The Boer-Mulders function is interpreted as a difference between quarks with transverse momentum and transverse spin up and quarks with transverse momentum and transverse spin down in an unpolarized hadron. It is not hard to realize that changing the chirality of transversely polarized quarks in an unpolarized hadron would flip the sign of the Boer-Mulders function which therefore means the Boer-Mulders function is chiral odd. Chiral odd functions can only be non-zero when convoluted with another chiral odd function as is the case when the Boer-Mulders function appears in either the SIDIS or Drell-Yan cross-section.

The most surprising fact about the Sivers and Boer-Mulders functions is that they both change sign under naive time reversal. Naive time reversal is defined as reversing time but not swapping initial and final states [14]. The Sivers and Boer-Mulders functions are therefore said to be T-odd functions, and as a result, were originally believed to be forbidden correlations. However it was shown that the Sivers function could be non-zero from gluon exchange during the initial state in the Drell-Yan process and gluon exchange during the final state in the SIDIS process [25, 26]. Most surprisingly, it was shown that a non-zero Sivers function and a non-zero Boer-Mulders function are expected to have opposite sign in SIDIS and Drell-Yan [27]. That is

$$f_{1T}^\perp|_{Drell-Yan} = -f_{1T}^\perp|_{SIDIS}, \quad (2.23)$$

$$h_1^\perp|_{Drell-Yan} = -h_1^\perp|_{SIDIS}. \quad (2.24)$$

### 2.3.2 Transversity and Pretzelosity

Unlike the Sivers and Boer-Mulders TMDs, the transversity,  $h_1(x, k_T)$ , and pretzelosity,  $h_{1T}^\perp$ , TMDs are predicted to be universal functions of a spin 1/2 hadron. The transversity is defined for transversely polarized hadrons as the difference between quarks polarized in the same direction as their parent hadron and quarks polarized in the opposite direction to their parent hadron. The transversity distribution is then similar to the helicity distribution,  $g_{1L}$ , but for transverse polarizations. The pretzelosity function is a correlation between transversely polarized partons and their transverse momentum in a transversely polarized hadron. As with the Boer-Mulders TMD, both the transversity and the pretzelosity TMDs are chiral odd and are therefore convoluted with another chiral odd function.

## 2.4 Semi-Inclusive Deep Inelastic Scattering

Semi-Inclusive Deep Inelastic Scattering (SIDIS) is the process where a lepton scatters electromagnetically off a nucleon and subsequently the scattered lepton and at least one fragmenting hadron are detected. As the name implies, SIDIS is related to the DIS reaction only SIDIS includes the addition of a detected hadron. SIDIS is denoted as

$$l(\ell, \lambda_l) + N(P, S) \rightarrow l(\ell') + h(P_h) + X(P_X), \quad (2.25)$$

where  $\lambda_l$  is the helicity of the incoming lepton,  $S$  is the spin of the nucleon,  $h$  is the detected hadron and  $P_h$  is the detected hadron's four momentum. The leading order one photon exchange Feynman diagram for the SIDIS process is shown in Fig. 2.6.

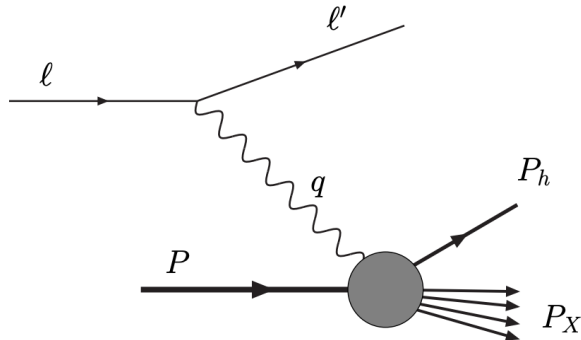


Figure 2.6: The semi-inclusive deep inelastic scattering leading order Feynman diagram

In addition to the kinematic variables used to describe DIS, Eq. [2.3-2.7], one more variable is needed to

describe the SIDIS process,

$$z = \frac{P \cdot P_h}{P \cdot q} \stackrel{\text{frame}}{=} \frac{E_h}{E - E'}, \quad (2.26)$$

which is interpreted as the fraction of possible energy the detected hadron can obtain. The transverse spin-dependent SIDIS cross-section can be described in a model independent way using structure functions as [14]

$$\begin{aligned} \frac{d\sigma}{dx dy d\psi dz d\phi_h dP_{h\perp}^2} &= \frac{\alpha^2}{xyQ^2} \frac{y^2}{2(1-\varepsilon)} \left(1 + \frac{\gamma^2}{2x}\right) \left\{ F_{UU,T} + \varepsilon F_{UU,L} + \sqrt{2\varepsilon(1+\varepsilon)} \cos \phi_h F_{UU}^{\cos \phi_h} \right. \\ &\quad + \varepsilon \cos(2\phi_h) F_{UU}^{\cos 2\phi_h} + \lambda_l \sqrt{2\varepsilon(1-\varepsilon)} \sin \phi_h F_{LU}^{\sin \phi_h} \\ &\quad + |S_\perp| \left[ \sin(\phi_h - \phi_S) \left( F_{UT,T}^{\sin(\phi_h - \phi_S)} + \varepsilon F_{UT,L}^{\sin(\phi_h - \phi_S)} \right) \right. \\ &\quad \left. + \varepsilon \sin(\phi_h + \phi_S) F_{UT}^{\sin(\phi_h + \phi_S)} + \varepsilon \sin(3\phi_h - \phi_S) F_{UT}^{\sin(3\phi_h - \phi_S)} \right. \\ &\quad \left. + \sqrt{2\varepsilon(1+\varepsilon)} \sin \phi_S F_{UT}^{\sin \phi_S} + \sqrt{2\varepsilon(1+\varepsilon)} \sin(2\phi_h - \phi_S) F_{UT}^{\sin(2\phi_h - \phi_S)} \right] \\ &\quad + |S_\perp| \lambda_l \left[ \sqrt{1-\varepsilon^2} \cos(\phi_h - \phi_S) F_{LT}^{\cos(\phi_h - \phi_S)} + \sqrt{2\varepsilon(1-\varepsilon)} \cos \phi_S F_{LT}^{\cos \phi_S} \right. \\ &\quad \left. + \sqrt{2\varepsilon(1-\varepsilon)} \cos(2\phi_h - \phi_S) F_{LT}^{\cos(2\phi_h - \phi_S)} \right] \}, \end{aligned} \quad (2.27)$$

where

$$\varepsilon = \frac{1 - y - \frac{1}{4}\gamma^2 y^2}{1 - y + \frac{1}{2}y^2 + \frac{1}{4}\gamma^2 y^2}, \quad (2.28)$$

and  $\gamma = \frac{2M_x}{Q}$ ,  $\psi$  is the azimuthal scattering angle of the lepton around the lepton beam with respect to the transverse spin direction of the target and where this cross-section is defined in the  $\gamma$ -nucleon reference frame. The  $\gamma$ -nucleon reference system is a lab frame where the virtual photon is along the z-axis and the xz-plane is determined by the lepton plane. Fig. 2.7 shows the  $\gamma$ -nucleon lab frame and the relevant azimuthal angles.

The 14 structure functions, labeled  $F$ , in Eq. 2.27 are coefficients to the azimuthal angles from the  $\gamma$ -nucleon reference frame. The superscript denotes which azimuthal angle coefficient they correspond to and the three subscripts represent the beam, target and virtual photon polarization from left to right respectively. The subscript polarizations are  $U$  for unpolarized,  $L$  for longitudinally polarized and  $T$  for transversely polarized. The cross-section, Eq. 2.27, is determined similarly to the DIS cross-section, Eq. 2.11, in that

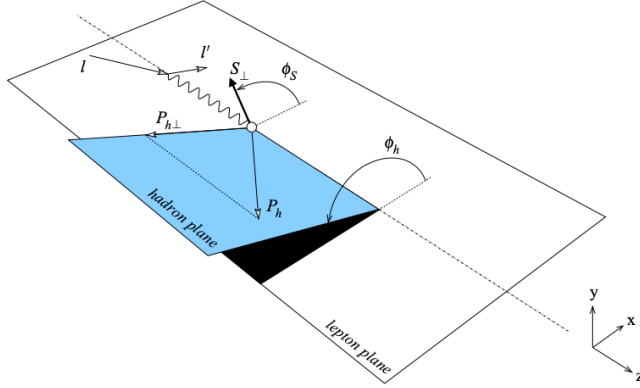


Figure 2.7: The  $\gamma$ -nucleon lab frame, where the target nucleon is at rest and the virtual photon momentum is pointing along the z-axis. The lepton scattering plane defines the xz-plane where the outgoing lepton defines the positive x-direction. This image was taken from [14].

structure functions are used to generically parameterize the hadronic tensor.

In the TMD regime the structure functions are related to TMD functions and fragmentation functions (FF). For SIDIS, the TMD regime is defined as the detected hadron's transverse momentum being small compared to the virtual photon momentum,  $P_{hT} \ll Q$ . Then in this regime the model independent structure functions are equal to a convolution of a TMD and a FF where the convolution is defined as

$$\mathcal{C}[w(p_T, k_T) f D] = x \sum_q e_q^2 \int d^2 p_T d^2 k_T \delta^{(2)}(p_T - k_T - P_{h\perp}/z) w(p_T, k_T) f^q(x, p_T^2) D^q(z, k_T^2), \quad (2.29)$$

where  $w$  is a weight  $f$  is a TMD function and  $D$  is a FF. For the structure functions related to transverse target polarization, the relations between structure functions and TMDs at leading order are [14]

$$F_{UT,T}^{\sin(\phi_h - \phi_S)} = \mathcal{C} \left[ -\frac{\hat{h} \cdot p_T}{M} f_{1T}^\perp D_1 \right] \propto f_{1T}^\perp \otimes D_1, \quad (2.30)$$

$$F_{UT,L}^{\sin(\phi_h - \phi_S)} = 0, \quad (2.31)$$

$$F_{UT}^{\sin(\phi_h + \phi_S)} = \mathcal{C} \left[ -\frac{\hat{h} \cdot k_T}{M_h} h_1 H_1^\perp \right] \propto h_1 \otimes H_1^\perp, \quad (2.32)$$

$$F_{UT}^{\sin(3\phi_h - \phi_S)} = \mathcal{C} \left[ \frac{2(\hat{h} \cdot p_T)(\mathbf{p}_T \cdot \mathbf{k}_T) + \mathbf{p}_T^2(\hat{h} \cdot \mathbf{k}_T) - 4(\hat{h} \cdot p_T)^2(\hat{h} \cdot \mathbf{k}_T)}{2M^2 M_h} h_{1T}^\perp H_1^\perp \right] \propto h_{1T}^\perp \otimes H_1^\perp, \quad (2.33)$$

$$F_{LT}^{\cos(\phi_h - \phi_S)} = \mathcal{C} \left[ \frac{\hat{h} \cdot p_T}{M} g_{1T} D_1 \right] \propto g_{1T} \otimes D_1, \quad (2.34)$$

and the leading order structure functions related to an unpolarized target are

$$F_{UU,T} = \mathcal{C}[f_1 D_1] \propto f_1 \otimes D_1, \quad (2.35)$$

$$F_{UU,L} = 0 \quad (2.36)$$

$$F_{UU}^{\cos 2\phi_h} = \mathcal{C} \left[ -\frac{2(\hat{h} \cdot \mathbf{k}_T)(\hat{h} \cdot p_T) - \mathbf{k}_T \cdot p_T}{M M_h} h_1^\perp H_1^\perp \right] \propto h_1^\perp \otimes H_1^\perp, \quad (2.37)$$

where the unit vector  $\hat{h} = P_{h\perp}/|P_{h\perp}|$  and  $D_1$  and  $H_1^\perp$  are fragmentation functions.

The fragmentation functions are functions of  $z$  and describe the probability for a quark to hadronize to a specific hadron. These fragmentation functions depend on the quark spin, the hadron type and polarization, and the quark  $k_T$ . In Eq. [2.30- 2.36] the fragmentation function  $D_1$  refers to an unpolarized quark fragmenting to an unpolarized hadron and  $H_1^\perp$  refers to a transversely polarized quark fragmenting to an unpolarized hadron.

The SIDIS cross-section, Eq. 2.27, can be rewritten in terms of asymmetries. These asymmetries are defined as

$$A_{BeamTarget}^{w_i(\phi_h, \phi_S)} = \frac{F_{BeamTarget}^{w_i(\phi_h, \phi_S)}}{F_{UU,T} + \varepsilon F_{UU,L}}, \quad (2.38)$$

where  $w_i(\phi_h, \phi_S)$  is the azimuthal angle associated with this asymmetry and *Beam* and *Target* represent the polarization of the beam and target. The asymmetry amplitude, Eq. 2.38, is a structure function divided by the spin-independent structure functions. This asymmetry amplitude is defined because it is easier to measure experimentally. In order to determine an asymmetry amplitude, the number of counts experimentally measured are fit using a function in the form of Eq. 2.27. The parameters of this fit are the

coefficients to each azimuthal amplitude. The results of the fit then determine the spin-dependent asymmetry amplitudes without needing to determine luminosity and therefore have reduced systematic uncertainties.

### 2.4.1 SIDIS TMD Results

COMPASS and HERMES measured the asymmetry amplitude  $A_{UT,T}^{\sin(\phi_h - \phi_S)}$  in SIDIS from a transversely polarized proton target [28, 29]. The comparison of the results between these two collaborations is shown in Fig. 2.8. The asymmetry amplitude  $A_{UT,T}^{\sin(\phi_h - \phi_S)}$  is related to the Sivers function and was measured to be non-zero at a level up to 5%.

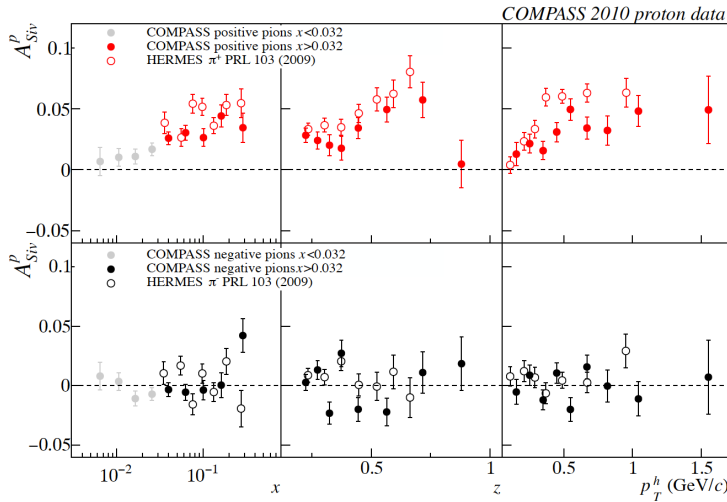


Figure 2.8: The asymmetry amplitude related to the Sivers function measured by COMPASS [28] and HERMES [29]

The top plot in Fig. 2.8 is the Sivers amplitude for a  $\pi^+$  detected hadron. A positively charged final state hadron is dominated by u-quark scattering and therefore by the u-quark Sivers function. This is the case for three reasons. Firstly because the SIDIS reaction is weighted by  $e_q^2$  which therefore makes the u-quark scattering four times more likely. Secondly the so-called favored FF, where the detected hadron has the same charge as the quark which fragmented, is larger than the unfavored FF. Therefore a detected  $\pi^+$  most likely resulted from a positive fragmenting quark. Thirdly the proton target is composed of twice as many u-quarks as d-quarks in this scattering kinematic region. For these three reasons the results in Fig. 2.8 imply that the u-quark Sivers function from the SIDIS reaction is positive.

The bottom plots in Fig. 2.8 suggest that the d-quark Sivers function in the SIDIS reaction is negative. The bottom results in Fig. 2.8 are from the combination of u-quark scattering and fragmenting unfavorably and d-quark scattering and fragmenting favorably. As was mentioned the charge weighting in the SIDIS reaction and the proton quark composition results in the u-quark scattering with a higher probability. On

the other hand the previous effect is canceled out by the fact that the favored FF for the d-quark fragmenting is larger than the unfavored FF for the u-quark fragmenting. Therefore the results in the bottom of Fig. 2.8 are for an approximately equal combination from u-quark scattering and d-quark scattering. As the u-quark asymmetry amplitude is positive, the d-quark asymmetry amplitude must therefore be negative and so also must the d-quark Sivers function. Anselmino et. al. extracted the Sivers function using both HERMES and COMPASS data and BELLE data for fragmentation functions [30]. These results are shown in Fig. 2.9.

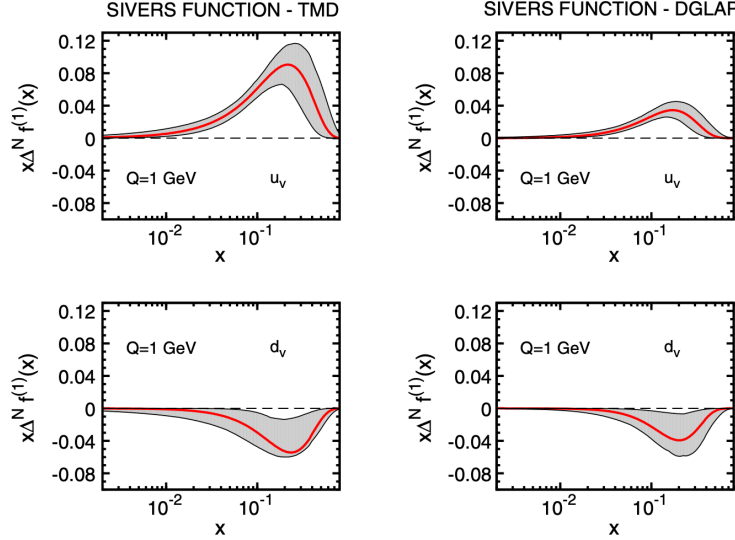


Figure 2.9: The valence quark distributions for the first moment of the Sivers function. The left plots are using TMD evolution and the right plots are using  $Q^2$  evolution to globally include all measured data. This image was taken from [30]

Results for the TMD asymmetry amplitude,  $A_{UU}^{\cos 2\phi_h}$ , related to the Boer-Mulders function were measured by the COMPASS collaboration from SIDIS [31]. As can be seen from the convolution of the structure function, Eq. 2.37, and the definition of asymmetry amplitudes in SIDIS, Eq. 2.38, this asymmetry amplitude is a convolution of the Boer-Mulders function and a fragmentation function. The COMPASS results for  $A_{UU}^{\cos 2\phi_h}$  are shown in Fig. 2.10. Notably the Boer-Mulders asymmetry amplitude is higher for negatively scattered hadrons than for positively scattered hadrons suggesting that the Boer-Mulders function is larger for d-quarks than for u-quarks.

Three SIDIS experiments measured data related to the transversity distribution from the structure function  $F_{UT}^{\sin(\phi_h + \phi_S)}$ . These three experiments were HERMES [32, 33], COMPASS [28, 34–37], and JLab HALL A [38]. The FF data to determine  $H_1^\perp$  from the structure function,  $F_{UT}^{\sin(\phi_h + \phi_S)}$ , comes from BELLE [39, 40] and BABAR [41] data in  $e^+e^-$  annihilation data. Anselmino et. al. extracted the transversity distribution [42] from all this data and their results are shown in Fig. 2.11.

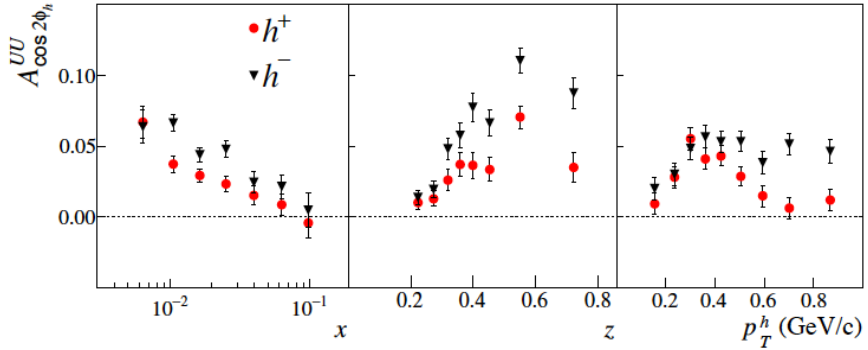


Figure 2.10: COMPASS SIDIS data from muons scattered off of a deuteron target for positively scattered hadrons (red) and negatively scattered hadrons (black). The asymmetry amplitude is related to the Boer-Mulders functions. This image was taken from [31]

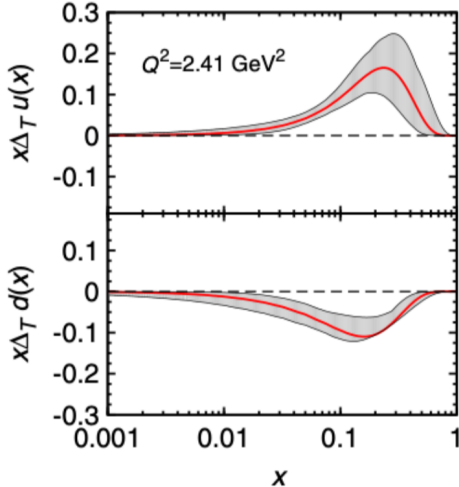


Figure 2.11: The transversity distribution for u-quarks (top) and d-quarks (bottom) determined from SIDIS data and  $e^+e^-$  data. Image taken from [42].

## 2.5 Drell-Yan

The Drell-Yan process is the reaction where a quark and an anti-quark annihilate and the end product results in two oppositely charged leptons which can be detected. The Drell-Yan process is denoted as

$$H_a(P_a) + H_b(P_b, S) \rightarrow \gamma^* + X \rightarrow l(\ell) + l'(\ell') + X \quad (2.39)$$

where  $H_a$  and  $H_b$  are hadrons which carry the quark and anti-quarks and in this thesis only the target hadron,  $H_b$  is considered to be polarized with spin  $S$ . In this thesis the quark and anti-quark pair annihilate to form a virtual photon,  $\gamma^*$  and additionally the only final state detected leptons considered are a muon

and an anti-muon pair. The leading order one photon exchange diagram is shown in Fig. 2.12.

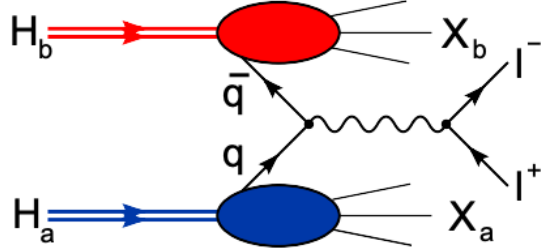
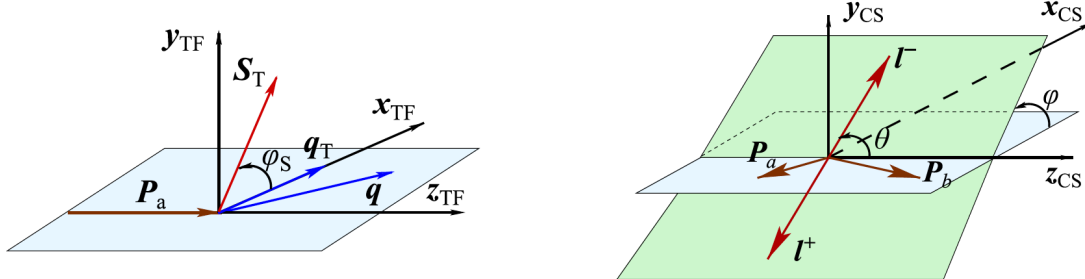


Figure 2.12: The Drell-Yan leading order diagram

The angles used to define the general Drell-Yan cross-section are defined with the use of two reference frames. The target frame (TF), Fig. 2.13a, defines the  $\phi_S$  angle and the Collins-Soper (CS), Fig. 2.13b, frame defines the additional  $\phi$  and  $\theta$  angles. The  $\phi_S$  angle is defined in the TF as the angle between the transverse momentum of the virtual photon and the transverse spin of the target. The  $\phi$  and  $\theta$  angles, in the CS frame, are defined as the azimuthal and polar angle of the negatively charged muon.



(a) The target frame where the z-axis is along the beam and the x-axis is in the direction of the transverse momentum of the virtual photon.

(b) The Collins-Soper frame is defined in the rest frame of the virtual photon where the z-axis bisects the beam and target momentum vectors.

Figure 2.13: Drell-Yan analysis frames.

The target frame is defined in the lab frame where the beam is along the z-axis and the transverse momentum of the virtual photon is along the x-axis. The y-axis in the target frame is then chosen so the coordinate system is right handed. The Collins-Soper frame is defined in the rest frame of the virtual photon where the xz-plane coincides with the hadron plane and the z-axis is chosen so it bisects the momentum vectors  $P_a$  and  $-P_b$ . The CS frame is defined from the target frame as a boost first along the z-axis and then a boost along the x-axis so the rest frame of the virtual photon is reached.

The leading order model independent Drell-Yan differential cross-section for a polarized target is [43, 44]

$$\begin{aligned}
\frac{d\sigma}{d^4 q d\Omega} = & \frac{\alpha_{em}^2}{F q^2} \left\{ \left( (1 + \cos^2 \theta) F_U^1 + (1 - \cos^2 \theta) F_U^2 + \sin 2\theta \cos \phi F_U^{\cos \phi} + \sin^2 \theta \cos 2\phi F_U^{\cos 2\phi} \right) \right. \\
& + S_L \left( \sin 2\theta \sin \phi F_L^{\sin \phi} + \sin^2 \theta \sin 2\phi F_L^{\sin 2\phi} \right) \\
& + |S_T| \left[ \left( F_T^{\sin \phi_S} + \cos^2 \theta \tilde{F}_T^{\sin \phi_S} \right) \sin \phi_S + \left( F_T^{\sin(\phi+\phi_S)} \sin(\phi + \phi_S) + F_T^{(\sin \phi - \phi_S)} \sin(\phi - \phi_S) \right) \sin 2\theta \right. \\
& \left. \left. + \left( F_T^{\sin(2\phi+\phi_S)} \sin(2\phi + \phi_S) + F_T^{\sin(2\phi-\phi_S)} \sin(2\phi - \phi_S) \right) \sin^2 \theta \right] \right\}, \tag{2.40}
\end{aligned}$$

where  $F = 4\sqrt{(P_a \cdot P_b)^2 - M_a^2 M_b^2}$  is the flux,  $S_L$  is the longitudinal spin,  $|S_T|$  is the transverse spin and  $\Omega$  is the solid angle of the outgoing negatively charged muon. The twelve model independent structure functions in Eq. 2.40 are labeled as  $F_{Target polarization}^{azimuthal angle coefficient}$ . The phase space when the TMD regime is valid in DY scattering is when  $q_T \ll q$ . In this regime the structure functions are equal to a convolution of a beam and a target TMD function, where the convolution is defined similarly to the SIDIS case, Eq. 2.29, as

$$\begin{aligned}
\mathcal{C}[w(k_{aT}, k_{bT}) f_a \bar{f}_b] = & \frac{1}{N_c} \sum_q e_q^2 \int d^2 k_{aT} d^2 k_{bT} \delta^{(2)}(q_T - k_{aT} - k_{bT}) \\
& \times w(k_{aT}, k_{bT}) \left[ f_a^q(x, k_{aT}^2) f_b^{\bar{q}}(x, k_{bT}^2) + f_a^{\bar{q}}(x, k_{aT}^2) f_b^q(x, k_{bT}^2) \right], \tag{2.41}
\end{aligned}$$

where  $N_c = 3$  is the number of color charges. The leading order DY structure functions in the TMD phase space are related to TMD functions as [43]

$$F_U^1 = \mathcal{C}[f_1 \bar{f}_1] \propto f_{1,Beam}^{\bar{u}} \otimes f_{1,Target}^u, \quad (2.42)$$

$$F_U^{\cos 2\phi} = \mathcal{C} \left[ \frac{2(\vec{h} \cdot \vec{k}_{aT})(\vec{h} \cdot \vec{k}_{bT}) - \vec{k}_{aT} \cdot \vec{k}_{bT} h_1^\perp \bar{h}_1^\perp}{M_a M_b} \right] \propto h_{1,Beam}^{\perp \bar{u}} \otimes h_{1,Target}^{\perp u}, \quad (2.43)$$

$$F_L^{\sin 2\phi} = -\mathcal{C} \left[ \frac{2(\vec{h} \cdot \vec{k}_{aT})(\vec{h} \cdot \vec{k}_{bT}) - \vec{k}_{aT} \cdot \vec{k}_{bT} h_1^\perp \bar{h}_{1L}^\perp}{M_a M_b} \right] \propto h_{1,Beam}^{\perp \bar{u}} \otimes h_{1L,Target}^{\perp u}, \quad (2.44)$$

$$F_T^1 = -\mathcal{C} \left[ \frac{\vec{h} \cdot \vec{k}_{bT}}{M_b} f_1 \bar{f}_{1T}^\perp \right] \propto f_{1,Beam}^{\bar{u}} \otimes f_{1T,Target}^{\perp u}, \quad (2.45)$$

$$F_T^{\sin(2\phi - \phi_S)} = -\mathcal{C} \left[ \frac{\vec{h} \cdot \vec{k}_{aT}}{M_a} h_1^\perp \bar{h}_1 \right] \propto h_{1,Beam}^{\perp \bar{u}} \otimes h_{1,Target}^u, \quad (2.46)$$

$$F_T^{\sin(2\phi + \phi_S)} = -\mathcal{C} \left[ \frac{2(\vec{h} \cdot \vec{k}_{bT})[2(\vec{h} \cdot \vec{k}_{aT})(\vec{h} \cdot \vec{k}_{bT}) - \vec{k}_{aT} \cdot \vec{k}_{bT}] - \vec{k}_{bT}^2 (\vec{h} \cdot \vec{k}_{aT})}{2M_a M_b^2} h_1^\perp \bar{h}_{1T}^\perp \right] \propto h_{1,Beam}^{\perp \bar{u}} \otimes h_{1T,Target}^{\perp u}, \quad (2.47)$$

where  $\vec{h} = \vec{q}_T/q_T$  is a unit vector and furthermore the assumption in this thesis is that the beam  $\bar{u}$ -quark annihilates with the target  $u$ -quark. The additional leading order structure functions are zero

$$F_U^2 = F_U^{\cos \phi} = F_L^{\sin \phi} = F_T^2 = F_T^{\sin(\phi - \phi_S)} = F_T^{\sin(\phi + \phi_S)} = 0. \quad (2.48)$$

The differential cross-section, Eq. 2.40, can be rewritten in terms of asymmetry amplitudes and depolarization factors. The asymmetry amplitudes are defined similarly to the case in SIDIS, Eq. 2.38, and again for the reason that asymmetries can be determined to a higher precision than structure functions. For Drell-Yan these asymmetry amplitudes are

$$A_{Target}^{w_i(\phi, \phi_S)} = \frac{F_{Target}^{w_i(\phi, \phi_S)}}{F_U^1 + F_U^2}. \quad (2.49)$$

The asymmetry amplitudes are the result of different virtual photon polarizations decaying to a final state lepton pair. The depolarization factor is defined as the ratio of the virtual photon polarization to produce

such an asymmetry to that of a transversely polarized virtual photon. The depolarization is defined for each asymmetry amplitude as

$$D_{[f(\theta)]} = \frac{f(\theta)}{1 + A_U^1 \cos^2 \theta}, \quad (2.50)$$

where the function  $f(\theta)$  corresponds to virtual photon angular decay responsible for the given asymmetry. The Drell-Yan differential cross-section, Eq. 2.40, now simplifies to [44]

$$\begin{aligned} \frac{d\sigma}{d^4 q d\Omega} = & \frac{\alpha_{em}^2}{F q^2} \hat{\sigma}_U \left\{ \left( 1 + D_{[\sin^2 \theta]} \cos 2\phi A_U^{\cos 2\phi} \right) \right. \\ & + S_L D_{[\sin^2 \theta]} \sin 2\phi A_L^{\sin 2\phi} \\ & \left. + |S_T| \left[ A_T^{\sin \phi_S} \sin \phi_S + \left( A_T^{\sin(2\phi+\phi_S)} \sin(2\phi+\phi_S) + A_T^{\sin(2\phi-\phi_S)} \sin(2\phi-\phi_S) \right) D_{[\sin^2 \theta]} \right] \right\}, \end{aligned} \quad (2.51)$$

where  $\hat{\sigma}_U = F_U^1(1 + \cos^2 \theta)$  is the unpolarized DY cross-section. For the data taking conditions in 2015 it is assumed that the target is transversely polarized so  $S_L = 0$  and therefore the Drell-Yan cross-section can be simplified to

$$\begin{aligned} \frac{d\sigma}{d^4 q d\Omega} = & \frac{\alpha_{em}^2}{F q^2} \hat{\sigma}_U \left\{ \left( 1 + D_{[\sin^2 \theta]} \cos 2\phi A_U^{\cos 2\phi} \right) \right. \\ & \left. + |S_T| \left[ A_T^{\sin \phi_S} \sin \phi_S + \left( A_T^{\sin(2\phi+\phi_S)} \sin(2\phi+\phi_S) + A_T^{\sin(2\phi-\phi_S)} \sin(2\phi-\phi_S) \right) D_{[\sin^2 \theta]} \right] \right\}. \end{aligned} \quad (2.52)$$

### 2.5.1 Drell-Yan Sivers Result

The first Drell-Yan results for the Sivers asymmetry amplitude, in an attempt to verify the sign change between Drell-Yan and SIDIS, came from hadron-hadron collisions at STAR [45]. Their result measured the Sivers amplitude from  $pp^\uparrow \rightarrow Z^0 X$  and  $pp^\uparrow \rightarrow W^\pm X$  and are shown in Fig. 2.14. The statistical significance is poor and the  $Q^2$  scale is very different from that used to measure a Sivers function in SIDIS however. As of the date of this thesis it has not been concluded on a sign change of the Sivers function between Drell-Yan and SIDIS.

### 2.5.2 Left-Right Asymmetry

An asymmetry of interest for measuring high energy spin related phenomena is the analyzing power. This asymmetry is denoted  $A_N$  and is responsible for a left-right asymmetry for a suitable definition of left and

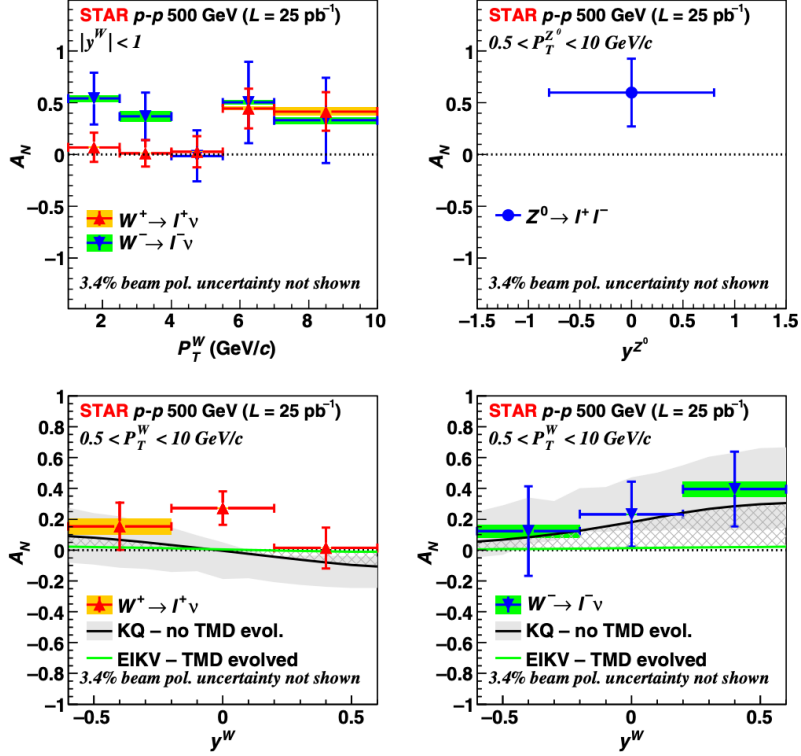


Figure 2.14: All plots show a left-right asymmetry from STAR data which is related to the Sivers function. The top right plot is for  $Z^0$  production while the other three plots are for  $W^\pm$  production.  $Q^2$  evolution and resulting error bars from EIKV [46] and KQ [47]. Image taken from [45].

right. The cross-section for spin 1/2 particles scattering where one of the initial particles is polarized can be written

$$I(\theta, \phi) = I_0(\theta)(1 + SA_N \cos(\phi)) \quad (2.53)$$

where  $I_0$  is the unpolarized cross-section,  $S$  is the beam or target polarization percentage and  $\phi$  is the azimuthal scattering angle of the outgoing measured particle. Working in the target frame for Drell-Yan scattering from a transversely polarized target, the azimuthal angle can be redefined in terms of the  $\phi_S$  angle by noting that  $\phi = \frac{\pi}{2} - \phi_S$ . Eq. 2.53 can then be written in the form of the Drell-Yan cross-section, Eq. 2.51, as

$$\begin{aligned}
\frac{d\sigma}{d^4 q d\phi_S} &= \frac{\alpha_{em}^2}{F q^2} \hat{\sigma}_U \left( 1 + |S_T| A_N \cos\left(\frac{\pi}{2} - \phi_S\right) \right) \\
&= \frac{\alpha_{em}^2}{F q^2} \hat{\sigma}_U \left( 1 + |S_T| A_N \sin(\phi_S) \right) \\
&= \frac{\alpha_{em}^2}{F q^2} \hat{\sigma}_U \left( 1 + |S_T| A_T^{\sin \phi_S} \sin(\phi_S) \right),
\end{aligned} \tag{2.54}$$

where this relation is obtained from Eq. 2.51 by integrating over all angle except  $\phi_S$  and where the polarization  $S$  is assumed to be transverse. Therefore the analyzing power,  $A_N$ , is the same as the Sivers asymmetry amplitude,  $A_T^{\sin \phi_S}$ , for Drell-Yan scattering.

An analysis technique for measuring  $A_N$  is by forming a left-right asymmetry. The left-right asymmetry is defined as

$$A_{lr} = \frac{1}{|S_T|} \frac{\sigma_l - \sigma_r}{\sigma_l + \sigma_r}, \tag{2.55}$$

where  $\sigma_{l(r)}$  is the cross-section for producing a final state to the left(right). In the target frame the definition of left scattering is  $\int_{\phi_S=0}^{\phi_S=\pi} \frac{d\sigma}{d^4 q d\phi_S} d\phi_S$  and definition of right scattering is  $\int_{\phi_S=\pi}^{\phi_S=2\pi} \frac{d\sigma}{d^4 q d\phi_S} d\phi_S$ . It is straight forward to show the relationship between  $A_{lr}$  and  $A_N$  as

$$\begin{aligned}
A_{lr} &= \frac{1}{|S_T|} \frac{\int_{\phi_S=0}^{\phi_S=\pi} \frac{d\sigma}{d^4 q d\phi_S} d\phi_S - \int_{\phi_S=\pi}^{\phi_S=2\pi} \frac{d\sigma}{d^4 q d\phi_S} d\phi_S}{\int_{\phi_S=0}^{\phi_S=\pi} \frac{d\sigma}{d^4 q d\phi_S} d\phi_S + \int_{\phi_S=\pi}^{\phi_S=2\pi} \frac{d\sigma}{d^4 q d\phi_S} d\phi_S} \\
&= \frac{1}{|S_T|} \frac{\phi_S - |S_T| A_N \cos \phi_S \Big|_0^\pi - (\phi_S - |S_T| A_N \cos \phi_S) \Big|_\pi^{2\pi}}{\phi_S - |S_T| A_N \cos \phi_S \Big|_0^\pi + (\phi_S - |S_T| A_N \cos \phi_S) \Big|_\pi^{2\pi}} \\
&= \frac{1}{|S_T|} \frac{4|S_T| A_N}{2\pi} \\
&= \frac{2A_N}{\pi}.
\end{aligned} \tag{2.56}$$

Another method to determine  $A_N$ , is with the transverse spin asymmetry (TSA) defined as

$$\begin{aligned}
A_{TSA} &= \frac{1}{|S_T|} \frac{\frac{d\sigma^\uparrow}{d\phi_s} - \frac{d\sigma^\downarrow}{d\phi_s}}{\frac{d\sigma^\uparrow}{d\phi_s} + \frac{d\sigma^\downarrow}{d\phi_s}} \\
&= \frac{1}{|S_T|} \frac{1 + |S_T| A_N \sin \phi_S - (1 + |S_T| A_N \sin(\phi_S + \pi))}{1 + |S_T| A_N \sin \phi_S + (1 + |S_T| A_N \sin(\phi_S + \pi))} \\
&= A_N \sin \phi_S.
\end{aligned} \tag{2.57}$$

To understand how  $A_N$  is related to the Sivers function, it is illustrative to write the Drell-Yan differential cross-section under the TMD assumptions as [47]

$$\frac{d\sigma^{H_a H_b \rightarrow l^+ l^- X}}{d\eta dM^2 d^2 q_T} = \hat{\sigma}_0 \sum_q e_q^2 \int d^2 k_{aT} d^2 k_{bT} \delta^{(2)}(k_{aT} + k_{bT} - q_T) f_{\bar{q}/H_a}(x_a, k_{aT}) f_{q/H_b}(x_b, k_{bT}), \quad (2.58)$$

$\eta$  is rapidity and  $f_{\bar{q}(q)/H_a(b)}$  is a TMD function. Inserting this cross-section into the transverse spin asymmetry, Eq. 2.57, and using proper TMD functions for the given transverse polarization gives

$$A_{TSA} = A_N \sin \phi_S \quad (2.59)$$

$$= -\frac{1}{S} \frac{\sum_q e_q^2 \int d^2 k_{aT} d^2 k_{bT} \delta^{(2)}(k_{aT} + k_{bT} - q_T) f_{\bar{q}/H_a}(x_a, k_{aT}) \frac{k_{bT}}{M_b} f_{1T}^{\perp q}(x_b, k_{bT}) S \sin \phi_S}{\sum_q e_q^2 \int d^2 k_{aT} d^2 k_{bT} \delta^{(2)}(k_{aT} + k_{bT} - q_T) f_{\bar{q}/H_a}(x_a, k_{aT}) f_{q/H_b}(x_b, k_{bT})}.$$

Several experiments measured large values for  $A_N$  at different center of mass energies. Fig. 2.15 shows the results of  $A_N$  from hadron-hadron collisions from four different experiments over a range of center of mass energies.

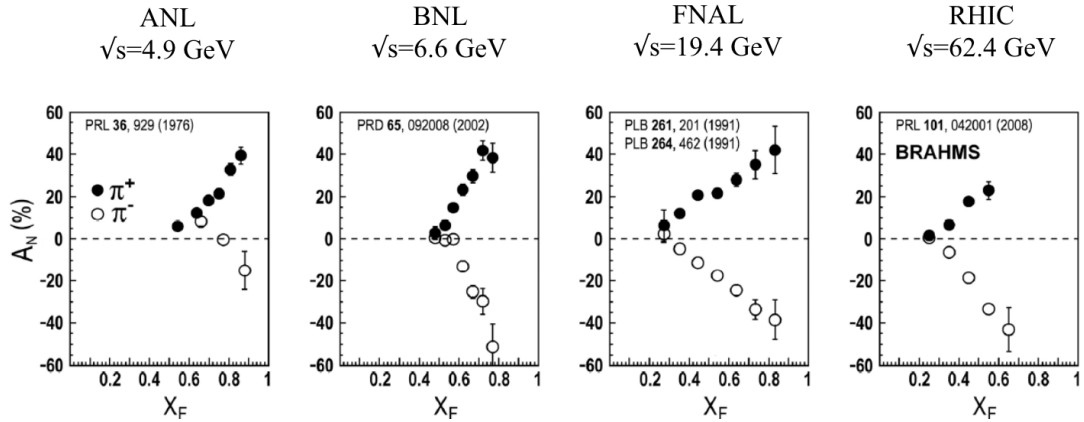


Figure 2.15: Large  $A_N$  values where found at ANL [6], BNL [48], FNAL [49, 50] and RHIC [51].

### 2.5.3 Weighted Asymmetries from Drell-Yan

The proton TMD functions, determined from Drell-Yan in Eqs. 2.42-2.47, are convoluted with a TMD function from the beam pion. The Drell-Yan convolution, Eq. 2.41, makes it difficult to determine a single TMD function and for this reason model assumptions are made in the global analysis to extract the individual TMDs from the convolutions. An alternative method involving weighted asymmetries however, makes it possible to disentangle the convolution and determine a  $k_T^2$  moment of a TMD function both for SIDIS [13, 52, 53] and for Drell-Yan [54–57].

The deconvolution by weighted asymmetries works by multiplying a given structure function by an appropriate weight and integrating over the virtual photon transverse momentum,  $q_T$ . The simplest Drell-Yan structure function to deconvolute is  $F_U^1$ . By integrating Eq. 2.42 over  $q_T$  the convolution equation becomes

$$\begin{aligned}
\int d^2 q_T F_U^1 &= \int d^2 q_T \mathcal{C}[f_{1,a} \bar{f}_{1,b}] \\
&= \int d^2 q_T \frac{1}{N_c} \sum_q e_q^2 \int d^2 k_{aT} d^2 k_{bT} \delta^{(2)}(q_T - k_{aT} - k_{bT}) \\
&\quad \times \left[ f_{1,a}^q(x_a, k_{aT}^2) f_{1,b}^{\bar{q}}(x_b, k_{bT}^2) + f_{1,a}^{\bar{q}}(x_a, k_{aT}^2) f_{1,b}^q(x_b, k_{bT}^2) \right] \\
&= \frac{1}{N_c} \sum_q e_q^2 f_{1,a}^q(x_a) f_{1,b}^{\bar{q}}(x_b) + f_{1,a}^{\bar{q}}(x_a) f_{1,b}^q(x_b) \\
&\stackrel{\text{COMPASS}}{\approx} \frac{4}{27} f_{1,\pi}^{\bar{u}}(x_\pi) f_{1,\text{proton}}^u(x_{\text{proton}}),
\end{aligned} \tag{2.60}$$

where  $f_1(x) = \int d^2 k_T f_1(x, k_T^2)$  is a TMD function integrated over  $k_T$ . In Eq. 2.60 the weight was 1 and no assumptions were needed to perform the integration. The answer is a TMD function for the beam multiplied by a TMD function from the target. The final equality in Eq. 2.60 is valid in the COMPASS kinematic region and shows how straight forward this method can make TMD extraction.

Deconvoluting the additional Drell-Yan structure functions, Eqs 2.43-2.47, is similar to Eq. 2.60 but requires a different weight. The Sivers TMD function can be extracted from the  $F_T^1$  structure function using a weight equal to  $|q_T|/M_b$ . This can be seen by multiplying  $F_T^1$  by the weight  $|q_T|/M_b$ , and integrating over  $q_T$  to remove the Dirac delta function as follows

$$\begin{aligned}
\int d^2 q_T \frac{|q_T|}{M_b} F_T^1 &= - \int d^2 q_T \frac{|q_T|}{M_b} \mathcal{C} \left[ \frac{\vec{q}_T \cdot \vec{k}_{bT}}{|q_T|M_b} f_{1,a} \bar{f}_{1T,b} \right] \\
&= - \int d^2 q_T \frac{|q_T|}{M_b} \frac{1}{N_c} \sum_q e_q^2 \int d^2 k_{aT} d^2 k_{bT} \delta^{(2)}(q_T - k_{aT} - k_{bT}) \\
&\quad \times \frac{\vec{q}_T \cdot \vec{k}_{bT}}{|q_T|M_b} \left[ f_{1,a}^q(x_a, k_{aT}^2) f_{1T,b}^{\bar{q}\perp}(x_b, k_{bT}^2) + f_{1,a}^{\bar{q}}(x_a, k_{aT}^2) f_{1T,b}^{q\perp}(x_b, k_{bT}^2) \right] \\
&= - \frac{1}{N_c} \sum_q e_q^2 \int d^2 k_{aT} d^2 k_{bT} \\
&\quad \times \frac{(\vec{k}_{aT} + \vec{k}_{bT}) \cdot \vec{k}_{bT}}{M_b^2} \left[ f_{1,a}^q(x_a, k_{aT}^2) f_{1T,b}^{\bar{q}\perp}(x_b, k_{bT}^2) + f_{1,a}^{\bar{q}}(x_a, k_{aT}^2) f_{1T,b}^{q\perp}(x_b, k_{bT}^2) \right].
\end{aligned} \tag{2.61}$$

To simplify further we make use of the fact that the unpolarized quark distribution function is even in  $k_T$

which means

$$\int_{-\infty}^{\infty} d^2 k_{aT} \vec{k}_{aT} \cdot \vec{k}_{bT} f_{1,a}(x_a, k_{aT}^2) = 0, \quad (2.62)$$

and therefore only even terms in  $k_T^2$  need to be considered. Eq. 2.61 can then be further simplified as

$$\begin{aligned} \int d^2 q_T \frac{|q_T|}{M_b} F_T^1 &= -\frac{2}{N_c} \sum_q e_q^2 \left[ f_{1,a}^q(x_a) f_{1T,b}^{(1)\bar{q}\perp}(x_b) + f_{1,a}^{\bar{q}}(x_a) f_{1T,b}^{(1)q\perp}(x_b) \right] \\ &\stackrel{COMPASS}{\approx} -\frac{8}{27} f_{1,\pi}^{(\bar{u})}(x_\pi) f_{1T,proton}^{(1)u\perp}(x_{proton}), \end{aligned} \quad (2.63)$$

where the  $f_{1T}^{(1)q\perp}(x) = \int d^2 k_T \frac{k_T^2}{2M} f_{1T}^{q\perp}(x, k_T^2)$  is the first  $k_T^2$  moment of the Sivers function and the general  $k_T$  moment of a TMD is defined as  $f^{(n)}(x) = \int d^2 k_T \left( \frac{k_T^2}{2M} \right)^n f(x, k_T^2)$ .

The essential steps in deconvolution the TMD functions are to multiply by a weight which gets rid of any  $q_T$  terms outside of the Dirac delta function and to only include even terms in  $k_T$ . The remaining two transverse spin-dependent structure functions can also be deconvoluted in a similar fashion to give

$$\begin{aligned} \int d^2 q_T \frac{|q_T|^3}{2M_a M_b^2} F_T^{\sin(2\phi+\phi_S)} &= -\frac{2}{N_c} \sum_q e_q^2 \left[ h_{1,a}^{(1)\bar{q}\perp}(x_a) h_{1T,b}^{(2)q\perp}(x_b) + (q \leftrightarrow \bar{q}) \right] \\ &\stackrel{COMPASS}{\approx} -\frac{8}{27} h_{1,\pi}^{(1)\bar{u}\perp}(x_\pi) h_{1T,proton}^{(2)u\perp}(x_{proton}), \end{aligned} \quad (2.64)$$

$$\begin{aligned} \int d^2 q_T \frac{|q_T|}{M_a} F_T^{\sin(2\phi-\phi_S)} &= -\frac{2}{N_c} \sum_q e_q^2 \left[ h_{1,a}^{(1)\bar{q}\perp}(x_a) h_{1,b}^{(2)q}(x_b) + (q \leftrightarrow \bar{q}) \right] \\ &\stackrel{COMPASS}{\approx} -\frac{8}{27} h_{1,\pi}^{(1)\bar{u}\perp}(x_\pi) h_{1,proton}^{(2)u}(x_{proton}), \end{aligned} \quad (2.65)$$

where Eq. 2.64 can be used to determined the proton pretzelosity function and Eq. 2.65 can be used to determine the proton transversity function.

For experimentally determining the  $k_T^2$  moments of TMD functions the following weighted asymmetries amplitudes are defined

$$A^{Y W_Y} X(x_a, x_b) = \frac{\int d^2 q_T W_Y F_X^Y}{\int d^2 q_T F_U^1}, \quad (2.66)$$

where  $Y$  is the azimuthal modulation of interest,  $W_Y$  is the appropriate weight and  $X$  denotes the targets polarization. For example the Sivers weighted asymmetry amplitude is as follows

$$A^{\sin \phi_S \frac{q_T}{M_b}} = \frac{\int d^2 q_T \frac{q_T}{M_b} F_T^{\sin \phi_S}}{\int d^2 q_T F_U^1} \underset{COMPASS}{\approx} -2 \frac{f_{1T,proton}^{(1)u\perp}(x_{proton})}{f_{1,proton}}. \quad (2.67)$$

### 2.5.4 J/ $\Psi$ Production

The production of J/ $\Psi$  hadrons potentially offers an alternative mechanism for studying TMD related effects. As of yet however, there is no confirmation on the J/ $\Psi$  production mechanism and therefore it impossible to say if TMD effects are present from J/ $\Psi$  production. Still there are many models which can be tested, some of which assume TMD functions contribute to produce J/ $\Psi$  hadrons.

One of the most popular J/ $\Psi$  production models, is the color evaporation model [58]. In this model the J/ $\Psi$  production results from gluon-gluon fusion and quark and anti-quark annihilation. This is depicted as

$$\sigma \Big|_{H_a H_b \rightarrow J/\Psi X \rightarrow l^+ l^- X} = \sigma_{q\bar{q} \rightarrow c\bar{c}} + \sigma_{gg \rightarrow c\bar{c}}, \quad (2.68)$$

where  $\sigma_{q\bar{q}(gg) \rightarrow c\bar{c}}$  is the cross-section for quark-quark annihilation (gluon-gluon fusion) to a  $c\bar{c}$  final state. In the case of quark-quark annihilation there is interest in a model duality between Drell-Yan and J/ $\Psi$  production.

The spin and parity J/ $\Psi$  quantum numbers are the same as the spin and parity of a photon. For this reason it is hypothesized that there is a duality between the Drell-Yan process and J/ $\Psi$  production [59–61]. This duality transforms the electromagnetic coupling and Drell-Yan invariant mass to a new J/ $\Psi$  coupling and J/ $\Psi$  mass given as

Drell–Yan Production	J/ $\Psi$ Production
$16\pi^2 \alpha^2 e_q^2$	$(g_q^{J/\Psi})^2 (g_l^{J/\Psi})^2$

$$16\pi^2 \alpha^2 e_q^2 \rightarrow (g_q^{J/\Psi})^2 (g_l^{J/\Psi})^2 \quad (2.69)$$

$$\frac{1}{M^4} \rightarrow \frac{1}{(M^2 - M_{J/\Psi}^2)^2 + M_{J/\Psi}^2 \Gamma_{J/\Psi}^2}, \quad (2.70)$$

where  $M^2 = Q^2$ ,  $M_{J/\Psi}^2 \approx 9.59 \text{ (GeV}/c^2)^2$  is the J/ $\Psi$  mass squared and  $\Gamma_{J/\Psi}$  is the full J/ $\Psi$  width.

This duality is only expected when quark-quark annihilation dominates over gluon-gluon fusion however. Under this duality assumption, the TSA related to the analyzing power offers an interesting avenue for studying TMDs. Assuming quark-antiquark annihilation dominates and that duality relations, Eq 2.69 and Eq. 2.70, are valid then the TSA can be written for J/ $\Psi$  production as written [62]

$$A_{TSA}^{J\Psi} = -\frac{1}{S} \frac{\sum_q (g_q^V)^2 \int d^2 k_{aT} d^2 k_{bT} \delta^{(2)}(k_{aT} + k_{bT} - q_T) f_{\bar{q}/H_a}(x_a, k_{aT}) \frac{k_{bT}}{M_b} f_{1T}^{\perp q}(x_b, k_{bT}) S \sin \phi_S}{\sum_q (g_q^V)^2 \int d^2 k_{aT} d^2 k_{bT} \delta^{(2)}(k_{aT} + k_{bT} - q_T) f_{\bar{q}/H_a}(x_a, k_{aT}) f_{q/H_b}(x_b, k_{bT})}. \quad (2.71)$$

In the case of COMPASS with  $u\bar{u}$  annihilation dominating, then the unknown couplings,  $g_q^V$ , cancel and are not needed to study TMD functions.

## Chapter 3

# The COMPASS Experiment at CERN

The COmmon Muon Proton Apparatus for Structure and Spectroscopy (COMPASS) experiment is a fixed target experiment at CERN, located in France in the North Area. COMPASS started taking data in 2002 in the same hall as the earlier European Muon Collaboration (EMC), New Muon Collaboration (NMC) and Spin Muon Collaboration (SMC) experiments. COMPASS has studied hadron structure through (SI)DIS, Drell-Yan and Primakoff reactions and has performed hadron spectroscopy measurements.

CERN is the European Organization for Nuclear physics research. It is located part in France and part in Switzerland and includes various experiments and accelerators providing beam to these experiments. The accelerator beam lines are connected and feed beam to each other resulting in an increase in beam momentum at each successive accelerator. A schematic of the accelerators at CERN is shown in Fig. 3.1, where the accelerator that sends beam to COMPASS is the Super Proton Synchrotron (SPS).

The COMPASS spectrometer is a two-stage spectrometer. The two stages are in series where each stage contains various tracking detectors and a muon wall filter at the end of each stage. Any particles that penetrate through the active area of either of the muon wall filters are with a high probability, muons. Both stages also contain an electromagnetic and hadron calorimeter. The stages are both centered around a strong spectrometer magnet used for determining charged particle momentum. The first stage downstream of the target is the large angle spectrometer (LAS) and it is centered around the SM1 magnet, which has an integrated field of 1 Tm. This stage detects tracks with larger polar scattering angles approximately between 26 mrad and 160 mrad. The second stage is the small angle spectrometer (SAS) and it detects particle tracks having a scattering angle between roughly 8 mrad and 45 mrad. This stage is centered around the SM2 magnet which has an integrated field of 4.4 Tm.

The left and right side of the spectrometer are referred to by the mountains that surround the spectrometer. When looking down the beam line, the left side is referred to as the Jura side, which roughly corresponds to the west side. The right side is referred to as the Saleve side, which roughly corresponds to the east side. A graphic of the 2015 setup is shown in Fig 3.2.

This chapter gives an overview of the general COMPASS data taking setup and highlights the specific

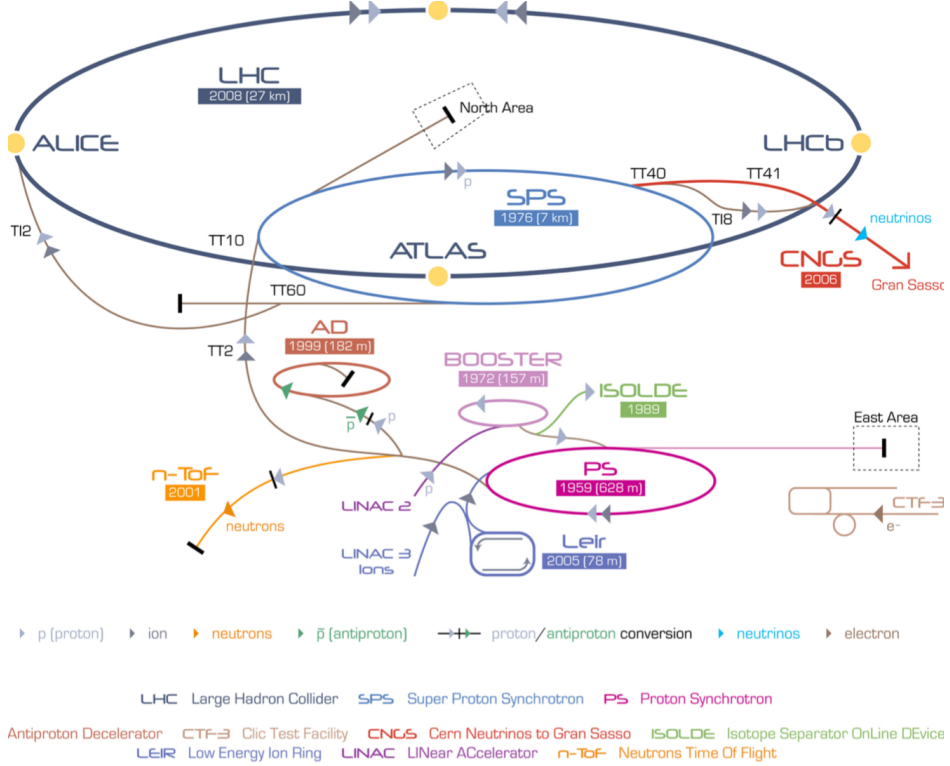


Figure 3.1: The CERN experiments and accelerators. This figure is taken from [63].

features in 2015. All the data in this thesis was obtained with the 2015 setup. For a more thorough review of the spectrometer see reference [64]. This chapter is roughly organized by how the data taking occurs and concludes with an extra section summarizing the unique features of the 2015 Drell-Yan data taking conditions.

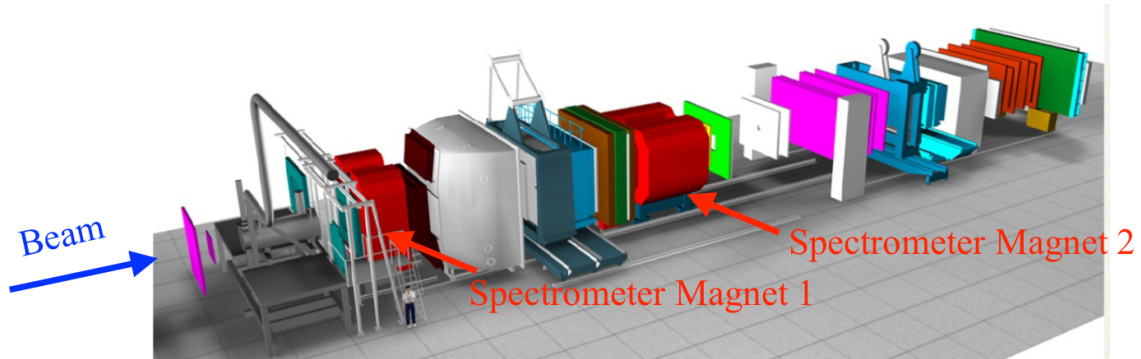


Figure 3.2: A schematic of the 2015 COMPASS setup. This figure was taken from [65].

### 3.1 The Beam

The COMPASS spectrometer receives beam from the Super Proton Synchrotron along the M2 beam line. A schematic of the components in the M2 beam line is shown in Fig. 3.3. The SPS is the second largest accelerator at CERN with a circumference of almost 7 km, which accelerates protons up to an energy of 450 GeV. The SPS extracts beam to the famous Large Hadron Collider (LHC) and as well sends beam to various experiments in the North Area at CERN. While the COMPASS spectrometer is above ground, the SPS is below ground and the M2 beam line must bend the beam from below ground to ground level.

There are several different beam types and energies available to COMPASS. The beam types used for the physics programs are a tertiary muon beam up to 190 GeV/ $c$  and secondary hadron beam with an energy up to 280 GeV/ $c$ . Both of the previous beam types can have a positive or negative charge. As well as the other two beam types it is also possible to have a low intensity tertiary electron beam, mainly used for calibrations.

The beginning of the M2 beam line is the T6 target. The SPS can accelerate primary protons up to 400 GeV/ $c$  to impinge on this T6 target, which produces a secondary beam. The nominal proton intensity on the T6 target is  $100 \times 10^{11}$  spill $^{-1}$ . The T6 target is made of beryllium and has an adjustable length. The longer the T6 target the higher the secondary intensity, where 500mm is the longest and typical target length used for physics data taking. The reaction of the proton beam with the T6 mainly produces secondary protons, pions and kaons. Following this reaction a series of dipole and quadrupole magnets select the momentum and charge of interest.

The SPS spill structure varies throughout the data taking year depending mainly on the needs of the Large Hadron Colider. In 2015, the average intensity provided was  $0.6 \times 10^8$  s $^{-1}$  and the typical spill structure was two 4.8 second spills every 36 seconds.

#### 3.1.1 Muon Beam

The muon beam is a tertiary beam which results from a weak decay of the secondary beam. After the initial proton reaction on T6 the resulting secondary particles are momentum and charge selected and sent through a 600m tunnel with focusing and de-focusing (FODO) quadrupole magnets. In this tunnel the secondary pions and kaons can decay as

$$\pi^{-(+)} \rightarrow \mu^{-(+)} + \bar{\nu}_{\mu^-}(\nu_{\mu^+}) \quad (3.1)$$

and

$$K^{-(+)} \rightarrow \mu^{-(+)} + \bar{\nu}_{\mu^-}(\nu_{\mu^+}), \quad (3.2)$$

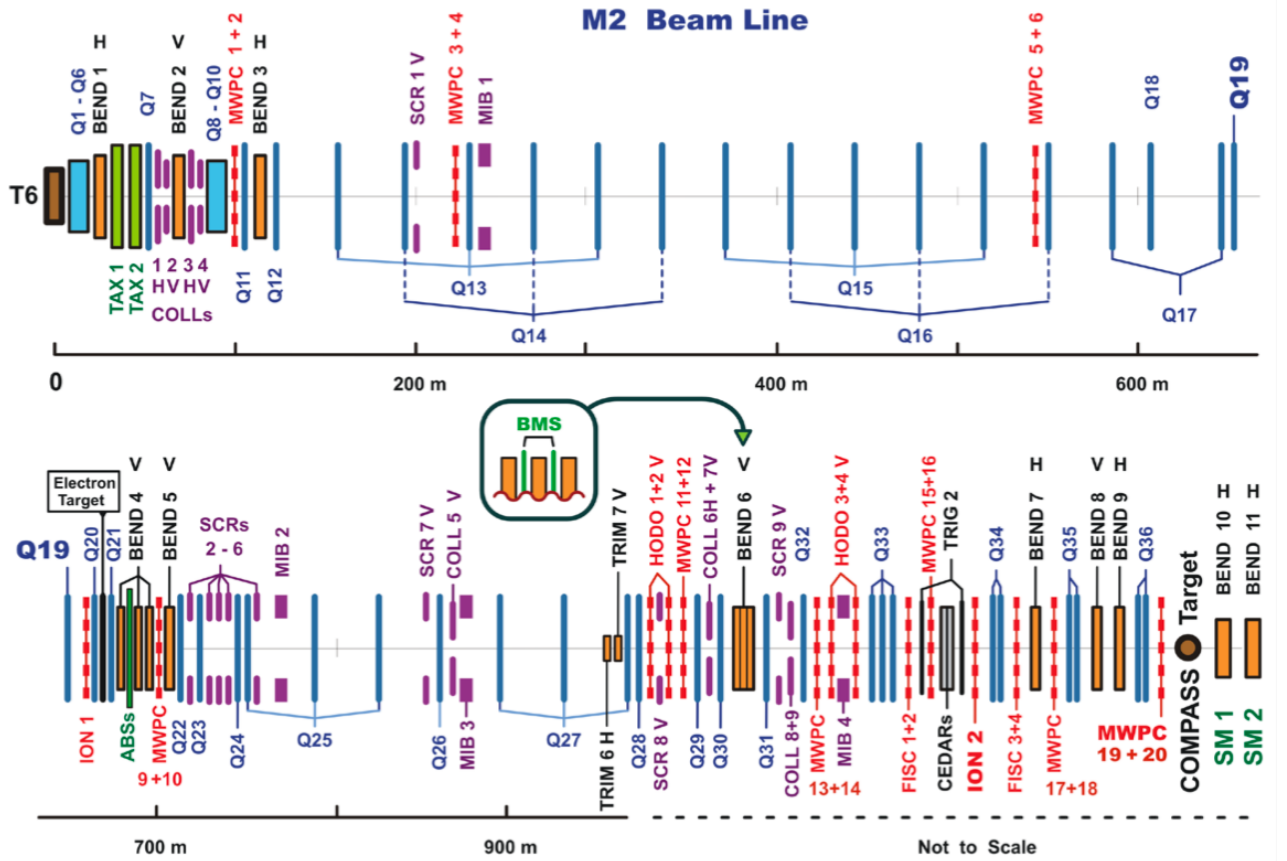


Figure 3.3: The M2 beam line at CERN. This image is taken from [66].

where  $K^{-(+)}$  is a kaon of negative or positive charge. At the end of the tunnel, a series of nine 1.1 m long beryllium absorbers, referred to as the ABS in Fig. 3.3, remove the remaining hadron component that did not decay. A 172 GeV/c secondary pion beam is chosen to achieve a 160 GeV/c tertiary muon beam. Due to the fact that the neutrino in the reactions 3.1 and 3.2 is always left handed, the muon will naturally be longitudinally polarized. For the muon momentum chosen, the muon beam achieves a polarization of 80%.

### 3.1.2 Hadron Beam

To deliver a hadron beam to COMPASS the ABS absorbers are not used. The decayed muons used for the tertiary muon beam have a lower momentum than the hadron beam and are therefore removable by magnetically rejecting these lower momentum muons. In the case of a negative hadron beam as in 2015, the composition of the beam is approximately 97 %  $\pi^-$ , 2.5% kaons and 0.5%  $\bar{p}$ . The 2015 Drell-Yan data taking was performed with a 190 GeV/ $c$  hadron beam.

### 3.1.3 Additional Beam Line Components

After the decay tunnel the beam is bent upwards along another FODO tunnel. The length of this tunnel is 250m and reaches the surface level approximately 100m before the COMPASS target. A series of three dipole magnets, called bend 6, then bend the beam to a horizontal position aimed at the COMPASS target. Both upstream and downstream of bend 6, there are three tracking detectors (BM01-BM06) that make up the Beam Momentum Station (BMS). The BMS is the upstream most component of the COMPASS spectrometer. It is able to determine the beam momentum to better than 1% of the beam momentum with an efficiency of approximately 93%. Bend 6 and the BMS are shown schematically in Fig. 3.4.

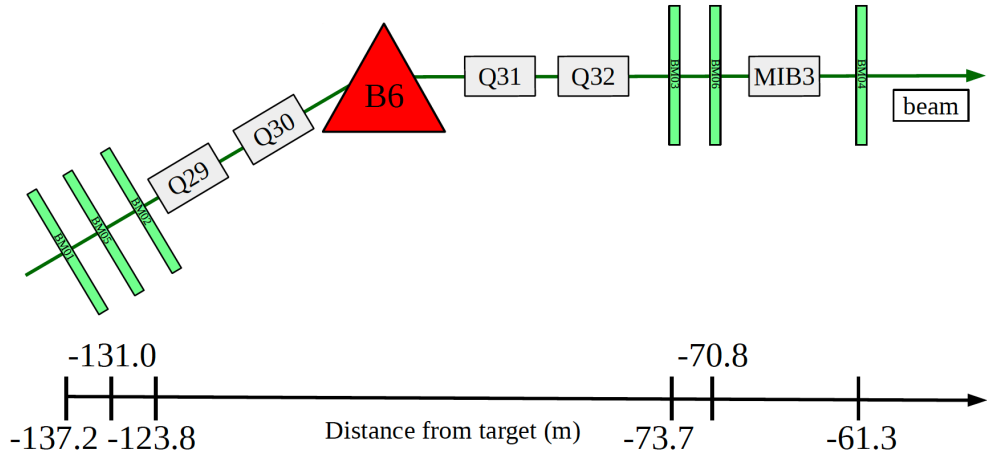


Figure 3.4: Bending the beam to a horizontal position. The BMS detectors (green boxes) are upstream and downstream of the bend 6 magnet (red triangle labeled B6). This image was taken from [64].

During the 2015 Drell-Yan setup the  $\pi^-$  beam intensity was too high for the BMS station to work properly. For this reason, special low intensity, approximately  $10^6 \text{ s}^{-1}$ ,  $\pi^-$  beams were used in 2014 to determine the momentum distribution during Drell-Yan data taking. The beam momentum distribution is shown in Fig. 3.5, where the average momentum is 190.9 GeV/ $c$  with a spread of  $\pm 3.2 \text{ GeV}/c$ .

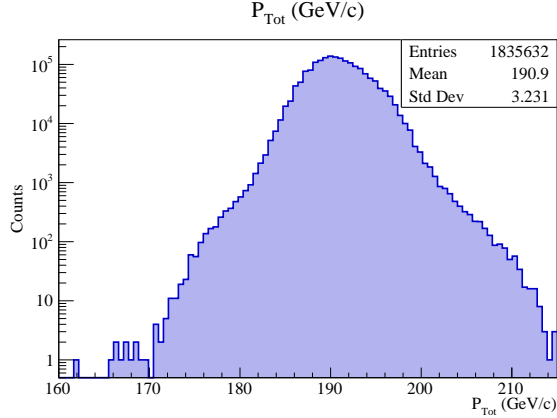


Figure 3.5: The momentum distribution of the  $\pi^-$  beam, determined during dedicated low intensity beam conditions. This figure was taken from [67].

Approximately 30 m upstream of the target are two Cherenkov counter (CEDAR) detectors. As the hadron beam has contamination from several components these CEDARS can be used to distinguish between the different components. The CEDARs general principle of operation is that two particles with the same momentum but different mass will emit Cherenkov radiation at different angles relative to their momentum. When a particle is traveling faster than the speed of light in a given medium, it emits Cherenkov radiation in a cone centered along its momentum axis. The faster the particle is traveling, the narrower the angle of the Cherenkov light cone. A schematic of the CEDAR operating principle is shown in Fig. 3.6. In 2015 the CEDARs were measured to be largely inefficient due to the high beam intensity and are not used for the analysis of this thesis.

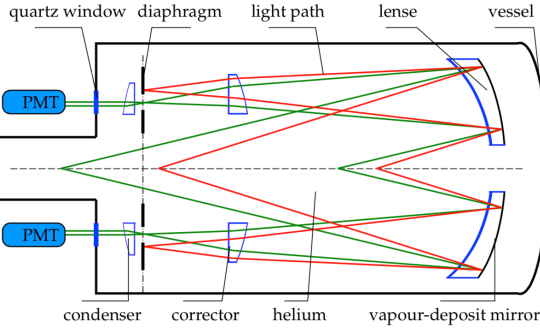


Figure 3.6: Light lines emitted inside CEDARs at COMPASS. The red(green) lines correspond to Cherenkov light emitted from a particle lower(higher) momentum. This image is taken from [66].

For years with a transversely polarized target, such as 2015, a chicane system of dipole magnets is setup in front of the target. The chicane first bends the beam away from the beam line and then back to the target such that the beam hits the target at an angle. A chicane magnet setup is used because a beam

hitting the target without any angle would then be deflected from the target magnet to the left or right of the spectrometer. For this reason the chicane gives the beam an angle before hitting the target such that the non-interacting beam exits the target traveling straight towards the spectrometer.

### 3.2 The Polarized Target

The polarized target at COMPASS is the most complicated and essential component of the spectrometer. It is located upstream of the tracking detectors and spectrometer magnets and downstream of the beam telescope detectors, described in section 3.3. The target consists of two or three cylindrical cells. The possible materials are either solid state ammonia ( $\text{NH}_3$ ) or deuterated lithium ( ${}^6\text{LiD}$ ) [68–70]. Fig. 3.7 shows a schematic of the target.

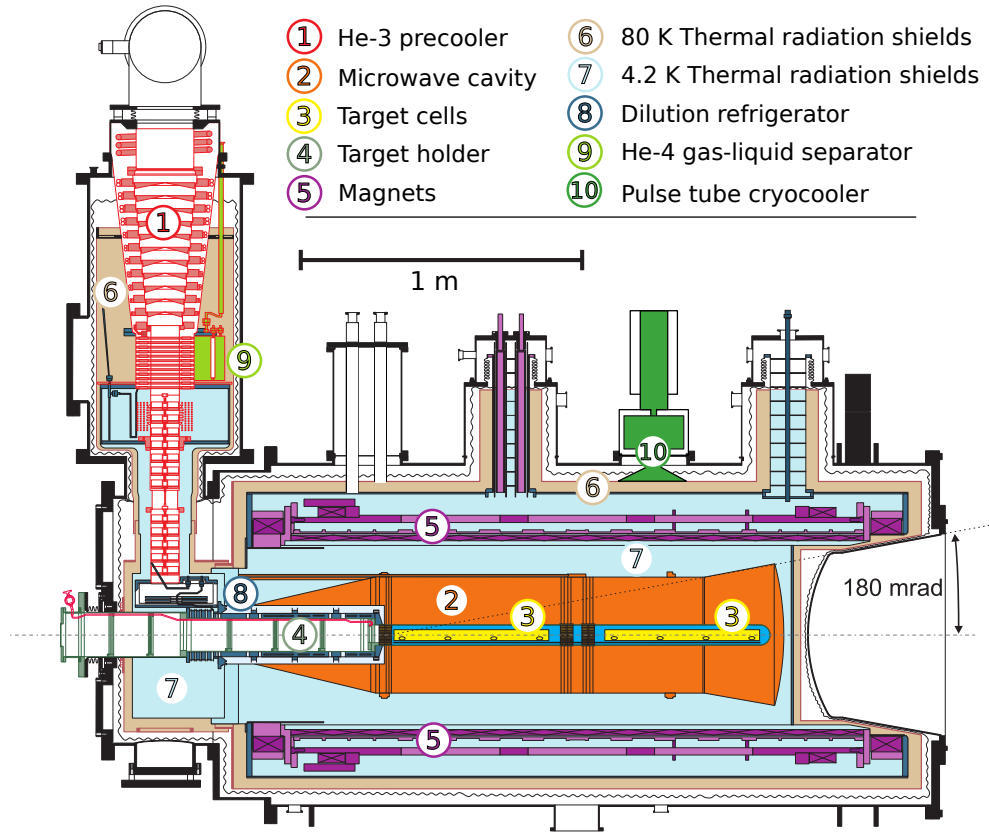


Figure 3.7: The polarized target at COMPASS. This image taken from [68].

Surrounding the cylindrical cells is a longitudinal super-conducting magnet capable of reaching a magnetic field of 2.5 T. This longitudinal magnet polarizes the protons or deuterons in the target material parallel or anti-parallel to the spectrometer axis. The target polarization is maintained by keeping the target in a liquid

helium bath of approximately 60 mK. This is called frozen spin mode where the temperature is maintained by a dilution refrigerator.

The target is polarized through the dynamic nuclear polarization (DNP) method [71]. This process works by first polarizing electrons in the target with the longitudinal magnet. With a high probability, the target electrons are all polarized in the same longitudinal direction for each target cell. Due to their much lower mass, electrons have a larger magnetic moment and therefore can be polarized at a much faster rate than protons or neutrons. At the same time the electrons are being longitudinally polarized, microwave electromagnetic radiation is sent through each target cell. For atoms that have a nuclear spin it is then possible to absorb a microwave and go to an excited state with the electron spin anti-parallel to the magnet field direction and the nuclear spin either parallel or anti-parallel to the magnet field direction depending on the microwave frequency. To ensure only one frequency enters each target cell, there is a microwave stopper between each target cell. The electron with the anti-aligned spin will then quickly have its spin realigned while the nucleon will take much longer to lose its polarization due to its smaller magnetic moment. This process can continue in this way resulting in a net nuclear polarization. Using the DNP method the target proton or deuteron can achieve a polarization of approximately 90% in three days.

The target also includes a 0.63 T transverse dipole magnet to change from longitudinal to transverse polarization. The target must first be longitudinally polarized before the transverse target magnet can change the polarization direction. Once the target is transversely polarized, the target polarization can no longer be increased as microwaves can no longer shine on the target in the polarization direction. Therefore the polarization will decrease exponentially. In 2015 the target was polarized for about half a day between data taking sub-periods and achieved an average polarization of 0.73%, including the effects of exponential polarization loss with time. The relaxation time of the target polarization was about 1000 hours in 2015.

The target polarization was measured with 10 NMR coils while the target cells were longitudinal polarized. In the 2015, each target cell had the most upstream and downstream coils in the center of the target cell and the other three coils on the outside perimeter as is shown in Fig. 3.8. Due to the fact that the polarization can only be measured with the longitudinal magnet on, the polarization is only measured at the start and finish of a transversely polarized data taking. The intermediate polarization is then determined by exponential interpolating between these two times.

In 2015 the setup was two transversely polarized target cells of 55 cm length and 2 cm in radius. The cells were separated by 20 cm and polarized in opposite directions. The polarization of the target cells was flipped every two weeks of data taking to reduce systematic effects from luminosity and geometrical spectrometer acceptance. Due to the fact that the beam needs to be precisely steered onto the target and that the chicane

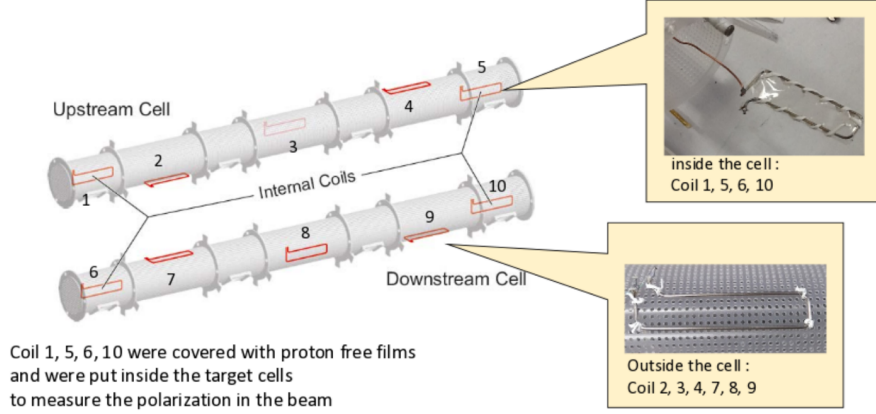


Figure 3.8: The empty polarized target cells side by side along with their NMR coil positions. This image taken from [72].

magnets upstream of the target are setup for only one transverse target magnet direction, the transverse target magnet only pointed downward in 2015. To achieve a polarization flip the target polarization had to therefore be rotated back to the longitudinal direction and the input microwaves had to be changed to achieve the desired polarization direction.

The target material in 2015 was solid state NH<sub>3</sub>. The protons in the three hydrogen atoms were the only nucleons with nuclear spin and therefore only some fraction of the target was able to be polarized. The fraction of polarized nucleons to total nucleons is called the dilution factor. Counting the ratio of unpolarized nitrogen nucleons to polarized hydrogen, one would expect the dilution to be 3/17. However to get a more accurate determination of the dilution factor the follow calculation was used

$$f = \frac{n_H \sigma_{\pi^- H}^{DY}}{n_h \sigma_{\pi^- H}^{DY} + \sum_A n_A \sigma_{\pi^- A}^{DY}}, \quad (3.3)$$

where  $f$  is the dilution factor,  $n_H$  is the number of hydrogen atoms in NH<sub>3</sub>,  $n_A$  is the number of other nucleons in NH<sub>3</sub>, and  $\sigma_{\pi^- H}^{DY}$  and  $\sigma_{\pi^- A}^{DY}$  are the Drell-Yan cross-sections for pion-hydrogen scattering and pion-nucleon scattering respectively. The cross-sections were determined using a parton-level Monte-Carlo

program MCFM [73]. The dilution factor was also further scaled down by studies of reconstruction migration between target cells. The average dilution factor in 2015 was determined to 0.18 in the invariant mass range of  $4.3(\text{GeV}/c)^2$  to  $8.5(\text{GeV}/c)^2$ .

### 3.3 Tracking Detectors

To determine when and where a reaction occurs in the polarized target, tracking detectors are able to position the products of the reaction. The goal of the tracking detectors is to determine a point in space where a particle traversed. The COMPASS tracking detectors attempt to do this for a wide range of angles, momenta and at different rates. For these reasons there are several planar tracking technologies used at COMPASS that can be divided into three categories: very small angle trackers, small angle trackers and large area trackers. As the name suggests, very small angle trackers measure tracks with small angle deflections from the beam axis which are essentially beam particles. The small area trackers measure particle tracks with low but non-zero scattering polar angle and have small central dead zones. The large area trackers are several meters in height and width and measure the largest deflection angles up to 180 mrad.

All of these trackers are split into stations. Each station corresponds to several detectors planes at roughly the same z-position along the beam line. Each station measures a track position in one or more orientation while most measure tracks in three or more orientations. The coordinate orientations measured are the X and Y coordinates, which are the horizontal and vertical directions respectively, and as well the U and V coordinates which are rotated at different angles with respect the X and Y coordinates.

#### 3.3.1 Very Small Angle Trackers

The very small angle trackers extend up to 3 cm away from the beam axis. This is the region with the highest number of particles and therefore these detectors must be able to handle the highest rates up to  $5 \times 10^7$  Hz. The two detector types that make up the very small angle trackers are either scintillating fiber detectors (SciFi) or silicon microstrip detectors. These two detector types are complementary to each other as the former have very good timing resolution, while the latter have very good spacial resolution.

There are three silicon stations possible at COMPASS. These stations have active detecting areas of  $5 \times 7 \text{ cm}^2$ . The spacial resolution of these detectors is nominally  $10 \mu\text{m}$  and the timing resolution is nominally 2.5 ns. For the 2015 setup, the beam intensity was too high for the silicon detectors to operate and therefore these detectors were not used.

There are 10 SciFi stations available at COMPASS. The active areas vary from  $3.9 \times 3.9 \text{ cm}^2$  to  $12.3 \times 12.3 \text{ cm}^2$

planar areas. As well the detection fiber diameters vary between detectors with the different diameters used at COMPASS being 0.5 nm, 0.75 nm and 1 nm. Several fibers are bundled together to determine a strip hit position and the resulting nominal spacial resolutions are 130  $\mu\text{m}$ , 170  $\mu\text{m}$  and 210  $\mu\text{m}$  respectively. The nominal timing resolution of these detectors is about 400 ps. In 2015 three SciFi stations made up the beam telescope and were placed upstream of the target to measure the beam trajectory and timing information. A fourth SciFi station was placed in the LAS section of the spectrometer.

### 3.3.2 Small Angle Trackers

The small angle trackers detect particles with non-zero deflection angles. These detectors have medium size active areas compared to the very small angle trackers and the large angle trackers. They cover 5 cm to 40 cm from the beam axis where the rate drops to approximate 10<sup>5</sup> Hz, two orders of magnitude lower than the rates the very small angle trackers receive. At COMPASS there are two types of small area tracking detectors: micromesh gaseous structure (micromegas) and gas electron multipliers (GEMs).

There are three micromega stations at COMPASS. All three stations are located sequentially after each other between the target and the first spectrometer magnet. As well all three detectors measure four coordinate projections and have an active area of 40x40 cm<sup>2</sup> with a 5 cm diameter dead zone. The micromegas operate by having a conversion region and a smaller amplification region. An ionized particle produced in the conversion region will drift through an electric field of around 3.2 kV/cm to the amplification region where the electric field is around 50 kV/cm. The electric field is too small for amplification in the conversion region but as the name suggest the electric field is high enough to amplify the signal in the amplification region. The amplified signal is then read out on strips. The conversion and amplification regions are separated by a metallic micromesh material. The electrons pass through the micromesh without resistance and are not rimmed out. The micromegas have good spacial resolution because the thickness of the amplification region is only 100  $\mu\text{m}$ , small enough to prevent much transverse spreading of the electron avalanche between strips. The separation of the larger conversion region from the smaller amplification region with the micromesh prevents electric field lines from being distorted in the conversion region and therefore prevents the primary electrons from drifting slower in the conversion region. This allows micromegas to operate at a higher rate than would be possible otherwise. This principle of operation is illustrated in Fig. 3.9. The strips in the central part of the detector are 360  $\mu\text{m}$  corresponding to a position resolution of about 100  $\mu\text{m}$  and the strips in the outer region are 460  $\mu\text{m}$  corresponding to a resolution of about 120  $\mu\text{m}$ . The nominal timing resolution is 9 ns. In 2015 the micromegas were upgraded to include a pixelized section covering much of the dead zone area.

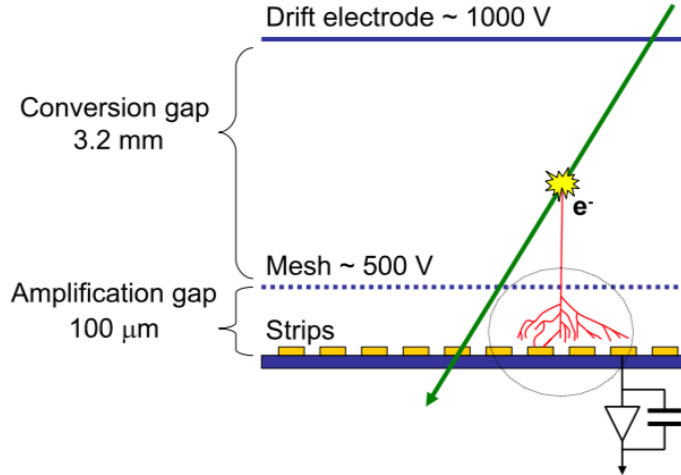


Figure 3.9: Principle of operation for the micromesh gaseous structures (micromegas). This image was taken from [64].

There are eleven GEM detectors located throughout the COMPASS spectrometer. The first GEMs are located after the first spectrometer magnet and the last GEMs are located near the end of the spectrometer. These detectors are positioned close to the beam axis. Each of them is mounted on a large area tracker, covering the dead zone region of the large area tracker. All eleven detectors have an active area of  $31 \times 31 \text{ cm}^2$  and a 5 cm diameter dead zone. In times of lower beam intensity, such as alignment runs, the dead zones can be turned on as an active area.

The GEM detectors are split into four regions where each region is separated by a polyimide foil ( $50 \mu\text{m}$  thick). The polyimide foil has approximately  $10^4 \text{ cm}^{-1}$  drifting holes of  $70 \mu\text{m}$  diameter, which are clad with copper on both sides. There is an electric potential of a few hundred volts between each pair of foil layers. The electron amplification occurs around the holes of each of the three foil dividers. This means GEM detectors speed up the amplification process by splitting the amplification avalanche into three locations. The process is sped up because the drifting electrons are accelerated multiple times, thereby speeding up their drifting velocity which therefore reduces the overall drift time from the ionization location to the strip readout. This allows the GEMs to operate at a higher rate than would otherwise be possible. The principle of operation is illustrated in Fig. 3.10. The nominal timing and spacial resolution of the GEM detectors is 10 ns and  $110 \mu\text{m}$  respectively. Two pixelized GEM detectors were also in operation but were not as crucial for the 2015 Drell-Yan measurement.

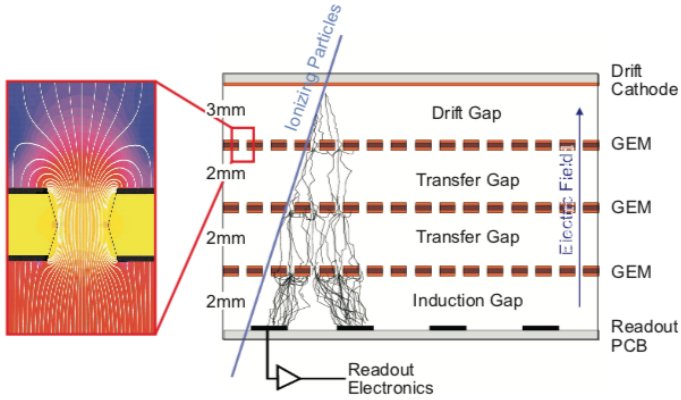


Figure 3.10: The operation principle of the gas electron multiplier (GEM) detectors. This image was taken from [64].

### 3.3.3 Large Area Trackers

The large area trackers measure the largest polar scattering angles at COMPASS. Their dead zones mostly coincide with a small area tracker, described in the previous section 3.3.2, which therefore means these detectors do not have to process the higher fluxes very close to the beam line. The most important feature of these detectors is that they have a large planar area. As a consequence however, their position and timing resolutions are not as good as the small and very small angle trackers. The types of large area trackers used at COMPASS are all gaseous detectors and include drift chambers (DCs), straw tube detectors (straws) and multi-wire proportional chambers (MWPCs).

The first four drift chambers downstream of the target are named DC00, DC01, DC04 and DC05. The first two, DC00 and DC01, have smaller active areas of  $180 \times 127 \text{ cm}^2$  and a circular dead zone of 30 cm diameter. These two drift chambers are positioned upstream of the SM1 magnet. The rates upstream of SM1 are higher. This is due to the fact that low energy particles are produced in the target, but are bent out of the acceptance of spectrometer by SM1. Therefore the detectors downstream of SM1 do not track these low energy particles and therefore DC00 and DC01 need to be able to process a higher particle flux. The next two drift chambers, DC04 and DC05, are downstream of SM1 and both have larger active areas of  $240 \times 204 \text{ cm}^2$  and as well have dead zones of 30 cm diameter. The active areas of all four of these DCs was roughly chosen to coincide with the acceptance of the SM1 yoke. DC05 was first installed for the 2015 Drell-Yan data taking and is further described in chapter 4. All four of these DCs measure four projection views corresponding to eight detector layers. A sketch of the principle of operation is shown in Fig. 3.11. The nominal spacial resolution for these detectors is  $250 \mu\text{m}$ .

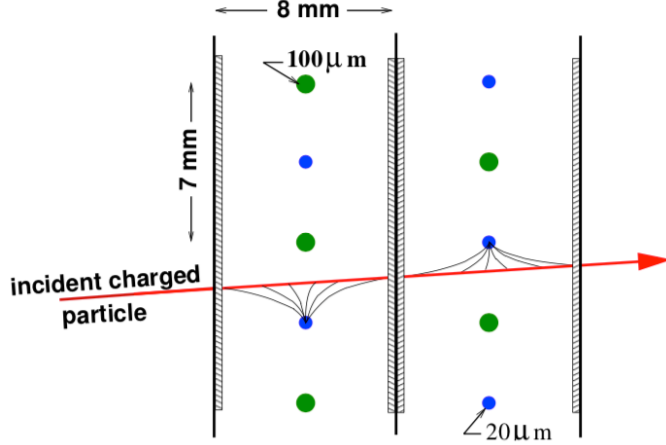


Figure 3.11: Side view of a drift cell in a drift chamber with the ionized drift electron lines coming from the incident charged particle. The larger circles (green) represent field wires and the smaller circles (blue) represent sense wires. This image was taken from [64].

Further downstream the spectrometer, downstream of the SM2 magnet, are the W45 drift chamber stations. The W45 drift chambers are the largest drift chambers at COMPASS. There are six W45 detector stations, which each have an active area of  $520 \times 260 \text{ cm}^2$  and a circular dead zone of 50 cm or 100 cm diameter. Each W45 station measures two projection views corresponding to four detector layers. The drift cells in W45 are  $40 \times 10 \text{ mm}^2$  and the spacial resolution is nominally  $1500 \mu\text{m}$ .

The two straw stations in operation during the 2015 data taking are named ST03 and ST05. ST03 was in the large angle spectrometer downstream of DC05 and consists of two stations measuring six projection views. ST05 was in the small angle spectrometer and measured three projection views. The active areas of each of the horizontal wire stations is  $350 \times 243 \text{ cm}^2$  and the active area of each of the rotated wires is  $323 \times 272 \text{ cm}^2$ . The principle of operation for the straw detectors is very similar to that of a drift chamber. However, instead of having the detector made up of connected drift cells the straw detectors are made of separated circular tubes. Each tube consist of a gold plated tungsten anode wire in the center and the walls of the tube make up a cathode. Due to the fact that the cathode completely surrounds the anode wire there is no electrical interference between neighboring anode wires as there is for drift chambers. For this reason the electric field in each tube is easier to control and the ionized electron drift speed is more linear than other detectors. Each straw detector plane is divided into sections where the straw tubes in the outer most section from the beam line have a diameter of 9.6 mm and the tubes close to the beam line have a diameter of 6.1 mm. In addition, in the central part of the detector there is a physical hole, dead zone of  $20 \times 20 \text{ cm}^2$ . The nominal position resolution for these detectors is  $400 \mu\text{m}$ . A frontal schematic is shown in Fig. 3.12.

For the reason that most of the detected muons are reconstructed in the large angle spectrometer and the fact that many of the high voltage modules were not operation for ST05 in 2015, ST05 was not used for track reconstruction for 2015 Drell-Yan data.

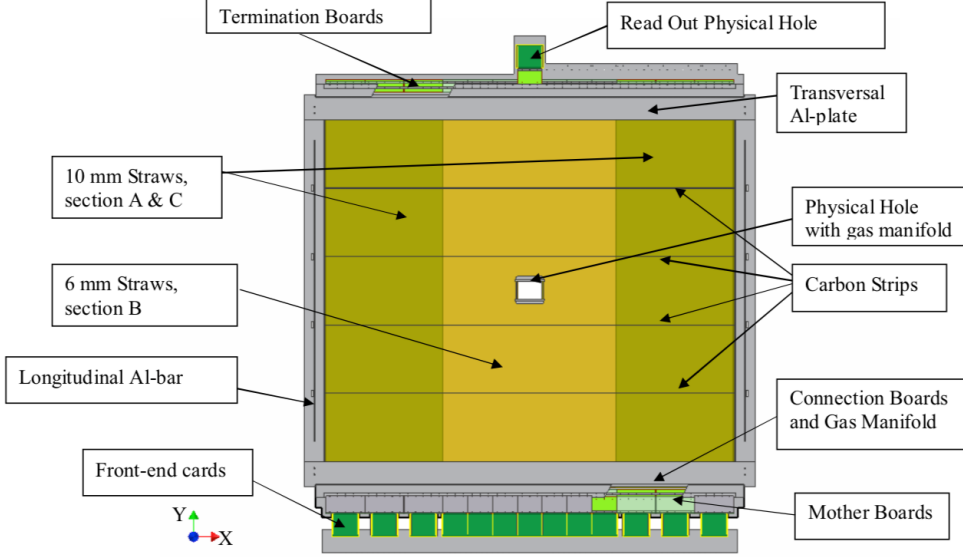


Figure 3.12: Front on view of the active area of a straw detector at COMPASS. This image was taken from [64].

The next type of large angle track is the richwall. This large area tracker operates similarly to the straw tube detectors. The detector consist of eight layers of mini drift tubes (MDT) shown in Fig. 3.13. The central part of each MDT includes a gold plated tungsten sense wire. The richwall is located upstream of the SM2 magnet and downstream of ST03. The richwall has an active area of  $5.27 \times 3.91 \text{ cm}^2$  and a central dead zone of  $1.02 \times 0.51 \text{ cm}^2$ . The nominal position resolution of this detector is  $600 \mu\text{m}$ .

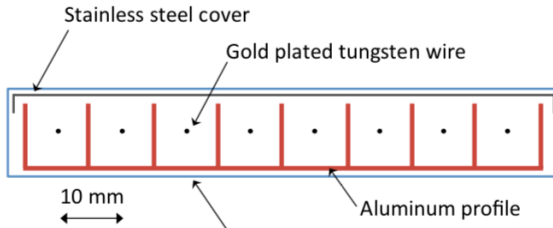


Figure 3.13: The richwall mini drift tubes. This image is taken from [66].

The final type of large area tracking detector at COMPASS is the MWPC. There are 14 of these stations located throughout the experiment. The MWPCs are separated into three categories distinguished by the coordinates they measure. The first type is called type A and consists of three projection views measuring an

x, u and v coordinate. The second type is type A\* and is the same as type A but measures the y coordinate in addition to the other three coordinates. Both type A and A\* have active areas of 178x120 cm<sup>2</sup>. The final type is type B which has a smaller active area of 178x90 cm<sup>2</sup> and measures the same projections as type A. There are seven stations of type A, one station of type A\* and six stations of type B. All three types have circular dead zones of diameters 16 cm, 20 cm and 22 cm for types A, A\* and B respectively.

The MWPCs operate on similar principles to the drift chambers but without a calibration drift curve. For this reason the MWPCs can be made to have one common gas volume between each station. Their position resolution is determined as

$$\frac{\text{sense wire separation}}{\sqrt{12}}, \quad (3.4)$$

which is the variance of a uniform distribution. The separation between sense wires is approximately 2 mm which corresponds to a spacial resolution of these detectors of around 600  $\mu\text{m}$ .

### 3.4 Particle Identification

In the COMPASS spectrometer there are four types of detectors used to determine particle identification (PID). These four detectors are the ring image Cherenkov (RICH) detector, electromagnet calorimeters (ECAL), hadron calorimeters (HCAL) and muon walls (MW). The RICH distinguishes between pions, kaons and protons; ECAL1 and ECAL2 measure the energy from photons and electrons; HCAL1 and HCAL2 measure the energy from hadrons; and MW1 and MW2 distinguish muons from all other particles. The RICH, ECAL1, HCAL1 and MW1 are in the large angle spectrometer in that respective order along the beam line. The small angle spectrometer includes ECAL2, HCAL2 and MW2 again in that respective order along the beam line.

The RICH detector operates similarly to the CEDARS, section 3.1.3. In the RICH, Cherenkov radiation is emitted from particles traveling through it at an angle dependent on the particle's velocity. The RICH is filled with a dielectric gas, C<sub>4</sub>F<sub>10</sub>, which has an index of refraction greater than air. The momentum of a particle going through the RICH is determined from bending radius around SM1. Therefore once the RICH determines the entering particle's velocity, the mass of particles can be distinguished. A sketch of the RICH and its operating principle is shown in Fig. 3.14. To distinguish between particles, the minimum momenta are: 2.5 GeV/c for pions, 9 GeV/c for kaons and 17 GeV/c for protons. The maximum momentum the RICH can distinguish between any of these particles is 50 GeV/c. This detector is located in the large angle spectrometer before any calorimeters.

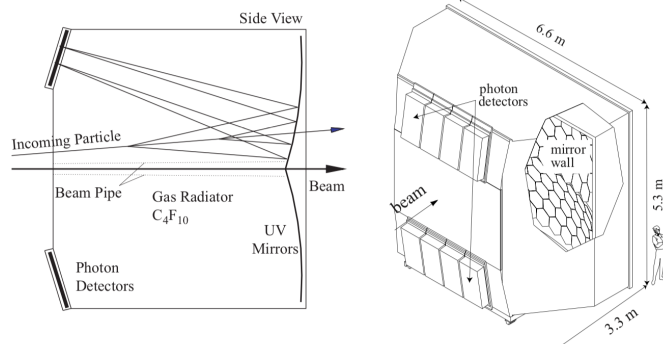


Figure 3.14: Side view demonstrating the principle of operation of the RICH detector. This image was taken from [64].

The ECALs and HCALs both measure the energy of entering particles. Both types of calorimeters do this by stopping a specific entering particle, where the amount of energy deposited in each respective calorimeter is proportional to the incoming particle's energy. ECALs are able to stop and measure electron and photon energies and HCALs stop and measure hadron energies. The energy knowledge along with the momentum determined from the tracking detectors enables the particle to be identified.

The ECALs are made of lead glass towers with photon multipliers attached to these towers on one side. An incoming photon or electron interacts with the lead glass to produce a light signal, which is readout with these photon multipliers. Other particles also interact with the material in the ECALs however hadrons and muons are able to exit through the detector unlike photons and electrons. A frontal view of ECAL1 is shown in Fig. 3.15 and a frontal view of ECAL2 is shown in figure Fig. 3.16.

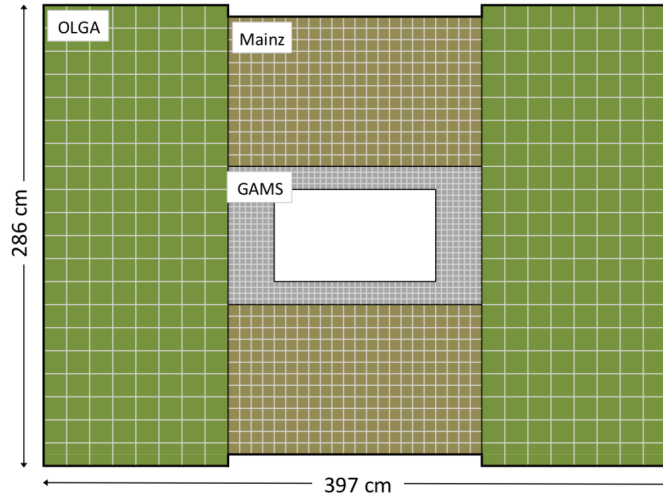


Figure 3.15: Frontal view of the electromagnetic calorimeter 1. This image is taken from [66].

The HCALs are sampling calorimeters, which are made of alternating layers of iron and scintillating

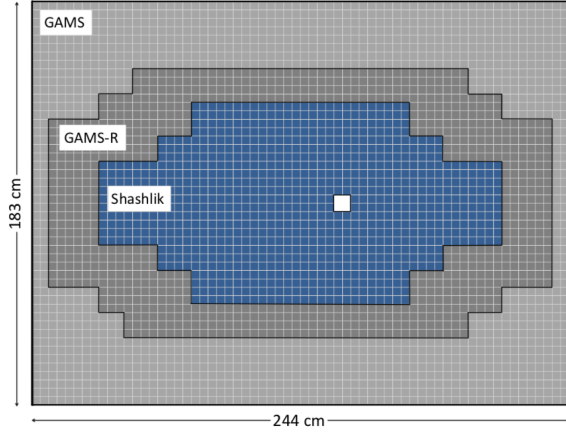


Figure 3.16: Frontal view of the electromagnetic calorimeter 2. This image is taken from [66].

material. An incoming hadron deposits all its energy in the HCAL by making a particle shower in the iron. This particle shower makes a signal in the scintillating material, which is then read out by photo multipliers. The HCALs are placed after the ECALs in each stage of the spectrometer because an electromagnetic shower happens within less material budget than a hadronic shower. The HCALs are effect at determining particle energies from particle with energies between 10 GeV and 100 GeV.

The two MWs are located after an HCAL in their respective stages. Due to their higher mass and absence of color charge, muons are able to pass through the most material budget of any of the particles detected at COMPASS. For this reason both MWs consist of an absorber and tracking detectors downstream of this absorber. Any particles that make it through the absorber are with a very high probability muons.

MW1 consists of eight tracking planes before a 60 cm iron absorber and the same number of tracking planes after this absorber. The tracking portions of MW1 are built similarly to the richwall, described in section 3.3.2, in that they are also made of MDT modules. The active area of MW1 is  $480 \times 410 \text{ cm}^2$  and includes a dead zone of  $140 \times 80 \text{ cm}^2$ . Each plane of this detector has a spacial resolution of 3 mm. A sketch of MW1 is shown in Fig. 3.17.

The second muon wall, MW2, is located downstream of a 2.4 m thick concrete absorber. MW2 consists of 12 planes each with an active area of  $450 \times 450 \text{ cm}^2$  and a dead zone of  $90 \times 70 \text{ cm}^2$ . The detector operates similarly to the straw detectors, section 3.3.2, in that the detector is made of drift tubes with a wire in the center of these tubes. The diameter of the drift tubes is 29 mm and the position resolution is about 1.4 mm.

There is one last absorber in the COMPASS spectrometer located before the H5 hodoscope at the end of the spectrometer hall. This absorber is called muon filter 3 (MW3) and ensures that the inner trigger is

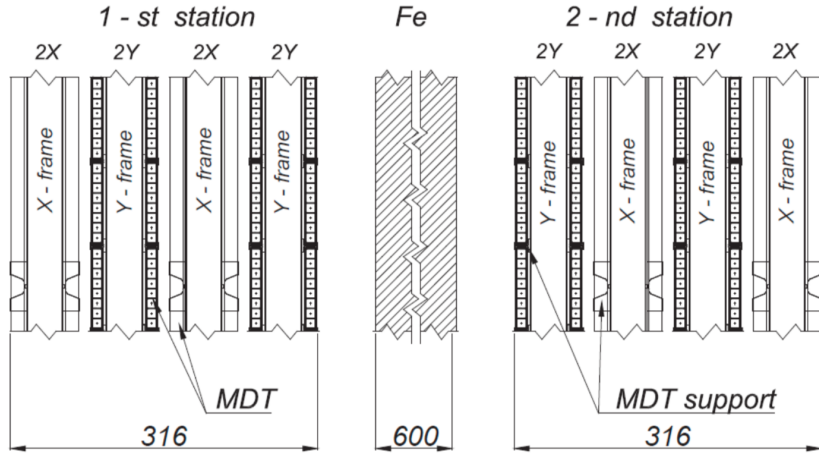


Figure 3.17: A side view sketch of the muon wall 1 detector. This image was taken from [64].

only triggered by a muon.

### 3.5 Trigger

The trigger system at COMPASS defines what is an event. Whenever the trigger signal is given, all the detector information within a few nanosecond timing window is recorded. Due to the fact that there are very many background events occurring as the beam impinges on the target, there is too much information going to the front end modules (FEMs) of the detectors for the FEMs to process and record all this information. For this reason only a certain subset of all the information is stored to disk. The trigger system must therefore have good timing resolution to make quick decisions on which data to record. At COMPASS the trigger systems consist of scintillating hodoscopes attached to PMTs. The timing resolution of these detectors is approximately 1 ns. A top view schematic of COMPASS showing where the relative positions of the hodoscopes for each trigger is shown in Fig. 3.18.

At COMPASS there are five different triggers used to register physics events. Each trigger type includes at least two hodoscopes at different z-positions in the spectrometer. The types of triggers are either target pointing, when the hodoscope slabs are horizontal; or energy loss, when the hodoscope slabs are vertical. The target pointing trigger is setup and used with higher polar scattering angles. As the name suggest, this trigger signals when a particle is scattered from the target. The energy loss trigger is used to trigger on lower  $Q^2$  interactions and signals when a particle is bent a specified amount. This concept is illustrated in Fig. 3.19.

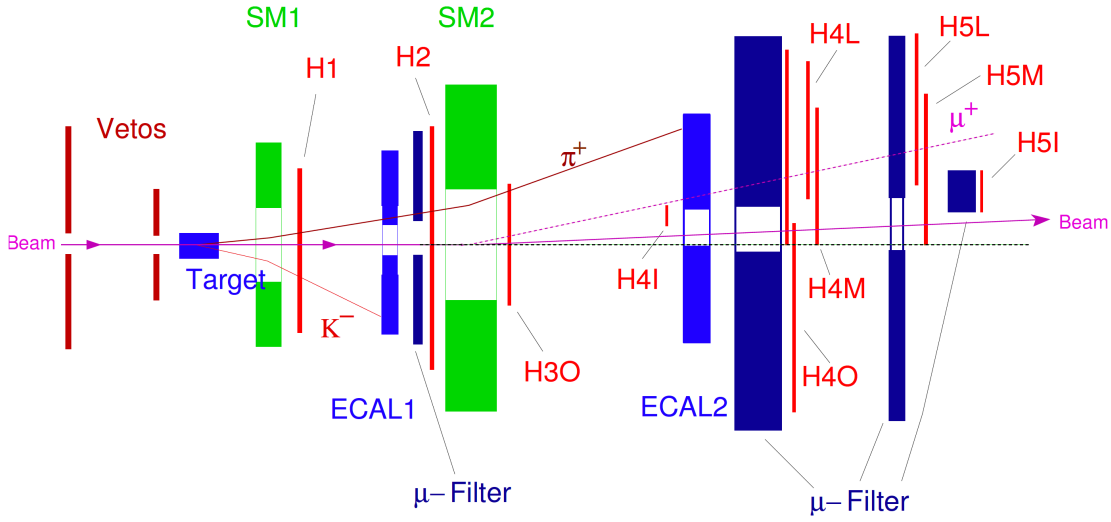


Figure 3.18: Top view of the spectrometer highlighting how different particles can signal a trigger. This image was taken from [74].

There are four triggers in SAS: the inner trigger (IT), the middle trigger (MT), the ladder trigger (LT) and the outer trigger (OT). The IT is an energy loss trigger and includes the hodoscopes HI04X and HI05X. The MT includes both energy loss and target pointing slabs. The hodoscopes in the MT are HM04X, HM05X, HM04Y and HM05Y. The MT hodoscopes whose names end with an X have vertical slabs and those ending with a Y have horizontal slabs. The LT is an energy loss trigger which consists of HL04X and HL05X. The final trigger in SAS, the OT, is a target pointing trigger and consists of hodoscopes HO03Y and HO04Y. The remaining trigger system is in LAS and is a target pointing trigger consisting of hodoscopes HG01Y and HG02Y. The kinematic coverage for the 2015 triggers is shown in Fig. 3.20.

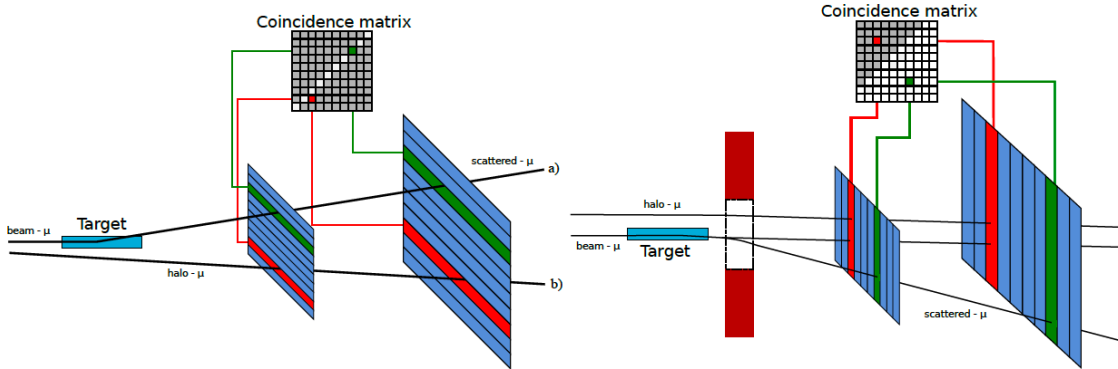


Figure 3.19: The two types of triggers (left is target pointing and right is energy loss) at COMPASS and an illustration of the coincidence matrix used to select events of interest. This image was taken from [75].

In addition to signaling when interesting events occur, it is also important to signal when background events

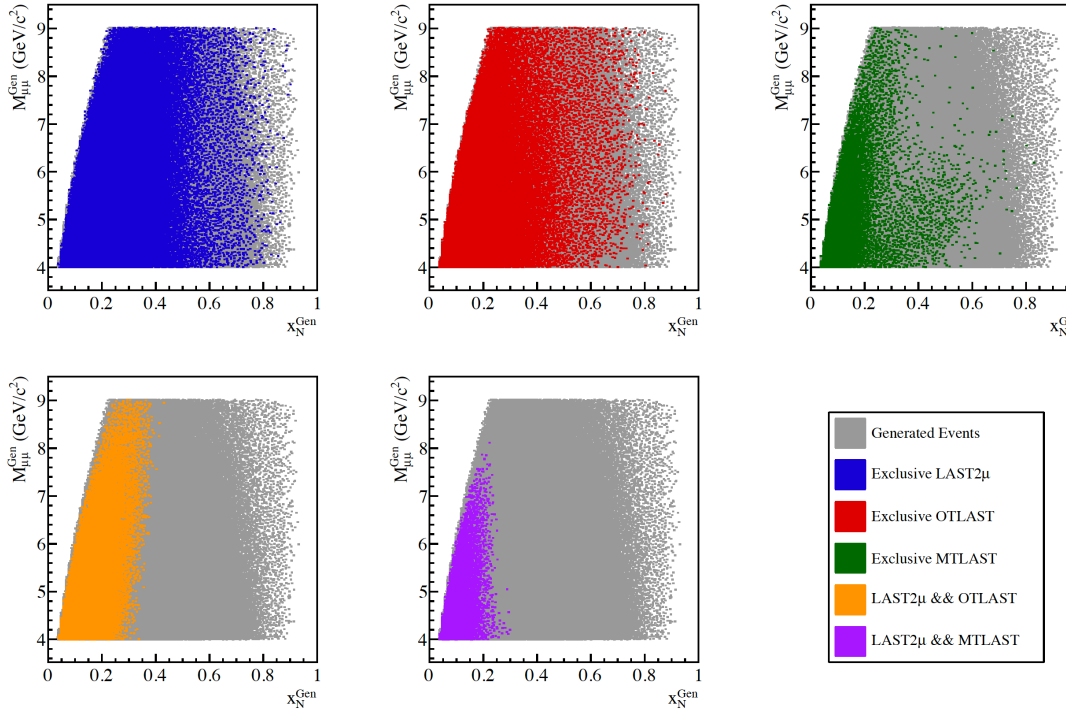


Figure 3.20: The kinematic coverage for the 2015 triggers determined from Monte-Carlo studies. This image was taken from [76].

are occurring. For this reason there is also a veto system upstream of the target as shown in Fig. 3.18. This veto trigger consists of hodoscopes attached to PMTs as well. It is centered on the beam axis but has a hole centered on the nominal beam line. The veto trigger is used to reject halo muons that surround the beam. Halo muons result from the beam decaying, as in Eq. 3.1 and Eq. 3.2, where this decay occurs upstream of the target but downstream of the ABS absorbers. The muon halo surrounds the hadron beam due to the muon's lower momentum, and it is for this reason that the veto hodoscopes, outside of the beam line, are able to reject events that would occur due to the halo.

There is one trigger in the spectrometer hall that is not a hodoscopes. This is the calorimeter trigger (CT). The CT can be used as a trigger when a particle deposits more than a certain energy threshold in the specified calorimeter. In 2015 this trigger was only used as an independent study of the other triggers at COMPASS. Particularly the CT was used to measure the trigger hodoscopes efficiencies.

The last trigger used at COMPASS is a random trigger. This trigger is setup outside of the spectrometer area and registers a signal when a radioactive source disintegrates. In this way the random trigger is truly random. In 2015 this trigger was used in studies of the beam flux.

In 2015, the goal was to measure two muons in the spectrometer. For this reason, two triggers must each signal a particle in coincidence for an event to be registered. For physics analysis the coincidence triggers

are either two muons in LAS (LASxLAS), one muon in LAS and one in the OT (LASxOT), or one muon in LAS and one muon in the MT (LASxMT). The LASxLAS trigger system covers the high  $Q^2$  and high  $x_{beam}$  phase space whereas the triggers including a SAS hodoscope cover lower  $Q^2$  values. In addition to the dimuon triggers there were three single muon triggers corresponding to a particle detected in LAS, MT or OT. These three single muon triggers, however, were pre-scaled down to record only one of every 500, 100 or 100 events respectively. For further tests, 2015 included a random trigger and a beam trigger pre-scaled down by 35000.

### 3.6 Data Acquisition

The data acquisition (DAQ) collects data from the over 250,000 detector channels and transfers this data to storage on magnetic tape at CASTOR (CERN Advanced STORage). Despite the triggering system used to reduce the data rate, the data still is recorded at event rates between 10 kHz to 100 kHz. A typical COMPASS event size is 45 kB. The DAQ is designed to process these data rates and size while minimizing the dead time associated with data collection and transfer. In 2015 the dead time was approximately 10%. The total data the DAQ recorded, after the spectrometer finished commissioning, was approximately 820 terabytes of raw data.

Data collection begins with the digitization of information from a detector channel. This digitization is performed by a time-to-digital converter (TDC) or an analogue-to-digital converter (ADC). These TDCs and ADCs are either on the detector FEMs or on custom COMPASS readout electronics named: GANDALF (Generic Advanced Numerical Device for Analog and Logic Functions), GeSiCA (Gem and Silicon Control and Acquisition) or CATCH (COMPASS Accumulate Transfer and Control Hardware). After digitization the data is transferred by optical fibers to an FPGA multiplexer where the data is buffered by spill and arranged by event. From there an FPGA switch sends the data to multiplexer slaves. The slaves are online computers that oversee the final steps for raw data and transfer this data to CASTOR.

### 3.7 Data Reconstruction

The COMPASS Reconstruction and AnaLysis Program (CORAL) reconstructs the raw data into physical quantities. For example CORAL is able to convert the raw data into particle tracks with momentum, charged and possibly an originating vertex location [77]. The raw data from the DAQ is digitized timing information from tracking detectors or digitized energy information for calorimeters. The process of reconstructing tracks takes the detector timing information and determines a position in space for a particular tracking detector

based on a calibration. CORAL then uses a Kalman Filter to determine straight tracks in regions with no or low magnetic field [78]. The tracks are then connected through the magnetic field using a fast lookup table for known possible bending radii. At this point a track is determined to have a momentum, charge and an associated  $\chi^2$  value. From there the tracks are extrapolated back to the target region and the intersection of at least two tracks is determined as a vertex. If in addition to the two intersecting tracks, a beam particle can be extrapolated forward to the same vertex location then the vertex is assigned to be a primary vertex. Otherwise the vertex is defined as a secondary vertex.

This reconstruction stage reduces the data volume by approximately a factor of 10. In 2015 there were several data reconstructions performed. Between each reconstruction improvements were made to detector calibrations, detector alignment, beam tracking and any other preprocessing improvements that could be made. The final two productions are the t3 production and the slot1 production. The results shown in this thesis are from either t3 or slot1 productions. The slot1 production was the last production. The difference between t3 and slot1 production is a new beam telescope reconstruction algorithm and an optimized alignment which a new detector descriptions. Specifically the hodoscopes for triggers were changed to be described a detector split in half as oppose to a detector split in fourths. The changes between t3 and slot1 resulted in a 10% increase in events.

After reconstruction has been performed the data is stored in data structured trees (DSTs). The usual procedure of reconstruction which gives physical values such as momentum and charge to tracks, results in data called miniDSTs. There is also the possibility to save more information, for example detector hit location information, to make so-called fatDSTs. These DSTs are in a format which can be processed by PHAST (PHysics Analysis Software Tool). PHAST is a COMPASS program written to further analyze physics data. With PHAST there is the possibility to loop over all the miniDSTs and make certain kinematical cuts and to produce so-called  $\mu$ DSTs based on these cuts. In 2015  $\mu$ DSTs were made for all the analysis data where a cut was applied to the miniDSTs saving only events with at least two muons. Both CORAL and PHAST are fully object-oriented C++ programs.

### 3.7.1 Monte-Carlo Production

Monte-Carlo data is simulated data which is performed in three steps. First a programs generates specific physics processes based on their theoretical probabilities. The generators of Monte-Carlo used for this thesis are PYTHIA versions 6 and 8 [79]. Next a GEANT4 simulation of COMPASS determines if a detector will register a hit from these generated physics processes. This saves the data in a raw data format which can be reconstructed by CORAL. Finally the simulated data is reconstructed by CORAL and analyzed in PHAST

the same as if the data were real data.

## 3.8 2015 Drell-Yan Data Taking

The 2015 Drell-Yan data taking is one of the main programs for the COMPASS-II experiment. The data taking began in April of 2015 and ended in November of that year. The physics data used for analysis started in July and finished at the end of data taking. The data recorded before July was used for calibrations and commissioning. The total analysis data was split into nine data periods labeled W07-W15 where each data period corresponded to approximately two weeks of beam time. The spin orientation of each target cell was reversed after the first sub-period of every period to reduce systematic effects arising from different geometric acceptances and luminosities of the up and downstream target cells.

### 3.8.1 Hadron Absorber

The previous sections in this chapter described the spectrometer setup generally and mentioned the specifics for the 2015 setup. The main unique hardware addition in 2015 is the hadron absorber. The hadron absorber was installed because the beam intensity is high and results in many main strong interactions in the target. For this reason the first tracking detectors upstream of SM1 have occupancies that are too high for a satisfactory tracking performance. Therefore the hadron absorber was installed to prevent all particles except muons from entering the spectrometer.

The hadron absorber was placed just downstream of the two target cells as can be seen in Fig. 3.21. The absorber corresponded to approximately 7.5 interactions lengths of material, where the material was mostly alumina ( $\text{Al}_2\text{O}_3$ ) and concrete. Inside the absorber was an aluminum target followed by a tungsten plug, each of radius 2.5 cm. The tungsten was used as a beam dump, while the aluminum was present to prevent back scattering from the tungsten beam plug. A side view showing the dimensions and materials used can be seen in Fig. 3.22. Both the aluminum target and tungsten plug served the double purposes as absorbers and also as unpolarized nuclear targets. In addition to the hadron absorber two 3 mm thick  ${}^6\text{Li}$  absorbers were added just downstream of the primary absorber to absorb thermal neutrons produced in the primary absorber. This  ${}^6\text{Li}$  absorber was proposed to improve the performance of the first tracking detector downstream of the target even with the hadron absorber installed.

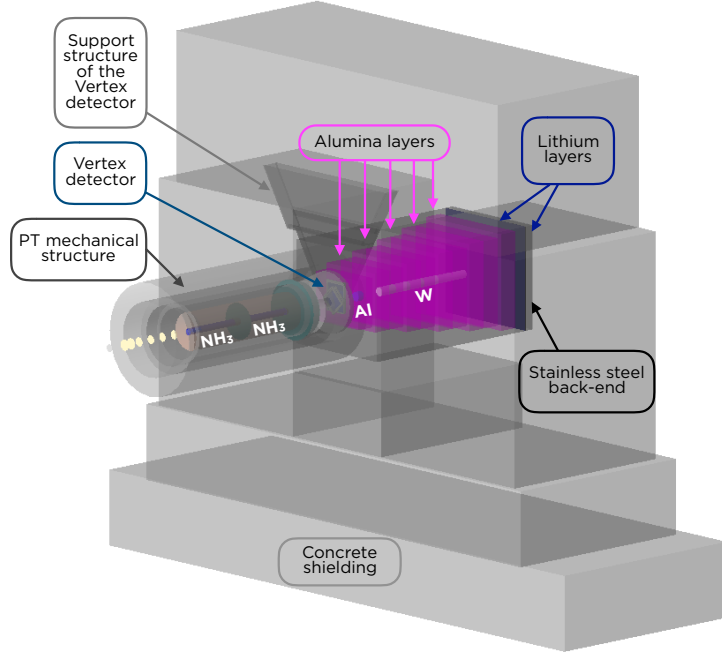


Figure 3.21: The hadron absorber downstream of the polarized target in 2015. This image was taken from [76].

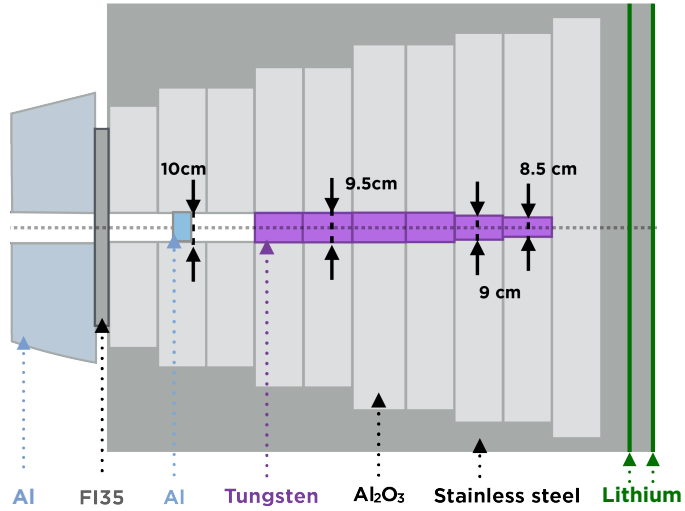


Figure 3.22: Side view of the hadron absorber used in 2015. This image was taken from [76].

# Chapter 4

## Drift Chamber 05

Drift Chamber 05 (DC05) is a large-area planar drift chamber. It was constructed in 2014 and 2015 at the University of Illinois and Old Dominion University and was then shipped to CERN for final assemble. DC5 was installed to the large angle spectrometer of COMPASS during the spring of 2015.

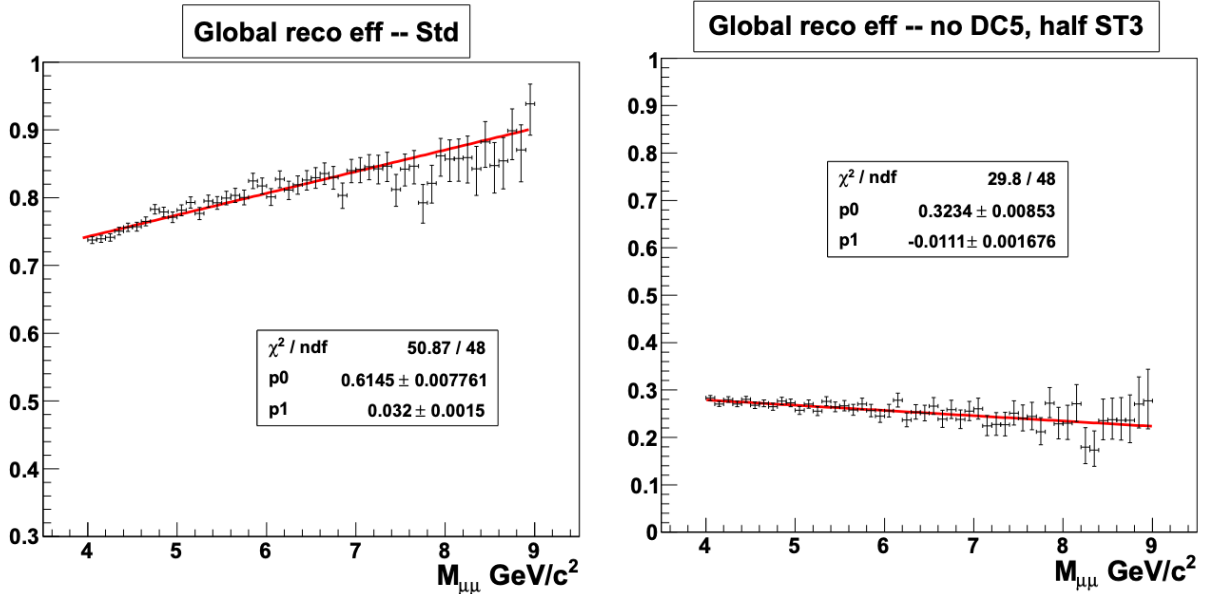
The DC5 detector is an import tracking detector, which successfully collected data from 2015 through 2018 and will continue to be an important component for track reconstruction in future measurements. The author of this thesis significantly contributed to the prototyping and construction at Illinois and the assembly at CERN and as well for performing calibrations and maintaining DC5.

### 4.1 Motivation for Drift Chamber 05

Simulations of the COMPASS spectrometer for Drell-Yan measurements determined that 96% of all events include a track in the large angle spectrometer [80]. For this reason the Drell-Yan trigger system was designed only to record events with at least one track in LAS. As DC5 was installed in LAS it is therefore very important in track reconstruction for Drell-Yan measurements. In fact it was so essential to have the LAS operating optimally that DC5 replaced an aging straw detector. Additional simulations with the Drell-Yan setup and this corresponding COMPASS Drell-Yan trigger showed that the global reconstruction efficiency drops below 30% without DC5 and half of another large area tracker in LAS [81]. That is to say the spectrometer reconstruction efficiency is very poor without DC05 and half of another LAS large area tracker with unstable performance. Fig. 4.1a and Fig. 4.1b show the nominal global reconstruction efficiency and the worst case scenario for Drell-Yan measurements respectively. For these reasons it was very important to have DC05 installed and working reliably.

### 4.2 Operating Principle

Drift chambers are tracking detectors which can detect the location of a high energy charge particle passing through them. A drift chamber is built up of an array of drift cells where at the center of each drift cell is



(a) Global reconstruction efficiency with all detectors working. This image was taken from [82] (b) Global reconstruction efficiency without DC05 and half of another LAS large area tracker. This image was taken from [82]

Figure 4.1: Reconstruction with and without DC05 included.

an anode signal wire (also called a sense wire). Surrounding the signal wire are cathodes which close off the drift cell. The cathodes are set at a higher high voltage than the anode and therefore there is an electric potential difference between the cathode to the anode. Fig. 4.2 shows an example of a drift chamber cell and the equipotential lines within the cell. In DC05 there are two cathode planes on top and bottom of the drift cell and a cathode field wire adjacent to either side of the sense wire as in Fig. 3.11.

Between the anodes and cathodes of a drift cell is a gas mixture. The high energy charged particles which enter the chamber ionize this gas mixture. For each track passing through the chamber, multiple primary ionization electrons are produced and these electrons drift to the signal wire. The number of primary ionization electrons produced however, is not enough to create a detectable signal on the sense wires. For this reason the electric field increases as the inverse of the distance from the sense wire which allows the primary ionization electrons to gain enough energy to further ionize the gas and ultimately produce an electron avalanche near the sense wire. The signal created from this electron avalanche is strong enough to detect. A typical detector is built so that an avalanche can occur before the sense wire but not before a cathode wire. This is accomplished by constructing the chamber with sense wires having a much smaller diameter than the field wires, meaning the electric field near the sense wire can be much larger than the electric field near the field wire.

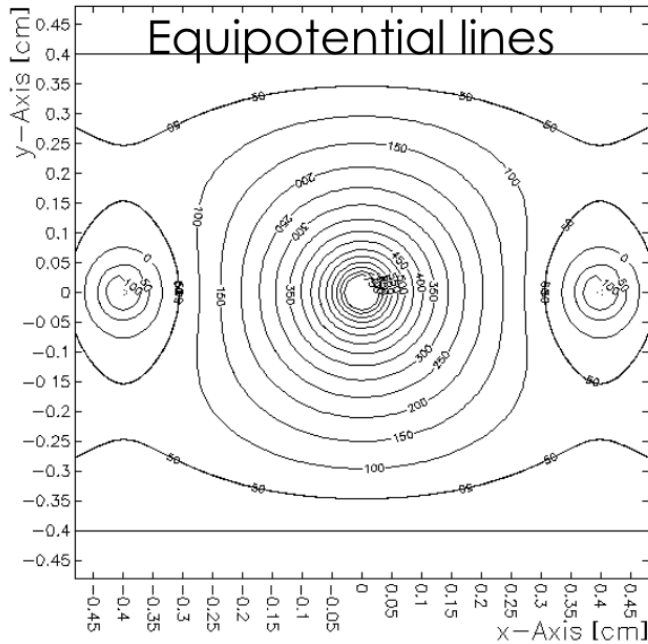


Figure 4.2: View down the axis of a drift cell and the equal voltages for this drift cell configuration. This image is taken from [83]

An important factor for a drift chamber is that the location of the primary ionized electrons can be determined within a drift cell. This knowledge allows for a better position determination of the passing track as compared to a multi-wire proportional chamber as multi-wire proportional chambers cannot measure an RT relation. Each sense wire records the time a signal was detected from a track. For the same track, the trigger records the time the track enter the drift chamber and therefore the difference in time between the sense wire time and the trigger time is the drift time. For a drift chamber it is possible to produce a calibration curve which determines the position within a drift cell for a given drift time. This calibration curve is so-called the RT relation.

Even with a properly calibrated RT relation the track location is ambiguous from only one drift cell. This is because a single drift cell can only determine a track location as a distance from the sense wire. Therefore it is ambiguous where along the sense wire the track passed and also if the track passed to the left or right of the sense wire. For this reason drift chambers are built with several planes in series. A drift cell with the same orientation but shifted with respect to the first drift cell is used to distinguish left and right ambiguity and another cell with an orientation at an angle with respect to the first is used to determine where along the wire the track passed.

### 4.3 Preparation for DC05

One of the first steps in preparation for constructing DC05 was to simulate the detector response using Garfield [84]. The purpose of these simulations was to determine an operating threshold capable of achieving a  $200 \mu\text{m}$  position resolution. With this position resolution goal in mind, Garfield simulated the electric potential field in each drift cell, as shown in Fig. 4.2, and was able to determine the arrival times for ionized electrons as a function of the number of primary ionized electrons for detection. This is important because the timing distribution for electron arrival times gets wider and therefore worsens the position knowledge as the number of primary electrons required for a signal increases. The variance of the electron arrival times was then used to determine the position resolution as a function of the number of primary electrons needed for detection. As is shown in Fig 4.3, the threshold should be tuned to detect the amplification of the fifth primary electron [83]. As is shown in Fig. 4.4 based on the simulation of the integrated induced current versus the drift arrival time, the threshold for detecting the signal should be no greater than 4 fC [83]. This threshold charge is determined by multiplying the induced current by the arrival time. The threshold was accordingly one of the design goals for the front-end electronics.

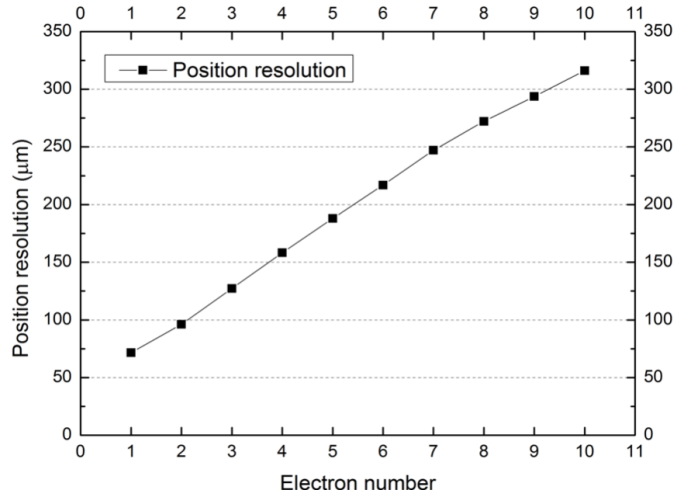


Figure 4.3: A simulation of the position resolution as a function of the number of primary electrons needed to record a signal. This image is taken from [83].

Two prototypes were built to gain hands on building expertise in preparation for construction. Both of these prototypes were constructed in a clean room in the Nuclear Physics Lab (NPL) at UIUC. Much of DC05 was built at the NPL as well. The two prototypes were called prototype A and prototype B. Prototype A, Fig. 4.5, consisted of 1 plane, eight sense wires, 9 field wires and was 50 cm in length. Prototype B on the other hand consisted of two planes with 16 sense wires per plane and a length of 163 cm. Prototype A

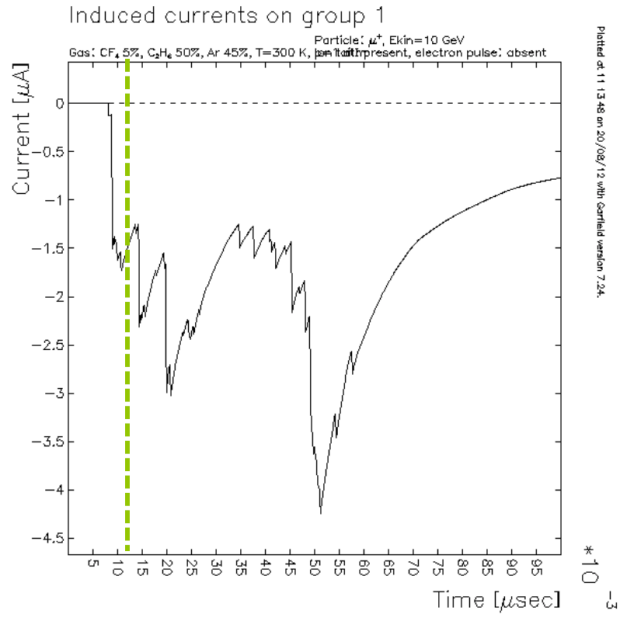


Figure 4.4: Garfield simulation of the induced signal current versus the arrival time. The green line corresponds to the arrival time of the fifth electron. This image is taken from [83].

was tested with beam at DESY and was shown to achieve 200  $\mu\text{m}$  resolution [85]. Both of these prototypes were built using similar materials and construction techniques as the full size detector. In particular these two prototypes were the needed experience for working with sense wires having a diameter of 20  $\mu\text{m}$ .

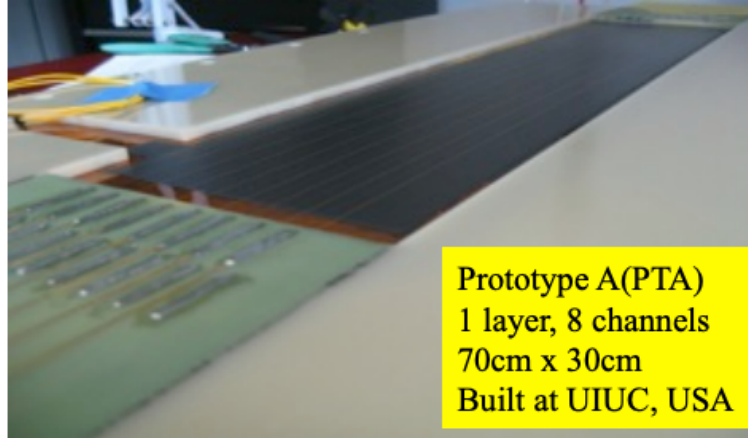


Figure 4.5: Inside view of prototype A. This image was taken from [85].

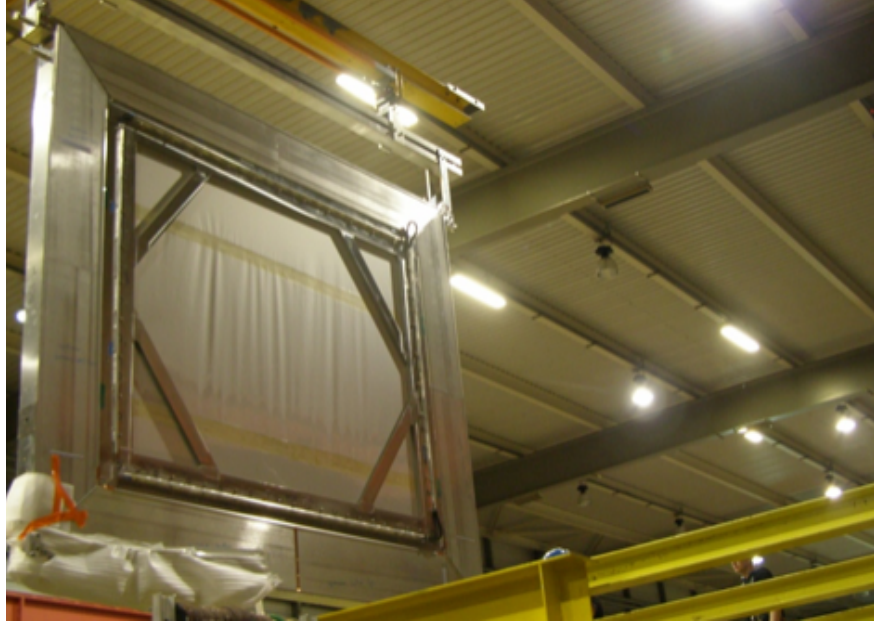


Figure 4.6: The completed DC05 being craned into the COMPASS large area spectrometer.

## 4.4 Design

The design of DC05, figure 4.6, was based off a previous large-area tracker at COMPASS. DC05 has an active area of  $249 \times 209\text{cm}^2$  and consists of eight detector planes. The eight planes of DC05 correspond to four views, where each view measures a coordinate. The coordinates measured from DC05 are the horizontal, vertical and  $\pm 10^\circ$  with respect to the horizontal. The horizontal and vertical coordinates consist of  $2 \times 256$  sense wires and the offset to horizontal coordinates each consist of  $2 \times 320$  wires for increased acceptance. In total DC05 includes 2304 sense wires and 2312 field wires. Each plane was made from a G-10 frame and five frames stacked together constituting a view. The whole detector was closed in with two precision, stainless steel stiffening frames, which were assembled with aluminized mylar as a gas window. The gas window served the double purpose of holding in all the gas and electrically isolating the sense and field wires.

The views of DC05 consist of three cathode layers and two anode layers. The cathodes layers were made from carbon paint sprayed on a  $25\ \mu\text{m}$  thin mylar layer. There were two single-layer cathodes layers and one layer with carbon on two sides within each view. Fig. 4.7 shows a side view of the layers of DC05. Additionally a 30 cm circular so-called beam killer was added to the cathodes to control the efficiency in the central part of the detector. The cathodes were nominally set to -1675 V and the beam killer voltage was set to -900 V for zero efficiency in the high flux central region. The voltage on the beam killer can however be raised above the amplification threshold if the beam flux is reduced and it is desirable to study the central region.

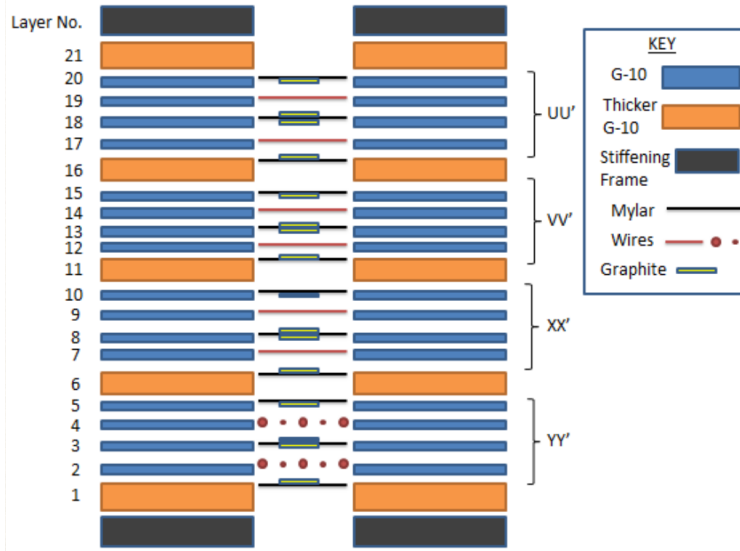


Figure 4.7: A side view sketch of the layers in DC05. This image taken from [86].

The anode layers were made from alternating  $20\ \mu\text{m}$  gold-plated tungsten sense wires and  $100\ \mu\text{m}$  gold-plated copper beryllium field wires, as depicted in figure 4.8. Gold plating was used for both sense and field wires to prevent aging effects. The field wires were also placed at  $-1675\ \text{V}$  and the sense wires were at  $0\ \text{V}$ . The nominal gain of DC05 is approximately  $10^4$ .

During data taking, DC05 is filled with a mixture 45% argon, 45% ethane and 10%  $\text{CF}_4$ . The noble gas, argon, is the gas that is ionized and amplified, while ethane is used as a quencher and  $\text{CF}_4$  is used to reduce aging effects. The quencher, ethane, absorbs photons from the electron avalanche which could pair

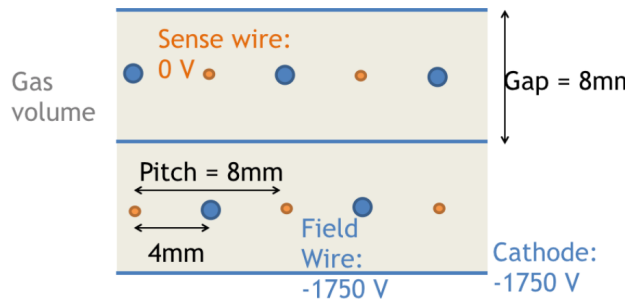


Figure 4.8: The drift cell dimensions of one plane in DC05. This image taken from [86].

produce and therefore make more electrons which would distort the electric field in a drift cell. The quencher therefore is used to reduce the avalanche and ensure the drift cell electric field lines are closer to their design values.

## 4.5 Construction

The construction of DC05 was carried out as precisely as possible starting with the precision from the stainless steel stiffening frames. The overall flatness of the detector was designed to be flat within  $+50 \mu\text{m}$   $-0\mu\text{m}$ . To achieve this the stiffening frames were cut with the highest relative accuracy by cutting the two frames on top of each other to a precision of  $50 \mu\text{m}$  everywhere in their plane. The precision from the stiffening frames was transferred to the anode and cathode frames through 40 positioning pins. The G-10 frames were milled from strips at the NPL using a precision milling machine. Each four strips were then epoxied together on top of one of the stiffening frames to best transfer the precision of the stiffening frame.

The Atlas Tool and Die Works company machined the stiffening frames out of stainless steel. It was very important to construct the detector from stainless steel as DC05 resides in a strong fringe field from the first spectrometer magnet. The gluing procedure was carried out in teams at the NPL. The epoxy used was STYCAST 1266 which is a two component and has low viscosity. The epoxy was applied to both G-10 frames glued together at a lap joint and allowed to dry for 24 hours. The PCB boards were similarly epoxied to the G-10 frames.

The cathodes had mylar stretched and epoxied to them using a custom built stretching machine at CERN. Fig. 4.9 shows the process of stretching mylar on a cathode. An external Swiss company then spray painted carbon on them which was then polished till the resistance was approximately  $30 \text{ k}\Omega/\text{m}$ . All the sense and field wires were hand soldered as shown in Fig. 4.10, and sequentially verified for position using a microscope. It was estimated the position placement of each sense wire was at least as good as half the diameter of a sense wire or precise to  $10 \mu\text{m}$ .

The final assemble was done at CERN. This consisted of stacking each of the 21 G-10 frames on top of the stiffening frame, Fig. 4.11, and attaching copper electronic shielding all along the exterior of the detector to reduce electronic noise.

There were various tests performed throughout the construction process for quality assurance before the final installation. The starting tests were measuring thickness and position of important cuts on the G-10 strips using a micrometer. G-10 strip thicknesses were iteratively milled until they reached better than  $50 \mu\text{m}$  in thickness accuracy. The thickness deviation of the whole detector including the stainless steel



Figure 4.9: Stretching mylar on a cathode plane at CERN

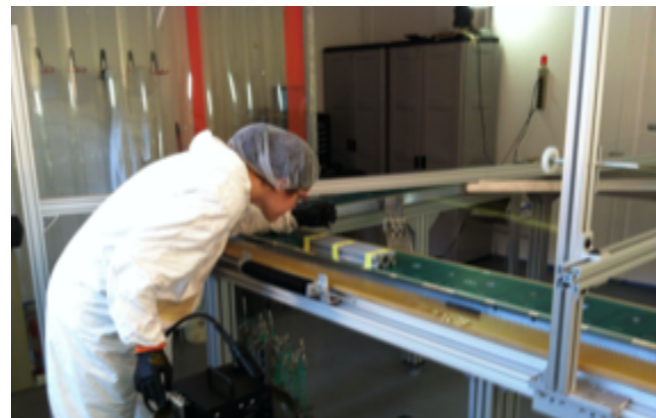


Figure 4.10: Hand soldering DC05 wires in the clean room at the NPL

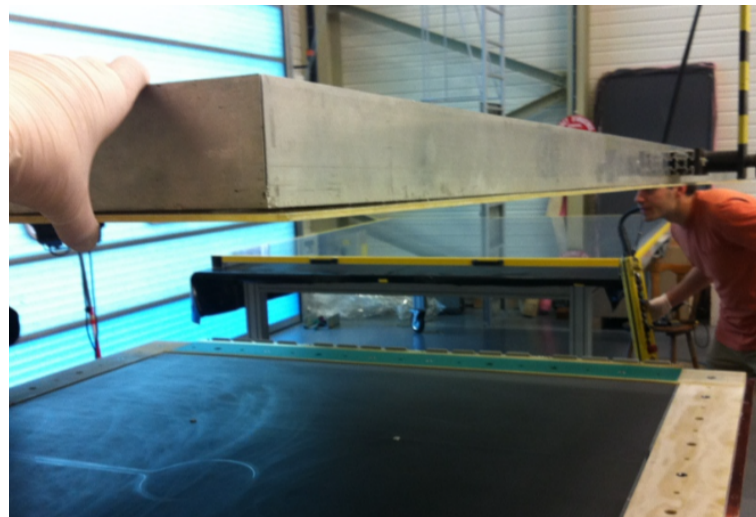


Figure 4.11: The process of stacking the G-10 frames at CERN

stiffening frames was better than  $750\ \mu\text{m}$ . The mechanical tension of the sense wires was tested for stability by ensuring the voltage difference between sense and field wires could reach as high as 2400 V in air. In addition the wire tension was cross-checked by determining the resonance frequency with which the wires vibrated. The resonance frequency was determined by placing the wires in a constant magnetic field and varying a sinusoidal current across each wire till the wires vibrated maximally. The leakage current between sense and field wires was verified to be less than 100 nA at nominal voltage in air. Finally amplification tests were first performed using a strontium-90 source and verifying the counts per electronics board increased below the radioactive source.

## 4.6 2015 Performance

The overall performance of DC05 was checked using the COMPASS reconstruction software CORAL (discussed in sec 3.7). In all cases the view of study was excluded from the reconstruction algorithm and the individual hit information for the view of interest was saved to get an unbiased measurement. The performance of DC05 is determined by judging its response to real tracks. In other words tracks that are not falsely reconstructed, so-called ghost tracks. To ensure these real tracks with higher quality for performance evaluation, only tracks with a primary vertex near the polarized target are considered.

The efficiency was found to be between 85% and 90% depending on the plane. The efficiency was determined by searching for a hit in the DC05 plane of interest within a road of 1.2 mm from the reconstructed track location. The road distance was chosen to be approximately six resolution deviations which is standard at COMPASS. Fig. 4.12 shows the efficiency of one plane of DC05. Using the so called RT relation, figure 4.13, the location of a track within a drift cell can be most accurately determined. This RT relation is tuned as a calibration to minimize the track residuals. The RT relation also varies depending on the beam type, intensity and the trigger type.

The double layer residual was used to determine the position resolution. The double layer residual is the difference between the expected positions of the two planes in a view. The double residual is defined as

$$\Delta u_{\text{double residual}} = (u_{\text{plane 1}} - u_{\text{track}}) - (u_{\text{plane 2}} - u_{\text{track}}) = u_{\text{plane 1}} - u_{\text{plane 2}}, \quad (4.1)$$

where  $u_{\text{plane 1(2)}}$  is the hit position on plane 1(2) determined from the detector of interested and  $u_{\text{track}}$  is the hit position determined from reconstruction. As can be seen in Eq. 4.1, the double layer residual is independent of the track resolution and only depends on the difference between detector hit positions. As the detector was constructed with a known difference between these two cell hit positions, the double residual

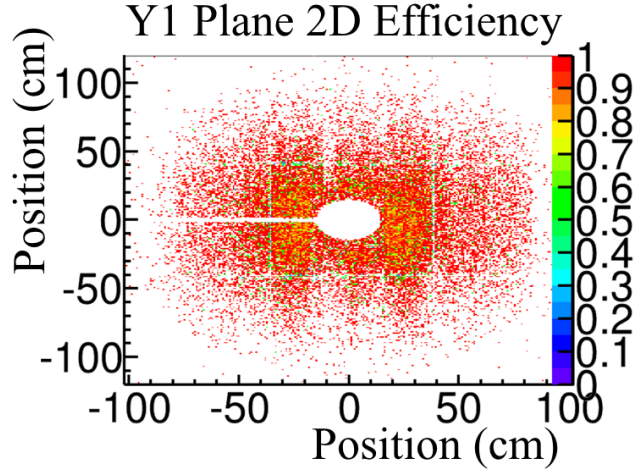


Figure 4.12: Two dimensional efficiency on the DC05Y1 plane. The center region with zero efficiency is a result of the beam killer. This image taken from [87].

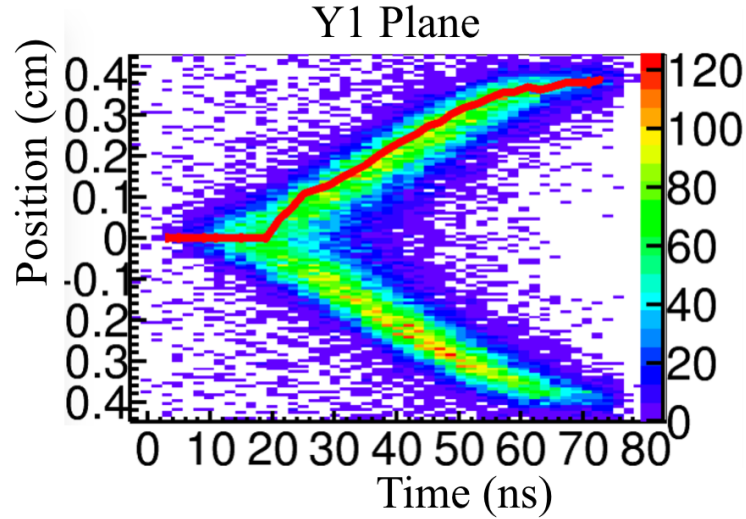


Figure 4.13: Time versus position relation, or RT relation, after calibrating. The red fit shows the calibration determined. This image taken from [87]

distribution is expected to be a constant value. Therefore the variance of the double residual distribution is the addition of the variance of the two individual planes. That is

$$\sigma_{\text{double residual}}^2 = \sigma_{\text{plane 1}}^2 + \sigma_{\text{plane 2}}^2 = 2 * \sigma_{\text{plane 1}}^2, \quad (4.2)$$

where  $\sigma_{\text{plane 1(2)}}$  is the position resolution of plane 1(2). It is assumed that the position resolution is the same for each plane and therefore

$$\sigma_{\text{plane 1}} = \sigma_{\text{plane 2}} = \frac{\sigma_{\text{double residual}}}{\sqrt{2}} \quad (4.3)$$

For the 2015 Drell-Yan physics taking the resolution achieved was approximately  $430 \mu\text{m}$ . This was determined by fitting the double residual with a Gaussian to extract the variance and assuming equal variance per plane in a view as is shown in Fig. 4.14. The difference between the position resolution for the full detector and that of the prototypes is attributed to be due to the large area of the detector and the high beam flux in the data taking. It is not ruled out that software improvement can be made in the future to improve the position resolution. One possible solution would be to include a different RT calibration curve for each section of the detector depending on the particle flux.

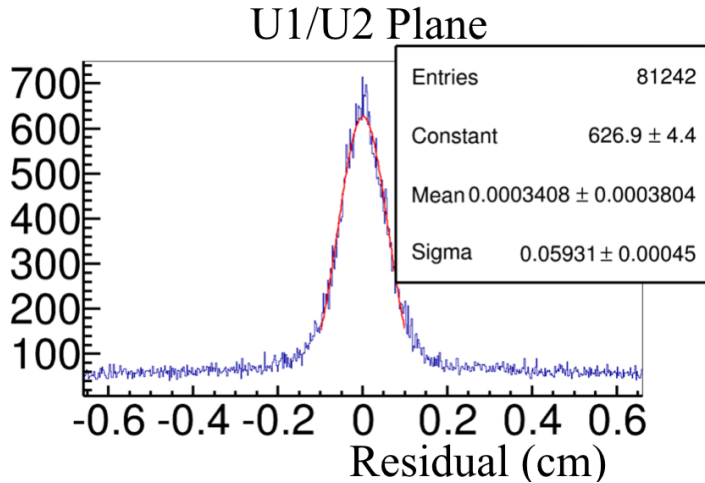


Figure 4.14: The double residual distribution for the U plane together with a Gaussian fit in red to determine the variance of the distribution. This image taken from [87].

# Chapter 5

## Spectrometer Alignment

The alignment of the COMPASS spectrometer is important for track reconstruction. Alignment is a part of pre-processing which ensures all the tracking detectors are centered relative to each other and therefore enables the track resolution to be as accurate as possible. Without accurate alignment, track reconstruction is not possible. The author of this thesis oversaw collection of alignment data and was responsible for performing the alignment of the COMPASS spectrometer in 2015 including a bi-weekly publication the alignment file for the collaboration.

The objective of the alignment procedure is to produce a file called the detectors.dat. This file describes the parameters for all detectors at COMPASS and in particular, gives their orientation in space. For a tracking detector plane, there are four parameters the iterative alignment procedure updates: the horizontal central position, the vertical central position, the angle and the pitch. The pitch refers to a sense wire distance for wire chambers or central strip separation distance for detectors with strip readouts. One or two detectors.dat files were produced for each data taking period, depending on how many alignment runs were recorded that period. The goal of the alignment procedure is to have all four parameters aligned relative to a global reference frame in the COMPASS lab system.

The alignment procedure works by minimizing the distance between all the detector plane hit positions and a track position. The detector hit position is the location the detector measures a particle passed through the plane and the track position is the location the reconstruction measures the particle passed through the detector plane. The distance between this detector plane hit position and the track position will from here on be referred to as the residual distance. Fig. 5.1 provides a simplified example of the setup. One residual is determined per track per detector associated with the track. The task of simultaneously minimizing all the residuals is difficult because there are over 300 detectors planes described in the detectors.dat. To accomplish this minimization, a large amount of quality data is needed and several specific matrix manipulations are utilized in the minimization procedure. This chapter gives an overview of the alignment procedure and includes some results from 2015. For a more complete review see reference [88].

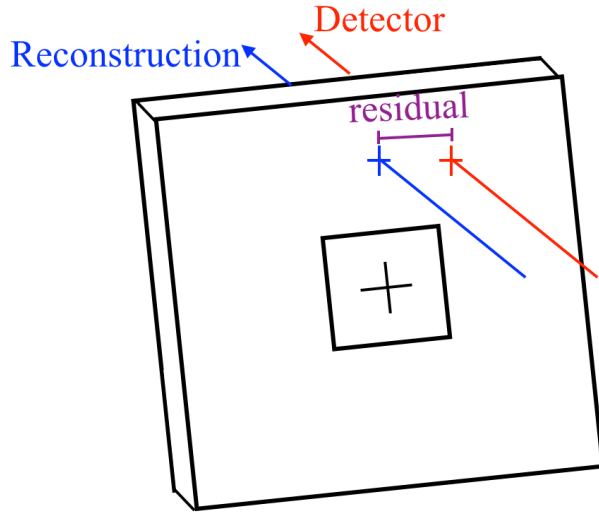


Figure 5.1: An exaggerated alignment example where the reconstructed track (blue) is in a different location than the true track position (red). The alignment minimizes the residual distance (purple) for all the detectors in the spectrometer and tracks in the data sample.

## 5.1 Data Sample to Align the Spectrometer

The alignment data is produced from a dedicated low intensity muon beam. The intensity in 2015 was approximately  $10^5 \mu^-/\text{spill}$ . A muon beam is desirable for alignment data because the beam muons interact less and therefore allows the alignment procedure to assume straight tracks in the minimization problem. The lower intensity is chosen because this allows for the assumption that only one track occurs per event and also the low intensity beam ensures a reduction of detector pile up effects. Reduction in pile up effects, makes reconstruction in the central detector areas possible, and therefore the beam killers on DC00, DC01, DC04 and DC05 can be set to an amplification voltage and as well all the GEM detectors can have their central high voltages turned up to an amplification voltage.

A dedicated trigger system is setup during alignment runs to maximize the illumination of the tracking detectors. The triggers used are a beam trigger, veto trigger and a halo trigger. While this trigger was good for illuminating the detectors, there were some timing shifts relative to the normal Drell-Yan trigger in 2015. For this reason some of the drift chambers used a different calibration curve shifted in time a few nanoseconds.

Two alignment runs of good quality are recorded either at the beginning, middle or end of a data taking period. The first alignment run is with the spectrometer magnets off and the second is with the spectrometer magnets on. The spectrometer magnets off run is used as a first iteration for the alignment procedure to initialize the tracking detector positions. The final alignment positions are then determined

from the spectrometer magnets on data. Within a data taking period, no detectors are allowed to be moved or have their working conditions changed. For this reason, only one detectors.dat file is needed for each data taking period.

One physics run was also used to align detectors far from the beam line. Physics data is the data that is used for the analysis techniques in chapter 6 and chapter 7. Particularly, the outer region of the straw detectors did not receive enough statistics from the aligning runs. Therefore the alignment of the outer straw regions was performed with normal physics data. The runs used for alignment analysis in 2015 are listed in Table 5.1.

In 2015 the alignment runs were performed when the target solenoid was polarizing the target. The chicane magnets, discussed in section 3.1.3, upstream of the target were therefore turned off to ensure the beam momentum was traveling along the target axis. Normally to achieve the reduced intensity, the T6 target is switched to an air target. However in 2015, the T6 target head was not able to switch between the different target lengths and therefore the maximum 500 mm target head was always in use. Therefore to achieve the desired lower intensity, a set of collimators upstream of the target reduced the aperture of the beam line until the correct intensity was achieved.

<b>Period</b>	<b>Sub-period</b>	<b>Magnets off run</b>	<b>Magnets on run</b>	<b>Physics run</b>	<b>detectors.dat name</b>
W07	one & two	259360	259361	259363	detectors.259361.transv.dat
W08	one & two	260072	260073	260100	detectors.260073.transv.dat
W09	one	260625	260626	260661	detectors.260626.transv.dat
	two	260625	260876	261312	detectors.260876.transv.dat
W10	one	261512	261513	261602	detectors.261513.transv.dat
	two	261512	261513	261974	detectors.261970.transv.dat
W11	one & two	262423	262425	262612	detectors.262370.transv.dat
W12	one & two	263139	263140	263175	detectors.263140.transv.dat
W13	one & two	263636	263637	263851	detectors.263637.transv.dat
W14	one & two	none	264428	264429	detectors.264163.transv.dat
W15	one & two	264614	264722	264736	detectors.264619.transv.dat

Table 5.1: COMPASS 2015 alignment data runs

## 5.2 Procedure

The starting point for alignment is an initial detectors.dat file with the tracking detector positions determined from a survey. In the case of 2015, the starting detectors.dat was the last detectors.dat file from 2014 and verified with surveys after the data taking. The surveys are performed with the spectrometer magnets off and the precision from a survey is around 1 mm. Almost all of the detectors at COMPASS have a position resolution better than the survey precision however. Furthermore, several detectors near SM1 can shift in

position due to the fringe field and therefore need a position determination with the spectrometer magnets on. For these reasons the alignment procedure is needed to improve on the survey precision and achieve the best possible track resolutions.

Between periods the starting detectors.dat file was the final detectors.dat from the previous week. Only for the first period were the survey positions used as a starting position. However, as long as the detector was not intentionally moved for repairs, it is expected that the shifts in detector position only change due to temperature effects and therefore do not change much.

### Alignment Parameters

To best describe each detector relative to every other detector there are two reference systems of interest.

The first reference system is the COMPASS main reference system labeled  $Oxyz$ . This reference system can also be referred to as the COMPASS lab system, where the z-axis is along the beam momentum direction, the y-axis points vertically and the x-axis is such that the coordinate system is right handed. The origin of this reference system is at the center of the target from the original COMPASS setup.

The second reference system is the local reference system, which is labeled as  $O'uvz$ . This reference system is different for each detector and has its origin at the center of each detector center. The z-axis coincides with the z-axis in the COMPASS main reference system, while the u-axis is in the direction along the measured coordinate of the detector, and the v-axis is perpendicular to the direction of the measured coordinate of this detector. As an example, a drift chamber with vertical wires measures a coordinate along the horizontal direction and therefore its u-axis is in the horizontal direction and its v-axis is in the vertical direction. A drift chamber with horizontal wires, however, measures a coordinate along the vertical direction and therefore its u-axis is in the vertical direction and its v-axis is in the horizontal direction.

The alignment parameters are defined in  $O'uvz$ . The alignment procedure updates the starting detectors.dat file by the shifts

$$\delta u: \text{shift in } u \text{ direction}, \quad (5.1)$$

$$\delta\theta: \text{shift in rotation angle}, \quad (5.2)$$

$$\delta z: \text{shift in } z \text{ direction}, \quad (5.3)$$

$$\delta p: \text{shift in pitch}. \quad (5.4)$$

The shift in z direction has never converged however. As a result the z-coordinate from the survey is used

as the final z position and the shift in pitch is used as an effective shift in the z direction.

### Residual Function

The goal of the alignment procedure is to minimize the sum of all the residuals from each track and each detector associated with the track. Due to the fact that the alignment tracks are assumed to be straight, each track can be defined by four parameters. The track parameters,  $\alpha_T$ , are

i:  $(x^0, y^0)$  the x and y coordinates at the main reference origin,

ii:  $(t_x^0, t_y^0)$  the tangents of the track momentum in the x and y directions at the origin of the main reference system,

where the track parameters are defined for each track. The alignment parameters,  $\alpha_D$ , on the other hand are defined for each detector and are the same for all tracks. The alignment procedure minimizes the  $\chi^2$  function

$$\chi^2 = \sum_{i=1}^{i=n_{\text{tracks}}} \sum_{j=1}^{j=n_{\text{detectors}}} \frac{F_{i,j}^2(\alpha_{T,i}, \alpha_{D,j})}{\sigma_j^2}, \quad (5.5)$$

where  $\sigma_j^2$  is the position resolution of detector j and  $F_{i,j}$  is the residual distance of each detector j for each track i it is associated with.

The residual distance, F, depends on the track parameters and the detector parameters. For magnets-off data the tracks are not bent at all and are therefore straight tracks throughout the whole spectrometer. The x and y coordinates at position z are

$$x = x^0 + t_x^0(z - z^0), \quad (5.6)$$

$$y = y^0 + t_y^0(z - z^0), \quad (5.7)$$

where  $z^0$  refers to the position at the origin in  $Oxyz$ . Rotating these track positions from the main references system,  $Oxyz$ , to the detector reference system,  $O'uvz$ , the residual distance is

$$F = \cos(\theta)[x^0 + t_x^0(z - z^0)] + \sin(\theta)[y^0 + t_y^0(z - z^0)] - u, \quad (5.8)$$

where u is the measured hit position from the detector at position z. To show the dependence on the alignment parameters

$$F(\alpha_T, \alpha_D + \delta\alpha_D) = (1 + \delta p) \left\{ \cos(\theta + \delta\theta)[x^0 + t_x^0(z - z^0)] + \sin(\theta + \delta\theta)[y^0 + t_y^0(z - z^0)] \right\} - (u + \delta u). \quad (5.9)$$

In Eq. 5.9, the change in pitch would intuitively affect the  $u$  position, however the change in pitch was moved to the track coordinates to make derivatives of  $F$  independent of  $u$ . This has no effect on the minimization of  $F$ .

In the case of magnets-on data, the track positions need to have further modifications from Eq. 5.9. The magnetic field will bend the tracks so the track positions determined in Eq. 5.6 need to have further corrections. The track positions with SM1 and SM2 on are

$$x = x^0 + \delta x + (t_x^0 + \delta t_x)(z - z^0), \quad (5.10)$$

$$y = y^0 + \delta y + (t_y^0 + \delta t_y)(z - z^0), \quad (5.11)$$

where the  $\delta_x$ ,  $\delta t_x$ ,  $\delta_y$  and  $\delta t_y$  changes are determined from CORAL during the reconstruction process. Even though the spectrometer magnets have nominally vertical magnetic fields, there are still fringe fields that are not vertical. It is for this reason that CORAL also calculates an updated track position in the  $y$ -coordinate.

The residual dependence on the alignment parameters defined for magnetic fields on is then

$$\begin{aligned} F(\alpha_T, \alpha_D + \delta\alpha_D) = (1 + \delta p) & \left\{ \cos(\theta + \delta\theta)[x^0 + \delta x + (t_x^0 + \delta t_x)(z - z^0)] \right. \\ & \left. + \sin(\theta + \delta\theta)[y^0 + \delta y + (t_y^0 + \delta t_y)(z - z^0)] \right\} - (u + \delta u). \end{aligned} \quad (5.12)$$

## $\chi^2$ Minimization

The  $\chi^2$  function, Eq. 5.5, is analytically minimized. That is, the derivatives of Eq. 5.5 with respect to all the track and alignment parameters are set to zero and these alignment parameters are solved for. This can be written

$$\frac{1}{2} \frac{\partial \chi^2}{\partial \alpha_k} = \sum_i^{n_{\text{tracks}}} \sum_j^{n_{\text{detectors}}} \frac{1}{\sigma_j^2} \frac{\partial F_{i,j}}{\partial \alpha_k} F_{i,j} = 0. \quad (5.13)$$

To perform this calculation the residual function is Taylor expanded in the track and alignment parameters as

$$F = F^0 + \sum_k \frac{\partial F}{\partial \alpha_k} \alpha_k. \quad (5.14)$$

Using this approximation for  $F$ , Eq. 5.13 can be written as a matrix equation where the dimensions of the matrix are  $(4n_{\text{detector}} + 4n_{\text{tracks}}) \times (4n_{\text{detector}} + 4n_{\text{tracks}})$ . This matrix form is written as

$$\begin{aligned}
& \left[ \begin{array}{ccc|cc}
\sum_i^{n_{\text{tracks}}} \sum_j^{n_{\text{detectors}}} \frac{1}{\sigma_j^2} \frac{\partial F_{i,j}}{\partial \alpha_{D_1}} \frac{\partial F_{i,j}}{\partial \alpha_{D_1}} & \cdots & \sum_j^{n_{\text{detectors}}} \frac{1}{\sigma_j^2} \frac{\partial F_{i,j}}{\partial \alpha_{D_1}} \frac{\partial F_{i,j}}{\partial \alpha_{T_{4n_{\text{tracks}}}}} \\
\vdots & \ddots & \vdots \\
\sum_j^{n_{\text{detectors}}} \frac{1}{\sigma_j^2} \frac{\partial F_{i,j}}{\partial \alpha_{T_{4n_{\text{tracks}}}}} \frac{\partial F_{i,j}}{\partial \alpha_{D_1}} & \cdots & \sum_j^{n_{\text{detectors}}} \frac{1}{\sigma_j^2} \frac{\partial F_{i,j}}{\partial \alpha_{T_{4n_{\text{tracks}}}}} \frac{\partial F_{i,j}}{\partial \alpha_{T_{4n_{\text{tracks}}}}}
\end{array} \right] \begin{bmatrix} \alpha_{D_1} \\ \vdots \\ \alpha_{T_{4n_{\text{tracks}}}} \end{bmatrix} \quad (5.15) \\
& = - \begin{bmatrix} \sum_i^{n_{\text{tracks}}} \sum_j^{n_{\text{detectors}}} \frac{1}{\sigma_j^2} \frac{\partial F_{i,j}}{\partial \alpha_{D_1}} F_{i,j}^0 \\
\vdots \\
\sum_j^{n_{\text{detectors}}} \frac{1}{\sigma_j^2} \frac{\partial F_{i,j}}{\partial \alpha_{T_{4n_{\text{tracks}}}}} F_{i,j}^0
\end{bmatrix}.
\end{aligned}$$

To solve Eq. 5.15, the matrix on the left side must be inverted. A normal alignment run however, results in over 200,000 tracks meaning this matrix is huge and infeasible to invert. Fortunately many of the entries in the matrix are zero which allows that this matrix inversion can be reduced to the inversion of several smaller matrices.

To perform the matrix inversion, note that Eq. 5.15 can be written

$$\left[ \begin{array}{c||ccc}
\sum_i C_i & \dots & G_i & \dots \\
\hline
\vdots & \ddots & 0 & 0 \\
G^T & 0 & \Gamma_i & 0 \\
\vdots & 0 & 0 & \ddots
\end{array} \right] \begin{bmatrix} \alpha_\alpha \\ \vdots \\ \alpha_{T_i} \\ \vdots \end{bmatrix} = \begin{bmatrix} \sum_i b_i \\ \vdots \\ \beta_i \\ \vdots \end{bmatrix}, \quad (5.16)$$

where  $\sum_i C_i$  and  $\sum_i b_i$  include only derivatives of  $F_{i,j}$  with respect to alignment parameters,  $\Gamma_i$  and  $\beta_i$  include only derivatives of  $F_{i,j}$  with respect to track parameters and  $G_i$  includes derivatives of  $F_{i,j}$  with respect to both alignment and track parameters. Then reference [89] shows that Eq. 5.16 can be inverted to give the alignment parameters as

$$\alpha_\alpha = C'^{-1} b', \quad (5.17)$$

where

$$C' = \sum_i C_i - \sum_i G_i \Gamma_i^{-1} G_i^T, \quad (5.18)$$

and

$$b' = \sum_i b_i - \sum_i G_i \Gamma_i^{-1} \beta_i. \quad (5.19)$$

### 5.3 Results

The spectrometer alignment is performed in iterative steps. In each iteration of the alignment procedure, the matrix inversion, Eq 5.16, is performed and the alignment parameters are updated. All alignment tracks reconstructed in the first alignment iterations are based off of two pivot detectors. That is straight track parameters were determined from these two pivot detectors and all detectors were aligned relative to these pivot detectors. In 2015 the pivot detectors were GM05 in LAS and GM08 in SAS. After each iteration the detector parameters are updated to reduce the overall  $\chi^2$  value. Each new iteration is performed using the same data set and the alignment parameters are better described with each iteration.

The procedure used in 2015 was as follows:

1. Align with magnets off data. In this stage all the spectrometer detectors except the outer regions of the straw detectors are aligned. This includes all the detectors downstream of the polarized target but does not include the beam telescope detectors. Magnets off data is used as a first iteration and therefore only alignment in the u-coordinate is performed.
2. Align the same spectrometer detectors with magnets on data. In these iterations the detectors are aligned for u-coordinate, angle and pitch.
3. Align the beam telescope detectors with magnets on data. In these iterations the previous detectors are all used as pivots. The beam telescope is therefore aligned relative to the spectrometer detectors.
4. Finally the outer region of the straws are aligned with physics data. For this alignment, the spectrometer detectors are again used as the pivot.

The quality of the alignment was monitored after each iteration and checked that the procedure was converging. In practice four iterations of each of the previous steps were found to be sufficient for convergence. To ensure the alignment data was from quality tracks, only tracks with momentum reconstructed and having reduced  $\chi^2$  less than 30 were considered.

As all detectors but the pixel detector planes measure a coordinate in one direction only, the detector positions are only updated in their measured direction. This can lead to detectors being well misaligned in the direction orthogonal to their measured coordinate however. To account for this, detector planes were updated to match the u-position from a detector plane measuring a different coordinate in the same detector station. For example DC04X planes had their y-coordinate determined from the DC04Y planes and DC04Y planes had their x-coordinate determined from DC04X planes.

After each alignment iteration the quality of the alignment is accessed for each individual detector and for the spectrometer as a whole. The quality distributions to check after each iteration are described in the following list.

- i) The residual distribution,  $\Delta u$ , of each detector. That is a distribution of

$$\Delta u = u_{\text{track}} - u_{\text{detector}}, \quad (5.20)$$

where this distribution indicates if the detector is shifted along the direction of its measured coordinate. This distribution is expected to be a Gaussian with a zero mean and an RMS value comparable to the position resolution of the detector. Any deviation from a zero mean indicates the detector is shifted and a large RMS value indicates the detector is not performing as expected. If the detector is not performing as expected the most obvious reason is the calibrations used for that detector are not accurate. Fig. 5.2 shows an example of this distribution to monitor.

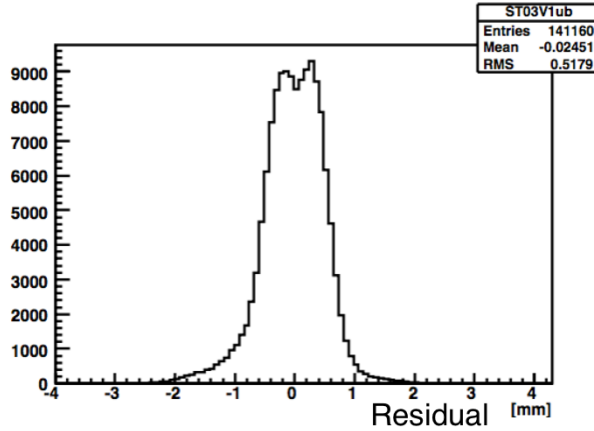


Figure 5.2: The residual distribution for a straw detector plane

- ii) The change in the residual as a function of the detector's v-coordinate. In a wire detector for example, this is the change in the residual as a function of the distance along the wire. This distribution, Fig. 5.3, is expected to be uniformly zero. A slope in this distribution indicates that the detector's angle is misaligned.
- iii) The change in the residual as a function of the detector's u-coordinate. For a wire detector, this is the change in the residual as a function of the distance perpendicular to the wire. This distribution, Fig. 5.4, is also expected to be uniformly zero. A slope in this distribution indicates that the detector is misaligned in its z-coordinate or that its pitch is not described well. Due to the fact that the

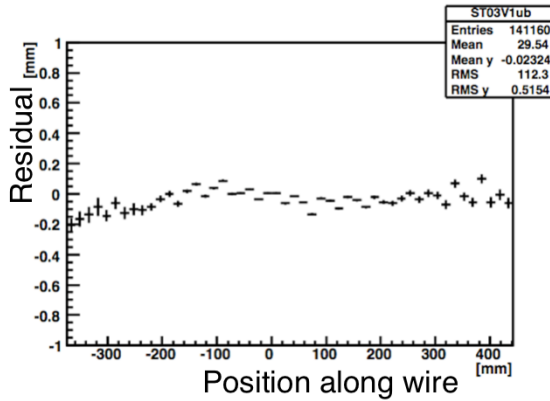


Figure 5.3: The residual as a function of the detector v-coordinate for a straw detector

alignment data is performed with straight tracks, the alignment in the z-coordinate has never been able to converge. For this reason the pitch of the sensors on the detector is allowed to change to account for this effective shift in z-position. The sensor pitch however, is never expected to be larger than the true detector pitch distance. If the detector pitch is determined to be too large after the alignment, this indicates a problem.

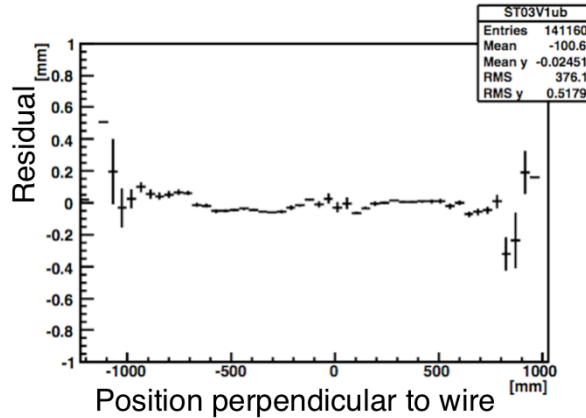


Figure 5.4: The residual as a function of the detector u-coordinate for a straw detector

- iv) The reduced  $\chi^2$ , Fig. 5.5, distribution of the reconstructed tracks. With better alignment the track reduced  $\chi^2$  distribution will approach a theoretical distribution of a reduced  $\chi^2$  distribution.
- v) The global number of tracks reconstructed. Better alignment implies that more detectors can be associated with a track and therefore more tracks will be reconstructed.

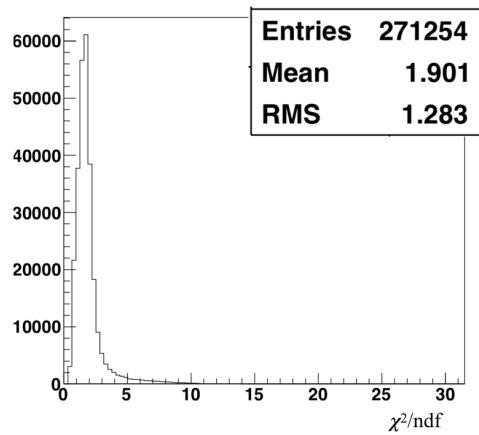


Figure 5.5: The reduced  $\chi^2$  from alignment data tracks

# Chapter 6

## Analysis of High Mass Drell-Yan Transverse Spin Phenomena

This chapter goes over the analysis techniques and results from the 2015 transversely polarized Drell-Yan data taking. The chapter begins by describing the data collection setup and the event selection criteria followed by the analysis techniques used to determine asymmetry amplitudes. The analysis techniques described are: the standard transverse spin-dependent asymmetry (TSA) analysis, Sec 6.2, the double ratio analysis, Sec 6.3, the  $q_T$  weighted asymmetry analysis, Sec 6.4, and finally the left-right asymmetry analysis, Sec 6.5. All of these analyses are related in that they measure TMD effects from the Drell-Yan process. For this reason the event selection and kinematical asymmetry binning described in the opening sections will be the same for all analyses in this chapter unless stated otherwise.

### 6.1 Data Sample

#### 6.1.1 Data Collection

The data sample is from the 2015 COMPASS Drell-Yan measurement. In this measurement a 190 GeV/c  $\pi^-$  beam impinged on a transversely polarized NH<sub>3</sub> target and two oppositely charged muons were detected in the spectrometer. Fig. 6.1 gives a visual of the basic setup and chapter 3 goes over the spectrometer setup and beam in more details. The COMPASS spectrometer began taking commissioning data in April of 2015. The data collected for this analysis, after the commissioning phase, is from July 8 through November 12 of 2015. After November 12, the SPS stopped providing beam to COMPASS. The data is split into 9 periods lasting approximated 2 weeks each and labeled W07-W15. During each data period the spectrometer conditions were frozen so no detector changes could affect the spectrometer acceptance. Sec 3.2 describes the polarized target in more details. In summaray, the NH<sub>3</sub> target was split into two oppositely polarized cells separated by 20 cm with one cell polarized vertically up and one cell polarized vertically down in the lab frame. Each data period is split into two sub-periods to reduce systematic effects of acceptance and luminosity dependencies. The polarization of both cells was flipped between sub-periods. A summary of the analysis data taking from each period is shown in Table 6.1.

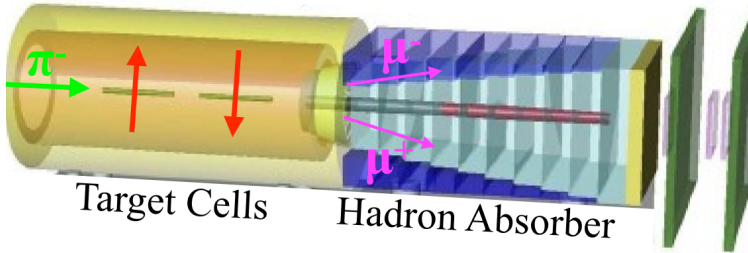


Figure 6.1: Basic pictorial setup of the target region in 2015 COMPASS Drell-Yan data collection.

Period	Sub-period	Polarization	First-Last run	Begin date	End date
W07	one	↓↑	259363 - 259677	July 9	July 15
	two	↑↓	259744 - 260016	July 16	July 22
W08	one	↑↓	260074 - 260264	July 23	July 29
	two	↓↑	260317 - 260565	July 29	August 5
W09	one	↓↑	260627 - 260852	August 5	August 12
	two	↑↓	260895 - 261496	August 12	August 26
W10	one	↑↓	261515 - 261761	August 26	September 1
	two	↓↑	261970 - 262221	September 4	September 9
W11	one	↓↑	262370 - 262772	September 11	September 22
	two	↑↓	262831 - 263090	September 23	September 30
W12	one	↑↓	263143 - 263347	September 30	October 7
	two	↓↑	263386 - 263603	October 8	October 14
W13	one	↓↑	263655 - 263853	October 15	October 21
	two	↑↓	263926 - 264134	October 22	October 28
W14	one	↑↓	264170 - 264330	October 28	November 2
	two	↓↑	264429 - 264562	November 4	November 8
W15	one	↓↑	264619 - 264672	November 9	November 11
	two	↑↓	264736 - 264857	November 12	November 16

Table 6.1: COMPASS 2015 data taking periods

### 6.1.2 Stability Tests

To ensure the data analyzed were recorded during stable beam and spectrometer conditions, stability of the analysis data was performed on a spill-by-spill and run-by-run basis. The data was recorded in runs with a maximum of 200 spills per run. One spill can have several thousand events.

#### Bad Spill Analysis

To determine if a given spill is deemed unstable several macro variables were averaged over per spill and compared to neighboring spill averages. These macro variables were chosen specifically to be sensitive to the general stability conditions of the data collection and are listed in the following itemized list. The analysis criteria for an bad spill events was two oppositely charged muons. A muon is defined as having crossed 15 radiation lengths of material.

- number of beam particles divided by the number of events
- number of beam particles divided by the number of primary vertices
- number of hits per beam track divided by the number of beam particles
- number of primary vertices divided by the number of events
- number of outgoing tracks divided by the number of events
- number of outgoing particles from a primary vertex divided by the number of primary vertices
- number of outgoing particle from primary vertex divided by the number of events
- number of outgoing particles from primary vertex divided by the number of events
- number of hits from outgoing particles divided by the number outgoing particles
- number of  $\mu^+$  tracks divided by the number of events
- number of  $\mu^+$  tracks from primary vertex divided by the number of events
- number of  $\mu^-$  tracks divided by the number of events
- number of  $\mu^-$  tracks from primary vertex divided by the number of events
- $\sum \chi^2$  of outgoing particles divided by the number of outgoing particles
- $\sum \chi^2$  of all vertices divided by the number of all vertices in an event
- Trigger rates (LASxLAS, OTxLAS, LASxMT)

If the data collected was stable during a spill the average values from the macro variables in the above itemized list are expected to be constant from one spill to the next. To determine if a spill was recorded in unstable conditions the spill of interest is compared with its neighboring 2500 spills occurring before and after in time. If the spill of interest is over a specified sigma deviation from any of the neighboring spills too many times, the spill is marked as a bad spill. If a spill fails this bad spill criteria for any of the macro variables in the above itemized list, the spill is deemed bad and not included in the analysis. The criteria for the sigma distance and number of times a spill crosses this distance to be deemed a bad are different for each data taking period. In addition to checking the nearest neighbor spills, an entire run is marked bad if the run has less than 10 spills or greater than 70% bad spills. Table 6.2 describes the bad spill impact on each period.

## Bad Run Analysis

The stability of the spectrometer is also verified by a run-by-run check in parallel to the spill-by-spill checks. The run-by-run analysis compares kinematic distributions and the average of these distributions per run to the kinematic distributions and averages from the other runs in a given period. The distributions tested are:  $x_N$ ,  $x_\pi$ ,  $x_F$ ,  $q_T$ ,  $M_{\mu\mu}$ ,  $P_{\mu^+}$ ,  $P_{\mu^-}$ ,  $P_\gamma$ ,  $P_{\pi^-}$ , and vertex x, y and z positions. The quantities in the run-by-run analysis are expected to influence the asymmetries measured, however their distributions and averages are not expected to have spin-influenced effects from the limited statistics in just a single run.

The distributions are compared with an unbinned-Kolmogorov test and the averages over a distribution are compared based on their deviations from each other. The unbinned-Kolmogorov test is made between all the runs in a given period. A run is marked bad if it is incompatible with most of the runs in a period. Additionally, the mean for each distribution in a run is compared with the average from a given period. When an average kinematical variables from a run is more than five standard deviations from the average within a period, the run is rejected. The results of the bad spill rejection after having already applied the bad spill rejection are shown in Table 6.2.

Period	Bad Spill Rejection	Bad Spill and Bad Run Rejection
W07	11.79%	17.94%
W08	18.00%	21.19%
W09	14.76%	17.11%
W10	15.88%	17.80%
W11	22.49%	26.14%
W12	12.71%	13.79%
W13	22.32%	22.73%
W14	8.91%	10.70%
W15	3.94%	3.94%

Table 6.2: Stability analysis rejection percentages

### 6.1.3 Event Selection

The cuts in the event selection were chosen to ensure the event consisted of two oppositely charged muons resulting from a pion collision in the transversely polarized target. The event selection was initially filtered from miniDSTs to  $\mu$ DSTs where only events with at least two muons detected were kept in the  $\mu$ DSTs. The cuts used in this analysis are described in the following enumerated list, where the event selection is performed on the  $\mu$ DSTs and the events used are from the slot1 reconstruction. A summary of the number of events remaining after the last cuts is shown in Table 6.3.

1. Two oppositely charged particles from a common best primary vertex having an invariant mass between

$4.3 \text{ GeV}/c^2$  and  $8.5 \text{ GeV}/c^2$ . A primary vertex is defined as any vertex with an associated beam particle. In case of multiple common primary vertices the best primary vertex is determined by CORAL tagging the vertex as best primary (PHAST method `PaVertex::IsBestPrimary()`). In the case that CORAL did not tag any of the common vertices as the best primary the vertex with the smallest spatial  $\chi^2$  value is used as the best primary vertex. The mass range of  $4.3 \text{ GeV}/c^2$  through  $8.5 \text{ GeV}/c^2$  is deemed the high mass range. Fig. 6.2 shows the mass invariant mass distribution and the background components. The mass range between  $4.3$  and  $8.5 \text{ GeV}/c^2$  corresponds to over 96 % Drell-Yan events.

2. A dimuon trigger fired. A dimuon trigger firing means there are at least two particles in coincidence in this event. The dimuon triggers used were a coincidence between two particles in the large angle spectrometer, LAS-LAS trigger, or a particle in the large angle spectrometer and a particle in the Outer hodoscope, LAS-Outer trigger. The triggering process is further described in Sec 3.5. The LAS-Middle trigger was used as a veto on beam decay muons. A beam decay muon results from the decay of a beam pion, kaon or anti-proton into a muon depicted as  $\pi^- \rightarrow \mu^- + \bar{\nu}_{\mu^-}$ ,  $K^- \rightarrow \mu^- + \bar{\nu}_{\mu^-}$ , or  $\bar{p} \rightarrow \mu^- + \bar{\nu}_{\mu^-}$  respectively. A beam decay muon can then be in coincidence with a positive muon from another decay or strong reaction in the target resulting in an unwanted background process. The LAS-Middle trigger was used as a veto because this trigger was found to have many events resulting from a beam pion decaying to a muon.
3. Both particles are muons. A muon was defined as having crossed 30 radiation lengths of material between the particles first and last measured points. This criteria has been previously been determined to be effective at distinguishing between muons and hadrons. In the data production no detectors were used from upstream of the hadron absorber so the absorber is not included in the determination of material crossed.
4. The first measured point for both particles occurs before 300 cm and the last measured point occurs after 1500 cm. This cut ensures both particles have positions upstream of the first spectrometer magnet and downstream of the first muon filter.
5. The timing of both muons is defined. This checks that the time relative to the trigger time is determined for both muons so further timing cuts can be performed.
6. Both muons are in time within 5 nanoseconds. This track time for each muon is defined relative to the trigger time as in the previous cut. This cut rejects uncorrelated muons.
7. The muon track's spacial reduced  $\chi^2$  are individually less than 10. This cut ensures track quality.

8. A validation that each muon crossed the trigger it was associated as having triggered. This trigger validation cut was performed by extrapolating (PHAST Method PaTrack::Extrapolate()) each muon track back to the two hodoscopes it fired and determining if the muon crossed the geometric acceptance of both of these hodoscopes.
9. The event does not occur in the bad spill or run list. Many tests were performed to test the basic stability of the spectrometer and beam as described in Sec 6.1.2. The spills placed on the bad spill list were deemed to occur during unstable data taking conditions.
10. The Drell-Yan kinematics are physical. That is  $0 < x_\pi x_N < 1$  and  $-1 < x_F < 1$ .
11. The transverse momentum of the virtual photon,  $q_T$ , is between 0.4 and 5.0 GeV/c. The lower limit ensures the azimuthal angular resolution is sufficient and the upper cut further ensures the kinematic distributions are physically possible and not badly reconstructed events.
12. The vertex originated within the z-positions of the transversely polarized target cells defined by the target group.  $-294.5 \text{ cm} < Z_{\text{vertex}} < -239.3 \text{ cm}$  for the upstream target and  $-219.5 \text{ cm} < Z_{\text{vertex}} < -164.3 \text{ cm}$  for the downstream target.
13. The vertex is within the radius of the polarized target measured to be 1.9 cm.

Cuts	W07	W08	W09	W10	W11	W12	W13	W14	W15	WAll	Remaining
High Mass $\mu^- \mu^+$ with a common best primary vertex	19410	19184	19654	20707	31371	23563	20561	13154	7697	175301	100.00 %
Good Spills	15947	14899	16217	16895	23041	20184	16026	11796	7422	142427	81.70 %
$0 < x_\pi x_N < 1, -1 < x_F < 1$	15932	14886	16200	16885	23022	20171	16013	11794	7414	142317	81.70 %
$0.4 < q_T < 5(\text{GeV}/c)$	14342	13385	14609	15239	20667	18101	14365	10588	6636	127932	60.75 %
Z Vertex within NH <sub>3</sub>	4256	4024	4330	4552	6369	5503	4411	3130	2028	38603	15.05 %
Vertex Radius < 1.9cm	4175	3950	4257	4474	6252	5414	4334	3078	1987	37921	12.21 %

Table 6.3: Numbers of selected di-muon events in this analysis of 2015 COMPASS data

#### 6.1.4 Binning

The asymmetries are measured in bins of  $x_N$ ,  $x_\pi$ ,  $x_F$ ,  $q_T$ , and  $M_{\mu\mu}$ .  $x_N$  and  $x_\pi$  are the momentum fractions of the target nucleon and beam pion respectively,  $x_F = x_\pi - x_N$ ,  $q_T$  is the transverse momentum of the virtual photon and  $M_{\mu\mu}$  is the invariant mass of the di-muon. The binning was determined by requiring equal statistical population in each kinematic bin. In addition, the asymmetries are determined in an integrated bin using all the analysis data. The binning limits of the analysis are summarized in Table 6.4.

Kinematics	Lowest limit	Upper limit bin 1	Upper limit bin 2	Upper limit bin 3
$x_N$	0.0	0.13	0.19	1.0
$x_\pi$	0.0	0.40	0.56	1.0
$x_F$	-1.0	0.22	0.41	1.0
$q_T$ (GeV/c)	0.4	0.86	1.36	5.0
$M_{\mu\mu}$ (GeV/c <sup>2</sup> )	4.3	4.73	5.50	8.5

Table 6.4: Analysis binning limits

### 6.1.5 Analysis Notation

Table 6.5 summarizes the general notations used in the asymmetry analysis definitions and derivations used throughout this chapter.

Table 6.5: Notations used for defining the asymmetry analysis

Notation	Description
1(2)	target cell number. 1=upstream, 2=downstream
$\uparrow (\downarrow)$	target cell vertical polarization direction, up(down)
$ S_T $	fraction of polarized target nucleons
$l(r)$	virtual photon detected left(right) of spin
$J(S)$	spectrometer Jura(Saleve) side meaning west(east) side

## 6.2 Transverse Spin-Dependent Asymmetries

This section describes the standard TSA analysis, in Drell-Yan, for which the results of 2015 data are published in reference [90]. The main motivation for this analysis was to conclude on the sign flip of the Sivers function flip between the Drell-Yan and SIDIS processes using data from the same experimental setup for both processes. The results shown are those determined by the COMPASS Drell-Yan analysis group.

The kinematical distributions shown for this analysis are the same as for the remaining analyses in this chapter. This results from the fact that all the analyses in this chapter use the same event selection and cuts. The only exception to this is for the  $q_T$ -weighted analysis, Sec 6.4, which cannot cut on  $q_T$  and therefore has a different  $q_T$  distribution as is explained in Sec 6.4.1.

As was noted in the event selection 6.1.3, the data considered are in the invariant mass range [4.3–8.5 GeV/c<sup>2</sup>]. Fig. 6.2 shows the invariant mass range from the 2015 COMPASS data. All cuts except a cut on invariant mass are included in Fig. 6.2 and as well a fit to show the background processes is included.

The fit is determined from Monte-Carlo data, described in Table 6.7, and combinatorial background analysis. The Monte-Carlo data simulated all hard processes with a decay to two oppositely charged muons and can be reconstructed in the COMPASS spectrometer. Combinatorial background analysis estimates the

background as  $N_{combinatorial} = 2\sqrt{N_{\mu^+\mu^+}N_{\mu^-\mu^-}}$ . As can be seen from the Monte-Carlo curves in Fig. 6.2, there are two distinguishable background peaks. The lower mass peak at about  $3 \text{ GeV}/c^2$  corresponds to  $J/\Psi$  production and the higher mass peak at around  $3.6 \text{ GeV}/c^2$  corresponds to  $\Psi'$  production. All the analyses in this chapter use the mass range between  $4.3$  and  $8.5 \text{ GeV}/c^2$  and as Fig. 6.2 shows, the Drell-Yan process dominates in this mass range. The background percentage was estimated to be below  $4\%$  in this mass range.

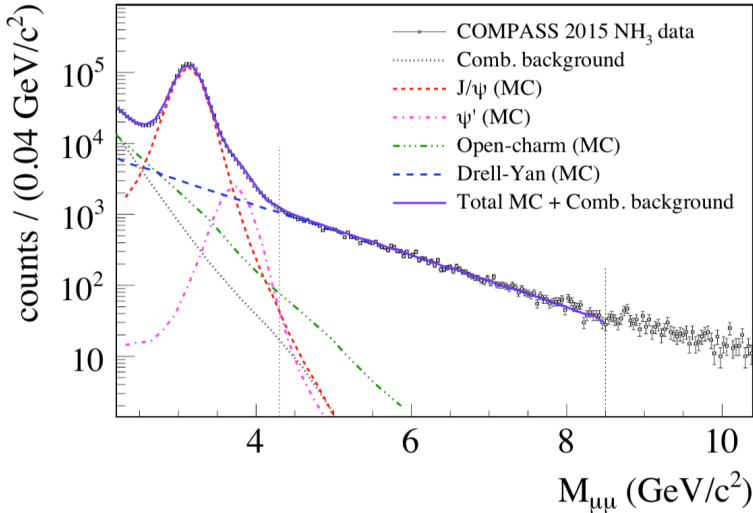
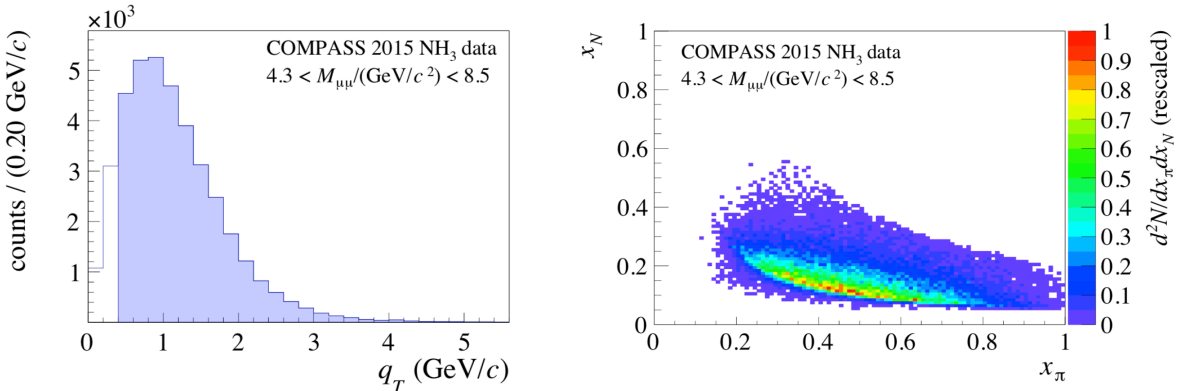


Figure 6.2: The 2015 COMPASS invariant dimuon mass distribution and a fit to this data. The data fit is from Monte-Carlo and combinatorial background analysis and is provided to show the background processes. This image is taken from [90].

Fig. 6.3a shows the transverse virtual photon momentum,  $q_T$ , distribution. With the cut on  $q_T$  between  $[0.4-5(\text{GeV}/c)]$ , the average  $q_T$  is  $1.2 \text{ GeV}/c$  while the average  $M_{\mu\mu}$  is  $5.3 \text{ GeV}/c^2$ . As stated in chapter 2, the regime where TMD functions are the theoretical model for parton distributions is when  $q_T \ll M_{\mu\mu}$ . While the average  $q_T$  is less than the average  $M_{\mu\mu}$ , it is not excluded that the results in this chapter are outside of the TMD regime. Nevertheless all the results presented in this chapter are determined assuming the TMD description is valid.

The distribution of  $x_\pi$  versus  $x_N$  is shown in Fig. 6.3b. The Bjorken-x of the proton,  $x_N$ , is almost exclusively above  $0.1$  and as well Bjorken-x for the pion,  $x_\pi$  is in its valence region. For these reasons it is safe to say that the Drell-Yan reaction studied in the following analyses is the result of the pion's anti-u-quark annihilating with the proton's u-quark.

The results from TSA analysis are determined from an extended unbinned maximum likelihood fit to the data. The virtual photon depolarization values are determined on an event by event basis unlike the other analyses in this chapter. The published integrated results of the 2015 data for the leading order and



(a) The  $q_T$  distribution where the shaded region shows the data used in the high mass analysis and the unshaded region shows the full distribution without a  $q_T$  cut. This image is taken from [90].

(b) The 2-dimensional distribution of  $x_\pi$  vs.  $x_N$ . Both  $x_\pi$  and  $x_N$  are safely in their respective valence regions. This image is taken from [90].

Figure 6.3: High mass Drell-Yan kinematic variables:  $q_T$  and  $x_N$  vs.  $x_\pi$ .

sub-leading order TSAs are shown in Fig. 6.4. The leading order TSAs are non-zero with approximate significance of: 1 sigma for the Sivers TSA,  $A_T^{\sin(\phi_S)}$ , 1.2 sigma for the pretzelosity TSA,  $A_T^{\sin(2\phi_{CS}+\phi_S)}$  and 2 sigma for the transversity TSA,  $A_T^{\sin(2\phi_{CS}-\phi_S)}$ .

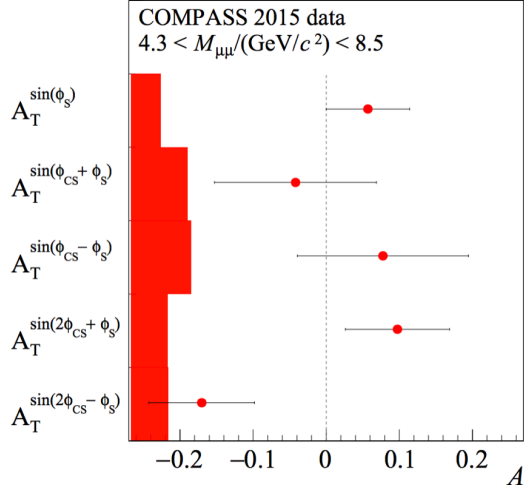


Figure 6.4: The integrated TSAs with statistical error bars and systematic uncertainty bands.  $A_T^{\sin(\phi_S)}$ ,  $A_T^{\sin(2\phi_{CS}+\phi_S)}$ , and  $A_T^{\sin(2\phi_{CS}-\phi_S)}$  are leading order TSAs and  $A_T^{\sin(\phi_{CS}+\phi_S)}$  and  $A_T^{\sin(\phi_{CS}-\phi_S)}$  are sub-leading order TSAs.

The comparison of the Sivers TSA,  $A_T^{\sin(\phi_S)}$ , with the expected sign flip is shown in Fig. 6.5. The positive solid theory curves show the expected Sivers TSA assuming the Sivers function flips sign between Drell-Yan and SIDIS. The main difference in these three theory curves is the  $Q^2$  evolution which is also the main

uncertainty in each prediction. As can be seen the Sivers TSA is compatible with the expected sign change. However, the error bars on the Sivers asymmetry amplitude are too large to conclusively distinguish between the three theory curves or even to definitively conclude on the sign change between Drell-Yan and SIDIS. That being said, the amplitude  $A_T^{\sin(\phi_S)}$  is 2 sigma away from being incompatible with a sign flip.

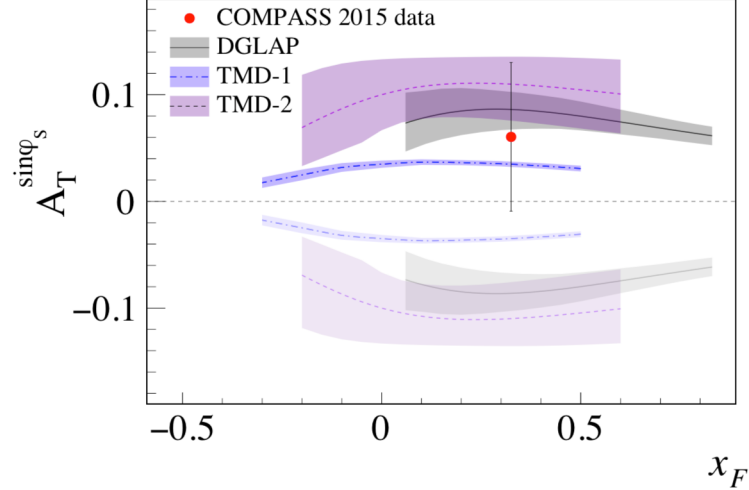


Figure 6.5: The Sivers TSA along with theory curves for the expected sign change (solid curves) and without the sign change (opaque curves). Theory curves and uncertainties are calculated using  $Q^2$  evolution from DGLAP [91], TMD-1 [92], TMD-2 [93]. This image is taken from [90].

### 6.3 Double Ratio Analysis

The double ratio method is used to determine spin-dependent asymmetry amplitudes. This means the asymmetry amplitudes  $A_T^{\sin \phi_S}$ ,  $A_T^{\sin(2\phi + \phi_S)}$  and  $A_T^{\sin(2\phi - \phi_S)}$  can be determined from the 2015 transversely polarized Drell-Yan data. The benefit of this method is that the spectrometer acceptance does not affect the determination of the asymmetry amplitudes. The author of this thesis performed the analysis in this section and found results consistent with those determined from TSA analysis.

#### 6.3.1 Asymmetry Extraction

The double ratio is defined as

$$R_D(\Phi) = \frac{N_1^\uparrow(\Phi)N_2^\uparrow(\Phi)}{N_1^\downarrow(\Phi)N_2^\uparrow(\Phi)}, \quad (6.1)$$

where  $N$  represents the counts, 1(2) is the upstream(downstream) target cell and  $\uparrow(\downarrow)$  denotes the transverse polarization direction. The number of counts,  $N(\Phi)$ , is defined as

$$N(\Phi) = L * \sigma(\Phi) * a(\Phi), \quad (6.2)$$

where  $L$  is the luminosity,  $\sigma$  is the cross-section and  $a$  is the spectrometer acceptance. In Eq. 6.2 the acceptance is a function of detector efficiencies and the spectrometer acceptance. When assuming the spin-dependent Drell-Yan cross-section, Eq. 2.52, the number of counts,  $N(\Phi)$ , can be written

$$N(\Phi) = a(\Phi)L\sigma_U \left( 1 \pm D_{[\theta]} |S_T| A_T^w \sin(\Phi) \right). \quad (6.3)$$

where  $+(-)$  is for target polarized up(down),  $D_{[\theta]}$  is the virtual photon depolarization factor and  $|S_T|$  is the target polarization percentage. The depolarization factor,  $D_{[\theta]}$  is defined in Eq. 2.50. It can be thought of as the probability for the virtual photon to decay and produce such an asymmetry amplitude to that for a transversely polarized photon decay. The target polarization percentage,  $|S_T|$  is defined as  $fP$ , where  $f$  is the dilution factor, Eq. 3.3, and  $P$  is the target polarization percentage. Therefore the double ratio can be written

$$\begin{aligned} R_D(\Phi) &= \frac{a_1^\uparrow(\Phi)L_1^\uparrow\sigma_U \left( 1 + D_{[\theta]1}^\uparrow |S_{T1}^\uparrow| A_T^w \sin(\Phi) \right) a_2^\uparrow(\Phi)L_2^\uparrow\sigma_U \left( 1 + D_{[\theta]2}^\uparrow |S_{T2}^\uparrow| A_T^w \sin(\Phi) \right)}{a_1^\downarrow(\Phi)L_1^\downarrow\sigma_U \left( 1 - D_{[\theta]1}^\downarrow |S_{T1}^\downarrow| A_T^w \sin(\Phi) \right) a_2^\downarrow(\Phi)L_2^\downarrow\sigma_U \left( 1 - D_{[\theta]2}^\downarrow |S_{T2}^\downarrow| A_T^w \sin(\Phi) \right)} \\ &= \left( \frac{a_1^\uparrow(\Phi)a_2^\uparrow(\Phi)}{a_1^\downarrow(\Phi)a_2^\downarrow(\Phi)} \right) \left( \frac{L_1^\uparrow L_2^\uparrow}{L_1^\downarrow L_2^\downarrow} \right) \frac{\left( 1 + D_{[\theta]1}^\uparrow |S_{T1}^\uparrow| A_T^w \sin(\Phi) \right) \left( 1 + D_{[\theta]2}^\uparrow |S_{T2}^\uparrow| A_T^w \sin(\Phi) \right)}{\left( 1 - D_{[\theta]1}^\downarrow |S_{T1}^\downarrow| A_T^w \sin(\Phi) \right) \left( 1 - D_{[\theta]2}^\downarrow |S_{T2}^\downarrow| A_T^w \sin(\Phi) \right)}. \end{aligned} \quad (6.4)$$

As is described in Sec 6.1.1, the data is collected in two week periods where the conditions of the spectrometer are frozen for each data taking period. For this reason the following reasonable acceptance assumption is made

$$\frac{a_1^\uparrow(\Phi)a_2^\uparrow(\Phi)}{a_1^\downarrow(\Phi)a_2^\downarrow(\Phi)} = C. \quad (6.5)$$

where  $C$  is a constant. In addition  $L_2^{\downarrow(\uparrow)} = rL_1^{\uparrow(\downarrow)}$  where  $r$  is a constant reduction factor and therefore the luminosity terms cancel out as

$$\frac{L_1^\uparrow L_2^\uparrow}{L_1^\downarrow L_2^\downarrow} = \frac{L_1^\uparrow r L_1^\downarrow}{L_1^\downarrow r L_1^\uparrow} = 1. \quad (6.6)$$

Finally the asymmetry amplitudes and target polarizations are assumed to be small so the double ratio can be simplified to

$$\begin{aligned}
R_D(\Phi) &= C \frac{\left(1 + D_{[\theta]1}^\uparrow |S_{T1}^\uparrow| A_T^w \sin(\Phi)\right) \left(1 + D_{[\theta]2}^\uparrow |S_{T2}^\uparrow| A_T^w \sin(\Phi)\right)}{\left(1 - D_{[\theta]1}^\downarrow |S_{T1}^\downarrow| A_T^w \sin(\Phi)\right) \left(1 - D_{[\theta]2}^\downarrow |S_{T2}^\downarrow| A_T^w \sin(\Phi)\right)} \\
&\approx C \frac{1 + \left[D_{[\theta]1}^\uparrow |S_{T1}^\uparrow| + D_{[\theta]2}^\uparrow |S_{T2}^\uparrow|\right] A_T^w \sin(\Phi)}{1 - \left[D_{[\theta]1}^\downarrow |S_{T1}^\downarrow| + D_{[\theta]2}^\downarrow |S_{T2}^\downarrow|\right] A_T^w \sin(\Phi)} \\
&\approx C \left(1 + \left[D_{[\theta]1}^\uparrow |S_{T1}^\uparrow| + D_{[\theta]2}^\uparrow |S_{T2}^\uparrow|\right] A_T^w \sin(\Phi)\right) \left(1 + \left[D_{[\theta]1}^\downarrow |S_{T1}^\downarrow| + D_{[\theta]2}^\downarrow |S_{T2}^\downarrow|\right] A_T^w \sin(\Phi)\right) \\
&\approx C \left(1 + \left[D_{[\theta]1}^\uparrow |S_{T1}^\uparrow| + D_{[\theta]2}^\uparrow |S_{T2}^\uparrow| + D_{[\theta]1}^\downarrow |S_{T1}^\downarrow| + D_{[\theta]2}^\downarrow |S_{T2}^\downarrow|\right] A_T^w \sin(\Phi)\right).
\end{aligned} \tag{6.7}$$

Then making the assumption that the polarizations,  $S_T$ , and the virtual photon depolarization factors,  $D_\Phi$  are approximately constant throughout a data period, the asymmetry amplitude of interest can be determined by fitting the double ratio with the function

$$f(\Phi) = [p0](1 + 4[p1]\sin(\Phi)), \tag{6.8}$$

where  $[p0]$  and  $[p1]$  are fit parameters and  $[p1]$  represents the asymmetry amplitude of interest. The  $[p1]$  parameter is later corrected for average polarization and virtual photon depolarization factors.

The double ratio,  $R_D$ , is determined as a function of  $\Phi$ , where the angle  $\Phi$  depends on which asymmetry amplitude is being determined. The assumption made in the measured counts formula, Eq. 6.3, is that all angles except the spin-dependent  $\Phi$  angle are integrated over. When this is the true, all the Drell-Yan cross-section fourier components integrate to zero except the constant term. The following table, Table 6.6, list which  $\Phi$  angle is used to determine which spin-dependent asymmetry amplitude.

Table 6.6: Measured counts as a function of each  $\Phi$  angle

Asymmetry Amplitude	Corresponding TMD Function	$\Phi$ Angle	$\Phi$ Range (radians)
$A_T^{\sin(\phi_S)}$	Sivers	$\phi_S$	$[-\pi, \pi]$
$A_T^{\sin(2\phi - \phi_S)}$	Transversity	$2\phi - \phi_S$	$[-3\pi, 3\pi]$
$A_T^{\sin(2\phi + \phi_S)}$	Pretzelosity	$2\phi + \phi_S$	$[-3\pi, 3\pi]$

The variance of the double ratio, assuming Poisson counting statistics, is

$$\sigma_{R_D}^2 = R_D^2(\Phi) \left( \frac{1}{N_1^\uparrow(\Phi)} + \frac{1}{N_2^\uparrow(\Phi)} + \frac{1}{N_1^\downarrow(\Phi)} + \frac{1}{N_2^\downarrow(\Phi)} \right). \tag{6.9}$$

### 6.3.2 Results

The results of the asymmetry amplitudes are determined in each of the nine periods and then combined as a weighted average. The asymmetries are calculated this way to minimize the effects of acceptance changes between periods as the spectrometer was kept stable within each period but had the options for detector changes and repairs between periods. As well this weighted average method allows for future measurements to be combined as a weighted average with the final overall results without the need to know individual period results. This resulting asymmetry amplitudes are determined from a weighted average as

$$A = \frac{\sum_{\text{period}} A_{\text{period}} \sigma_{\text{period}}^{-2}}{\sum_{\text{period}} \sigma_{\text{period}}^{-2}}, \quad \delta A = \sqrt{\sum_{\text{period}} \frac{1}{\sigma_{\text{period}}^{-2}}}. \quad (6.10)$$

For each period and each kinematical bin, the asymmetry is determined by fitting the double ratio and with Eq. 6.8. The results of the fit actually determines the quantity

$$A_T^w \langle D_{[\theta]} \rangle \langle |S_T| \rangle. \quad (6.11)$$

The asymmetry amplitude is ultimately determined by dividing the fit results by the average polarization and average virtual photon depolarization values per period.

To determine the asymmetry amplitude, the double ratio is binned in eight bins in  $\Phi$ . Eight bins are chosen due to the low statistics from Drell-Yan data. Fig. 6.6 shows an example of the binned double ratio and fit results.

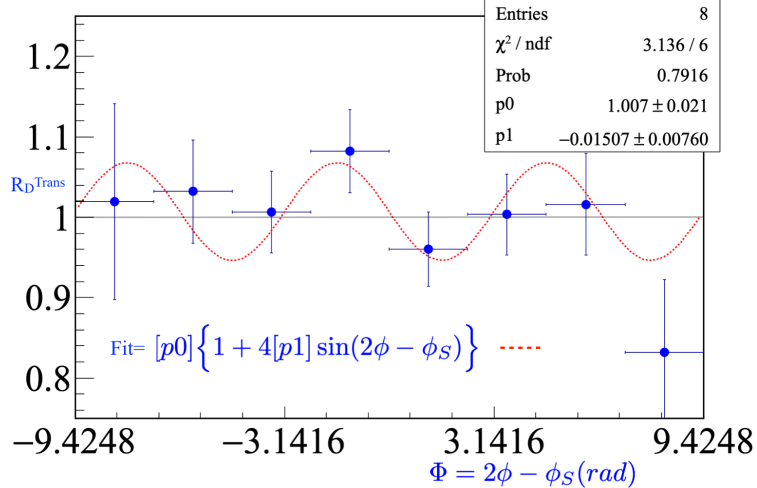


Figure 6.6: An example double ratio and corresponding fit (red) to determine the amplitude  $A_T^{\sin(2\phi - \phi_S)}$

The results for all the spin-dependent asymmetry amplitudes are shown in Fig. 6.7. As can be seen, the significance of the integrated asymmetry amplitudes is: over 1 sigma above zero for the Sivers,  $A_T^{\sin\phi_S}$ , over 3 sigma above zero for prezelosity,  $A_T^{\sin(2\phi+\phi_S)}$ , and 3 sigma below zero for transversity,  $A_T^{\sin(2\phi-\phi_S)}$ .

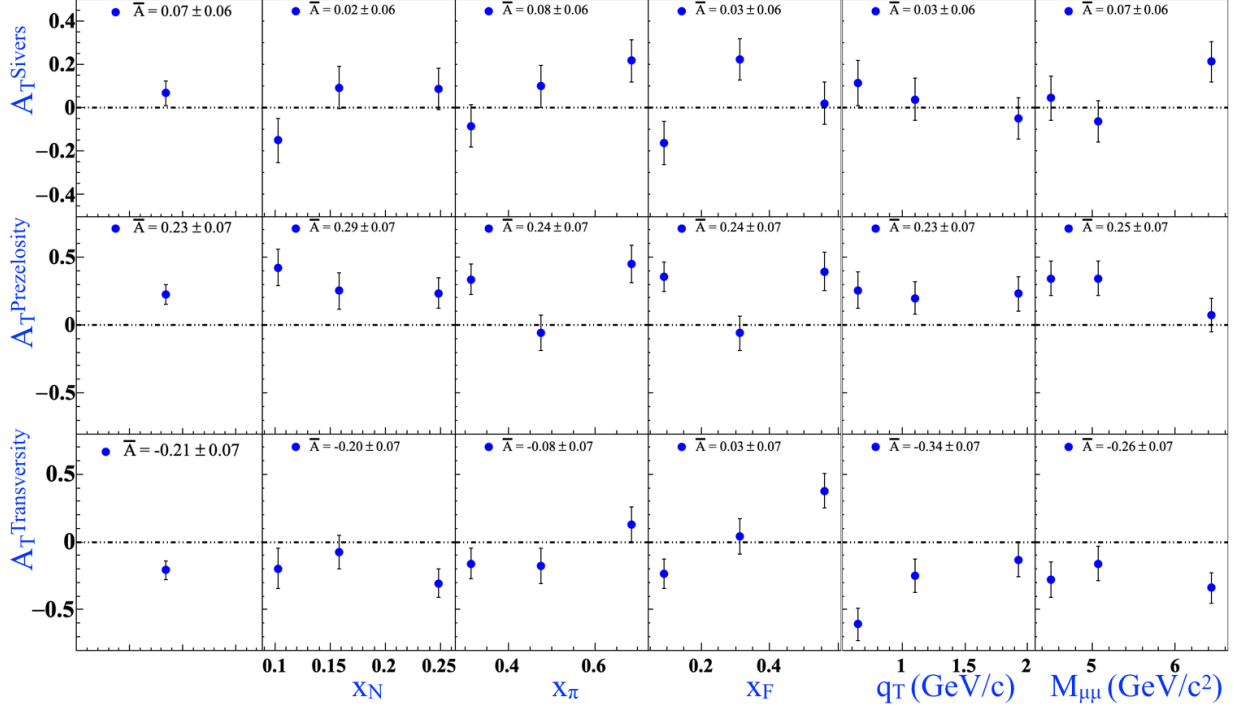


Figure 6.7: The results and statistical error bars for the transverse spin-dependent asymmetry amplitudes  $A_T^{\sin\phi_S}$  (top),  $A_T^{\sin(2\phi+\phi_S)}$  (middle) and  $A_T^{\sin(2\phi-\phi_S)}$  (bottom) determined from the double ratio method.

## 6.4 $q_T$ -Weighted Asymmetries

The  $q_T$  weighted asymmetries analysis is used to determine three asymmetry amplitudes related to TMD functions. This analysis determined the three amplitudes:  $A_T^{\sin(\phi_S)q_T/M_N}$ ,  $A_T^{\sin(2\phi+\phi_S)q_T^3/(2M_\pi M_N^2)}$  and  $A_T^{\sin(2\phi-\phi_S)q_T/M_\pi}$  which are related to the Sivers, prezelosity and transversity TMD PDFs respectively.

The theoretical introduction and motivation for measuring  $q_T$ -weighted asymmetries is provided in Sec 2.5.3. The author of this thesis was a cross checker for the  $q_T$ -weighted asymmetry results which is a required step for any results to become public. For the full details of the  $q_T$ -weighted analysis see reference [94].

### 6.4.1 Event Selection

The results for this analysis were released prior to the slot1 reconstruction production and therefore this analysis uses the t3 reconstruction. For  $q_T$ -weighted asymmetries the results depend on the full range of the  $q_T$  distribution. In the other analyses in this chapter however, a cut was placed on high and low  $q_T$  values to ensure better azimuthal angular resolution and quality reconstructed events. This cut cannot be applied for  $q_T$ -weighted analysis because it will affect the weighting used to determine the asymmetry amplitudes. On the other hand the combinatorial background and badly reconstructed events from the high  $q_T$  phase space should be cut. The next section goes into the details and the remedy for a  $q_T$  related cut. All of the other cuts from Sec 6.1.3 are the same except for this  $q_T$  cut. Figure 6.9 provides the final cut order and the remaining statistics after each cut for this  $q_T$ -weighted analysis.

#### High $q_T$

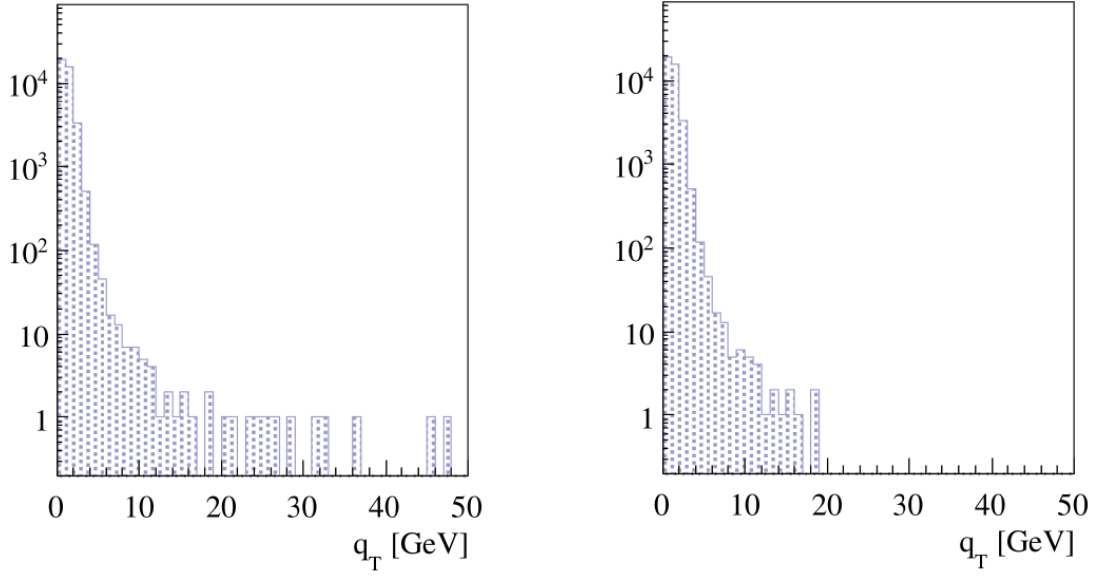
The  $q_T$  distribution without any  $q_T$  cuts is shown in Fig. 6.8a. As can be seen the  $q_T$  distribution reaches values much higher than the maximum 5 GeV/c cut from the other analyses in this chapter. The most fundamental problem with this  $q_T$  distribution is that some of the events violate conservation of momentum. A first remedy to the high  $q_T$  values then is to add a cut which demands momentum conservation. This is achieved by demanding that the momentum sum of the detected muons is physically possible,  $\ell^+ + \ell^- < 190$  GeV/c. Note that this cut does not take into account the momentum spread of the beam due to the fact that the beam momentum spread is expected to be small. Fig. 6.8b shows how this cut affects the  $q_T$  distribution. As can be seen,  $q_T$  still reaches values much higher than the 5 GeV/c cut from the other TMD analyses. The remaining high  $q_T$  events still have the potential to be poorly reconstructed events or combinatorial background and for this reason an additional cut was put on the individual muons transverse momentum such that  $\ell_T^\pm < 7$  GeV/c.

### 6.4.2 Binning

As with the other analyses in this chapter, the asymmetry is determined in bins of the Drell-Yan physical kinematic variables:  $x_N$ ,  $x_\pi$ ,  $x_F$ ,  $M_{\mu\mu}$  and an overall integrated value. No  $q_T$  binning is used however, because a full integration of the  $q_T$  variable needs to be taken into account to form the weighted asymmetry.

### 6.4.3 Asymmetry Method

The weighted asymmetry amplitudes  $A_T^{\sin(\phi_S)q_T/M_N}$ ,  $A_T^{\sin(2\phi+\phi_S)q_T^3/(2M_\pi M_N^2)}$  and  $A_T^{\sin(2\phi-\phi_S)q_T/M_\pi}$  are determined using a modified double ratio. As with the double ratio method from Sec 6.3, the modified double



(a)  $q_T$  distribution without cuts on  $q_T$ . All other cuts expect the  $q_T$  cut from Sec 6.1.3 are applied. This image is from [94]

(b)  $q_T$  distribution after the momentum conservation cut is added,  $\ell^+ + \ell^- < 190$  GeV/c. All other cuts expect the  $q_T$  cut from Sec 6.1.3 are applied. This image is from [94]

Figure 6.8:  $q_T$  distributions without and with momentum conservation cuts.

Cuts	Events	% Remaining
$\mu^+\mu^-$ from best primary vertex, $4.3 < M_{\mu\mu} < 8.5$ GeV/c <sup>2</sup>	1,159,349	100.00
Triggers: (2LAS or LASxOT) and not LASxMiddle	868,291	74.89
$Z_{first} < 300$ cm, $Z_{last} > 1500$ cm	784,379	67.66
$\Delta t$ defined	776,643	66.99
$ \Delta t  < 5$ ns	337,081	32.18
$\chi^2_{track}/ndf < 10$	370,054	31.92
$\ell^+ + \ell^- < 190$ GeV/c	219,304	18.92
$\ell_T^\pm < 7$ GeV/c	219,014	18.89
Trigger Validation	168,939	14.57
Good Spills	137,812	11.89
$0 < x_\pi x_N < 1$ , $-1 < x_F < 1$	137,802	11.89
Z Vertex within NH <sub>3</sub>	42,646	3.68
Vertex Radius < 1.9cm	39,088	3.37

Figure 6.9: Event selection statistics for  $q_T$ -weighted asymmetry analysis from all periods combined

ratio does not depend on the spectrometer acceptance. The modified double ratio is defined as

$$R_{DM}^W(\Phi) = \frac{N_1^{\uparrow W} N_2^{\uparrow W} - N_1^{\downarrow W} N_2^{\downarrow W}}{\sqrt{(N_1^{\uparrow W} N_2^{\uparrow W} + N_1^{\downarrow W} N_2^{\downarrow W})(N_1^{\uparrow} N_2^{\uparrow} + N_1^{\downarrow} N_2^{\downarrow})}}, \quad (6.12)$$

where similar notation is used from the previous analyses where  $\uparrow(\downarrow)$  is the transverse polarization direction, 1(2) denotes the upstream(downstream) cell,  $N^W$  is the weighted counts,  $W$  is the weight used and  $N$  denotes the unweighted counts. The angles  $\Phi$ , in the modified double ratio, are the same used for the double ratio, Table 6.6, and give access to asymmetry amplitudes related to the same corresponding TMD functions. Under the same reasonable acceptance ratio assumption, Eq. 6.5, from the double ratio method the acceptance cancels out in the double ratio method. Using this assumption, the modified double ratio reduces to

$$R_{DM}^W(\Phi) \approx 2\tilde{D}_{\sin\Phi}\langle S_T \rangle A_T^{\sin(\Phi)W} \sin\Phi, \quad (6.13)$$

where  $\tilde{D}_{\sin\Phi}$  is an integrated virtual photon depolarization factor defined as

$$\tilde{D}_{\sin\phi_S} = 1, \quad \tilde{D}_{\sin(2\phi \pm \phi_S)} = \frac{\int a(\theta) \sin^2 \theta d\cos\theta}{\int a(\theta)(1 + \cos^2 \theta)d\cos\theta} = \frac{1 - \langle \cos^2 \theta \rangle}{1 + \langle \cos^2 \theta \rangle}. \quad (6.14)$$

The statistical error for the modified double ratio is

$$\sigma_{R_{DM}^W}^2 = \frac{\sum_{c,p} \sigma_{N_c^p W}^2 4(N_1^\uparrow N_2^\uparrow) N_1^\downarrow N_2^\downarrow)^2}{\sum_{c,p} \sigma_{N_c^p}^2 (N_1^\uparrow N_2^\uparrow + N_1^\downarrow N_2^\downarrow)^4} \sum_{c,p} \frac{1}{N_c^p}, \quad (6.15)$$

where  $\sigma_{N_c^p W}^2 = \sum(W_c^p)^2$  is the sum of event weights,  $c$  is cell 1 or cell 2 and  $p$  is polarization  $\uparrow$  or  $\downarrow$ .

The weighted asymmetry amplitudes are determined by forming the modified double ratio in eight bins in the appropriate  $\Phi$  angle and fitting this distribution. If an infinite number of bins were used and there was sufficient data, the modified double ratio would be the function form of Eq. 6.13. Due to the limited statistics however,  $R_{DM}^W$  must be binned in a finite number of bins. Therefore to account for the fact that ratio is determined in a finite number of  $\Phi$  bins, the average value of Eq. 6.13 over the bin width is used as the fit distribution. This means the functional fit is

$$\langle R_{DM}^W \rangle = \frac{1}{\Delta\Phi} \int_{\Phi_i - \frac{\Delta\Phi}{2}}^{\Phi_i + \frac{\Delta\Phi}{2}} R_{DM}^W(\Phi') d\Phi' = \frac{2}{\Delta\Phi} \sin\left(\frac{\Delta\Phi}{2}\right) R_{DM}^W(\Phi_i), \quad (6.16)$$

where  $\Delta\Phi = \frac{2\pi}{8}$  for eight bins in  $\Phi$ . Fig. 6.10 shows the double ratio as a function of  $\Phi = \phi_S$  for period W07 in one bin of  $x_N$ . One  $R_{DM}^W$  is determined for each of the 3 (number of bins)  $\times$  9 (number of periods)  $\times$  3 (number of asymmetry amplitudes) = 81 modified double ratios.

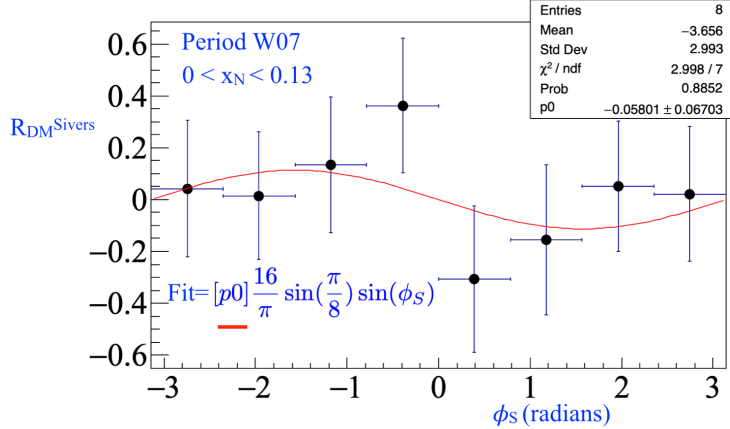


Figure 6.10: The double ratio as a function of  $\phi_S$  used to determine the Sivers asymmetry amplitude. This is for period W07 and the lowest bin in  $x_N$ . The red line shows the fit. The results of the fit are shown in the statistics box.

#### 6.4.4 Results

As explained in Sec 6.3.2, the asymmetry amplitudes are determined for each period and the final asymmetry is determined as a period weighted average as in Eq. 6.10. For the same reason as the previous analyses and explained in Sec 6.3.2, the polarization and virtual photon depolarization factors from each period are used to correct the asymmetry amplitude determined in each period. The final results are shown in Fig. 6.11 along with the results from the release values. As can be seen the results agree with those results obtained for the release which was a requirement before the results could be released to the public [95].

### 6.5 Left-Right Asymmetries

This section goes over the analysis details for measuring the left-right asymmetry from the transversely polarized Drell-Yan data. A theoretical introduction showing how the left-right asymmetry is related to the Sivers TMD PDF and related past results for this asymmetry are given in Sec 2.5.2. In short the measured asymmetry can be defined as

$$A_{lr} = \frac{1}{|S_T|} \frac{\sigma_l - \sigma_r}{\sigma_l + \sigma_r}, \quad (6.17)$$

which when assuming the leading order Drell-Yan cross-section, Eq. 2.52, is related to the Sivers asymmetry amplitude as

$$A_{lr} = \frac{2A_T^{\sin(\phi_S)}}{\pi}. \quad (6.18)$$

There are many ways to determine the left-right asymmetry. The relevant techniques for the 2015

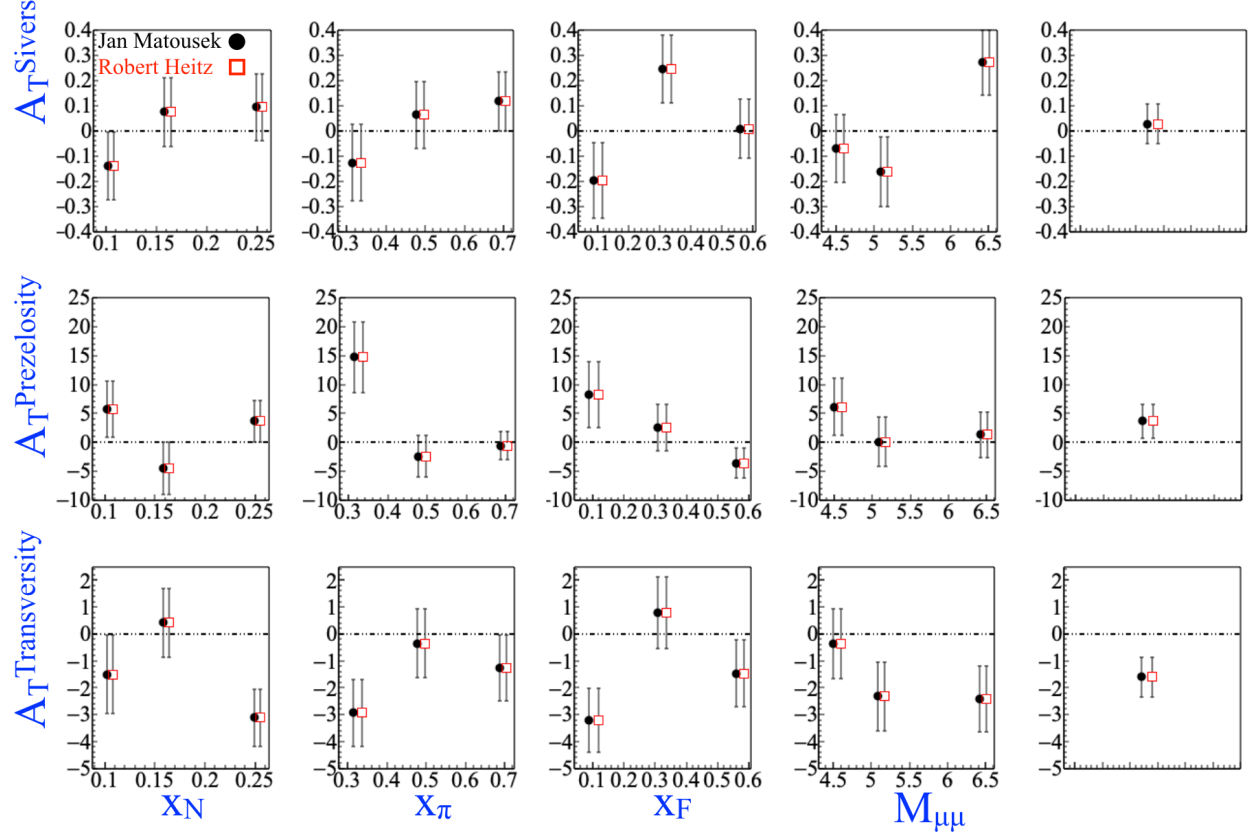


Figure 6.11: The comparison of weighted asymmetry amplitude results from the released values from Jan Matousek (black) and the cross checker Robert Heitz (red). From the top row down the asymmetry amplitudes are  $A_T^{\sin(\phi_S)q_T/M_N}$ ,  $A_T^{\sin(2\phi+\phi_S)q_T^3/(2M_\pi M_N^2)}$  and  $A_T^{\sin(2\phi-\phi_S)q_T/M_\pi}$  respectively.

COMPASS setup are described and compared to ensure confidence of the end results.

### 6.5.1 Asymmetry Extractions

#### Geometric Mean

The most basic method to determine the left-right asymmetry is

$$A_{lr,simple} = \frac{1}{|S_T|} \frac{N_l - N_r}{N_l + N_r}, \quad (6.19)$$

where  $N_l = \int_{\phi_S=0}^{\phi_S=\pi} N(\phi_S)d\phi_S$  denotes the counts measured left and  $N_r = \int_{\phi_S=\pi}^{\phi_S=2\pi} N(\phi_S)d\phi_S$  denotes the counts measured right. Eq. 6.19 can be used to determine the left-right asymmetry per target cell. An intuitive picture of left and right defined in the target frame is shown in Fig. 6.12. This simple method to determine the left-right asymmetry is intuitive and can be helpful for visualizing the forthcoming methods to determine  $A_{lr}$ . Left and right in all definitions in this section are determined relative to the target spin

direction as

$$\begin{aligned} \text{Left} : \hat{q}_T \cdot (\hat{S}_T \times \hat{P}_\pi) &> 0 \\ \text{Right} : \hat{q}_T \cdot (\hat{S}_T \times \hat{P}_\pi) &< 0, \end{aligned} \quad (6.20)$$

where  $\hat{q}_T$ ,  $\hat{S}_T$  and  $\hat{P}_\pi$  are unit vectors in the target reference frame for the virtual photon transverse momentum, the target spin and the beam pion momentum respectively.

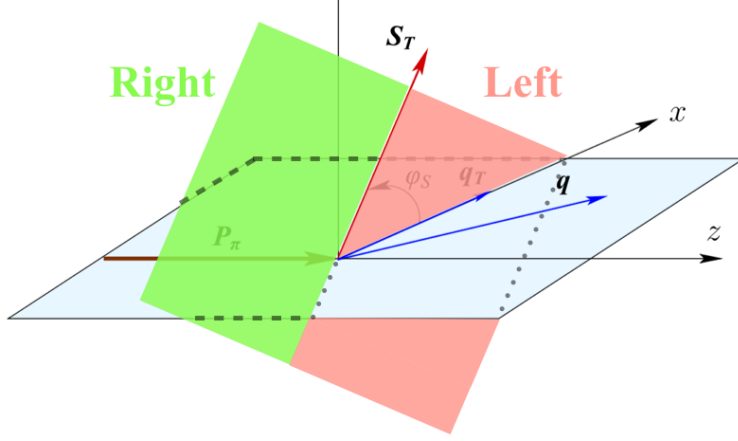


Figure 6.12: The definition of the left plane (red) and right plane (green) defined from a target spin up configuration in the target frame

The simple definition of the left-right asymmetry, Eq. 6.19, is unfortunately dependent on the spectrometer acceptance. This can be realized from the fact that the definition of the detected counts, Eq. 6.2, depends on the spectrometer acceptance  $a(\phi_S)$  which therefore means  $A_{lr,simple}$  also depends on the spectrometer acceptance. This is a problem because the spectrometer acceptance can change with time and space and therefore can be dependent on the physical kinematics which produced the event. Such dependencies can cause unphysical false asymmetries in the measurement of  $A_{lr}$  and must therefore be removed or must be included as systematic effects.

Forming the geometric mean asymmetry is a way to determine the left-right asymmetry without acceptance effects from the spectrometer. The geometric mean asymmetry is defined as

$$A_{lr,geo} = \frac{1}{|S_T|} \frac{\sqrt{N_l^\uparrow N_r^\downarrow} - \sqrt{N_r^\uparrow N_l^\downarrow}}{\sqrt{N_l^\uparrow N_l^\downarrow} + \sqrt{N_r^\uparrow N_r^\downarrow}}, \quad (6.21)$$

which also defines a left-right asymmetry per target cell. It is not difficult to simplify the geometric mean

asymmetry as

$$A_{lr,geo} = \frac{1}{|S_T|} \frac{\kappa_{geo} \sqrt{\sigma_l \sigma_l} - \sqrt{\sigma_r \sigma_r}}{\kappa_{geo} \sqrt{\sigma_l \sigma_l} + \sqrt{\sigma_r \sigma_r}} = \frac{1}{|S_T|} \frac{\kappa_{geo} \sigma_l - \sigma_r}{\kappa_{geo} \sigma_l + \sigma_r}, \quad (6.22)$$

where  $\kappa_{geo}$  is a ratio of acceptances defined for the geometric mean as

$$\kappa_{geo} = \frac{\sqrt{a_J^\uparrow a_S^\downarrow}}{\sqrt{a_S^\uparrow a_J^\downarrow}}, \quad (6.23)$$

where  $J$  stands for the Jura spectrometer side and  $S$  stands for Saleve spectrometer side which are the west and east sides respectively. The assumption made for the notation in Eq. 6.23, which will be made throughout this section, is that the target is polarized exactly vertical in the target frame. If this assumption is violated, the Jura and Saleve acceptances blend into each other and Eq. 6.23 is no longer the correct notation for the acceptance ratio. The assumption is violated when the trajectories of the beam particle and the target polarization do not make a right angle in the laboratory frame, in which case the target will no longer be polarized vertically in the target frame. However the target will be assumed to be vertically polarized in the target frame strictly for ease of notation.

Relation 6.22 is equal to  $A_{lr}$  if  $\kappa_{geo} = 1$ . However as stated previously, time effects can vary  $\kappa_{geo}$  from unity. These effects are estimated through false asymmetry analysis and included in the systematic uncertainties described in Sec 6.5.2. Equation 6.21 is therefore to a good approximation an acceptance free method to determine  $A_{lr}$ . It is also defined for the upstream and downstream cells independently and therefore can be used as a consistency check between the two target cells.

The statistical uncertainty of the geometry mean is

$$\delta A_{lr,geo} = \frac{1}{|S_T|} \frac{\sqrt{N_l^\uparrow N_l^\downarrow N_r^\uparrow N_r^\downarrow}}{\left( \sqrt{N_l^\uparrow N_l^\downarrow} + \sqrt{N_r^\uparrow N_r^\downarrow} \right)^2} \sqrt{\frac{1}{N_l^\uparrow} + \frac{1}{N_l^\downarrow} + \frac{1}{N_r^\uparrow} + \frac{1}{N_r^\downarrow}}, \quad (6.24)$$

which reduces to  $\frac{1}{|S_T|} \frac{1}{\sqrt{N}}$ , where  $N = N_l^\uparrow + N_l^\downarrow + N_r^\uparrow + N_r^\downarrow$ , in the case of equal statistics per target cell meaning  $N_l^\uparrow = N_l^\downarrow = N_r^\uparrow = N_r^\downarrow = N/4$ .

## Two-Target Geometric Mean

The previous geometric mean asymmetry determined an  $A_{lr}$  per target cell. As described in Sec 6.1 however, COMPASS had two oppositely polarized target cells in 2015. It is desirable from a statistical point of view and for comparison purposes to determine one  $A_{lr}$  from the 2015 COMPASS setup. This can be accomplished by modifying the geometric mean to add both target cells as follows:

$$A_{lr,2Targ} = \frac{1}{|S_T|} \frac{\sqrt[4]{N_{1,l}^{\uparrow} N_{1,l}^{\downarrow} N_{2,l}^{\uparrow} N_{2,l}^{\downarrow}} - \sqrt[4]{N_{1,r}^{\uparrow} N_{1,r}^{\downarrow} N_{2,r}^{\uparrow} N_{2,r}^{\downarrow}}}{\sqrt[4]{N_{1,l}^{\uparrow} N_{1,l}^{\downarrow} N_{2,l}^{\uparrow} N_{2,l}^{\downarrow}} + \sqrt[4]{N_{1,r}^{\uparrow} N_{1,r}^{\downarrow} N_{2,r}^{\uparrow} N_{2,r}^{\downarrow}}}. \quad (6.25)$$

As in the basic geometric mean asymmetry, Sec 6.5.1, left and right are determined relative to the spin direction of the target as in Eq. 6.20. Similarly to Eq. 6.22, the two-target geometric mean asymmetry can be written as

$$A_{lr,2Targ} = \frac{1}{|S_T|} \frac{\kappa_{2Targ} \sqrt[4]{\sigma_l \sigma_l \sigma_l \sigma_l} - \sqrt[4]{\sigma_r \sigma_r \sigma_r \sigma_r}}{\kappa_{2Targ} \sqrt[4]{\sigma_l \sigma_l \sigma_l \sigma_l} + \sqrt[4]{\sigma_r \sigma_r \sigma_r \sigma_r}} = \frac{1}{|S_T|} \frac{\kappa_{2Targ} \sigma_l - \sigma_r}{\kappa_{2Targ} \sigma_l + \sigma_r}, \quad (6.26)$$

,

where now  $\kappa_{2Targ}$  is the ratio of acceptances from all targets and polarizations. This inclusive acceptance ratio is defined as

$$\kappa_{2Targ} = \frac{\sqrt[4]{a_{1,J}^{\uparrow} a_{1,S}^{\downarrow} a_{2,J}^{\uparrow} a_{2,S}^{\downarrow}}}{\sqrt[4]{a_{1,S}^{\uparrow} a_{1,J}^{\downarrow} a_{2,S}^{\uparrow} a_{2,J}^{\downarrow}}}. \quad (6.27)$$

In this case the acceptance ratio is expected to vary less with time and therefore be closer to unity than the normal geometric mean acceptance ratio, Eq. 6.23. This is a consequence of having the different target cells oppositely polarized. Rewriting Eq. 6.27 with sub-period superscripts instead of target polarization superscripts results in the relation

$$\kappa_{2Targ} = \frac{\sqrt[4]{a_{1,J}^{one} a_{1,S}^{two} a_{2,J}^{two} a_{2,S}^{one}}}{\sqrt[4]{a_{1,S}^{one} a_{1,J}^{two} a_{2,S}^{two} a_{2,J}^{one}}}, \quad (6.28)$$

where sub-period *one* is with the upstream target polarized up and the downstream target polarized down and vice versa for sub-period *two*. From Eq. 6.28 it is more evident that the acceptance ratio terms for sub-period *two* are reciprocal to the terms for sub-period *one* and therefore the acceptance ratio is expected to be more stably close to unity.

Finally the statistical uncertainty of the two target geometric mean is

$$\delta A_{lr,2Targ} = \frac{1}{|S_T|} \frac{LR}{(L+R)^2} \sqrt{\sum_{c,p} \left( \frac{1}{N_{c,l}^p} + \frac{1}{N_{c,r}^p} \right)}, \quad (6.29)$$

where  $L$  can be thought of as the left counts and equals to  $\sqrt[4]{N_{1,l}^{\uparrow} N_{1,l}^{\downarrow} N_{2,l}^{\uparrow} N_{2,l}^{\downarrow}}$  and  $R$  can be thought of as the right counts and equals  $\sqrt[4]{N_{1,r}^{\uparrow} N_{1,r}^{\downarrow} N_{2,r}^{\uparrow} N_{2,r}^{\downarrow}}$ . As with the geometric mean asymmetry, in the case of equal statistic populations in each direction and target polarization, the statistical uncertainty for the two-target geometric mean also reduces to  $\frac{1}{|S_T|} \frac{1}{\sqrt{N}}$ , where  $N$  is the sum of all counts.

## 6.5.2 Systematic Studies

Several tests were performed to estimate the systematic uncertainty of the left-right asymmetry. The systematic uncertainties are determined by adding all non-zero systematic uncertainties in quadrature. The impact from each source of systematic error is summarized in Table. 6.9.

### Period Compatibility (Time Dependence)

The asymmetries calculated for each time period in each kinematic bin are shown in Fig. 6.13.

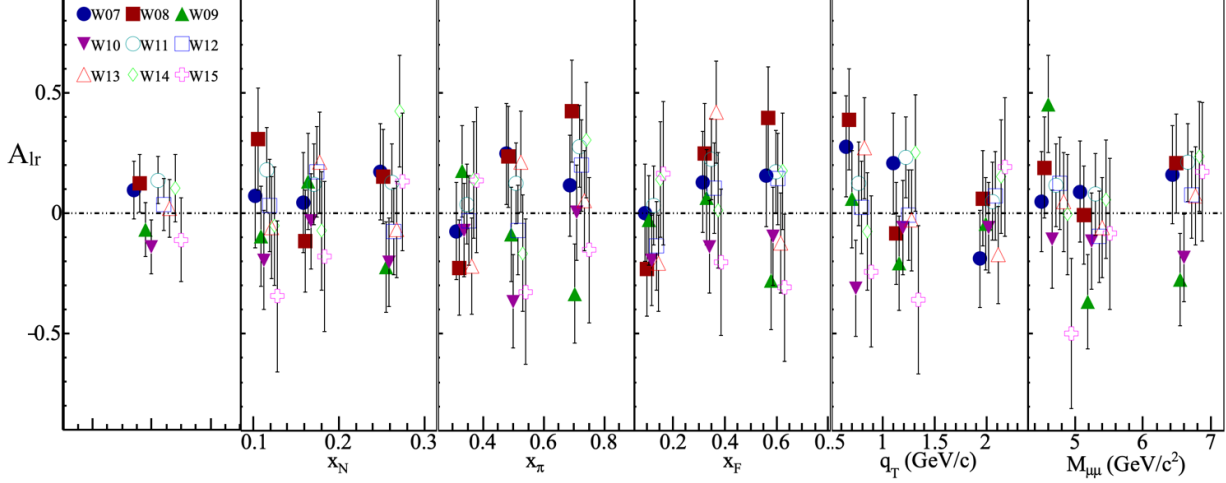


Figure 6.13:  $A_{lr}$  determined for each period

By eye the asymmetry fluctuations appear to be statistically compatible. To quantify the compatibility of the asymmetries between the periods, a pull distribution is formed where the pull value is defined as

$$\Delta A_i = \frac{A_i - \langle A \rangle}{\sqrt{\sigma_{A_i}^2 - \sigma_{\langle A \rangle}^2}}, \quad (6.30)$$

and is determined for each period and kinematic bin. There are therefore 3 (number of bins) x 5 (number of kinematics) x 9 (number of periods) = 135 entries in the pull distribution. The pull distribution is shown in Fig. 6.14 along with a Gaussian fit to determine the distributions width and average. If the asymmetries all come from the same parent distribution then, due to the central limit theorem, the pull distribution will be a Gaussian distribution with zero mean and unit variance. The discrepancy of the pull distribution from a standard Gaussian distribution is used to determine a systematic error as

$$\frac{\sigma_{\text{systematic}}}{\sigma_{\text{statistical}}} = \sqrt{|\sigma_{\text{pull}}^2 - 1|} + \frac{\mu_{\text{pull}}}{2}. \quad (6.31)$$

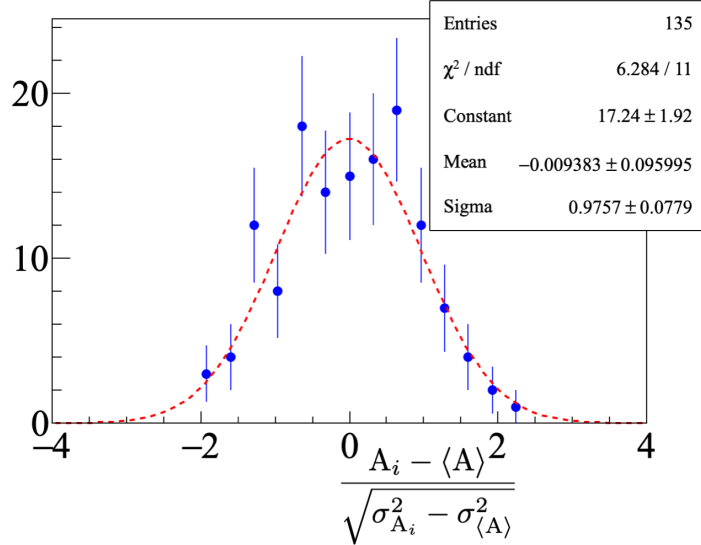


Figure 6.14: Pull distribution from the two-target geometric mean

As the asymmetries in different kinematic bins are formed using the same data set, the asymmetries between kinematic binnings are correlated. For this reason an uncorrelated pull distribution is also formed for each kinematic bin and also compared with a standard Gaussian distribution. These distributions are shown in Fig. 6.15 along with the results of their respective Gaussian fits. For these uncorrelated pull distributions there are now only 3 (number of bins) x 9(number of periods) = 27 entries in each kinetically binned pull distributions and only 9 (number of periods) bins in the integrated pull distribution.

Even though the Gaussian fits did not give exactly a standard Gaussian, the fit parameters are well compatible with a standard Gaussian within the errors of the fit. Therefore no systematic error was assigned due to incompatibility of the periods.

### Left/Right Event Migration

The spectrometer has finite resolution for any measured quantity. For this reason events measured as left outgoing could really be events that are right outgoing and vice versa. This left-right misidentification has the result of diluting spin-dependent effects by effectively having a sample from an unpolarized target along with the sample from the polarized target. Therefore the asymmetry  $A_{lr}$  reduces from left-right misidentification and this effect is included as a systematic effect.

A Monte-Carlo data set was analyzed to determine the left-right misidentification percentage. Four Monte-Carlo processes were generated corresponding to three background processes and a spin-independent signal process. The generator used was PYTHIA8 and the data was generated and reconstructed on NCSA's Blue Waters at Urbana-Champaign. The background processes simulated were JPs $\psi$  production, Psi' pro-

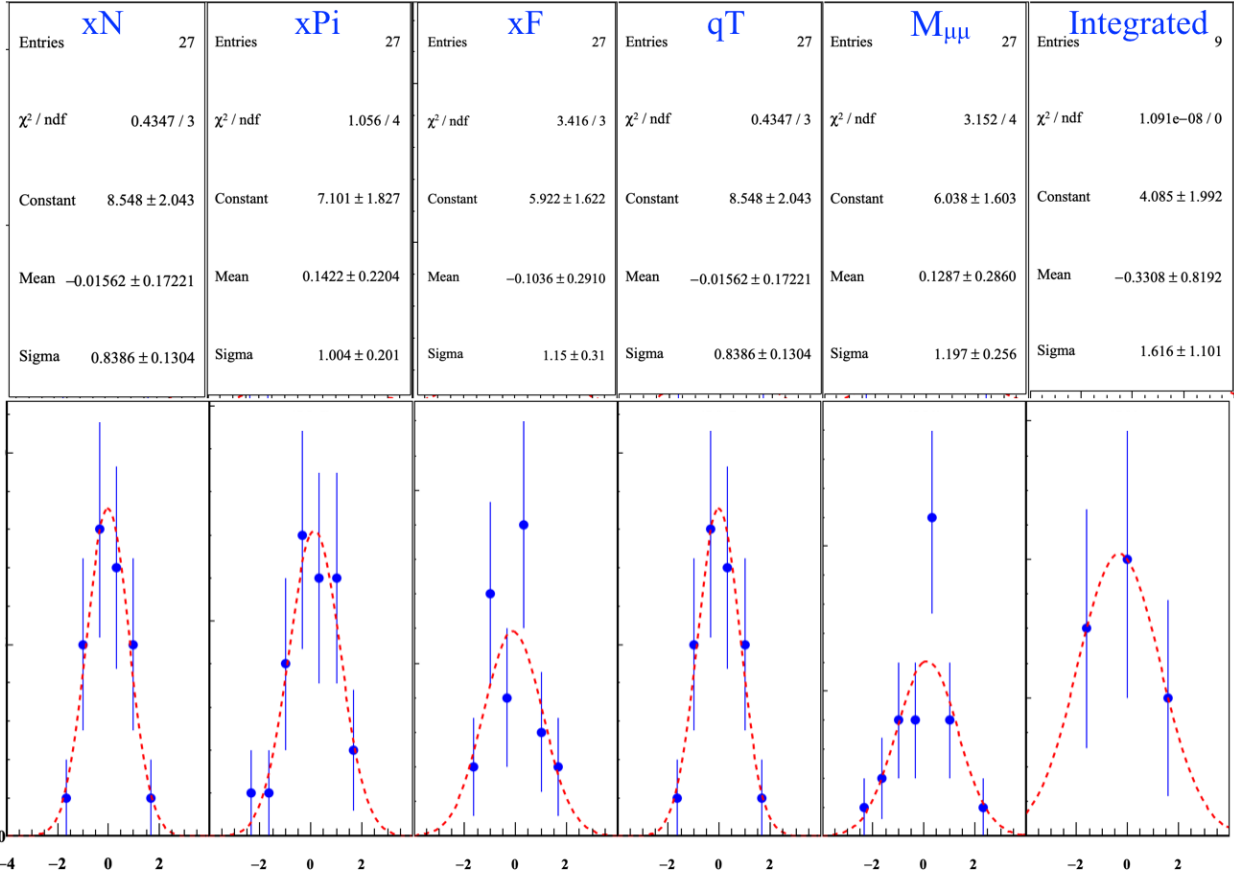


Figure 6.15: Uncorrelated pull distributions and Results of the Gaussian fit for the pull distributions

duction and open charm (OC) production. Each of these backgrounds can decay into two final state muons which results in a background contamination to the Drell-Yan signal. Table 6.7 gives the parameters used for the Monte-Carlo generated.

Table 6.7: Monte-Carlo settings produced on Blue Waters

Description	Monte-Carlo Setting	Setting
Event generator	PYTHIA8	
Pion PDF	GRVPI1	
Proton PDF	NNPDF23	
Proton/Neutron mixing ratio	1.96	
Initial state radiation	on	
Final state radiation	on	
Multiple parton interactions	on	
GEANT4 detector simulation	TGEANT	
Simulated detector efficiency distributions	uniform	

The generated Monte-Carlo data corresponds to a  $4\pi$  spectrometer acceptance. The COMPASS spec-

trometer on the other hand, does not have a full  $4\pi$  acceptance. Therefore to produce simulated data that corresponds to the actual data taking conditions, a GEANT4 [96] based detector simulation, called TGEANT [97], simulated the COMPASS spectrometer response to the generated data. The data from TGEANT was then reconstructed with the same reconstruction software as real data.

Misidentification was estimated by comparing the data input to TGEANT with the output reconstructed data. The same analysis and cuts were performed on the simulated and then reconstructed data as were performed on the real data set. Fig. 6.16 shows the rate of events identified correctly and incorrectly as a function of  $\phi_S$ . Fig. 6.16 is made by comparing which outgoing direction the generated events emerged with the outgoing direction the reconstructed events emerged.

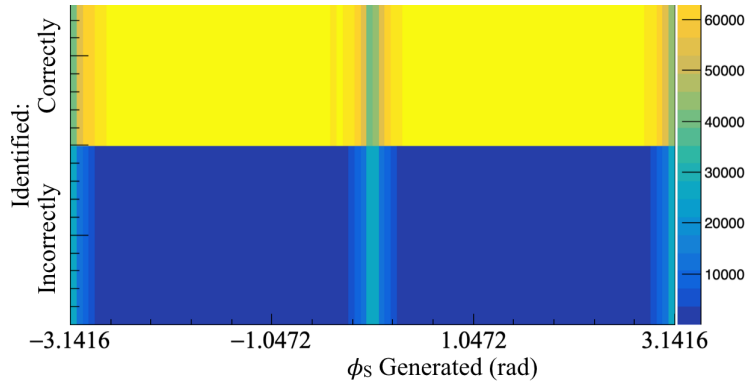


Figure 6.16: The rate of identified correctly and incorrectly left-right events as a function of  $\phi_S$ . This is determined by comparing the generated outgoing direction with the reconstructed outgoing direction. The left-right boundary is clearly visible at  $\phi_S = 0$  rad and  $\phi_S = -\pi$  rad and  $\phi_S = \pi$  rad

As is clearly visible in Fig. 6.16, there is a band of higher misidentification rate at the border between left and right. For this reason a cut on the  $\phi_S$  variable symmetric about the left-right border was tested to determine the percent of misidentification as a function of the amount of  $\phi_S$  cut. These results are shown in Fig. 6.17.

The systematic error for left-right migration is calculated as

$$\delta A_{lr,systematic} = \gamma * A_{lr} + \gamma * \delta A_{lr}, \quad (6.32)$$

where this expression is derived in Appendix A.2. No cut on  $\phi_S$  was ultimately used for the asymmetry determination. This is to avoid loss of statistics and due to the fact that the systematic error is already small with no cut in  $\phi_S$ . The integrated systematic error due to left-right event migration was determined to be 9% of the statistical error.

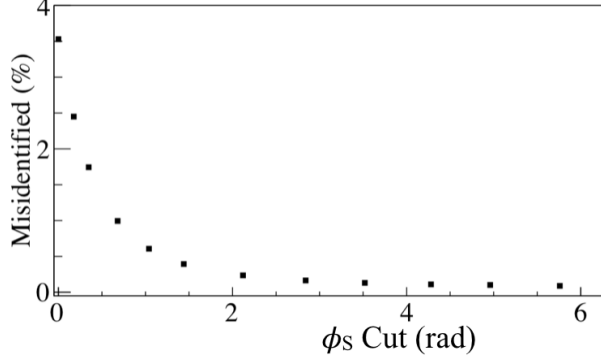


Figure 6.17: Percent left-right migration as a function of the amount of  $\phi_S$  cut.

## False Asymmetries

### Acceptance From False Asymmetries

As was pointed out in Sec. 6.5.1 and Sec. 6.5.1, the asymmetry measurement assumes the acceptance does not change with time and therefore the acceptance ratio,  $\kappa$  is unitary. Any deviation from a unitary acceptance ratio is estimated with a false asymmetry and is taken as a systematic error. To determine if acceptance does change with time, a false asymmetry is calculated where the only way the false asymmetry could be non-zero is if acceptance changes with time. This false asymmetry for the two-target geometric mean is

$$A_{lr, \text{False}} = \frac{1}{|S_T|} \frac{\sqrt[4]{N_{1,r}^{\uparrow} N_{1,l}^{\downarrow} N_{2,l}^{\uparrow} N_{2,r}^{\downarrow}} - \sqrt[4]{N_{1,l}^{\uparrow} N_{1,r}^{\downarrow} N_{2,r}^{\uparrow} N_{2,l}^{\downarrow}}}{\sqrt[4]{N_{1,r}^{\uparrow} N_{1,l}^{\downarrow} N_{2,l}^{\uparrow} N_{2,r}^{\downarrow}} + \sqrt[4]{N_{1,l}^{\uparrow} N_{1,r}^{\downarrow} N_{2,r}^{\uparrow} N_{2,l}^{\downarrow}}} \quad (6.33)$$

$$= \frac{1}{|S_T|} \frac{\alpha_{2Targ} \sqrt[4]{\sigma_r \sigma_l \sigma_l \sigma_r} - \sqrt[4]{\sigma_l \sigma_r \sigma_r \sigma_l}}{\alpha_{2Targ} \sqrt[4]{\sigma_r \sigma_l \sigma_l \sigma_r} + \sqrt[4]{\sigma_l \sigma_r \sigma_r \sigma_l}} = \frac{1}{|S_T|} \frac{\alpha_{2Targ} - 1}{\alpha_{2Targ} + 1},$$

where  $\alpha_{2Targ}$  is an acceptance ratio and is defined as

$$\alpha_{2Targ} = \frac{\sqrt[4]{a_{1,S}^{\uparrow} a_{1,S}^{\downarrow} a_{2,J}^{\uparrow} a_{2,J}^{\downarrow}}}{\sqrt[4]{a_{1,J}^{\uparrow} a_{1,J}^{\downarrow} a_{2,S}^{\uparrow} a_{2,S}^{\downarrow}}}. \quad (6.34)$$

The false asymmetry, Eq. 6.33, can be simplified as

$$A_{lr, \text{False}} = \frac{1}{|S_T|} \frac{\sqrt[4]{N_{1,S} N_{2,J}} - \sqrt[4]{N_{1,J} N_{2,S}}}{\sqrt[4]{N_{1,S} N_{2,J}} + \sqrt[4]{N_{1,J} N_{2,S}}}. \quad (6.35)$$

That is  $A_{lr, \text{False}}$  is the normalized difference of counts from each target cell assuming the upstream target is always polarized down and the downstream target is always polarized up. Given that the polarization flips for both upstream and downstream target cells,  $A_{lr, \text{False}}$  is an asymmetry where physical effects cancel out.

The kinematic dependencies of the false asymmetry are shown in Fig. 6.18 and the kinematic dependencies of the acceptance ratio,  $\alpha_{2Targ}$ , are shown in Fig. 6.19.

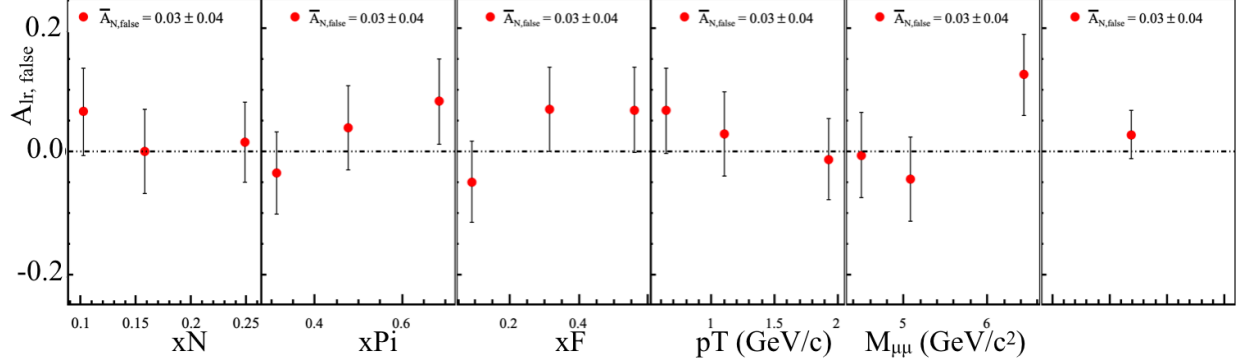


Figure 6.18: False asymmetry,  $A_{lr, False}$ , to estimate fluctuations in acceptance in time

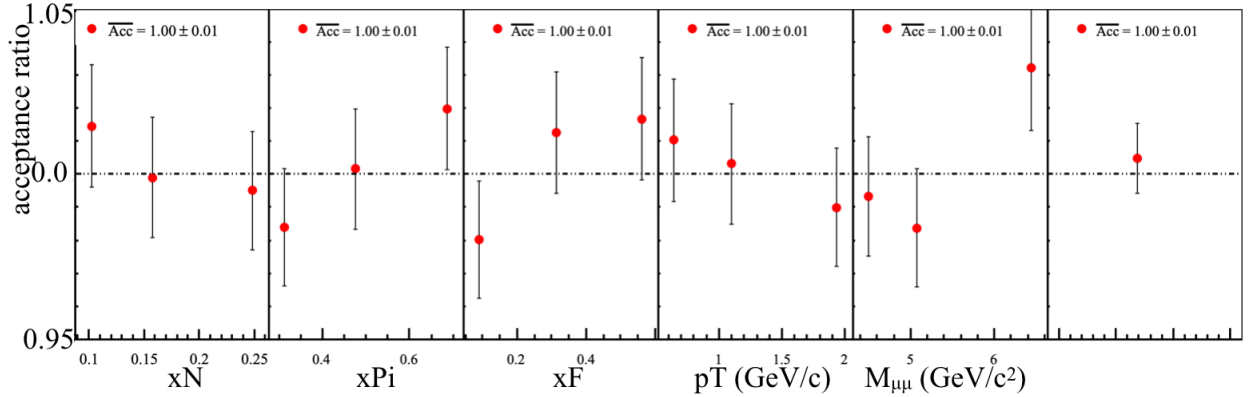


Figure 6.19: Acceptance ratio  $\alpha_{2Targ}$ , Eq. 6.34, used to determine the systematic effects from acceptance changes in time

While  $\alpha_{2Targ}$  is an acceptance ratio it is not the same as,  $\kappa_{2Targ}$  the acceptance ratio in the true asymmetry. However  $\alpha_{2Targ}$  is similar to  $\kappa_{2Targ}$  in that  $\alpha_{2Targ}$  will only be different from unity as a result of time changes in the spectrometer. Therefore it is assumed  $\alpha_{2Targ}$  can be used as a good estimate of the true acceptance ratio fluctuations. The systematic error due to acceptance fluctuations is determined as

$$\delta A_{lr, systematic} = \frac{1}{|S_T|} \left( \frac{|\alpha_{2Targ} - 1|}{2} + \delta_{\frac{|\alpha_{2Targ} - 1|}{2}} \right), \quad (6.36)$$

where this expression is derived in Appendix A.1. The kinematic dependence of the systematic error normalized to the statistical error is shown in Fig. 6.20. The binned average systematic error due to acceptance is 20% of the statistical error.

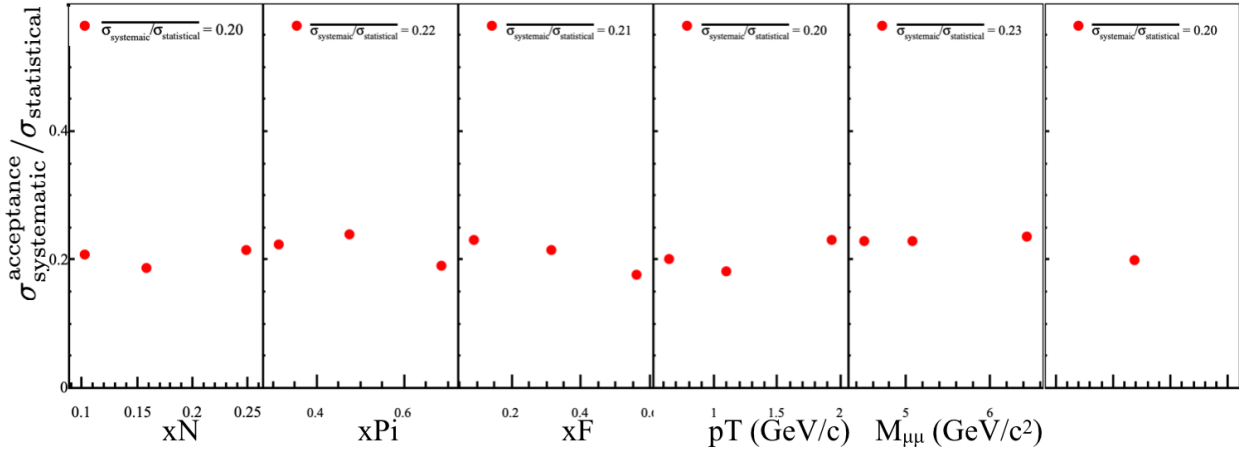


Figure 6.20: Systematic uncertainty due to acceptance effects normalized to the statistical error.

### Further False Asymmetry Effects

Although the list of systematic effects specifically studied is quite exhaustive there is always the potential for other systematic effects not considered. Studies of the changes in time from additional false asymmetries were performed in an attempt to take into account all other systematic effects. All false asymmetries considered must be constructed in such a way that the physical process of interest cancels out. A false asymmetry could therefore only be non-zero from acceptance effects, luminosity or some other reason not considered. The additional false asymmetries are constructed in a way that luminosity effects cancel out and acceptance effects are approximately constant. With these assumptions, the pull values from Eq. 6.30 are expected to be distributed as a standard Gaussian distribution. Any deviation from a standard Gaussian is conservatively taken as a systematic effect from some unknown cause. The additional studied false asymmetries are summarized in the following enumerated list.

1. A false asymmetry similar to Eq. 6.33 but with the upstream left and right counts flipped defined as

$$A_{lr,F1} = \frac{1}{|S_T|} \frac{\sqrt[4]{N_{1,l}^\uparrow N_{1,r}^\downarrow N_{2,l}^\uparrow N_{2,r}^\downarrow} - \sqrt[4]{N_{1,r}^\uparrow N_{1,l}^\downarrow N_{2,r}^\uparrow N_{2,l}^\downarrow}}{\sqrt[4]{N_{1,l}^\uparrow N_{1,r}^\downarrow N_{2,l}^\uparrow N_{2,r}^\downarrow} + \sqrt[4]{N_{1,r}^\uparrow N_{1,l}^\downarrow N_{2,r}^\uparrow N_{2,l}^\downarrow}}. \quad (6.37)$$

This false asymmetry can be thought of as measuring the normalized counts on the Jura side minus the Saleve side. The period weighted average results of this false asymmetry are shown in Fig. 6.21. As Fig. 6.21 shows, the asymmetry is systematically less than zero by more than a standard deviation resulting from acceptance effects. The uncorrelated pull distributions from this false asymmetry are

shown in Fig. 6.22 along with the corresponding Gaussian fit results. Due to the fact that there are less entries in these pull distributions the Gaussian fit results are not necessarily that good. In an attempt to correct for this and to take into account the fit errors, a weighted average of the mean and standard deviation are made, as in Eq. 6.10, using weights as the inverse fit variances. The resulting systematic error is again determined as in Eq. 6.31 using the weighted mean and weighted standard deviation.

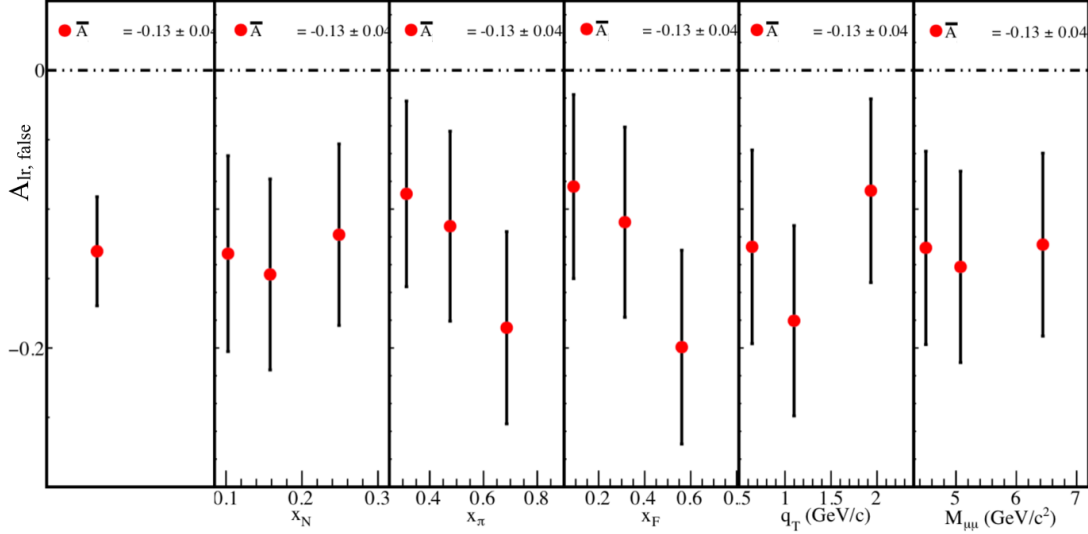


Figure 6.21: Two-target geometric mean false asymmetry. This is non-zero due to acceptance effects

2. A false asymmetries using only the information from the upstream or the downstream target defined as

$$A_{lr,F2} = \frac{1}{|S_T|} \frac{\sqrt{N_l^\uparrow N_r^\downarrow} - \sqrt{N_r^\uparrow N_l^\downarrow}}{\sqrt{N_l^\uparrow N_r^\downarrow} + \sqrt{N_r^\uparrow N_l^\downarrow}}. \quad (6.38)$$

This false asymmetry can also be thought of as measuring the normalized counts on the Jura side minus the Saleve side but for each target individually. Both this false asymmetry and the previous false asymmetry, Eq. 6.37, can be written as

$$A_{lr,F1/2} = \frac{1}{|S_T|} \frac{\alpha - 1}{\alpha + 1}, \quad (6.39)$$

where  $\alpha$  will be an acceptance ratio of Jura/Saleve. As the Jura/Saleve acceptance ratio is expected to be the same for the upstream and downstream targets, any difference between the two false asymmetries must be due to other reasons. A by-period comparison between the upstream and downstream

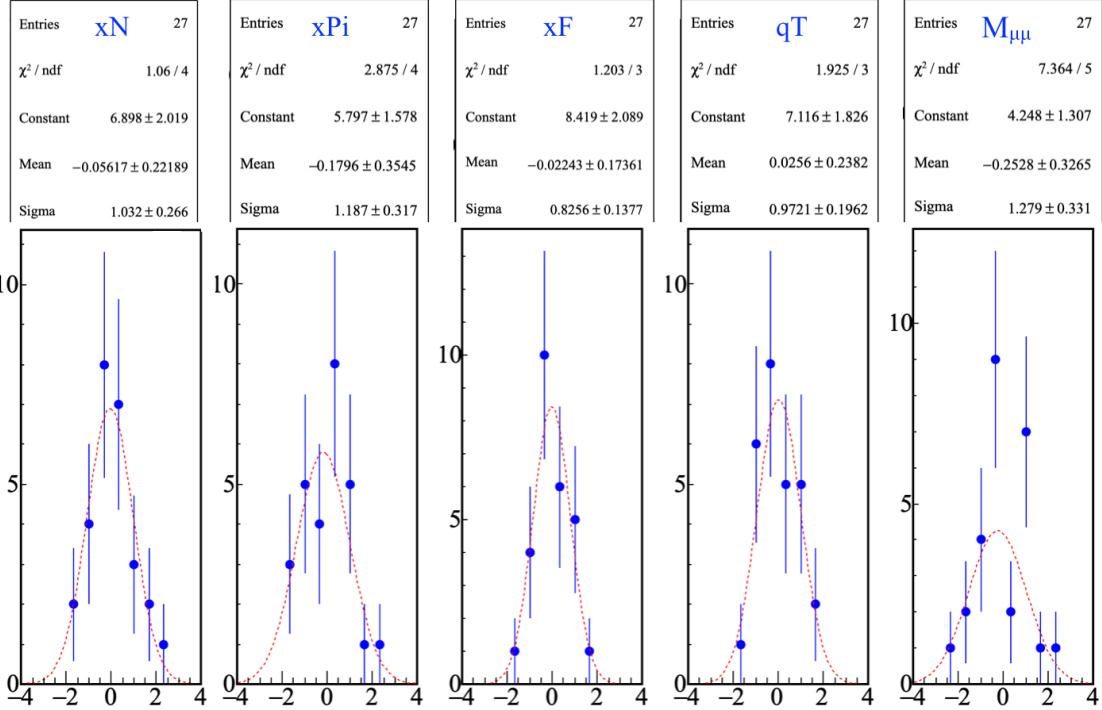


Figure 6.22: Uncorrelated pulls of the two-target geometric mean false asymmetry and Gaussian fit results

target is shown in Fig. 6.23 and as can be seen there are difference by-period between the upstream and downstream asymmetries. A combined pull distribution is made using the information from both upstream and downstream asymmetries and is shown in Fig. 6.24. As with the previous false asymmetry, lack of data leads to the same problems with the fit and therefore the same weighting method is used to determine a systematic error.

- Finally the same false asymmetry used to determine the acceptance fluctuations, Eq. 6.33, is also checked for compatibility and a systematic error is determined in the same way as the previous false asymmetries. The pulls are shown in Fig. 6.25 along with the corresponding fit parameters and errors.

A summary of the systematic error from each false asymmetry is shown in Table. 6.8.

Systematic error	$\langle \sigma_{\text{systematic}} / \sigma_{\text{statistical}} \rangle$
Two target Jura-Saleve	0.26
Combined one target	0.5
Two target acceptance estimation	0.29

Table 6.8: Summary of systematic error impacts from false asymmetries. The maximum systematic error is chosen as the systematic error.

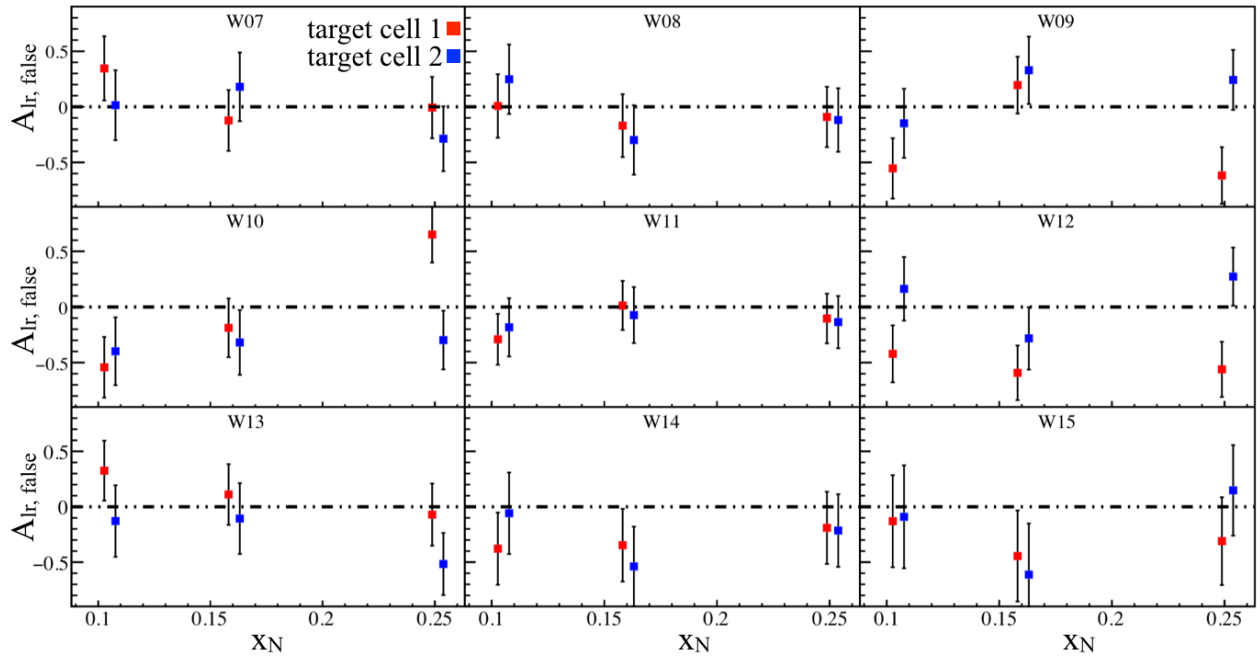


Figure 6.23: One target false asymmetries for the upstream target (red) and the downstream target (blue), as a function of  $x_N$ . Each graph is from a different period in time.

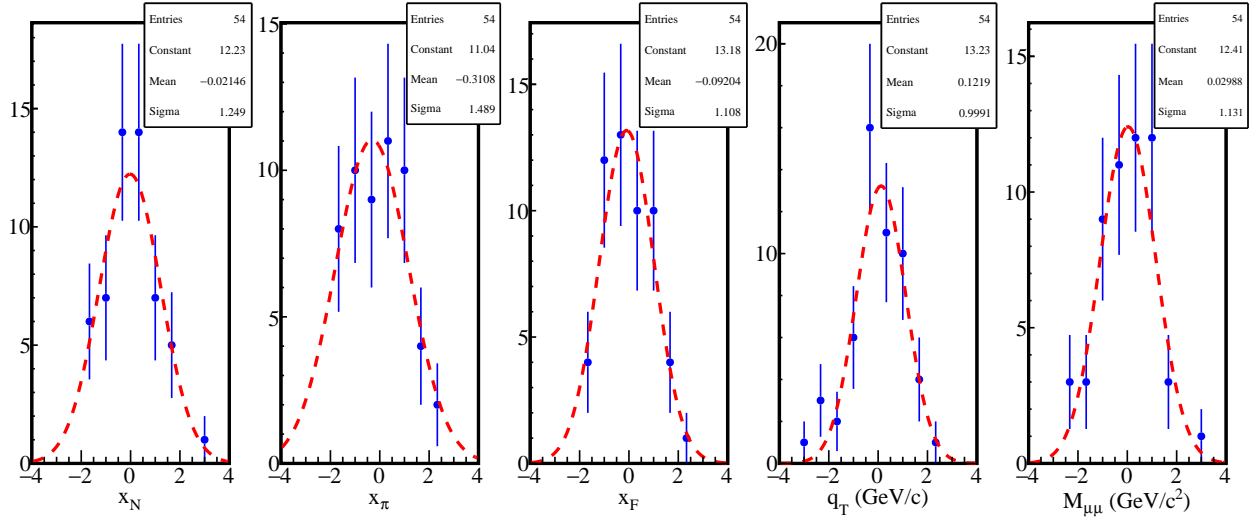


Figure 6.24: Pull values from one-target geometric mean false asymmetries. Both upstream and downstream values are used to make this pull

### Total Systematics

The total systematic uncertainty is determined by adding all non-zero systematic effects in quadrature as

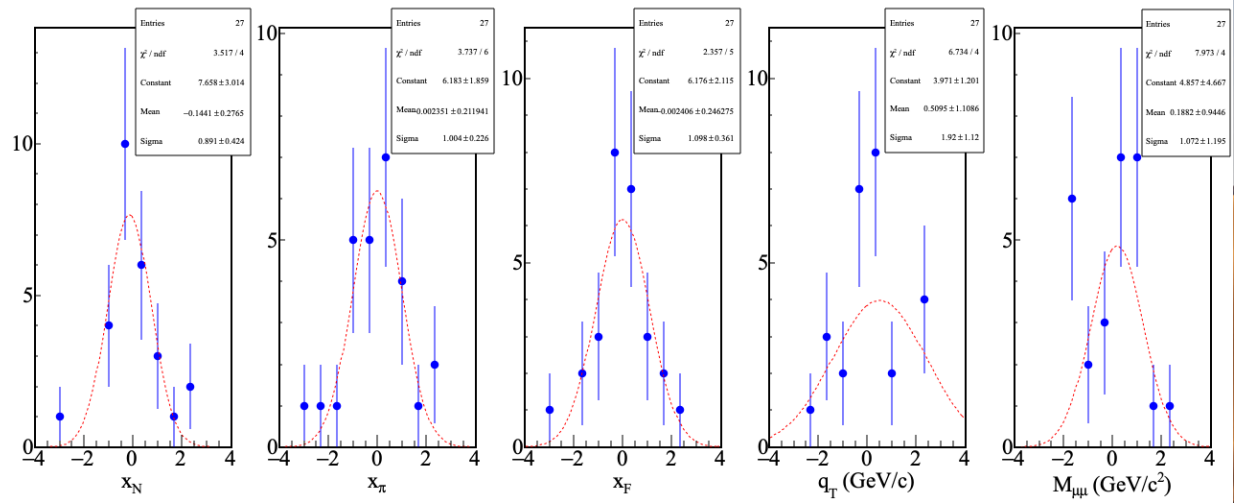


Figure 6.25: Pull distribution for a nearly acceptance free two-target false geometric mean asymmetry

$$\left\langle \frac{\sigma_{\text{systematic}}}{\sigma_{\text{statistical}}} \right\rangle = \sqrt{\sum_i^{\text{all systematic}} \left\langle \frac{\sigma_{\text{systematic},i}^2}{\sigma_{\text{statistical}}^2} \right\rangle}, \quad (6.40)$$

where all the systematic effects considered are summarized in Table. 6.9. For reference the integrated left-right asymmetry is  $\langle A_{lr} \rangle = 0.030$  and the integrated statistical error is  $\langle \sigma_{\text{statistical}} \rangle = 0.039$ .

Systematic Uncertainty	$\langle \sigma_{\text{systematic}}/\sigma_{\text{statistical}} \rangle$	$\langle \sigma_{\text{systematic}} \rangle$
Period compatibility	0.0	0.0
Left-Right migration	0.09	0.004
Target Polarization	0.05	0.003
Dilution Factor	0.05	0.003
Acceptance fluctuation	0.2	0.008
False asymmetry	0.5	0.020
<b>Total</b>	<b>0.55</b>	<b>0.022</b>

Table 6.9: Summary of systematic uncertainty impacts to the integrated asymmetry

### 6.5.3 Results

The left-right asymmetry is extracted per period, corrected for the target polarization and ultimately combined as a weighed average, Eq. 6.10, to get an overall result as in Sec 6.3.2.

The results for the geometric mean are shown in Fig. 6.26 and the results for the two-target geometric mean are shown in Fig. 6.27. The numerical values for the two-target geometric mean systematic uncertainty are summarized in Table 6.9. To verify the results in this section are correct, an independent cross-check

was performed by a member from the University of Turin and no discrepancies were found. The results of the cross-check are provided in Appendix B.1.

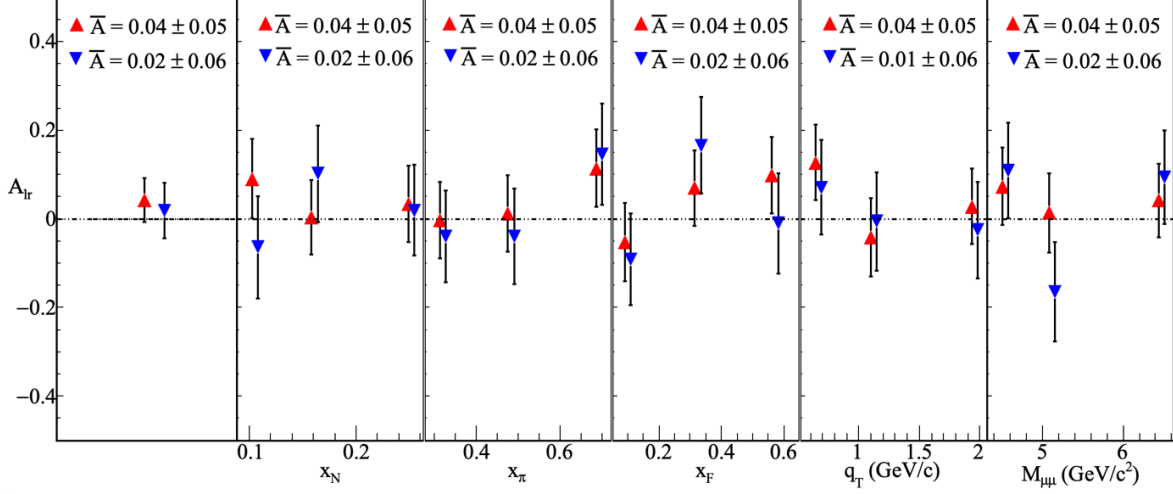


Figure 6.26:  $A_{lr}$  determined from the geometric mean method for the upstream target cell (red) and the downstream target cell (blue) for all kinematic binnings

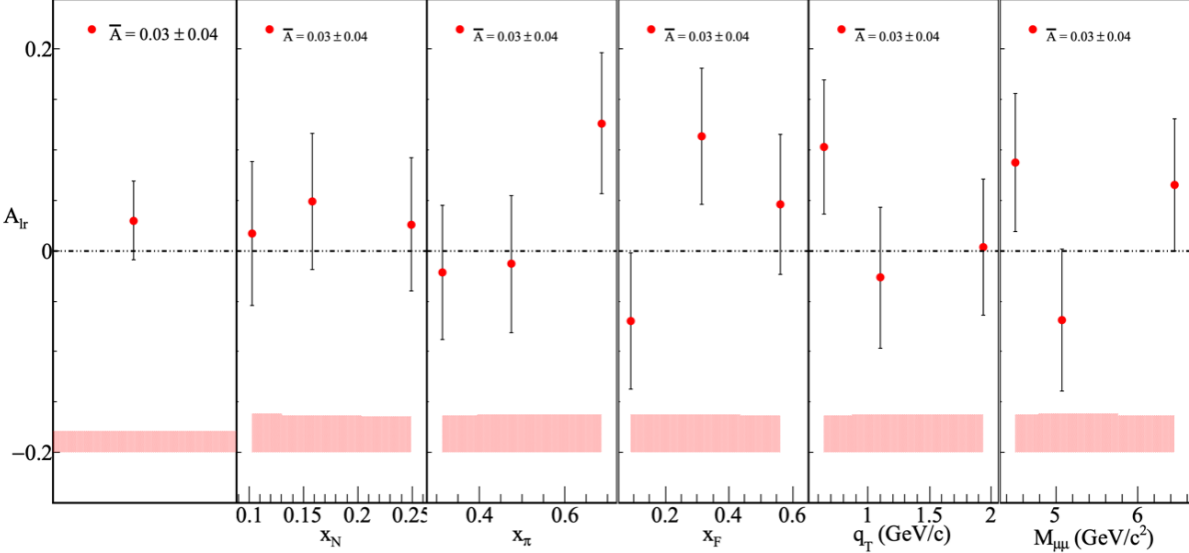


Figure 6.27:  $A_{lr}$  determined by the two-target geometric mean method for all kinematic binnings

It was shown in Sec 2.5.2 that the left-right asymmetry is related to the Sivers amplitude as

$$A_{lr} = \frac{2A^{\sin(\phi_S)}}{\pi} = \frac{2A_N}{\pi}, \quad (6.41)$$

where  $A_N$  is the analyzing power. The Sivers amplitude was measured to be approximately 1 sigma above zero from the unbinned maximum likelihood method, Fig. 6.5, the double ratio method, Fig. 6.7, and the left-right asymmetry. Adjusting the left-right asymmetry, as in Eq. 6.41, shows the amplitude determined from the left-right asymmetry is statistically consistent with the Sivers amplitude determined from the double ratio method, Fig. 6.28. Therefore all methods to determine the Siver amplitude in this chapter are consistent with the sign flip hypothesis between the Drell-Yan and SIDIS processes. On the other hand, the statistical error bars are too large to definitively conclude the sign flip assumption holds. There are also no clear trends in the kinematic variable binning due to the large statistical error bars.

It is interesting to note that Eq. 6.41 was derived with the assumption that the leading order Drell-Yan cross-section, Eq. 2.52, is sufficient. It is not theoretically ruled out however, that the left-right asymmetry results from higher order amplitudes in addition to the Sivers amplitude. As Fig. 6.28 shows, the left-right asymmetry is slightly less significant above zero than the Sivers amplitude determined from the double ratio method. This could indicate the need to include higher order terms in the Drell-Yan cross-section.

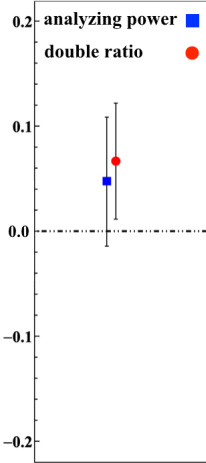


Figure 6.28: The left-right asymmetry adjusted (analyzing power, blue) to be compared with Sivers amplitude determined from the double ratio method (red).

In regards to the sign flip, Fig. 6.29 shows that the Sivers amplitude determined from the left-right asymmetry is compatible with the results published from 2015 COMPASS data and is compatible with the sign flip between Drell-Yan and SIDIS.

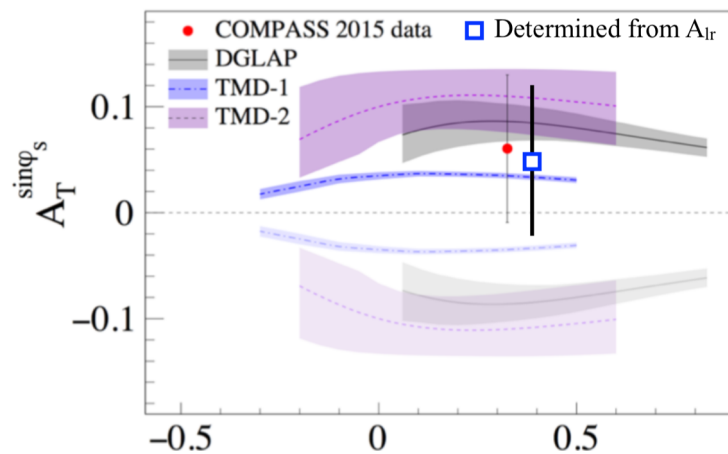


Figure 6.29: Including the left-right asymmetry to show it's compatibility with the sign flip.

# Chapter 7

## J/ $\Psi$ Transverse Spin Dependent Phenomena

This chapter describes the analysis performed in the intermediate invariant mass range at COMPASS. The biggest advantage about the intermediate mass range is an increase in statistics. The intermediate mass range for this thesis is defined as 2.5-4.3 GeV/ $c^2$ . The intermediate mass range contains approximately 1.6 times more events than the high mass range above 4.3 GeV/ $c^2$ . On the other hand, the intermediate mass range results from several reactions. Nevertheless, J/ $\Psi$  production is by far the most dominant reaction and therefore the this chapter assumes the results are from the J/ $\Psi$  reaction. A theoretical introduction related to transverse J/ $\Psi$  spin asymmetries is provided in Sec 2.5.4. As of yet, the exact mechanism for J/ $\Psi$  production is unknown and therefore the exact J/ $\Psi$  vertex coupling is unknown. Nevertheless, the analysis techniques in this chapter contribute to the transverse spin knowledge of J/ $\Psi$  production. The reaction of interest is

$$\pi^-(P_a) + P(P_b, S_T) \rightarrow J/\Psi + X \rightarrow \mu^-(\ell) + \mu^+(\ell') + X, \quad (7.1)$$

where the proton target,  $P$ , is transversely polarized with spin  $S_T$ .

The dimuon final state from J/ $\Psi$  production is indistinguishable from the Drell-Yan dimuon final state described the previous analyses in chapter 6. For this reason, similar event selection and data quality are used to study the dimuon production resulting from J/ $\Psi$  decays. On the other hand, the J/ $\Psi$  production has a higher background percentage from Drell-Yan and other components to be taken into account. The results presented in this chapter are determined from the left-right asymmetry analysis as in Sec 6.5, where again the left-right asymmetry is defined as

$$A_{lr} = \frac{1}{|S_T|} \frac{\sigma_l - \sigma_r}{\sigma_l + \sigma_r}. \quad (7.2)$$

### 7.1 Data Collection and Event Selection

The data collection is described in Sec 6.1.1 and the data stability tests are described in Sec 6.1.2. Both the Drell-Yan analysis and the J/ $\Psi$  production analysis study dimuon final states so the spectrometer data

taking conditions are the same. In particular the measurement in this chapter results from a 190 GeV/ $c$   $\pi^-$  beam impinged on a transversely polarized NH<sub>3</sub> target from the 2015 COMPASS spectrometer data taking conditions.

The event selection in this chapter is similar to the event selection in the previous chapter, Sec 6.1.3. The cuts are chosen to ensure two oppositely charged muons are detected with a vertex in the transversely polarized NH<sub>3</sub> target. Sec 6.1.3 describes the cut selection and the reason for each cut. The only event selection difference, from Sec 6.1.3, is the selected invariant mass. The nominal J/ $\Psi$  invariant mass and width are 3.096 GeV/ $c^2$  and  $92.9 \times 10^{-6}$  GeV/ $c^2$  respectively [11]. Therefore to ensure the events for this analysis result from J/ $\Psi$  production, the analysis invariant mass range should be where the J/ $\Psi$  signal to background is highest. This is in contrast to the Drell-Yan analyses which required the invariant mass to be above 4.3 GeV/ $c^2$ .

### 7.1.1 J/ $\Psi$ Invariant Mass Range

The COMPASS spectrometer has a finite mass resolution which therefore means the events resulting from J/ $\Psi$  production have an invariant mass spread larger than the nominal J/ $\Psi$  width. For this reason the cut on invariant mass should be a range much larger than the nominal J/ $\Psi$  width. Fig. 7.1 shows the 2015 dimuon invariant mass distribution and the other production components around the J/ $\Psi$  invariant mass.

As can be seen in Fig. 7.1, regardless of the analysis mass range chosen, there are still events resulting from the other background processes. The normalized systematic variance resulting from background processes is derived in Appendix A.3 as

$$\frac{\sigma_{\text{systematic}}^2}{\sigma_{\text{statistical}}^2} = \frac{(1-p)^2}{p^2}, \quad (7.3)$$

and the total variance from statistical fluctuations and background contributions is

$$\delta^2 A_{lr, J/\Psi} = \frac{(1-p)^2 + 1}{p^2} \sigma_{\text{statistical}}^2, \quad (7.4)$$

where  $p$  is the J/ $\Psi$  purity. Therefore the analysis invariant mass range should have a J/ $\Psi$  purity as high as possible to reduce the systematic error while still including as much data as possible to reduce the statistical error. The total error however, is dominated by statistical error for any purity larger than 50%. That being the case, Eq. 7.4 is derived assuming  $(1-p)$  is small and therefore a desired purity of 90% or greater was chosen to safely ensure Eq. 7.4 is valid.

The J/ $\Psi$  purity as a function of mass range is determined from a Monte-Carlo data set. The same Monte-

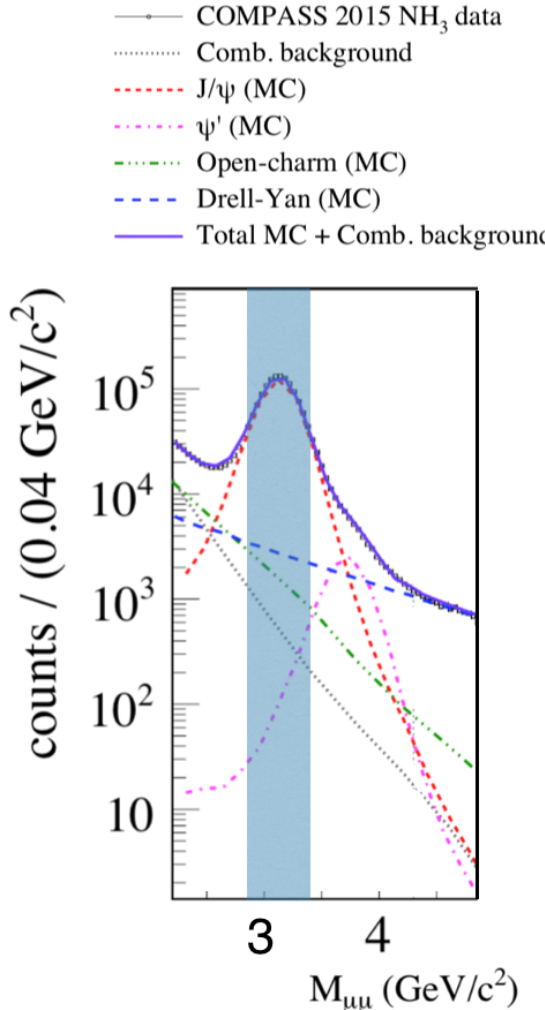


Figure 7.1: The 2015 COMPASS invariant dimuon mass distribution and a fit to this data. The data fit is from Monte-Carlo and combinatorial background analysis and is provided to show the background processes. The shaded blue region shows the analysis mass range for the analysis in this chapter. This image is taken from [90].

Carlo described in Table 6.7 was used to calculate the  $J/\Psi$  purity. In particular the processes included are Drell-Yan production, open charm production,  $\Psi'$  production and  $J/\Psi$  production. To determine the purity, the real data is fit using the Monte-Carlo data which determines the counts from each process. The Monte-Carlo fit is accomplished by normalizing the invariant mass distribution from each Monte-Carlo sample and then fitting using the sum of the four normalized distributions to fit the real data. The fit function is defined

as

$$F_{J/\Psi \text{ Fit}}(x) = N_{J/\Psi} h_{J/\Psi}(x) + N_{Drell-Yan} h_{Drell-Yan}(x) + N_{Open \text{ Charm}} h_{Open \text{ Charm}}(x) + N_{\Psi'} h_{\Psi'}(x), \quad (7.5)$$

where  $h(x)$  represents the number of counts from the normalized histogram distribution and the  $N$ 's are the fit parameters. Fig. 7.2 shows the four normalized Monte-Carlo invariant mass distributions and Fig. 7.3 shows the Monte-Carlo fit to the real data in one  $q_T$  bin.

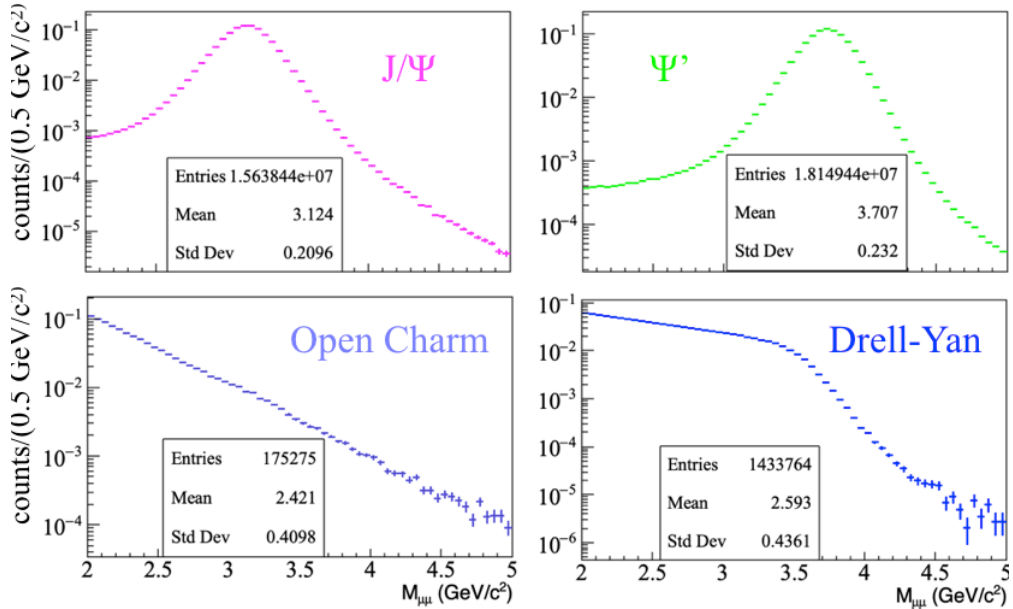


Figure 7.2: The normalized invariant mass distributions from the four simulated Monte-Carlo processes. These distributions are used to fit the real data.

Once the fits are performed, the  $J/\Psi$  purity in each invariant bin is determined as

$$p(x) = \frac{N_{J/\Psi} h_{J/\Psi}(x)}{N_{J/\Psi} h_{J/\Psi}(x) + N_{Drell-Yan} h_{Drell-Yan}(x) + N_{Open \text{ Charm}} h_{Open \text{ Charm}}(x) + N_{\Psi'} h_{\Psi'}(x)}. \quad (7.6)$$

Table 7.1 summarizes the  $J/\Psi$  purity as a function of the mass range. For this analysis an invariant mass range of  $2.87$ - $3.38$   $\text{GeV}/c^2$  was chosen to safely have a  $J/\Psi$  purity of 90% or greater. Tables 7.2 and 7.3 summarize the number of events remaining after each cut.

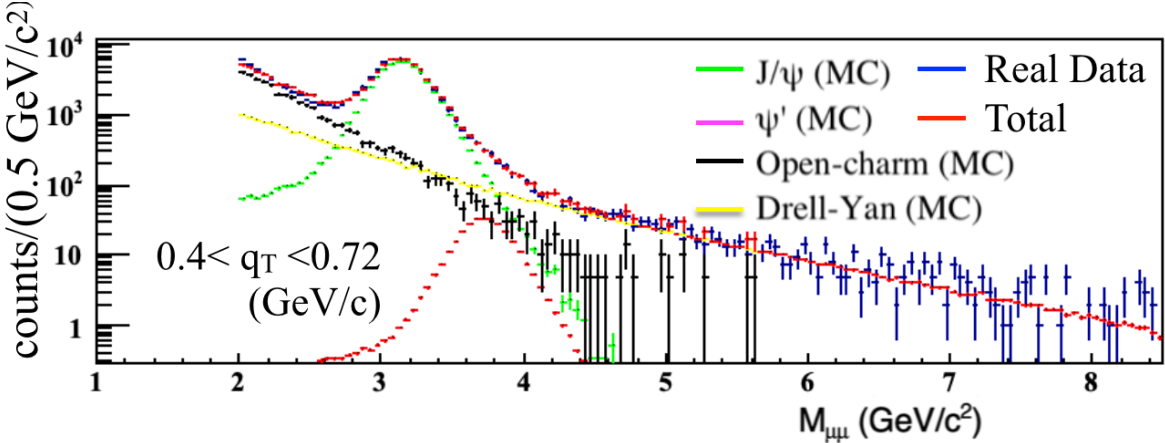


Figure 7.3: An example of the Monte-Carlo fit to real data in one  $q_T$  bin of the real data. This fit is used to determine the distribution of  $J/\Psi$  purity.

Mass range $\text{GeV}/c^2$	$J/\Psi$ Purity %
2.5-4.3	$79.7 \pm 2.9$
2.78-3.46	$88.9 \pm 2.0$
<b>2.87-3.38</b>	<b><math>91.3 \pm 1.5</math></b>
2.95-3.29	$92.9 \pm 1.0$
3.08-3.17	$94.0 \pm 1.0$

Table 7.1:  $J/\Psi$  purity as a function of the invariant mass range

Cuts	W07	W08	W09	W10	W11
$\mu^- \mu^+$ 2-8.5 $\text{GeV}/c^2$ with a common best primary vertex	1,573,372	1,572,255	1,620,593	1,683,263	2,598,485
Good Spills	1,298,306	1,223,877	1,333,335	1,374,620	1,901,071
$0 < x_\pi x_N < 1, -1 < x_F < 1$	1,298,278	1,223,851	1,333,307	1,374,599	1,901,033
$0.4 < q_T < 5 (\text{GeV}/c)$	1,121,908	1,056,835	1,151,253	1,187,125	1,641,463
Z Vertex within NH <sub>3</sub>	314,965	298,531	324,413	335,659	465,172
Vertex Radius < 1.9cm	308,278	292,114	317,985	328,658	455,580
$2.87 < M_{\mu\mu} < 3.38 (\text{GeV}/c^2)$	170,041	160,450	174,696	180,795	250,921

Table 7.2: Selected dimuon events for the first five data periods from the intermediate mass range analysis of 2015 COMPASS data

## 7.2 Binning

The analysis is determined as a function of the variables  $x_N$ ,  $x_\pi$ ,  $x_F$ ,  $q_T$  and  $M_{\mu\mu}$ . These are the same variables used to bin the high mass Drell-Yan analysis. The left-right asymmetry analysis is binned in each of the kinematic variables by requiring an equal amount of data per kinematic bin. The bin limits are also required to have a width of at least three times the resolution per variable. For this analysis there are enough events and the resolution per variable is good enough to have four kinematic bins. The bin limits are provided in Table 7.5 and the spectrometer resolutions are provided in Table 7.4.

Cuts	W12	W13	W14	W15	WAll	Remaining
$\mu^-\mu^+$ 2-8.5 GeV/c <sup>2</sup> with a common best primary vertex	1,932,425	1,680,706	1,094,525	640,095	14,395,719	100.00 %
Good Spills	1,659,030	1,314,489	982,131	616,734	11,703,593	81.3 %
$0 < x_\pi x_N < 1, -1 < x_F < 1$	1,658,996	1,314,470	982,125	616,720	11,703,379	81.3 %
$0.4 < q_T < 5$ (GeV/c)	1,432,115	1,134,223	846,897	532,045	10,103,864	70.2 %
Z Vertex within NH <sub>3</sub>	406,975	322,964	241,673	151,937	2,862,289	19.9 %
Vertex Radius < 1.9cm	398,610	316,149	236,019	148,834	2,802,227	19.5 %
$2.87 < M_{\mu\mu} < 3.38$ (GeV/c <sup>2</sup> )	219,110	173,701	129,346	81,808	1,540,868	10.7 %

Table 7.3: Selected dimuon events for the last four data periods and the total number of events from the intermediate mass range analysis of 2015 COMPASS data

The spectrometer resolution is determined from the Monte-Carlo data. The resolution is determined from the difference between the Monte-Carlo generated value and the reconstruction Monte-Carlo value. An example of this distribution is shown in Fig. 7.4 for the  $x_\pi$  variable. The distribution has a longer tail than a Gaussian distribution and for this reason a two Gaussian fit function is used to determine the distribution's width. The resolution is then determined as the width of the Gaussian with the larger amplitude, so-called leading order Gaussian. The actual spectrometer resolution is between the width of the leading order Gaussian and the RMS of the distribution. However the leading order Gaussian width is closer to the true resolution and is therefore used as the estimate for the spectrometer resolution.

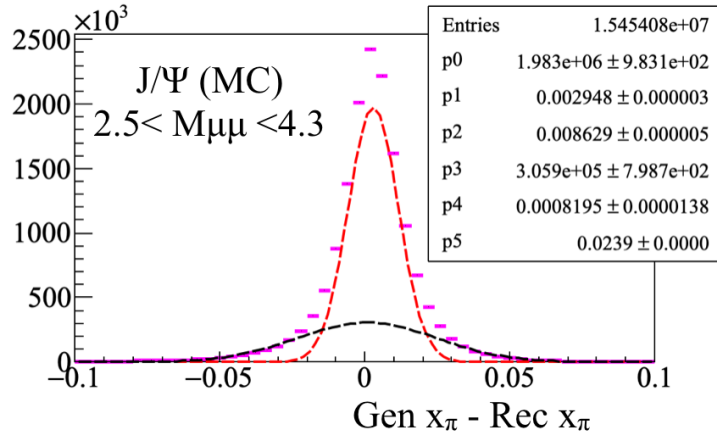


Figure 7.4: The distribution of generated  $x_N$  minus reconstructed  $x_N$ . The leading Gaussian width (red) is used to determine the resolution.

The distributions for the binning variables are shown in Fig. 7.5. This analysis is performed in the valence region for both the beam pion and target proton as the average  $x_\pi$  is about 0.09 and the average  $x_N$  is about 0.3. This means the dominant contribution to J/ $\Psi$  production is from quark-quark interactions. The average  $q_T$  value is below the minimum mass range of 2.87 GeV/c<sup>2</sup> for this analysis and therefore the

Variable	RMS	Leading Gaussian $\sigma$
$x_N$	0.01	0.006
$x_\pi$	0.0157	0.009
$x_F$	0.016	0.011
$q_T$	0.143	0.022

Table 7.4: COMPASS spectrometer resolutions in the intermediate mass range  $2.5\text{-}4.3\text{GeV}/c^2$

Variable	Lowest limit	Upper limit bin 1	Upper limit bin 2	Upper limit bin 3	Upper limit bin 4
$x_N$	0.0	0.062	0.083	0.11	1.0
$x_\pi$	0.0	0.21	0.28	0.38	1.0
$x_F$	-1.0	0.10	0.20	0.32	1.0
$q_T$ (GeV/c)	0.4	0.72	1.04	1.47	5.0
$M_{\mu\mu}$ (GeV/c $^2$ )	2.87	3.03	3.13	3.22	3.38

Table 7.5: The  $J/\Psi$  analysis bin limits for the four analysis bins

interpretation of this analysis assumes the TMD regime is valid.

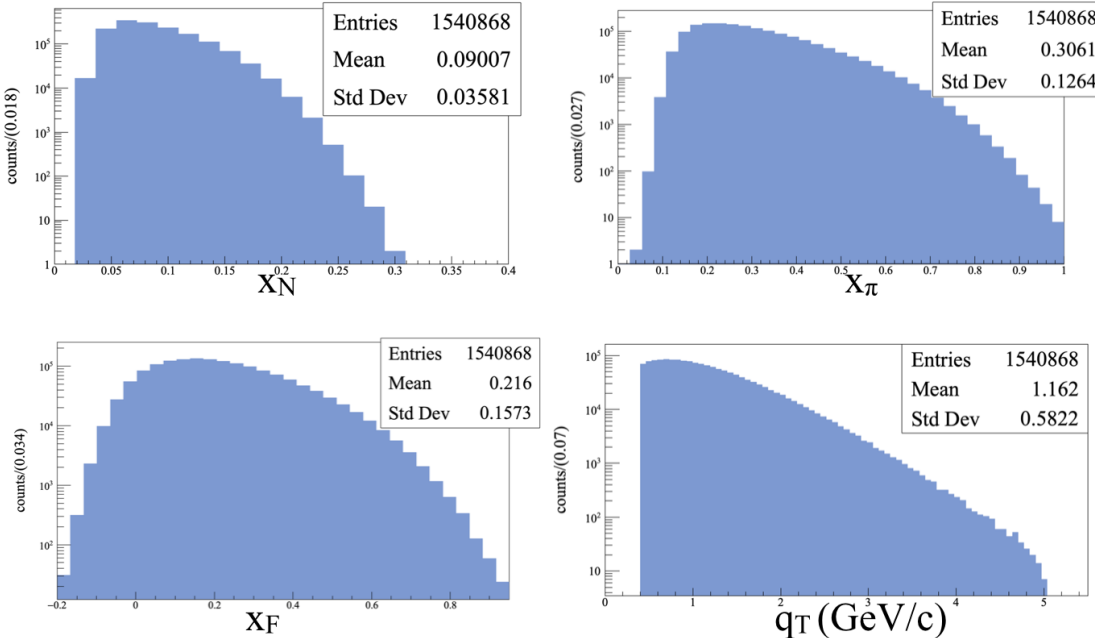


Figure 7.5: The binning variable distributions. The longitudinal momentum fractions  $x_N$  (top left) and  $x_\pi$  (top right) and the  $x_F$  (bottom left) and the virtual photon transverse momentum  $q_T$  (bottom right). These distributions are plotted from in the mass range  $2.87\text{-}3.38\text{ GeV}/c^2$ .

### 7.3 Asymmetry Extraction

The asymmetry extraction method used is the two-target geometric mean. This asymmetry method is described in detail in Secs 6.5- 6.5.1. The asymmetry is again defined as

$$A_{lr,2Targ} = \frac{1}{|S_T|} \frac{\sqrt[4]{N_{1,l}^{\uparrow} N_{1,l}^{\downarrow} N_{2,l}^{\uparrow} N_{2,l}^{\downarrow}} - \sqrt[4]{N_{1,r}^{\uparrow} N_{1,r}^{\downarrow} N_{2,r}^{\uparrow} N_{2,r}^{\downarrow}}}{\sqrt[4]{N_{1,l}^{\uparrow} N_{1,l}^{\downarrow} N_{2,l}^{\uparrow} N_{2,l}^{\downarrow}} + \sqrt[4]{N_{1,r}^{\uparrow} N_{1,r}^{\downarrow} N_{2,r}^{\uparrow} N_{2,r}^{\downarrow}}}, \quad (7.7)$$

where  $N$  represents the counts,  $l(r)$  denotes left(right), 1(2) denotes the target cell and  $\uparrow$  ( $\downarrow$ ) denotes the transverse polarization direction. The definitions of left and right are defined relative to the target spin as

$$\begin{aligned} \text{Left} : \hat{q}_T \cdot (\hat{S}_T \times \hat{P}_\pi) &> 0 \\ \text{Right} : \hat{q}_T \cdot (\hat{S}_T \times \hat{P}_\pi) &< 0, \end{aligned} \quad (7.8)$$

where  $\hat{q}_T$ ,  $\hat{S}_T$  and  $\hat{P}_\pi$  are unit vectors in the target reference frame for the virtual photon transverse momentum, the target spin and the beam pion momentum respectively. The advantage of this asymmetry method is that the acceptance from the upstream and downstream target cells cancel as was shown in Eq. 6.26. The statistical uncertainty for this asymmetry method can be written as

$$\delta A_{lr,2Targ} = \frac{1}{|S_T|} \frac{LR}{(L+R)^2} \sqrt{\sum_{c,p} \left( \frac{1}{N_{c,l}^p} + \frac{1}{N_{c,r}^p} \right)}, \quad (7.9)$$

where  $L = \sqrt[4]{N_{1,l}^{\uparrow} N_{1,l}^{\downarrow} N_{2,l}^{\uparrow} N_{2,l}^{\downarrow}}$  and  $R = \sqrt[4]{N_{1,r}^{\uparrow} N_{1,r}^{\downarrow} N_{2,r}^{\uparrow} N_{2,r}^{\downarrow}}$ . In the approximate case of equal statistical populations in each left-right direction and each target cell, the statistical uncertainty for the two-target geometric mean reduces to  $\frac{1}{|S_T|} \frac{1}{\sqrt{N}}$ , where  $N$  is the sum of all counts.

## 7.4 Systematic Studies

Similar tests as were performed for the high mass left-right asymmetry to determine the systematic error are also performed for the intermediate mass left-right asymmetry. For the full details on the previous tests see Sec 6.5.2. This section will give the results for systematic errors in the intermediate mass range and describe in detail the tests specific to this analysis. The overall systematic errors are determined by adding all non-zero systematic uncertainties in quadrature. The impact from each source of systematic error is summarized in Table. 7.7.

### 7.4.1 Period Compatibility (Time Dependence)

It is expected that the asymmetry calculation will vary in time due to statistical fluctuations. Fig. 7.6 shows the left-right asymmetry calculated for each period in time and Fig. 7.7 shows the left-right asymmetry time fluctuations for each bin in  $x_N$ . To quantify if the time fluctuations are greater than what is expected from

random statistical fluctuations, the pull distribution is checked for a larger width than one or a non-zero mean. More details on the pull distribution are given in Sec 6.5.2.

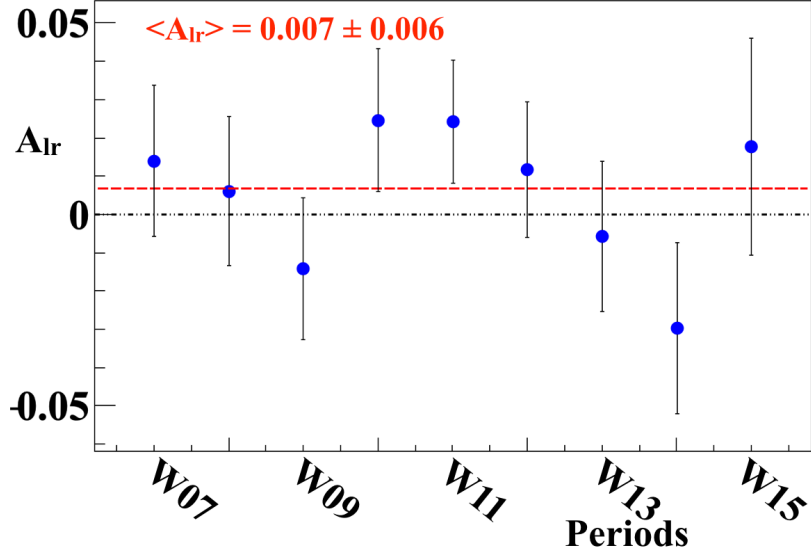


Figure 7.6: The left-right asymmetry in the  $J/\Psi$  mass region as a function of time. The red line is a constant fit and therefore shows the weighted averaged of the periods.

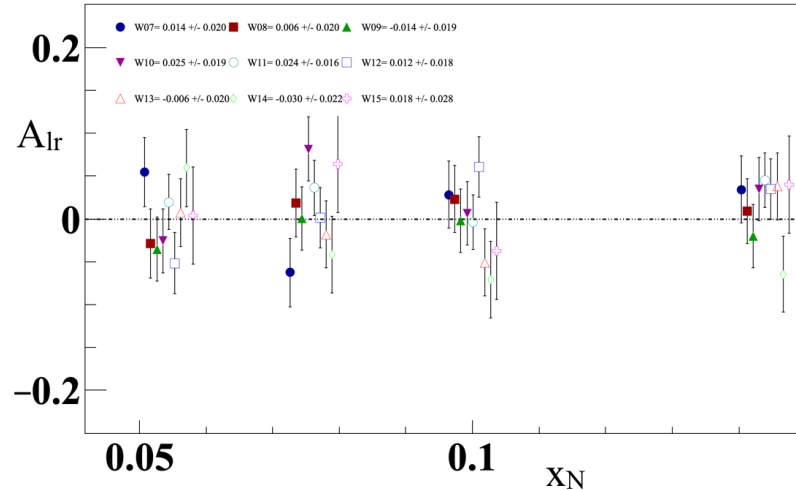


Figure 7.7: The left-right asymmetry time fluctuations in each bin of  $x_N$ .

The pull value is defined as

$$\Delta A_i = \frac{A_i - \langle A \rangle}{\sqrt{\sigma_{A_i}^2 - \sigma_{\langle A \rangle}^2}}, \quad (7.10)$$

where  $\langle A \rangle$  is the average asymmetry amplitude for the data set. The pull distribution is formed for each

kinematic variable in Fig. 7.8. For this analysis there are therefore 4 (number of bins)  $\times$  9 (number of periods) = 36 entries per pull distribution. The systematic error from period incompatibility is determined as

$$\frac{\sigma_{\text{systematic}}}{\sigma_{\text{statistical}}} = \sqrt{|\sigma_{\text{pull}}^2 - 1|} + \frac{\mu_{\text{pull}}}{2}, \quad (7.11)$$

where in this analysis the  $\sigma_{\text{pull}}^2$  and  $\mu_{\text{pull}}$  are determined as a weighted average of the mean and variance respectively from the pull distribution for each kinematic variable including the parameters from the integrated pull distribution. The fit values from each pull distribution give somewhat different estimates due to the errors associated with the fit. This is the reason the weighted average is performed to give the best estimate for the pull mean and standard deviation and therefore the most accurate systematic error calculation. The systematic error due to time incompatibility is determined to be 16% of the statistical error.

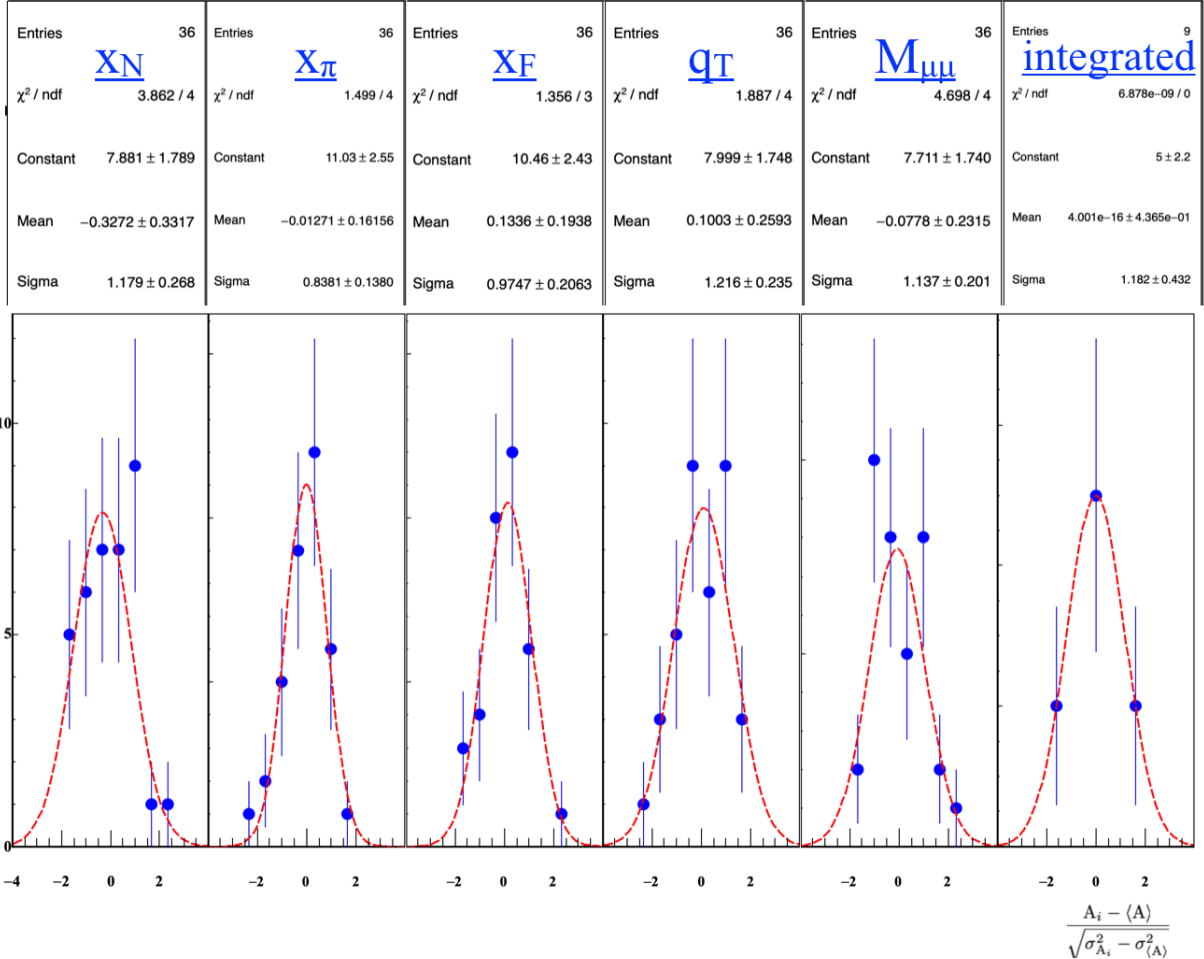


Figure 7.8: The uncorrelated pull distributions for each of the kinematical variables and a pull distribution from the integrated asymmetry from each time period.

### 7.4.2 Left/Right Event Migration

The left-right event migration systematic error is calculated the same as in Sec 6.5.2. The Monte-Carlo data used to determine the left-right event migration is described in Table 6.7. The effect of misidentified events as left when the event should be counted as a right event and vice-versa, dilutes the left-right asymmetry. It is as if there is an additional unpolarized contribution that dilutes the event sample.

The systematic error for left-right migration is derived in Appendix A.2 as

$$\delta A_{lr,systematic} = \gamma * A_{lr} + \gamma * \delta A_{lr}, \quad (7.12)$$

where  $\gamma$  is the fraction of misidentified left and right events.

As is clearly visible in Fig. 7.9, there is a band of higher misidentification rate at the border between left and right. For the  $J/\Psi$  mass region only about 3% of events were misidentified resulting in a systematic error of 4.4% of the statistical error.

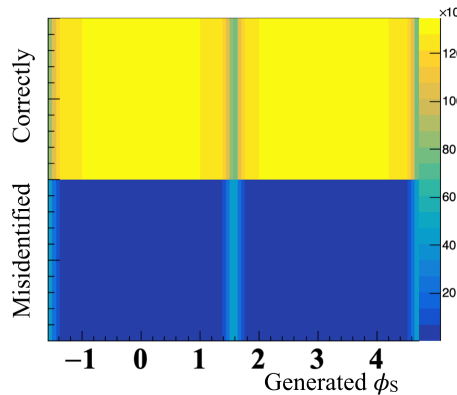


Figure 7.9: The left-right migration as a function of the generated  $\phi_S$  angle in the mass range 2.87-3.38.

### 7.4.3 $J/\Psi$ Purity

The systematic error due to a  $J/\Psi$  purity less than unity was discussed in Sec 7.1.1. The invariant mass range was chosen specifically such that the  $J/\Psi$  purity is 90% or higher to reduce the systematic error associated with impurities. The systematic error is derived in Appendix A.3 as

$$\frac{\sigma_{systematic}}{\sigma_{statistical}} = \frac{(1-p)}{p}. \quad (7.13)$$

Table 7.1 summarized the impurity as a function of the analysis mass range and the impurity in this analysis mass range is 91.3%. This corresponds to a systematic error of 9.5% of the statistical error.

#### 7.4.4 False Asymmetries

##### Acceptance From False Asymmetries

The acceptance fluctuations are determined from the false asymmetry defined as

$$A_{lr, False} = \frac{1}{|S_T|} \frac{\sqrt[4]{N_{1,r}^\uparrow N_{1,l}^\downarrow N_{2,l}^\uparrow N_{2,r}^\downarrow} - \sqrt[4]{N_{1,l}^\uparrow N_{1,r}^\downarrow N_{2,r}^\uparrow N_{2,l}^\downarrow}}{\sqrt[4]{N_{1,r}^\uparrow N_{1,l}^\downarrow N_{2,l}^\uparrow N_{2,r}^\downarrow} + \sqrt[4]{N_{1,l}^\uparrow N_{1,r}^\downarrow N_{2,r}^\uparrow N_{2,l}^\downarrow}} = \frac{1}{|S_T|} \frac{\alpha_{2Targ} - 1}{\alpha_{2Targ} + 1}. \quad (7.14)$$

More details for acceptance fluctuations are discussed in Sec. 6.5.1 and Sec. 6.5.1. The kinematic dependences of the acceptance ratio,  $\alpha_{2Targ}$ , are shown in Fig. 7.10. As Fig. 7.10 shows the acceptance is only slightly greater than unity even though it can be above 1 by more than a sigma. The systematic error associated with acceptance fluctuations is defined as

$$\delta A_{lr, systematic} = \frac{1}{|S_T|} \left( \frac{|\alpha_{2Targ} - 1|}{2} + \delta_{\frac{|\alpha_{2Targ} - 1|}{2}} \right), \quad (7.15)$$

where this expression is derived in Appendix A.1. The normalized kinematic dependence of the systematic error to the statistical error are shown in Fig. 7.11. The average systematic error due to acceptance is 23% of the statistical error.

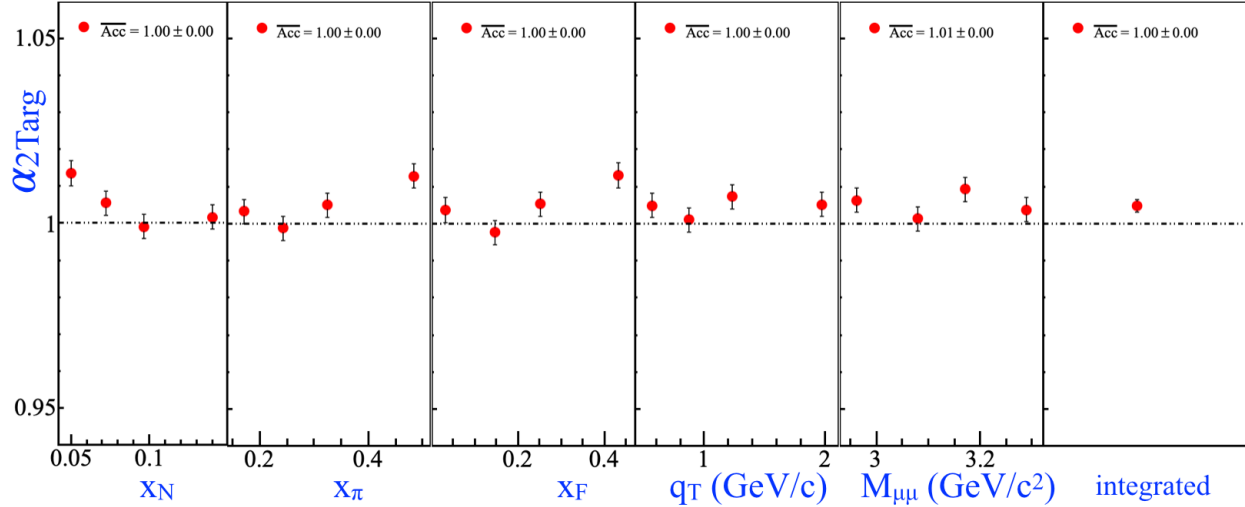


Figure 7.10: Acceptance fluctuations in each bin of the kinematic variables.

##### Further False Asymmetry Effects

Additional false asymmetries are analyzed to account for systematic errors which were not addressed directly. The false asymmetries are constructed in such a way that the cross-section and luminosity cancel out in

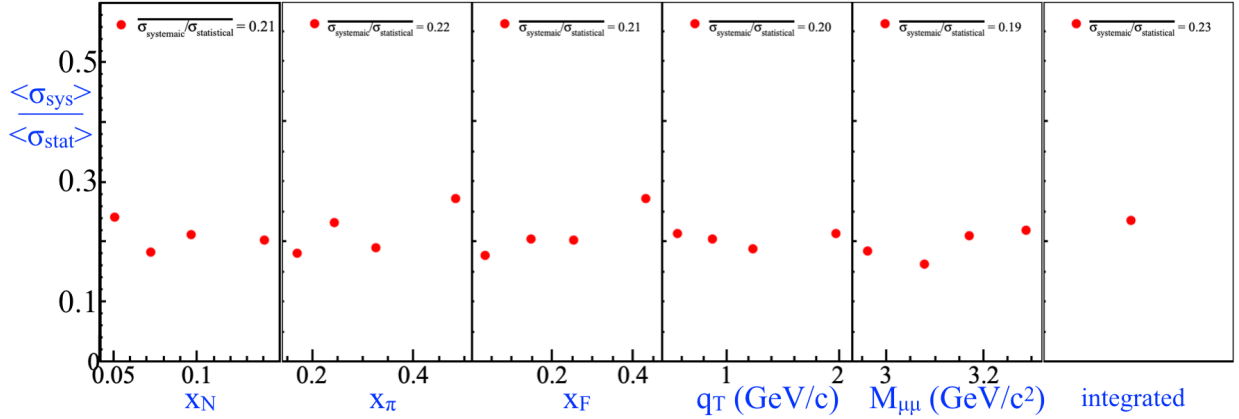


Figure 7.11: Systematic error divided by statistical error due to acceptance

the numerator and the denominator. Therefore these false asymmetries can only change in time due to acceptance effects or for some unknown reason. The false asymmetries constructed to study the intermediate mass analysis are described in the following enumerated list.

1. The false asymmetry used to determine the acceptance fluctuations, Eq. 7.14, is checked for compatibility and the uncorrelated pulls are shown in Fig. 7.12 along with the corresponding fit parameters and errors.
2. A false asymmetries using only the information from the upstream or the downstream target cell defined as

$$A_{lr,FA} = \frac{1}{|ST|} \frac{\sqrt{N_l^\uparrow N_r^\downarrow} - \sqrt{N_r^\uparrow N_l^\downarrow}}{\sqrt{N_l^\uparrow N_r^\downarrow} + \sqrt{N_r^\uparrow N_l^\downarrow}}. \quad (7.16)$$

The pulls for the upstream target cell are shown in Fig. 7.13 and the pulls for the downstream target cell are shown in Fig. 7.14.

The systematic error from each false asymmetry is determined using the Eq. 7.11. The uncorrelated pulls have only  $4$  (number of bins)  $\times$   $9$  (number of periods)  $= 36$  entries which results in large errors on the Gaussian fit results. In an attempt to correct for this and to take into account the fit errors, a weighted average of the mean and standard deviation is made using the fit parameters and fit errors as weights from the uncorrelated pull distributions. This is the same technique as was used to determine the systematic error from fluctuations in time. The resulting weighted mean and weighted standard deviation are then used to

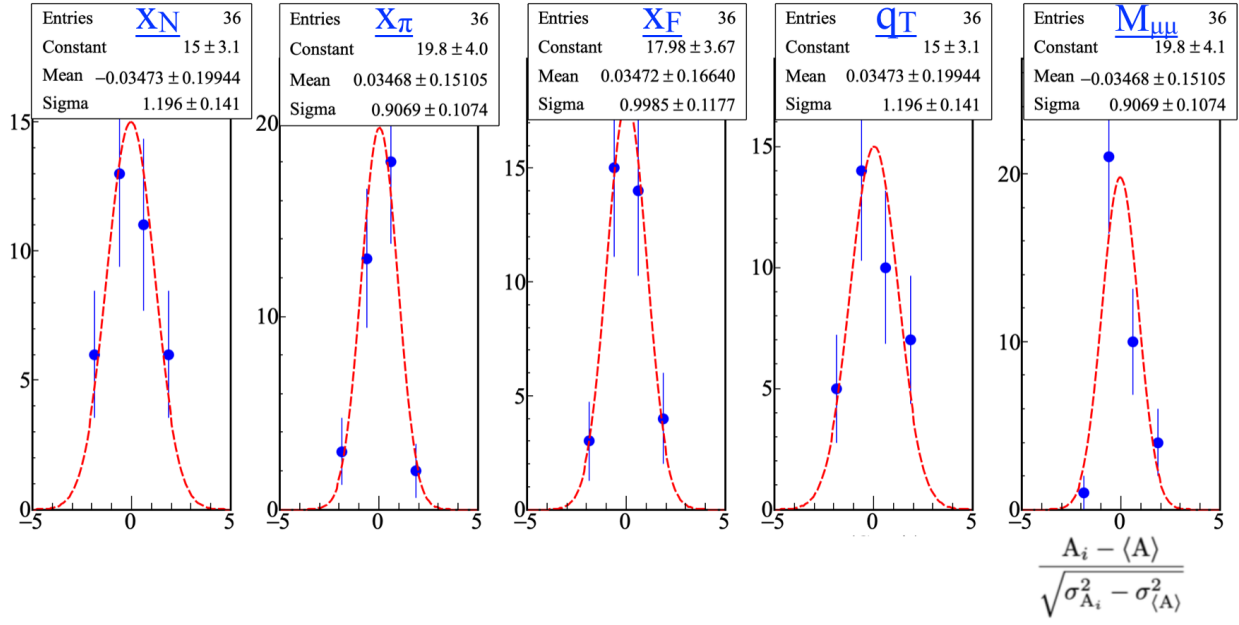


Figure 7.12: Pull distribution for a nearly acceptance free two-target false geometric mean asymmetry

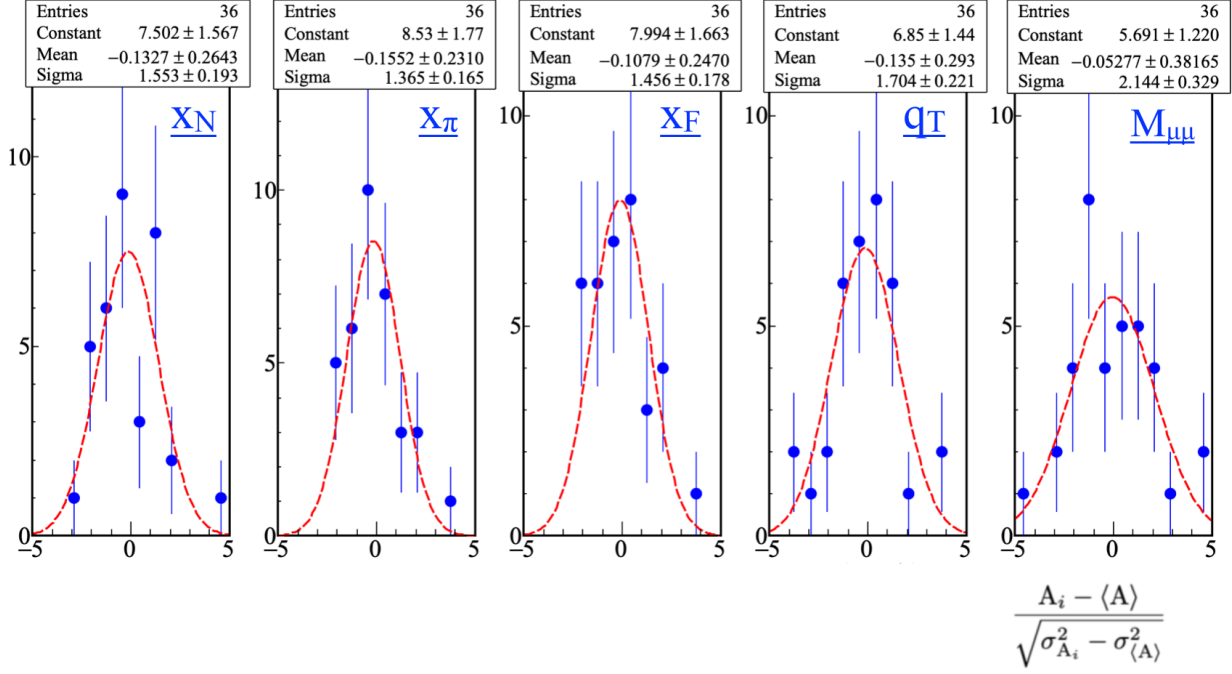


Figure 7.13: Pull distributions from the false asymmetry in the upstream target cell

calculate the systematic error. A summary of the systematic error from each false asymmetry is shown in Table 7.6. The systematic error due to additional factors is chosen as the largest systematic error from

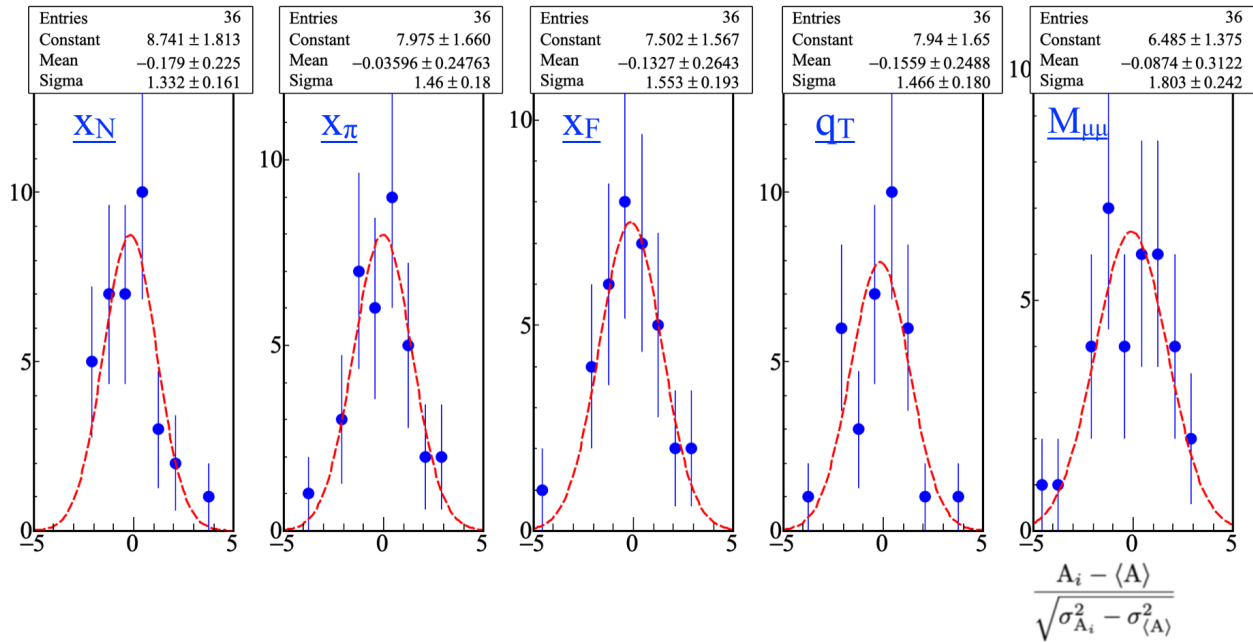


Figure 7.14: Pull distributions from the false asymmetry in the downstream target cell

Table 7.6.

Systematic error	$\langle \sigma_{\text{systematic}} / \sigma_{\text{statistical}} \rangle$
Two target acceptance estimation	0.19
Target Cell 1	1.20
Target Cell 2	1.11

Table 7.6: Summary of systematic error impacts from false asymmetries changes in time. The maximum systematic error is chosen as the systematic error.

#### 7.4.5 Total Systematics

The total systematic error is determined by adding all systematic errors in quadrature as

$$\left\langle \frac{\sigma_{\text{systematic}}}{\sigma_{\text{statistical}}} \right\rangle = \sqrt{\sum_i^{\text{all systematic}} \left\langle \frac{\sigma_{\text{systematic},i}^2}{\sigma_{\text{statistical}}^2} \right\rangle}, \quad (7.17)$$

where all the systematic effects considered are summarized in Table. 7.7. For reference the integrated left-right asymmetry is  $\langle A_{lr} \rangle = 0.0062$  and the integrated statistical error is  $\langle \sigma_{\text{statistical}} \rangle = 0.0065$ .

The integrated left-right asymmetry result and systematic error band is shown in Fig. 7.15 and the kinematic dependencies are shown in Fig. 7.16. Similarly to the left-right asymmetry for the high mass

Systematic error	$\langle \sigma_{\text{systematic}} / \sigma_{\text{statistical}} \rangle$	$\langle \sigma_{\text{systematic}} \rangle$
Period compatibility	0.16	0.001
Left-Right migration	0.044	0.0003
J/ $\Psi$ purity	0.095	0.0006
Target Polarization	0.05	0.0003
Dilution Factor	0.05	0.0003
Acceptance fluctuation	0.23	0.001
False asymmetry	1.2	0.008
<b>Total</b>	<b>1.24</b>	<b>0.008</b>

Table 7.7: Summary of systematic error impacts to the integrated asymmetry

Drell-Yan analysis, the integrated left-right asymmetry is 1 sigma above zero. The asymmetry shows a weak inverse dependence on  $x_F$  indicating the asymmetry could be related to quark distributions in the proton target. This can also be seen in the  $x_N$  dependence which is most significant in the highest  $x_N$  bin. Although the left-right asymmetry is model independent, it was discussed that the Sivers function could be the cause of for a non-zero left-right asymmetry. A positive left-right asymmetry would be consistent with the sign change hypothesis.

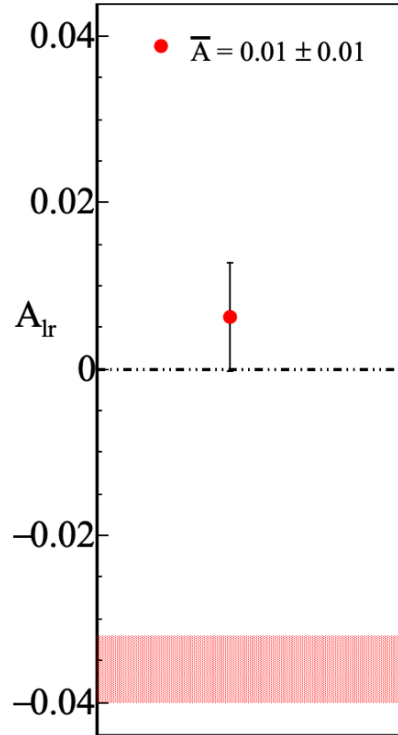


Figure 7.15: The integrated left-right asymmetry from the mass range 2.87-3.38 GeV/ $c^2$ . The systematic error bands are shown in red at the bottom of the plot.

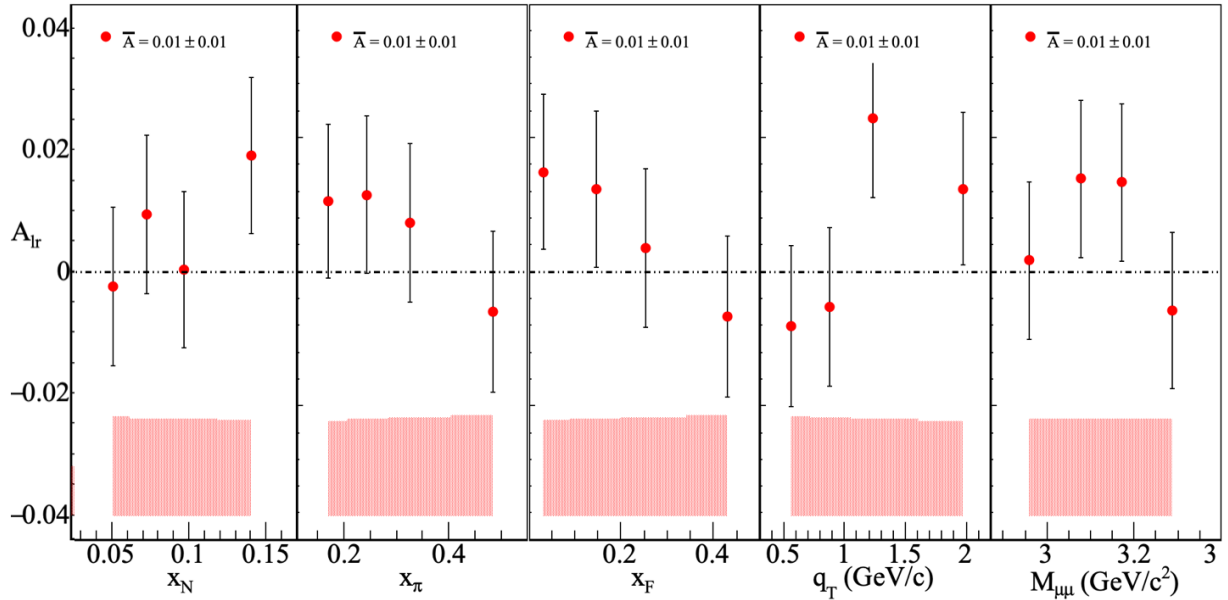


Figure 7.16: The kinematic dependencies of the left-right asymmetry from the mass range 2.87–3.38 GeV/ $c^2$ .

The Anselmino group derived an expression for the  $A_N$  asymmetry from J/ $\Psi$  production as [62]

$$A_N^{J\Psi} \propto f_{\bar{q}/H_a}(x_a, k_{aT}) \frac{k_{bT}}{M_b} \otimes f_{1T}^{\perp q}(x_b, k_{bT}), \quad (7.18)$$

and made predictions for the  $A_N$  asymmetry as a function of  $x_N$  and  $q_T$  shown in Fig. 7.17. As derived in Sec 2.5.2,  $A_N = \frac{\pi A_{lr}}{2}$ . More details are given in Sec 2.5.4, but their calculation assumed the dominant contribution to J/ $\Psi$  production is from quark-quark annihilation. Fig. 7.18 shows the results determined at COMPASS for the  $A_N$  asymmetry determined by modifying the left-right results in Fig. 7.16. The maximum  $A_N$  asymmetry, determined at COMPASS, is less than 0.05 which when comparing to the prediction in Fig. 7.17 is 2 sigma less than the prediction.

The incompatibility of the theory prediction, Fig. 7.17, and the results determined at COMPASS, Fig. 7.18, can be due to either a Siver function much lower than expected or gluon-gluon fusion contamination. At the present moment, the Siver's function from gluon-gluon fusion is not well known and therefore could be small or negative. Fig. 7.19 shows results for J/ $\Psi$  production from quark-quark annihilation and gluon-gluon fusion using the color evaporation model [58]. To determine the expected J/ $\Psi$  contribution from gluon-gluon fusion and quark-quark annihilation at COMPASS the results in Fig. 7.19 are weighted with the COMPASS  $x_F$  distribution in the intermediate mass range. The determined ratio of J/ $\Psi$  production from quark-quark annihilation to gluon-gluon fusion at COMPASS is 0.8. It is therefore not ruled out that

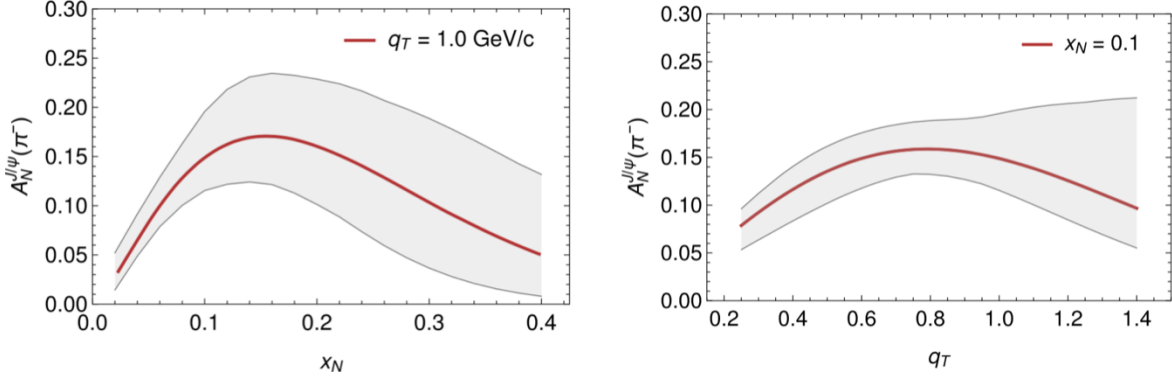


Figure 7.17: Predictions for the analyzing power,  $A_N$ , from  $J/\Psi$  production at COMPASS as a function of  $x_N$  and  $q_T$ . This image was taken from [62].

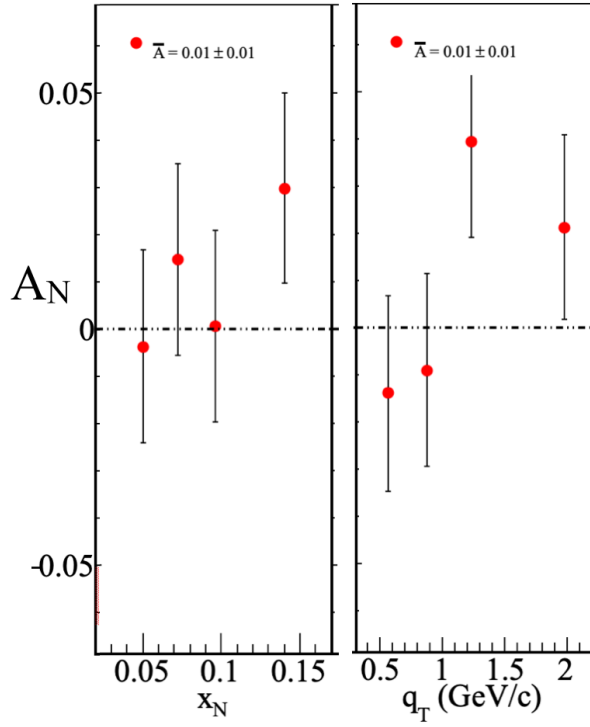


Figure 7.18: The analyzing power at COMPASS determined by modifying the left-right asymmetry as a function of  $x_N$  and  $q_T$  to be compared with the predictions in Fig. 7.17.

the results in Fig. 7.18 are reduced compared to the predictions in Fig. 7.17 due to gluon-gluon fusion.

Fig. 7.20 shows the Sivers amplitude determined from the left-right asymmetry along with theory curves for different percentages of gluon fusion as a contamination. It is assumed that the gluon Sivers function is zero. A short list of the possibilities which can be the cause for this discrepancy between data and theory are that the  $J\Psi$  model is incorrect, the pion gluon density is higher than expected or that the SIDIS Sivers function is lower than expected.

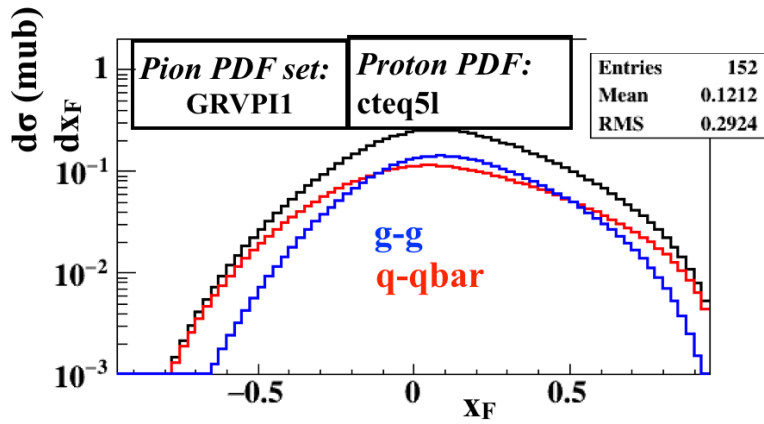


Figure 7.19:  $\text{J}/\Psi$  production cross-section from gluon-gluon fusion (blue) and quark-quark annihilation (red) and the sum (black) as a function of  $x_F$ . This plot is made assuming the color evaporation model [58].

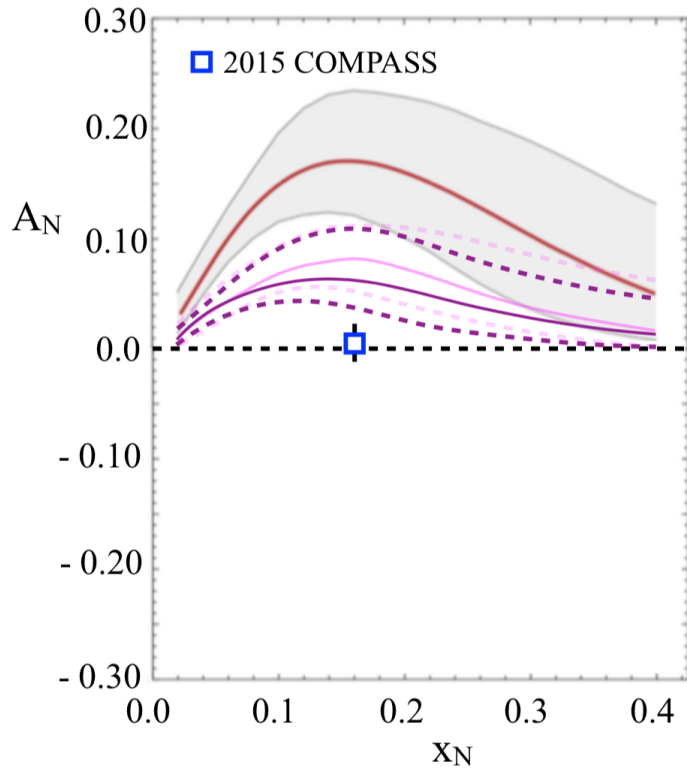


Figure 7.20: The Sivers amplitude determined from the left-right asymmetry with theory curves for no gluon contamination (gray), 51% gluon fusion (magenta) and 63% gluon fusion (purple).

# Chapter 8

## Conclusion

Mapping out the three dimensional momentum structure of the nucleon is a recent and exciting field. Both theoretical work and experiments have been contributing to the transverse momentum dependent parton distribution functions. This dissertation presents results from dimuon events that originate from a  $190\text{ GeV}/c$  negatively charged pion beam on a transversely polarized proton target. The measurements from this thesis expand the knowledge of parton distributions. Specifically the measurements in this thesis add knowledge to the transverse momentum dependent parton distribution functions. The measurements in the high invariant mass region, above  $4.3\text{ GeV}/c^2$ , constitutes the world's first ever Drell-Yan data from a transversely polarized target. The COMPASS spectrometer setup is unique in that it can perform spin-dependent measurements for Drell-Yan and semi-inclusive deep inelastic scattering in the same kinematic regions.

The analysis techniques in this thesis are constructed to measure azimuthal asymmetry amplitudes where the spectrometer acceptance cancels and therefore does not effect the measurement. Several analysis techniques are used and all find the Sivers asymmetry amplitude from Drell-Yan production to be approximately 1 sigma above zero. This result is consistent with the sign change hypothesis between semi-inclusive deep inelastic scattering and Drell-Yan production. At the same time, the statistical error bars are too large to distinguish between the major models of the Sivers function. For this reason the COMPASS collaboration performed another Drell-Yan data taking campaign in 2018 with similar data taking conditions. The results from the 2018 measurement are expected in 2019.

# References

- [1] E. Rutherford. The scattering of alpha and beta particles by matter and the structure of the atom. *Phil. Mag. Ser. 6*, 21:669–688, 1911. doi: 10.1080/14786440508637080.
- [2] Murray Gell-Mann. A Schematic Model of Baryons and Mesons. *Phys. Lett.*, 8:214–215, 1964. doi: 10.1016/S0031-9163(64)92001-3.
- [3] G. Zweig. An SU(3) model for strong interaction symmetry and its breaking. Version 2, 1964.
- [4] Richard P. Feynman. Very High-Energy Collisions of Hadrons. *Phys. Rev. Lett.*, 23:1415–1417, Dec 1969. doi: 10.1103/PhysRevLett.23.1415. URL <https://link.aps.org/doi/10.1103/PhysRevLett.23.1415>.
- [5] Dennis W. Sivers. Single Spin Production Asymmetries from the Hard Scattering of Point-Like Constituents. *Phys. Rev.*, D41:83, 1990. doi: 10.1103/PhysRevD.41.83.
- [6] R. D. Klem, J. E. Bowers, H. W. Courant, H. Kagan, M. L. Marshak, E. A. Peterson, K. Ruddick, W. H. Dragoset, and J. B. Roberts. Measurement of Asymmetries of Inclusive Pion Production in Proton-Proton Interactions at 6 and 11.8 GeV/c. *Phys. Rev. Lett.*, 36:929–931, Apr 1976. doi: 10.1103/PhysRevLett.36.929. URL <https://link.aps.org/doi/10.1103/PhysRevLett.36.929>.
- [7] Vincenzo Barone, Alessandro Drago, and Philip G. Ratcliffe. Transverse polarisation of quarks in hadrons. *Phys. Rept.*, 359:1–168, 2002. doi: 10.1016/S0370-1573(01)00051-5.
- [8] Elliott D. Bloom et al. High-Energy Inelastic e p Scattering at 6-Degrees and 10-Degrees. *Phys. Rev. Lett.*, 23:930–934, 1969. doi: 10.1103/PhysRevLett.23.930.
- [9] Martin Breidenbach, Jerome I. Friedman, Henry W. Kendall, Elliott D. Bloom, D. H. Coward, H. C. DeStaeler, J. Drees, Luke W. Mo, and Richard E. Taylor. Observed Behavior of Highly Inelastic electron-Proton Scattering. *Phys. Rev. Lett.*, 23:935–939, 1969. doi: 10.1103/PhysRevLett.23.935.
- [10] J. D. Bjorken and Emmanuel A. Paschos. Inelastic Electron Proton and gamma Proton Scattering, and the Structure of the Nucleon. *Phys. Rev.*, 185:1975–1982, 1969. doi: 10.1103/PhysRev.185.1975.
- [11] M. Tanabashi et al. Review of Particle Physics. *Phys. Rev.*, D98(3):030001, 2018. doi: 10.1103/PhysRevD.98.030001.
- [12] P. J. Mulders and R. D. Tangerman. The Complete tree level result up to order  $1/Q$  for polarized deep inelastic leptonproduction. *Nucl. Phys.*, B461:197–237, 1996. doi: 10.1016/S0550-3213(96)00648-7, 10.1016/0550-3213(95)00632-X. [Erratum: Nucl. Phys.B484,538(1997)].
- [13] Daniel Boer and P. J. Mulders. Time reversal odd distribution functions in leptonproduction. *Phys. Rev.*, D57:5780–5786, 1998. doi: 10.1103/PhysRevD.57.5780.
- [14] Alessandro Bacchetta, Markus Diehl, Klaus Goeke, Andreas Metz, Piet J. Mulders, and Marc Schlegel. Semi-inclusive deep inelastic scattering at small transverse momentum. *JHEP*, 02:093, 2007. doi: 10.1088/1126-6708/2007/02/093.

- [15] Juan Rojo et. al. The PDF4LHC report on PDFs and LHC data: results from Run I and preparation for Run II. *Journal of Physics G: Nuclear and Particle Physics*, 42(10):103103, sep 2015. doi: 10.1088/0954-3899/42/10/103103. URL <https://doi.org/10.1088%2F0954-3899%2F42%2F10%2F103103>.
- [16] B. Adeva, et al. (SMC collaboration). The Spin dependent structure function  $g(1)(x)$  of the proton from polarized deep inelastic muon scattering. *Phys. Lett.*, B412:414–424, 1997. doi: 10.1016/S0370-2693(97)01106-4.
- [17] A. Airapetian, et al. (HERMES collaboration). Flavor decomposition of the sea-quark helicity distributions in the nucleon from semiinclusive deep inelastic scattering. *Phys. Rev. Lett.*, 92:012005, Jan 2004. doi: 10.1103/PhysRevLett.92.012005. URL <https://link.aps.org/doi/10.1103/PhysRevLett.92.012005>.
- [18] A. I. Savin, et al. (COMPASS collaboration). COMPASS results on the nucleon spin structure. *Nucl. Phys. Proc. Suppl.*, 219-220:94–101, 2011. doi: 10.1016/j.nuclphysbps.2011.11.001.
- [19] L. A. Harland-Lang, A. D. Martin, P. Motylinski, and R. S. Thorne. The impact of the final HERA combined data on PDFs obtained from a global fit. *Eur. Phys. J.*, C76(4):186, 2016. doi: 10.1140/epjc/s10052-016-4020-1.
- [20] I. Abt, A. M. Cooper-Sarkar, B. Foster, V. Myronenko, K. Wichmann, and M. Wing. Study of HERA ep data at low  $Q^2$  and low  $x_{Bj}$  and the need for higher-twist corrections to standard perturbative QCD fits. *Phys. Rev.*, D94(3):034032, 2016. doi: 10.1103/PhysRevD.94.034032.
- [21] Emanuele R. Nocera, Richard D. Ball, Stefano Forte, Giovanni Ridolfi, and Juan Rojo. A first unbiased global determination of polarized PDFs and their uncertainties. *Nucl. Phys.*, B887:276–308, 2014. doi: 10.1016/j.nuclphysb.2014.08.008.
- [22] M. Hirai and S. Kumano. Determination of gluon polarization from deep inelastic scattering and collider data. *Nucl. Phys.*, B813:106–122, 2009. doi: 10.1016/j.nuclphysb.2008.12.026.
- [23] C. G. Callan and David J. Gross. High-Energy Electroproduction and the Constitution of the Electric Current. *Phys. Rev. Lett.*, 22:156–159, Jan 1969. doi: 10.1103/PhysRevLett.22.156. URL <https://link.aps.org/doi/10.1103/PhysRevLett.22.156>.
- [24] R. Heitz. COMPASS Measurements of Asymmetry Amplitudes in the Drell-Yan Process Observed from Scattering Pions off a Transversely Polarised Proton Target. EPS Conference on High Energy Physics, July 12-18, 2017. URL [https://wwwcompass.cern.ch/compass/publications/talks/t2017/Heitz\\_QCD\\_hadronic\\_physics\\_HEP2017.pdf](https://wwwcompass.cern.ch/compass/publications/talks/t2017/Heitz_QCD_hadronic_physics_HEP2017.pdf).
- [25] Stanley J. Brodsky, Dae Sung Hwang, and Ivan Schmidt. Final state interactions and single spin asymmetries in semiinclusive deep inelastic scattering. *Phys. Lett.*, B530:99–107, 2002. doi: 10.1016/S0370-2693(02)01320-5.
- [26] Stanley J. Brodsky, Dae Sung Hwang, and Ivan Schmidt. Initial state interactions and single spin asymmetries in Drell-Yan processes. *Nucl. Phys.*, B642:344–356, 2002. doi: 10.1016/S0550-3213(02)00617-X.
- [27] John C. Collins. Leading twist single transverse-spin asymmetries: Drell-Yan and deep inelastic scattering. *Phys. Lett.*, B536:43–48, 2002. doi: 10.1016/S0370-2693(02)01819-1.
- [28] M. Alekseev, et al. (COMPASS collaboration). Collins and Sivers asymmetries for pions and kaons in muon-deuteron DIS. *Phys. Lett.*, B673:127–135, 2009. doi: 10.1016/j.physletb.2009.01.060.
- [29] A. Airapetian, et al. (HERMES collaboration). Observation of the Naive-T-odd Sivers Effect in Deep-Inelastic Scattering. *Phys. Rev. Lett.*, 103:152002, 2009. doi: 10.1103/PhysRevLett.103.152002.
- [30] M. Anselmino, M. Boglione, and S. Melis. Strategy towards the extraction of the Sivers function with transverse momentum dependent evolution. *Phys. Rev. D*, 86:014028, Jul 2012. doi: 10.1103/PhysRevD.86.014028. URL <https://link.aps.org/doi/10.1103/PhysRevD.86.014028>.

- [31] C. Adolph, et al. (COMPASS collaboration). Measurement of azimuthal hadron asymmetries in semi-inclusive deep inelastic scattering off unpolarised nucleons. *Nucl. Phys.*, B886:1046–1077, 2014. doi: 10.1016/j.nuclphysb.2014.07.019.
- [32] A. Airapetian, et al. (HERMES collaboration). Single-spin asymmetries in semi-inclusive deep-inelastic scattering on a transversely polarized hydrogen target. *Phys. Rev. Lett.*, 94:012002, 2005. doi: 10.1103/PhysRevLett.94.012002.
- [33] A. Airapetian, et al. (HERMES collaboration). Effects of transversity in deep-inelastic scattering by polarized protons. *Phys. Lett.*, B693:11–16, 2010. doi: 10.1016/j.physletb.2010.08.012.
- [34] S. E. Ageev, et al. (COMPASS collaboration). A New measurement of the Collins and Sivers asymmetries on a transversely polarised deuteron target. *Nucl. Phys.*, B765:31–70, 2007. doi: 10.1016/j.nuclphysb.2006.10.027.
- [35] G. M. Alekseev, et al (COMPASS collaboration). Measurement of the Collins and Sivers asymmetries on transversely polarised protons. *Phys. Lett.*, B692:240–246, 2010. doi: 10.1016/j.physletb.2010.08.001.
- [36] C. Adolph, et al (COMPASS collaboration). Experimental investigation of transverse spin asymmetries in muon-p SIDIS processes: Collins asymmetries. *Phys. Lett.*, B717:376–382, 2012. doi: 10.1016/j.physletb.2012.09.055.
- [37] C. Adolph, et al. (COMPASS collaboration). Collins and Sivers asymmetries in muonproduction of pions and kaons off transversely polarised protons. *Phys. Lett.*, B744:250–259, 2015. doi: 10.1016/j.physletb.2015.03.056.
- [38] X. Qian, et. al. (Jefferson Lab Hall A). Single Spin Asymmetries in Charged Pion Production from Semi-Inclusive Deep Inelastic Scattering on a Transversely Polarized  ${}^3\text{He}$  Target at  $Q^2 = 1.4 - 2.7 \text{ GeV}^2$ . *Phys. Rev. Lett.*, 107:072003, Aug 2011. doi: 10.1103/PhysRevLett.107.072003. URL <https://link.aps.org/doi/10.1103/PhysRevLett.107.072003>.
- [39] K. Abe, et al. (Belle). Measurement of azimuthal asymmetries in inclusive production of hadron pairs in  $e^+ e^-$  annihilation at Belle. *Phys. Rev. Lett.*, 96:232002, 2006. doi: 10.1103/PhysRevLett.96.232002.
- [40] R. Seidl, et al. (Belle). Measurement of Azimuthal Asymmetries in Inclusive Production of Hadron Pairs in  $e^+ e^-$  Annihilation at  $s^{**}(1/2) = 10.58\text{-GeV}$ . *Phys. Rev.*, D78:032011, 2008. doi: 10.1103/PhysRevD.78.032011, 10.1103/PhysRevD.86.039905. [Erratum: *Phys. Rev.*D86,039905(2012)].
- [41] J. P. Lees, et al. (BaBar). Measurement of Collins asymmetries in inclusive production of charged pion pairs in  $e^+ e^-$  annihilation at BABAR. *Phys. Rev.*, D90(5):052003, 2014. doi: 10.1103/PhysRevD.90.052003.
- [42] M. Anselmino, M. Boglione, U. D'Alesio, S. Melis, F. Murgia, and A. Prokudin. Simultaneous extraction of transversity and Collins functions from new semi-inclusive deep inelastic scattering and  $e^+ e^-$  data. *Phys. Rev. D*, 87:094019, May 2013. doi: 10.1103/PhysRevD.87.094019. URL <https://link.aps.org/doi/10.1103/PhysRevD.87.094019>.
- [43] S. Arnold, A. Metz, and M. Schlegel. Dilepton production from polarized hadron hadron collisions. *Phys. Rev.*, D79:034005, 2009. doi: 10.1103/PhysRevD.79.034005.
- [44] A. Kotzinian. Description of polarized  $\pi^- + N$  Drell-Yan processes, 2010. URL [http://wwwcompass.cern.ch/compass/notes\\_public/2010-2.pdf](http://wwwcompass.cern.ch/compass/notes_public/2010-2.pdf).
- [45] L. Adamczyk, et. al. (STAR collaboration). Measurement of the Transverse Single-Spin Asymmetry in  $p^\uparrow + p \rightarrow W^\pm/Z^0$  at RHIC. *Phys. Rev. Lett.*, 116:132301, Apr 2016. doi: 10.1103/PhysRevLett.116.132301. URL <https://link.aps.org/doi/10.1103/PhysRevLett.116.132301>.
- [46] Miguel G. Echevarria, Ahmad Idilbi, Zhong-Bo Kang, and Ivan Vitev. QCD evolution of the Sivers asymmetry. *Phys. Rev. D*, 89:074013, Apr 2014. doi: 10.1103/PhysRevD.89.074013. URL <https://link.aps.org/doi/10.1103/PhysRevD.89.074013>.

- [47] Zhong-Bo Kang and Jian-Wei Qiu. Testing the Time-Reversal Modified Universality of the Sivers Function. *Phys. Rev. Lett.*, 103:172001, Oct 2009. doi: 10.1103/PhysRevLett.103.172001. URL <https://link.aps.org/doi/10.1103/PhysRevLett.103.172001>.
- [48] Allgower et. al. Measurement of analyzing powers of  $\pi^+$  and  $\pi^-$  produced on a hydrogen and a carbon target with a 22 – GeV/c incident polarized proton beam. *Phys. Rev. D*, 65:092008, May 2002. doi: 10.1103/PhysRevD.65.092008. URL <https://link.aps.org/doi/10.1103/PhysRevD.65.092008>.
- [49] D.L. Adams et. al. Comparison of spin asymmetries and cross sections in  $\pi^0$  production by 200 gev polarized antiprotons and protons. *Physics Letters B*, 261(1):201 – 206, 1991. ISSN 0370-2693. doi: [https://doi.org/10.1016/0370-2693\(91\)91351-U](https://doi.org/10.1016/0370-2693(91)91351-U). URL <http://www.sciencedirect.com/science/article/pii/037026939191351U>.
- [50] D.L. Adams et. al. Analyzing power in inclusive  $\pi^+$  and  $\pi^-$  production at high xf with a 200 gev polarized proton beam. *Physics Letters B*, 264(3):462 – 466, 1991. ISSN 0370-2693. doi: [https://doi.org/10.1016/0370-2693\(91\)90378-4](https://doi.org/10.1016/0370-2693(91)90378-4). URL <http://www.sciencedirect.com/science/article/pii/0370269391903784>.
- [51] Arsene et. al. (BRAHMS collaboration). Single-Transverse-Spin Asymmetries of Identified Charged Hadrons in Polarized  $pp$  Collisions at  $\sqrt{s} = 62.4$  GeV. *Phys. Rev. Lett.*, 101:042001, Jul 2008. doi: 10.1103/PhysRevLett.101.042001. URL <https://link.aps.org/doi/10.1103/PhysRevLett.101.042001>.
- [52] A. M. Kotzinian and P. J. Mulders. Longitudinal quark polarization in transversely polarized nucleons. *Phys. Rev.*, D54:1229–1232, 1996. doi: 10.1103/PhysRevD.54.1229.
- [53] A. M. Kotzinian and P. J. Mulders. Probing transverse quark polarization via azimuthal asymmetries in lepto-production. *Phys. Lett.*, B406:373–380, 1997. doi: 10.1016/S0370-2693(97)00708-9.
- [54] A. V. Efremov, K. Goeke, S. Menzel, A. Metz, and P. Schweitzer. Sivers effect in semi-inclusive DIS and in the Drell-Yan process. *Phys. Lett.*, B612:233–244, 2005. doi: 10.1016/j.physletb.2005.03.010.
- [55] A. N. Sissakian, O. Yu. Shevchenko, A. P. Nagaytsev, and O. N. Ivanov. Direct extraction of transversity and its accompanying T-odd distribution from the unpolarized and single-polarized Drell-Yan process. *Phys. Rev.*, D72:054027, 2005. doi: 10.1103/PhysRevD.72.054027.
- [56] A. Sissakian, O. Shevchenko, A. Nagaytsev, O. Denisov, and O. Ivanov. Transversity and its accompanying T-odd distribution from Drell-Yan processes with pion-proton collisions. *Eur. Phys. J.*, C46: 147–150, 2006. doi: 10.1140/epjc/s2006-02490-1.
- [57] Zhengxian Wang, Xiaoyu Wang, and Zhun Lu. Boer-Mulders function of pion meson and  $q_T$ -weighted  $\cos 2\phi$  asymmetry in the unpolarized  $\pi^- p$  Drell-Yan at COMPASS. *Phys. Rev.*, D95(9):094004, 2017. doi: 10.1103/PhysRevD.95.094004.
- [58] R. Vogt.  $J/\Psi$  production and suppression. *Physics Reports*, 310(4):197 – 260, 1999. ISSN 0370-1573. doi: [https://doi.org/10.1016/S0370-1573\(98\)00074-X](https://doi.org/10.1016/S0370-1573(98)00074-X). URL <http://www.sciencedirect.com/science/article/pii/S037015739800074X>.
- [59] M. Anselmino, V. Barone, A. Drago, and N. N. Nikolaev. Accessing transversity via  $J/\psi$  production in polarized p vector anti-p vector interactions. *Phys. Lett.*, B594:97–104, 2004. doi: 10.1016/j.physletb.2004.05.029.
- [60] V. Barone, Zhun Lu, and Bo-Qiang Ma. The  $\cos 2\phi$  asymmetry of Drell-Yan and  $J/\psi$  production in unpolarized  $pp$  scattering. *The European Physical Journal C*, 49(4):967–971, Mar 2007. ISSN 1434-6052. doi: 10.1140/epjc/s10052-006-0174-6. URL <https://doi.org/10.1140/epjc/s10052-006-0174-6>.
- [61] A. Sissakian, O. Shevchenko, A. Nagaytsev, and O. Ivanov. Transversity and T-odd PDFs from Drell-Yan processes with  $p p$ ,  $p D$  and  $D D$  collisions. *Eur. Phys. J.*, C59:659–673, 2009. doi: 10.1140/epjc/s10052-008-0806-0.

- [62] M. Anselmino, V. Barone, and M. Boglione. The Sivers asymmetry in DrellYan production at the  $J/\Psi$  peak at COMPASS. *Phys. Lett.*, B770:302–306, 2017. doi: 10.1016/j.physletb.2017.04.074.
- [63] CERN. TE-EPC-LPC in LHC, 2019. URL <http://te-epc-lpc.web.cern.ch/te-epc-lpc/machines/lhc/general.stm>.
- [64] P. Abbon, et al. COMPASS collaboration. The COMPASS experiment at CERN. *Nucl. Instrum. Meth.*, A577:455–518, 2007. doi: 10.1016/j.nima.2007.03.026.
- [65] COMPASS collaboration. COMPASS, Common Muon Proton Apparatus for Structure and Spectroscopy, 2019. URL <https://wwwcompass.cern.ch/>.
- [66] P. Abbon, et al (COMPASS collaboration). The COMPASS setup for physics with hadron beams. *Nuclear Instruments and Methods in Physics Research Section A: Accelerators, Spectrometers, Detectors and Associated Equipment*, 779:69 – 115, 2015. ISSN 0168-9002. doi: <https://doi.org/10.1016/j.nima.2015.01.035>. URL <http://www.sciencedirect.com/science/article/pii/S0168900215000662>.
- [67] B. Parsamyan A. Ivanov and R. Longo. Analysis of 2014 runs with BMS in, January, 16 2016. URL [https://twiki.cern.ch/twiki/pub/Compass/Drell\\_Yan/Subgroupmeeting/Longo\\_Beam2014.pdf](https://twiki.cern.ch/twiki/pub/Compass/Drell_Yan/Subgroupmeeting/Longo_Beam2014.pdf).
- [68] J. Matousek et al. Polarised target for Drell-Yan experiment in COMPASS at CERN, part I. In *22nd International Symposium on Spin Physics (SPIN 2016) Urbana, IL, USA, September 25-30, 2016*, 2017.
- [69] Jaakko Henrik Koivuniemi et al. Large COMPASS polarized solid state target for Drell-Yan physics. *PoS*, PSTP2015:015, 2015. doi: 10.22323/1.243.0015.
- [70] G. Nukazuka. Polarised Target for Drell-Yan Experiment in COMPASS at CERN II, 2016. URL [http://wwwcompass.cern.ch/compass/publications/talks/t2016/nukazuka\\_spin2016.pdf](http://wwwcompass.cern.ch/compass/publications/talks/t2016/nukazuka_spin2016.pdf). The 22nd International Spin Symposium.
- [71] A. Abragam and M. Goldman. Principles of dynamic nuclear polarisation. *Reports on Progress in Physics*, 41:395–467, 1978. doi: 10.1103/PhysRevD.16.2219.
- [72] K. Kondo, et al. Summary of the target polarization results 2015, September, 20 2016. URL [https://twiki.cern.ch/twiki/pub/Compass/Drell\\_Yan/WeeklyDYmeeting/Summary\\_of\\_Target\\_polarization\\_results\\_2015v2.pdf](https://twiki.cern.ch/twiki/pub/Compass/Drell_Yan/WeeklyDYmeeting/Summary_of_Target_polarization_results_2015v2.pdf).
- [73] Radja Boughezal, John M. Campbell, R. Keith Ellis, Christfried Focke, Walter Giele, Xiaohui Liu, Frank Petriello, and Ciaran Williams. Color singlet production at NNLO in MCFM. *Eur. Phys. J.*, C77(1):7, 2017. doi: 10.1140/epjc/s10052-016-4558-y.
- [74] C. Bernet, A. Bravar, J. Hannappel, D.v. Harrach, R. Hermann, E. Kabu, F. Klein, A. Korzenev, M. Leberig, M. Ostrick, J. Pretz, R. Windmolders, and J. Zhao. The COMPASS trigger system for muon scattering. *Nuclear Instruments and Methods in Physics Research Section A: Accelerators, Spectrometers, Detectors and Associated Equipment*, 550(1):217 – 240, 2005. ISSN 0168-9002. doi: <https://doi.org/10.1016/j.nima.2005.05.043>. URL <http://www.sciencedirect.com/science/article/pii/S0168900205012568>.
- [75] J. Barth, J. Bernhard, E. M. Kabuss, N. du Fresne and B. Vet. TRIGGER CONFIGURATION SUMMARY 2002-2012. COMPASS Internal Note, 2016.
- [76] Riccardo Longo. *Measurement of spin effects in the Drell-Yan process at the COMPASS experiment*. PhD thesis, University of Torino, 2018.
- [77] V. Yu. Aleksakhin, Y. Bedfer, S. Gerasimov, and A. Yu. Korzenev. Geometrical event reconstruction in the COMPASS experiment. *Phys. Part. Nucl. Lett.*, 4:350–362, 2007. doi: 10.1134/S1547477107040103. [Pisma Fiz. Elek. Chast. Atom. Yadra2007,no.4,588(2007)].
- [78] R. Fruhwirth. Application of Kalman filtering to track and vertex fitting. *Nucl. Instrum. Meth.*, A262: 444–450, 1987. doi: 10.1016/0168-9002(87)90887-4.

- [79] Torbjrn Sjstrand, Stefan Ask, Jesper R. Christiansen, Richard Corke, Nishita Desai, Philip Ilten, Stephen Mrenna, Stefan Prestel, Christine O. Rasmussen, and Peter Z. Skands. An Introduction to PYTHIA 8.2. *Comput. Phys. Commun.*, 191:159–177, 2015. doi: 10.1016/j.cpc.2015.01.024.
- [80] F. Gautheron, et al. (COMPASS collaboration). COMPASS-II Proposal. 2010, SPSC-P-340, CERN-SPSC-2010-014.
- [81] C. Quintans. LAS Reconstruction Efficiency - DC05/ST03. Drell-Yan Group Internal Communication, March, 12 2014. COMPASS DY.
- [82] C. Quintans. LAS Reconstruction Efficiency without DC05/ST03. Drell-Yan Group Internal Communication, March, 28 2014. COMPASS DY.
- [83] Ran Bi. Simulation of Properties of COMPASS Drift-Chamber Prototypes. APS Division of Nuclear Physics, October 23-26, 2013. URL [http://research.npl.illinois.edu/COMPASS/Talks/Practice-DNP2013/dnp\\_ran.pdf](http://research.npl.illinois.edu/COMPASS/Talks/Practice-DNP2013/dnp_ran.pdf).
- [84] R. Veenhof. Garfield - simulation of gaseous detectors, 1993. URL [http://cmd.inp.nsk.su/old/cmd2/manuals/cernlib/garfield/help/garfield\\_full.html](http://cmd.inp.nsk.su/old/cmd2/manuals/cernlib/garfield/help/garfield_full.html).
- [85] IhnJea Choi. DESY Test-Beam Measurement with COMPASS Drift Chamber Prototypes. APS Division of Nuclear Physics, October 23-26, 2013. URL [http://research.npl.illinois.edu/COMPASS/Talks/Practice-DNP2013/DNP\\_Choi\\_2013\\_10\\_25.pdf](http://research.npl.illinois.edu/COMPASS/Talks/Practice-DNP2013/DNP_Choi_2013_10_25.pdf).
- [86] R. Heitz. A Drift Chamber to Measure Charged Particles at COMPASS-II. APS Division of Nuclear Physics, October 23-26, 2013. URL [http://research.npl.illinois.edu/COMPASS/Talks/DNP2013/Heitz\\_DNP\\_Presentation.pdf](http://research.npl.illinois.edu/COMPASS/Talks/DNP2013/Heitz_DNP_Presentation.pdf).
- [87] R. Heitz. A Large-Area Planar Drift Chamber for the COMPASS Experiment at CERN. The 22nd International Spin Symposium, September 25-30, 2016. URL [http://wwwcompass.cern.ch/compass/publications/talks/t2016/heitz\\_spin2016\\_DC.pdf](http://wwwcompass.cern.ch/compass/publications/talks/t2016/heitz_spin2016_DC.pdf).
- [88] H. Pereira and J. M. Le Goff. Compass Spectrometer Alignment. COMPASS Internal Note, 2003.
- [89] Volker Blobel and Claus Kleinwort. A New method for the high precision alignment of track detectors. In *Advanced Statistical Techniques in Particle Physics. Proceedings, Conference, Durham, UK, March 18-22, 2002*, pages URL-STR(9), 2002. URL <http://www.ippp.dur.ac.uk/Workshops/02/statistics/proceedings//blobel1.pdf>.
- [90] M. Aghasyan, et al. (COMPASS collaboration). First measurement of transverse-spin-dependent azimuthal asymmetries in the Drell-Yan process. *Phys. Rev. Lett.*, 119(11):112002, 2017. doi: 10.1103/PhysRevLett.119.112002.
- [91] M. Anselmino, M. Boglione, U. D’Alesio, F. Murgia, and A. Prokudin. Study of the sign change of the Sivers function from STAR Collaboration W/Z production data. *JHEP*, 04:046, 2017. doi: 10.1007/JHEP04(2017)046.
- [92] Miguel G. Echevarria, Ahmad Idilbi, Zhong-Bo Kang, and Ivan Vitev. QCD Evolution of the Sivers Asymmetry. *Phys. Rev.*, D89:074013, 2014. doi: 10.1103/PhysRevD.89.074013.
- [93] Peng Sun and Feng Yuan. Transverse momentum dependent evolution: Matching semi-inclusive deep inelastic scattering processes to Drell-Yan and W/Z boson production. *Phys. Rev.*, D88(11):114012, 2013. doi: 10.1103/PhysRevD.88.114012.
- [94] Jan Matousek. *Nucleon spin structure studies in Drell-Yan process at COMPASS*. PhD thesis, University of Trieste, April 2018.
- [95] J. Matouek. Weighted transverse spin asymmetries in 2015 COMPASS Drell-Yan data. In *23rd International Symposium on Spin Physics (SPIN 2018) Ferrara, Italy, September 10-14, 2018*, 2018.

- [96] S. Agostinelli et al. Geant4a simulation toolkit. *Nuclear Instruments and Methods in Physics Research Section A: Accelerators, Spectrometers, Detectors and Associated Equipment*, 506(3):250 – 303, 2003. ISSN 0168-9002. doi: [https://doi.org/10.1016/S0168-9002\(03\)01368-8](https://doi.org/10.1016/S0168-9002(03)01368-8). URL <http://www.sciencedirect.com/science/article/pii/S0168900203013688>.
- [97] T. Szameitat. *New Geant4-based Monte Carlo Software for the COMPASS-II Experiment at CERN*. PhD thesis, Albert-Ludwigs-Universitaet Freiburg, 2017.

# Appendix A

## Systematic Error Derivations

### A.1 Systematic Error From Acceptance

For an asymmetry defined as

$$A_\alpha = \frac{1}{|S_T|} \frac{\alpha\sigma_l - \sigma_r}{\alpha\sigma_l + \sigma_r} \quad (\text{A.1})$$

where  $\alpha$  is an acceptance ratio.  $\alpha$  is assumed to be close to unity therefore let

$$\alpha = 1 \pm 2\epsilon, \quad (\text{A.2})$$

where  $\epsilon$  is a small positive number. The asymmetry can therefore be written

$$A_\alpha = \frac{1}{|S_T|} \frac{(1 \pm 2\epsilon)\sigma_l - \sigma_r}{(1 \pm 2\epsilon)\sigma_l + \sigma_r} = \frac{1}{|S_T|} \frac{\sigma_l - \sigma_r \pm 2\epsilon\sigma_l}{(\sigma_l + \sigma_r)(1 \pm \frac{2\epsilon\sigma_l}{\sigma_l + \sigma_r})}. \quad (\text{A.3})$$

From there Taylor expand the denominator to get

$$\begin{aligned} A_\alpha &\approx \frac{1}{|S_T|} \frac{\sigma_l - \sigma_r \pm 2\epsilon\sigma_l}{(\sigma_l + \sigma_r)} \left(1 \mp \frac{2\epsilon\sigma_l}{\sigma_l + \sigma_r}\right) \\ &= A_{lr} \pm \frac{1}{|S_T|} \frac{2\epsilon\sigma_l}{\sigma_l + \sigma_r} \mp A_{lr} \frac{2\epsilon\sigma_l}{\sigma_l + \sigma_r} \mp \frac{1}{|S_T|} \left(\frac{2\epsilon\sigma_l}{\sigma_l + \sigma_r}\right)^2. \end{aligned} \quad (\text{A.4})$$

Assuming  $A_{lr}$  is small and  $\sigma_l \approx \sigma_r$

$$A_\alpha \approx A_{lr} \pm \frac{\epsilon}{|S_T|}. \quad (\text{A.5})$$

The true asymmetry can now be written

$$A_{lr,systematic} \approx A_\alpha \mp \frac{\epsilon}{|S_T|}. \quad (\text{A.6})$$

Including the  $\frac{\epsilon}{|S_T|}$  term as an additive error and using standard error propagation the systematic error can

be approximated as

$$\delta A_{lr,systematic} = \frac{|\alpha - 1|}{2} \frac{1}{|S_T|} + \frac{\delta_{\frac{|\alpha-1|}{2}}}{|S_T|}. \quad (\text{A.7})$$

## A.2 Systematic Error From Left-Right Event Migration

Assuming the fraction of events miss-identified is  $\gamma$  and that the amount of miss-identified events reconstructed left equals the amount of outgoing events reconstructed right

$$A_{lr,measure} = \frac{1}{|S_T|} \frac{(l + \frac{\gamma}{2} N_{total}) - (r + \frac{\gamma}{2} N_{total})}{(l + \frac{\gamma}{2} N_{total}) + (r + \frac{\gamma}{2} N_{total})} = \frac{1}{|S_T|} \frac{l - r}{(l + r)(1 + \gamma \frac{N_{total}}{l+r})}, \quad (\text{A.8})$$

where  $N_{total}$  is the total events measure,  $l$  is the true events measured to the left that should be measured left and  $r$  is the number of events measure to the right that should be measured to the right.

Assuming  $\gamma$  is a small percentage, the denominator can be Taylor expanded to give

$$A_{lr,measure} \approx A_{lr} \left(1 - \gamma \frac{N_{total}}{l+r}\right). \quad (\text{A.9})$$

Including  $\gamma A_{lr,measure}$  as an additive error and using standard error propagation the systematic error can be approximated as

$$\delta A_{lr,systematic} = \gamma A_{lr,measure} + \gamma \delta A_{lr,measure}. \quad (\text{A.10})$$

## A.3 Systematic Error From Event Contamination

Often times the measured counts come from multiple sources where only a measurement from a single source is of interest. As long as the source of interest is dominates the total counts, a left-right asymmetry can still be determined for the source of interest. In this derivation there will be an assumed a signal source with counts  $N_S$  and a background source with counts  $N_{bg}$ , where the background takes into account all processes that are not of interest. Defining the purity of the signal as

$$p = \frac{N_S}{N_S + N_{bg}}, \quad (\text{A.11})$$

then the left-right asymmetry can be determined as

$$\begin{aligned}
A_{lr} &= \frac{1}{|S_T|} \frac{N_{l,S} + N_{l,bg} - (N_{r,S} + N_{r,bg})}{N_{l,S} + N_{l,bg} + (N_{r,S} + N_{r,bg})} \\
&= \frac{1}{|S_T|} \left\{ \frac{N_{l,S} - N_{r,S}}{N_{l,S} + N_{r,S} + N_{l,bg} + N_{r,bg}} + \frac{N_{l,bg} - N_{r,bg}}{N_{l,bg} + N_{r,bg} + N_{l,S} + N_{r,S}} \right\} \\
&= \frac{1}{|S_T|} \left\{ \frac{N_{l,S} - N_{r,S}}{\left( N_{l,S} + N_{r,S} \right) \left( 1 + \frac{N_{l,bg} + N_{r,bg}}{N_{l,S} + N_{r,S}} \right)} + \frac{N_{l,bg} - N_{r,bg}}{\left( N_{l,bg} + N_{r,bg} \right) \left( 1 + \frac{N_{l,S} + N_{r,S}}{N_{l,bg} + N_{r,bg}} \right)} \right\} \\
&= \frac{1}{|S_T|} \left\{ \frac{N_{l,S} - N_{r,S}}{\left( N_{l,S} + N_{r,S} \right) \left( \frac{1}{p} \right)} + \frac{N_{l,bg} - N_{r,bg}}{\left( N_{l,bg} + N_{r,bg} \right) \left( \frac{p}{1-p} \right)} \right\} \\
&= p A_{lr,S} + \frac{1-p}{p} A_{lr,bg}.
\end{aligned} \tag{A.12}$$

This means that by measuring the purity,  $p$ , and the left-right asymmetry,  $A_{lr}$ , the left-right asymmetry from the signal,  $A_{lr,S}$ , can be determined as

$$A_{lr,S} = \frac{1}{p} A_{lr} - \frac{1-p}{p^2} A_{lr,bg}. \tag{A.13}$$

Assuming a purity above 90% and a background left-right asymmetry,  $A_{lr,bg}$ , of 5%

$$A_{lr,S} = 1.11 A_{lr} - 0.123(0.05) = 1.11 A_{lr} - 0.006 \approx 1.11 A_{lr}. \tag{A.14}$$

The systematic error from a purity less than 1 can be determined as

$$\begin{aligned}
A_{lr,S} &= \frac{1}{p} A_{lr} = A_{lr} + \frac{1-p}{p} A_{lr} \\
\Rightarrow \sigma_{A_{lr,S}}^2 &= \sigma_{A_{lr}}^2 + \frac{(1-p)^2}{p^2} \sigma_{A_{lr}}^2 \\
\Rightarrow \sigma_{systematic}^2 / \sigma_{statistic}^2 &= \frac{(1-p)^2}{p^2}.
\end{aligned} \tag{A.15}$$

## Appendix B

### Cross-Check

#### B.1 Left-Right Asymmetry Cross-Check

To ensure the results obtained in this thesis are correct, an independent cross-check was performed by Michael Pesek of the University of Turin. The information provided was the event selection criteria and the definition for a left and a right event. Fig. B.1 shows the comparison of the left-right asymmetry results and as can be seen no discrepancies were found.

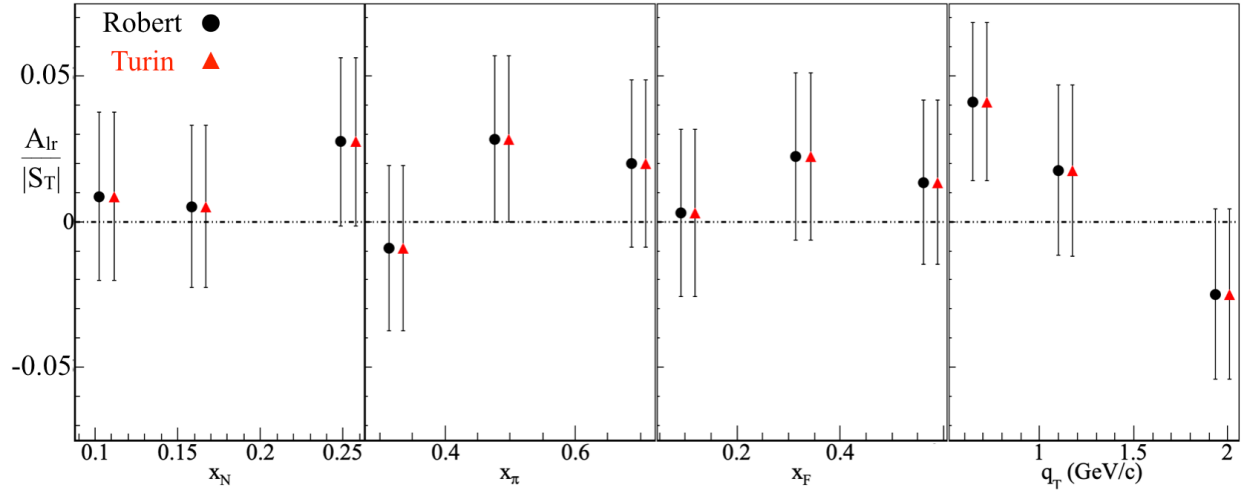


Figure B.1: The left-right asymmetry without corrections for polarization or dilution factor from the W07 period. The values from this thesis are the black circles and the cross-check values are the red triangles.